ABSTRACT

Title of Document:	LIGHT CONTROL OF CHEMICAL SYSTEMS: PHOTOCHEMICAL ELECTRON TRANSFER METHODS FOR RELEASING CALCIUM IONS AND THE PHOTOISOMERIZATION OF ALKENES TO MODULATE RHEOLOGICAL CHANGES.
	Romina R. Heymann Loor, Ph.D., 2021
Directed By:	Professor Daniel E. Falvey, Department of Chemistry and Biochemistry

Our research combines organic photochemistry with the engineering principles of rheology through the study of photorheological fluids (PR). The two photochemical systems researched show changes in the rheological properties brought about by the addition of light. The investigated systems are the photoisomerization of cinnamic acid derivatives in the surfactant, Cetyltrimethylammonium bromide (CTAB), and calcium release through degradation ethylenediaminetetraacetic acid (EDTA) caused by an electron transfer mechanism. The CTAB system shows how a change in molecular conformation can cause significant changes in the bulk property of a solution. The calcium EDTA system employs targeted electron transfer to cause calcium release, which gels the biopolymer alginate with inexpensive, readily available materials.

Chapter 2 details how the orientational binding, intermolecular interactions, and molecular geometry of cinnamic acid derivatives contribute to the rheological

changes in CTAB. ^{1}H NMR titration studies in CTAB identified binding patterns of the additives in CTAB. From those studies orientational binding models were developed for *trans*-ortho-methoxycinnamic acid (tOMCA), *cis*-ortho-methoxycinnamic acid (cOMCA), *meta*-methoxycinnamic acid (mMCA), *para*-methoxycinnamic (pMCA), *ortho*-hydroxycinnamic acid (oCoum), *meta*-hydroxycinnamic acid (mCoum), and *para*-hydroxycinnamic acid (pCoum). ^{1}H-^{1}H 2D NOESY spectra identified through space intermolecular interactions occurring within the micelle. Preliminary data into possible π-anion interaction between tOMCA molecules within the micelle is presented. Photolysis confirmed the creation of cis isomers for all additives but also identified coumarin by-products for oCoum. B3LYP calculations indicated out-of-plane geometry for all the cis isomers and possible intramolecular hydrogen bonding of oCoum. Finally, a model of binding interactions that lead to changes in the packing parameter of the surfactant and, therefore, a change into wormlike micelles for tOMCA versus cOMCA is introduced.

In chapters three and four, we investigated calcium release using sensitizers that promote photoinduced electron transfer. Anthraquinones derivatives were shown in Chapter 3 to release calcium in stoichiometry amounts with UV light irradiation. In Chapter 4, flavins produced 1000-fold calcium release to sensitizer concentration in the visible light spectrum. In both chapters, there are detailed calcium release studies, degradation studies, and alginate experiments. We present calcium release studies at acidic and neutral pH, quantum yields, degradation of EDTA, sensitizer reoxidation studies, sensitizer degradation data,

fluorescence, and transient spectra. While enough calcium was released to produce alginate gels, none were made in vitro at neutral and acidic pH.

LIGHT CONTROL OF CHEMICAL SYSTEMS: PHOTOCHEMICAL ELECTRON TRANSFER METHODS FOR RELEASING CALCIUM IONS AND PHOTOISOMERIZATION OF ALKENES TO MODULATE RHEOLOGICAL CHANGES.

By

Romina R. Heymann Loor

Dissertation submitted to the Faculty of the Graduate School of the
University of Maryland, College Park, in partial fulfillment
of the requirements for the degree of
Doctor of Philosophy
2021

Advisory Committee:
Professor Daniel E. Falvey, Chair
Professor Neil Blough
Professor Jeffery Davis
Professor Andrei Verdernikov
Professor Paul C. Gekker

© Copyright by

Romina R. Heymann Loor

2021

Dedication

Rev. Dr. Rashelle A Rogers (1976-2019) who never gave up living and loving life, even until the very end and to Dr. Rocio Loor, my mother.

Acknowledgments

It may take a village to raise a child, but I feel it took a small country to help me through this unexpectedly long Ph.D. journey. But, just like the nontraditional path I took to completion, so I will have to spend quite a bit of time showing gratitude to the wonderful people who have been part of this dissertation.

First and foremost, to my family. My mother, Mariana Rocio Loor, M.D., whose strength and courage in the face of raising three children, at times all on her own, while creating a life of integrity and love for us in a new country, will always be my model of greatness. My stubborn perseverance and ability to get back up are all because of your endless encouragement and example. My dad, Max Carlos Heymann, taught me to be fascinated by the world, science, and its people; thank you. I remember learning to marvel at nature by your side. Thank you both for all your sacrifices.

Much love to my brother Max Christian, my best friend, who somehow brings a much-needed perspective to my life and sometimes well-deserved reality checks. I'm probably still here because of you, lil brother; you are so loved. My "baby" brother Julian who seems to know how to remind me not to take myself too seriously and perhaps get up to no good- my Calvin and Hobbes. While distance may separate me from my family in Ecuador, it does not separate me from their support or love. To my "hermanitos"- Christina, Samantha, Valentina, and Adrian- you bring me happiness seeing all your adventures and growth. To all my family in the US and Ecuador- I love you- and thank you for your support. Insert here an

extensive list of aunts, uncles, first cousins, second cousins who all have wished me well and been by my side.

At the University of Maryland, I would like to thank my advisor Dr. Falvey. I don't think anyone else would have given me the space and time I needed to be able to finish. I am grateful for the help you have given me but most importantly, thank you for not giving up on me. To my committee in the department, Dr. Davis, Dr. Vedernikov, and Dr. Blough, thank you for being part of this process through all these years. A big thank you to my former lab mates Megan, Brian, Derek, Raffael, and Steven.

Dr. Mullen, thank you for listening all the times I didn't know how to move forward. I know I sat in your office more than once confused, but you took time out of your schedule to talk to me even though I wasn't your graduate student.

Dr. Yui-Fie, the NMR lab felt like a second home after all the late nights working and analyzing data. You were so generous with your time and knowledge. I would not have been able to finish my experiments without your help. You took me on as an assistant allowing me to learn about the maintenance of the NMR spectrometers and the science behind the spectra. I will always love the discovery in NMR.

Teaching was always been a calling for me. Thank you to Dr. Montague-Smith, Dr. Dixon, and Dr. Friedman; it was a pleasure to TA for you and be inspired by your teaching practices. I will never forget how much I enjoyed my time teaching a lecture during my GAAN fellowship. Thank you, Dr. Davis, for the opportunity to teach a class and learn from you. The experience of being one of the graduate

supervisors at the 44th International Chemistry Olympiad taught me so much about organization and what it takes to coordinate large labs. Thank you, Dr. Vedernikov, for your trust and guidance. To Diane Canter for always answering the phone to help me navigate copious amounts of paperwork.

Dr. Janie Dubois, my time working for you was an inspiration. You were my mentor, role model, and friend. To the team who worked in JIFSAN-FDA and Waters company partnership- thank you for the time I spent learning how to work in a team setting. It was an experience of a lifetime.

I could not have made it through as many years striving to finish without my friends. Tonette and Rashelle -from the first time I thought about graduate school while I taught high school until the very last moment you two stood by my side- our friendship never wavered. Rev. Dr. Rashelle Rogers, it is the memory of your struggle and friendship, your words that led me through all the struggles I've had to endure during this time. This is our doctorate.

Maria, Aaron, Dulith, Urszula, Shahnawaz, Apurva, Adi, and Rishvi - the time carving pumpkins, getting dressed up, and almost dying while traversing through the wilds of the DMV were some of the best memories of graduate school. I was lucky that we all fell in together. To the wonderful-Anna, Deana, and Dory- thank you for your amazing friendship and yummier brunches. To my adoptive brothers -Brad, Dave, Jarred- you are the epitome of strong, smart, and kind men. A special thanks to Dr. Ryan Burgin, who from England made sure I didn't butcher the English language too terribly.

To my former roommates who somehow became my friends, thank you for the many times you helped me, without knowing, to be able to get through everything in graduate school. The second list of beautiful people who came into my life and made it better – Johanna, Ciccio, Marilena, Maya, Diana, Ricky, Vale, Douglas, Sara, and Yanjia. Special hugs to Giulia and Tony, my very Italian friends, ensured I didn't feel alone on this last leg.

Finally, to Dr. Amy Boyd, a heartfelt thank you. You saved my dissertation with your mentorship program. The day I found the "Stuck to Unstoppable" women was when I finally started facing what was holding me back. Through loss and COVID, this amazing group of women from different disciplines and countries came together to make a small family. Tara- thank you -through you, I was able to find the hero's journey in my own struggles. Yvette- thank you for helping me see the need for strong habits and persistence with a touch of kindness and southern charm. Kristy- thank you for your pragmatic sense of work and life. Jeanette- thank you for your support and NY sassiness. Janelle – thank you for helping me get through my loss and for your support through it. There are more thank yous than I can finish so some more of the wonderful group- Sally, Erica, Linda, and Paula. To my final dissertation partner Leslie- you are a blessing – our early morning writing sessions kept me going. We are finishing together and strong! To my students. It has been a privilege and honor to be your mentor, coach, and tutor. Your trust in me made sure I would be able to finish. Finally, to the countless others I did not name but through small or large acts helped me - thank you.

Table of Contents

Dedication ii
Acknowledgments iii
Table of Contents vii
List of Tables x
List of Figures xii
List of Schemes xxiii
List of Abbreviations xxv
Chapter 1: Introduction 1
1.1 Research introduction and significance 1
1.2 Photochemistry Background 2
1.3 Photoisomerization 7
1.4 Photoinduced Electron Transfer 12
1.5 Self-Assembly of Surfactants 15
1.6 Rheological Measurements Background 17
Chapter 2: Elucidation of Binding Characteristics between CTAB and Cinnamic Acid Derivatives that Change Solution Rheology upon Photoisomerization. 22
2.1 Introduction 22
2.2 Experimental Section 26
2.2.1 Materials: 26
2.2.2 Photolysis Studies: 26
2.2.3 Titration Methodology: 27
2.2.4 NMR Spectroscopy Methodology: 28
2.2.5 Rheological Studies Methodology: 27
2.3 Results and Discussion: 28
2.3.1 Steady state and Dynamic Rheological Measurements 29
2.3.2 1-D ^{1}H NMR titrations studies of additives in CTAB 34
2.3.3 Photolysis studies of CTAB and Additives: 45
2.3.4 Two-Dimensional NOESY of additives with CTAB surfactant 50
2.3.4 B3LYP Calculations 64

2.3.5 Model of molecular interactions in CTAB micelles 67
2.4 Conclusion 69
Chapter 3: Release of Calcium Through Disruption of EDTA Chelator Binding by Anthraquinone Sensitizers Electron Donation. 72
3.1 Introduction 72
3.2 Materials and methods 76
3.2.1 Photolysis of samples 76
3.2.2 Calcium Dye Assay 77
3.2.3 1-Dimensional ^{1}H-NMR 78
3.2.4 Instrumentation 78
3.3 Results and Discussions 78
3.3.1 Calcium Release Experiments: 79
3.3.2 ^{1}H Nuclear Magnetic Resonance Results: 88
3.3.3 Alginate Results: 94
3.5 Conclusion 96
Chapter 4 Visible Light Initiated Release of Calcium Ions through Photochemical Electron Transfer Reactions.[118] 98
4.1. Introduction 98
4.2 Materials and Methods 101
4.2.1 Materials 101
4.2.2 Chemical Synthesis and Characterization 102
4.2.3 Photolysis of Samples 102
4.2.4 Calcium Assay 103
4.2.5 Quantum Yield 104
4.2.6 Laser Flash Photolysis 104
4.2.7 Peroxide testing: 105
4.2.8 1-Dimensional Co-axial ^{1}H-NMR 105
4.2.9 Instrumentation 106
4.3 Results and Discussion 106
4.3.1 Calcium Release 108
4.3.2 Quantum Yields of Calcium Release: 110
4.3.3 Reoxidation of Sensitizer: 111

4.3.4 Laser Flash Photolysis and Fluorescence..... 114
4.3.5 Experiments on EDTA degradation:..... 117
4.3.6 Effect of pH and wavelength on the amount of calcium released..... 123
4.3.7 Experiments on the effect of pH and wavelength on amount of Sensitizer degradation: 126
4.3.8 Alginate Gelation Experiments..... 130
4.4 Conclusions 131
Chapter 5 Conclusion and Future work 133
Appendix A: Supporting Information for Photoisomerization of Cinnamic Acid Derivatives in CTAB 137
Appendix B Supporting Information for Anthraquinone Ca-EDTA 151
Appendix C Supporting Information for Riboflavin Ca-EDTA..... 160
Bibliography..... 164

List of Tables

Table 2- 1 Name and abbreviation of additives used in study 28

Table 3- 1 Photophysical properties of anthraquinone derivatives used in this study** 73

Table 3- 2 Key Calcium release results with varying Sensitizer and Ca-EDTA concentrations 84

Table 3- 3 Relative Average Concentration Results from NMR photolysis time course in mM and percentage calculations 92

Table 4- 1 Key photophysical properties of flavin sensitizers. 107

Table 4- 2 Photolytic release of Ca^{2+} with various sensitizers at differing wavelengths 109

Table 4- 3 Relative quantitation results from the 50 μM RB, 1mM EDTA, pH = 4.3, 447 nm photolysis. 121

Table 4- 4 Sample data for 180 min of photolysis at varying starting pH and wavelengths of Photolysis μM sensitizer and 20 mM Ca-EDTA. 126

Table A- 1 Parameters for acquisition of ^{1}H NMR in Bruker 600 Mhz spectrometer, BBI prode..... 137

Table A- 2 Parameters for acquisition of ^{1}H NMR in Bruker 400 Mhz spectrometer, BBI probe..... 137

Table A- 3 Titration study chemical shifts (ppm) of aromatic protons 147

Table A- 4 Titration study chemical shifts change (Δ ppm) of aromatic protons 148

Table A- 5 Titration study chemical shifts (ppm) of CTAB protons 149

Table A- 6 Titration study chemical shifts change (Δ ppm) of CTAB protons ... 150

Table B- 2 Sample integration values for anthraquinone relative concentration calculations for photolysis time course 158

Table B- 3 ^{1}H NMR calculated relative concentrations for photolysis time course of 2.0 mM AQDS-2,6 in 10mM Ca-EDTA, 5mMtBOH Coaxial, 350 nm Rayonet 159

Table B- 4 ^{1}H NMR calculated relative concentrations for photolysis time course of 2.0 mM AQDS-1,5 in 10mM Ca-EDTA, 5 mM tBOH Coaxial, 350 nm Rayonet 159

Table C- 1 Table of Quantum yield calculation with standard error. 160

Table C- 3 Table of ^{1}H NMR experiment parameters 161

List of Figures

Figure 1- 1 Diagram describing the ground state, singlet excited state and triplet state electron spins and energy levels characterizing each. 3

Figure 1- 2 Jablonski diagram describing photon absorption and subsequent intramolecular excited state processes[15] 5

Figure 1- 3 Photoisomerization of stilbene, azobenzene and spiropyran at different corresponding wavelengths. 8

Figure 1- 4 Generalized schematic of a surface diagram with two potential energy surfaces in a photoreaction such as photoisomerization adapted from reference [18, 23, 24] 9

Figure 1- 5 Schematic representation of photoinduced electron transfer. 13

Figure 1- 6 a) General diagram of surfactant molecule b) cetyltrimethylammonium cationic surfactant and c) dodecyl sulfate anionic surfactant. [36] 15

Figure 1- 7 Surfactant self-assemblies as a relationship to P[34,37] 17

Figure 2- 1 Diagram of transition from spherical micelles to wormlike micelles triggered by light. 22

Figure 2- 2 Coumarate derivatives and methoxy-cinnamic acid derivatives used in our isomerization studies as additives and the abbreviations. 24

Figure 2- 3 Steady state rheology of 20 mM CTAB and 20mM additive before and after 5 hr photolysis a) tOMCA b) cOMCA. 29

Figure 2- 4 Dynamic rheology a) cisOMCA preUV b) cisOMCA postUV c) tOMCA preUV and d) tOMCA postUV 31
Figure 2- 5 Steady state rheology 20 mM CTAB to 20 mM additive. Pre and post photolysis on a Rayonet 254nm. a) mMCA b) pMCA c) oCOUM and d) mCOUM 32
Figure 2- 6 Dynamic Rheology of 20 mM CTAB: 20 mM additive. Post UV with Rayonet 254 nm. a) mMCA preUV b) mMCA post UV c) mCOUM preUV d) mCOUM post UV e) oCOUM preUV f) oCOUM postUV 33
Figure 2- 7 Conjugated region of additive tOMCA at various amounts in 20 mM CTAB titration a) 2 mM tOMCA b) 20mM CTAB c) 2 mM tOMCA:CTAB d) 5 mM tOMCA:CTAB e)10 mM tOMCA:CTAB f) 20 mM tOMCA:CTAB 36
Figure 2- 8 CTAB region of H-NMR at various amounts of tOMCA in 20 mM CTAB a) 2 mM tOMCA b) 20mM CTAB c) 2 mM tOMCA:CTAB d) 5 mM tOMCA:CTAB e) 10 mM tOMCA:CTAB f) 20 mM tOMCA:CTAB 37
Figure 2- 9 Substituent NMR Signals cOMCA in 20mM a) 2 mM cOMCA:CTAB b) 20mM CTAB c) 2 mM cOMCA:CTAB d) 5 mM cOMCA:CTAB e)10 mM cOMCA:CTAB f) 20 mM cOMCA:CTAB 38
Figure 2- 10 CTAB region NMR Signals cOMCA in 20mM a) 2 mM cOMCA:CTAB b) 20mM CTAB c) 1:10 , 2 mM cOMCA:CTAB d) 1:4, , 5 mM cOMCA:CTAB e) 1:2 ,10 mM cOMCA:CTAB f) 1:1, 20 mM cOMCA:CTAB 40
Figure 2- 11 Chemical shift difference graph versus concentration a) tOMCA b) cOMCA and c) a visual representation of the chemical shift difference starting with the difference between 2mM additive 0 mM CTAB to 2mM 20

mM CTAB. The second figure is 2mM additive to 20 mM additive 20 mM CTAB 41
Figure 2- 12 Chemical shift difference graph versus concentration a) mMCA b) pMCA and c) a visual representation of the shift magnitude and direction by color coding 42
Figure 2- 13 Chemical shift difference graph versus concentration a) oCoum b) mCoum c) pCoum and d) a visual representation of the shift magnitude and direction by color coding. 44
Figure 2- 14 Photolysis of tOMCA, 254 nm Rayonet a) 20 mM tOMCA, 20mM CTAB b) 30 min UV, 20 mM tOMCA, 20mM CTAB c) 20 mM tOMCA D_2O d) 30 min UV, 20 mM tOMCA 47
Figure 2- 15 Photolysis ^1H NMR studies of mCoum at 298 K. Photolysis with Rayonet 254 a) 20 mM mCoum, 20 mM CTAB b) 20 mM mCoum, 20 mM CTAB photolysis 60 min c) 20 mM mCoum D_2O d) 20 mM mCoum 60 min photolysis. 48
Figure 2- 16 Photolysis of 20mM oCoum at 254 nm in a Rayonet a) 0 min b) 30 min c) 60min. Red asterisks indicate coumarin proton signals. Blue asterisks denote cis-ortho-coumarate signals 50
Figure 2- 17 ^1H-^1H 2D NOESY of 10 mM tOMCA 20 mM CTAB at 303 K, 600 MHz Bruker magnet with BBI probe, D_2O solvent. Strongest NOESY cross peak layer. 52
Figure 2- 18 H-^1H 2D NOESY of 10 mM tOMCA 20 mM CTAB at 303 K, 600 MHZ Bruker magnet with BBI probe, D_2O solvent. 53

Figure 2- 19 Subset of the ^{1}H-^{1}H 2D NOESY focusing on the strongest NOESY signals for the tOMCA aromatic proton section. Sample was of 10 mM tOMCA 20 mM CTAB at 303 K, 600 MHZ Bruker magnet with BBI probe, D_2O solvent 55

Figure 2- 20 ^{1}H-^{1}H 2D NOESY of 10 mM cOMCA 20 mM CTAB at 298 K, 600 MHZ Bruker magnet with 5 mm BBI probe, D2O solvent. Strongest NOESY cross peak layer 56

Figure 2- 21 Diagram illustrating the strongest NOESY signals ls for tOMCA and cOMCA. 57

Figure 2- 22 ^{1}H-^{1}H 2D NOESY of 5 mM oCoum 20 mM CTAB at 298 K, 600 MHZ Bruker magnet with BBI probe, D2O solvent. Strongest NOESY cross peak layer. 58

Figure 2- 23^{1}H-^{1}H 2D NOESY of 5 mM mCoum 20 mM CTAB at 298 K, 600 MHZ Bruker magnet with BBI probe, D2O solvent. Strongest NOESY cross peak layer. 59

Figure 2- 24 Diagram illustrating the NOESY signals ls for a) oCoum and b) mCoum. 61

Figure 2- 25 ^{1}H-^{1}H 2D NOESY of 10 mM pCoum 20 mM CTAB at 298 K, 600 MHZ Bruker magnet with BBI probe, D2O solvent. Strongest NOESY cross peak layer. 62

Figure 2- 26 Diagram illustrating the NOESY signals ls for a) pCoum orientation with the carboxylate toward the headgroup and b) pCoum orientation with the hydroxy group toward the ammonium head group. 63

Figure 2- 27 DFT-B3LYP/6-31+G(d,p) 3-D molecule and dihedral angles for cis and trans OMCA isomers. 64
Figure 2- 28 DFT-B3LYP/6-31+G(d,p) 3-D molecular model with dihedral angles of cis and trans isomers for listed derivatives. 66
Figure 2- 29 Molecular model detailing the different interactions of tOMCA and cOMCA with CTAB that leads to the difference in packing parameter. 67

Figure 3- 1 Absorption spectrum for sensitizer anthraquinone 2,6-disulfonate and anthraquinone 2- sulfonate. 74
Figure 3- 2 Modified CPC Calcium assay steps for determination of photolysis calcium concentration. 77
Figure 3- 3 Variable AQS-2 Sensitizer to Ca-EDTA ratios. All solutions contained fixed 2.5 mM Ca-EDTA, photolysis at 350nm, Rayonet. 80
Figure 3- 4 Variable AQS-2 concentrations in 25 mM Ca-EDTA, 340 nm with cut-off filter, Hg-Xe lamp 81
Figure 3- 5 Photolysis at 254 nm light measuring for calcium release. Ca-EDTA concentration was at 25 mM. Each sensitizer used was at 2.5 mM 83
Figure 3- 6 Absorption spectra of the oxidized/reduced form of AQS2. Reaction conditions are as follows: AQS-2 = 0.5 M in Ca-EDTA= 25 mM, Xe-Hg Full Spectrum, Nitrogen Purge, 0.2 mM Ca release after 60min. 85
Figure 3- 7 Photolysis under Anaerobic and Aerobic conditions. Solutions consisted of 2.5 mM AQS2 sensitizer and 25mM Ca-EDTA at pH=7 87

Figure 3- 8 Anthraquinone H NMR, in D2O, 298K, 20 min photolysis at 350nm. 2.0 mM sensitizer, [Ca-EDTA] was set at 10 mM. 89

Figure 3- 9 AQS-2 ^{1}H-NMR photolysis time course. Solution contained 20 mM AQS-2, 10mM Ca-EDTA. 350nm photolysis lamp. 90

Figure 3- 10 ^{1}H NMR of EDTA and of Ca-EDTA causing the broadening of NMR signal. 93

Figure 3- 11 Diagram of alginate monomers and their box-like arrangement with a second monomer when a divalent ion is added, leading to the formation of gels 95

Figure 3- 12 Gelation of alginate by calcium from photolysis solution. Each solution had drops of 3% by weight BioA Alginate added. a) water control b) Ca-EDTA control c) photolysis of AQDS-2,6 with 254 nm Rayonet. The solution consisted of 10 mM AQDS-2,6 , 25 mM Ca-EDTA 96

Figure 4- 1 Examples of previously synthesized photolabile calcium cages nitr-5 Tsien[127] lab, DM-nitrophen by Ellis-Davies[135] lab and nitr-T a more recent addition by the del Campol ab[122] 98

Figure 4- 2 Depiction of photocatalyzed calcium release system used in our study 100

Figure 4- 3 Coaxial NMR set up a) the coaxial tube b) the coaxial tube in NMR tube before being placed in NMR, the lines show area where signal is collected. 105

Figure 4- 4 Photorelease of calcium from EDTA with RBTA using various light sources. Initial [Ca-EDTA]=25mM in water (pH 6.5-7.3)[118]..... 108
Figure 4- 5 Change in absorbance of sample containing [Ca-EDTA]= 12.5mM, [RB]= 40 μM. Spectra were taken before photolysis, after exposure to an unfiltered Xe-Hg lamp, and then after purging the solution with oxygen for 5 to 10 minutes.[118] 113
Figure 4- 6 LFP and Quenching Transient absorption spectrum of RB (123 μM) with 2.5 mM Ca-EDTA in phosphate buffered water (pH= 7.4). Waveforms at 660 nm with increasing [Ca-EDTA] are shown in the inset.[118]..... 115
Figure 4-7 Fluorescence quenching (λ_{ex} = 320 nm) of RB with varying concentrations of Ca-EDTA in water (pH = 6.8). Fluorescence quenching (inset) measured at 547 nm.[118]..... 117
Figure 4- 8 Stacked ^{1}H NMR of pre (blue) and post (red) photolysis of a solution containing 75 μM Riboflavin , 1.5 mM EDTA, at pH 7.3. Photolysis wavelength was 447 nm for 60min. The magnified window shows the formation of formate after photolysis 119
Figure 4- 9 Stacked 1H NMR of pre (red), 15 min (green) and 30 min (blue) photolysis of a solution containing 50 μM Riboflavin, 1.0 mM EDTA, at pH 4.3. Photolysis at 447 nm. 120
Figure 4- 10 ^{1}H NMR of pre (blue) and post (red) photolysis of a solution containing 75 μM Riboflavin, 1 mM Ca-EDTA, at pH 7.3. Photolysis wavelength was 447 nm for 30min using a 1 W, CW diode laser. The magnified window shows the appearance of formate after photolysis..... 122

Figure 4- 11 ^{1}H NMR at pH= 4 of a) Ca-EDTA b) RBTA c) pre UV solution of RBTA (2.1 μM) and Ca-EDTA (10mM) solution in H_2O/D_2O d) 40 min photolysis with a Hg lamp with a 360 nm cutoff filter of c. 123

Figure 4- 12 Photolysis solutions at 20 mM Ca-EDTA while varying wavelength, pH and riboflavin concentrations to identify factors that have the largest effect on calcium release. a) 350 nm , pH 4 wand 5 μM riboflavin. b) 447 nm , pH 4 riboflavin. c) 350 nm, pH 7. 124

Figure 4- 13 Photolysis of 20 mM Ca-EDTA with 50 μM Riboflavin for photolysis wavelength of 447 and 350 at pH 4 and pH 7. 125

Figure 4- 14 Possible degradation products from the photolysis of RF with Ca-EDTA..... 127

Figure 4- 15 Riboflavin degradation UV-Vis at various times, wavelengths and pH as stated on graph. Riboflavin was at 50 μM, Ca-EDTA at 5 mM. 128

Figure 4- 16 Comparison of percent calcium release and percent depletion of RB versus time. Each mixture contained 50 μM RB, 5 mM EDTA, a) and b) are pH= 4, c) and d) pH= 7.3; RF concentration was based on the loss of 445 nm molar wavelength and use of beer's law..... 129

Figure 4- 17 Ca-EDTA 20 mM, 20 μM RBTA, 60 min photolysis solution. 2% by weight alginate was added to the solution to both solutions. 130

Figure 5- 1 Molecular interactions in cinnamic acid derivative isomers and CTAB. Visualization of morphology change..... 133

Figure 5- 2 Depiction of photoinduced electron transfer by sensitizer and calcium release..... 134
Figure 5- 3 Visualization of Ca-EDTA degradation through photoinduced electron transfer reaction leading to the release of calcium 135

Figure A- 1 ^{1}H NMR spectra of 10 mM MCA, 20 mM CTAB in D_2O, 298 K. Photolysis with Rayonet 254 nm bottom 0 min and top 60 min. 138
Figure A- 2 ^{1}H NMR spectra of 10 mM MCA in D_2O, 298 K. Photolysis with Rayonet 254 nm a) 60 min b) 0 min 138
Figure A- 3 4 ^{1}H NMR spectra of 20 mM oCoum 20mM CTAB in D_2O, 298 K. Photolysis with Rayonet 254 nm a) 60 min b) 30 min c) 0 min 139
Figure A- 5 6 ^{1}H NMR spectra of 20 mCoum in D_2O, 298 K. Photolysis with Rayonet 254 nm a) 60 min b) 30 min c) 0 min..... 139
Figure A- 7 ^{1}H NMR spectra of 20 mCoum 20 mM CTAB in D_2O, 298 K. Photolysis with Rayonet 254 nm a) 60 min b) 0 min..... 140
Figure A- 8 ^{1}H NMR spectra of 20 pCoum in D_2O, 298 K. Photolysis with Rayonet 254 nm a) 0 min b) 30 min c) 60 min..... 140
Figure A- 9 ^{1}H NMR spectra of 20 pCoum 20 mM CTAB in D_2O, 298 K. Photolysis with Rayonet 254 nm a) 0 min b) 20 min c) 30 min 141
Figure A- 10 Aromatic chemical shift region of mMCA. ^{1}H NMR spectra, Bruker 600 MHz , 298 K a) 2 mM mMCA control b) 20 mM CTAB control c) 2 mM mMCA d) 3 mM mMCA e) 5 mM mMCA f) 6 mM mMCA g) 10 mM MCA h) 20 mM mMCA to 20 mM CTAB. 141

Figure A- 11 CTAB chemical shift region of mMCA. ^{1}H NMR spectra, Bruker 600 MHz , 298 K a) 2 mM mMCA control b) 20 mM CTAB control c) 2 mM mMCA d) 3 mM mMCA e) 5 mM mMCA f) 6 mM mMCA g) 10 mM MCA h) 20 mM mMCA to 20 mM CTAB. 142

Figure A- 12 Aromatic chemical shift region ^{1}H NMR spectra of pMCA. Bruker 600 MHz , 298 K a) 2 mM pMCA control b) 20 mM CTAB control c) 2 mM pMCA d) 3 mM pMCA e) 5 mM pMCA f) 6 mM pMCA g) 10 mM pMCA h) 20 mM pMCA to 20 mM CTAB. 142

Figure A- 13 CTAB chemical shift region of ^{1}H NMR spectra of pMCA. Bruker 600 MHz , 298 K a) 2 mM pMCA control b) 20 mM CTAB control c) 2 mM pMCA d) 3 mM pMCA e) 5 mM pMCA f) 6 mM pMCA g) 10 mM pMCA h) 20 mM pMCA to 20 mM CTAB. 143

Figure A- 14 Aromatic chemical shift region ^{1}H NMR spectra of oCoum. Bruker 600 MHz , 298 K a) 10 mM oCoum control b) 20 mM CTAB control c) 2 mM oCoum d) 3 oCoum mM e) 4 mM oCoum f) 5 mM oCoum g) 6 mM oCoum h) 7 mM oCoum i) 8 mM oCoum j) 10 mM oCoum k) 15 mM oCoum to 20 mM CTAB..... 143

Figure A- 15 CTAB chemical shift region ^{1}H NMR spectra of oCoum. Bruker 600 MHz , 298 K a) 10 mM oCoum control b) 20 mM CTAB control c) 2 mM oCoum d) 3 oCoum mM e) 4 mM oCoum f) 5 mM oCoum g) 6 mM oCoum h) 7 mM oCoum i) 8 mM oCoum j) 10 mM oCoum k) 15 mM oCoum to 20 mM CTAB..... 144

Figure A- 16 Aromatic chemical shift region ^{1}H NMR spectra of mCoum. Bruker 600 MHz , 298 K. a) 10 mM mCoum control b) 20 mM CTAB control c) 2 mM mCoum d) 5 mM mCoum e) 10 mM mCoum f) 20 mM mCoum in 20mMCTAB 144
Figure A- 17 CTAB chemical shift region ^{1}H NMR spectra of mCoum. Bruker 600 MHz , 298 K.a) 10 mM mCoum control b) 20 mM CTAB control c) 2 mM mCoum d) 5 mM mCoum e) 10 mM mCoum f) 20 mM mCoum in 20mMCTAB 145
Figure A- 18 Aromatic chemical shift region ^{1}H NMR spectra of pCoum. Bruker 600 MHz , 298 K a) 10 mM pCoum control b) 10 mM CTAB control c) 2 mM pCoum d) 5 mM pCoum e) 8 mM pCoum f) 10 mM pCoum g) 15 mM pCoum h) 20 mM pCoum in 20mMCTAB 145
Figure A- 19 CTAB chemical shift region ^{1}H NMR spectra of pCoum. Bruker 600 MHz , 298 K a) 10 mM pCoum control b) 10 mM CTAB control c) 2 mM pCoum d) 5 mM pCoum e) 8 mM pCoum f) 10 mM pCoum g) 15 mM pCoum h) 20 mM pCoum in 20mMCTAB 146

Figure B- 1 Sample error calculations and percent error for calcium release used in quantum yields 152
Figure B- 2 Calibration Curve Error Calculations using LINEST linearity test... 152
Figure B- 3 ^{1}H NMR of *tert*-butyl alcohol with DSS standard at 298 K and 303 K 153

Figure B- 4 ^{1}H NMR of *tert*-butyl alcohol 254 nm Rayonet 20 min photolysis, 298 K 153
Figure B- 5 ^{1}H NMR spectra AQS-2, 2.5mM in D_2O, 298 K 154
Figure B- 6 ^{1}H NMR spectra AQDS-1,5 2.5mM, in D_2O, 298 K 154
Figure B- 7 ^{1}H NMR spectra AQDS-2,6 2.5mM in D_2O, 298 K 155
Figure B- 8 ^{1}H NMR spectra of 2.5mM AQDS-2,6 in10mM Ca-EDTA, 298 K. Photolysis Rayonet 350 nm. Times points bottom to top : 0, 1, 5, 10, 20 min 156
Figure B- 9 H NMR spectra of 2.5mM AQDS1,5 in10mM Ca-EDTA, 298 K. Photolysis Rayonet 350 nm. Times points bottom to top : 0, 1, 5, 10, 20 min 157
Figure B- 10 Sample integration figure of anthraquinone region 157

Figure C- 1 Graph of Calcium release experiments used in Quantum Yield Calculations overlapped for Error Calculation 160
Figure C- 2 Control experiment illustrating the background level of free Ca^{2+} detected in our assay after photolysis (350 nm) for the given time in the absence of sensitizer. 161
Figure C- 4 ^{1}H NMR spectrum of RBTA in CD_3Cl 162
Figure C- 5 ^{1}H NMR or EDTA at acidic and neutral pH 163
Figure C- 6 Photolysis of RBTA (2.1 μM) and EDTA (25mM) in H_2O/D_2O with a Hg lamp with a 360 nm cutoff filter. Photolysis for 40 minutes 163

List of Schemes

Scheme 3- 1 Quinone one-electron reduction from a) oxidized quinone to b) semiquinone and then to fully reduced c) hydroquinone 72

Scheme 3- 2 Anthraquinone 1 electron and 2 electron reduction/oxidation..... 86

Scheme 4- 1 The reversible oxidation-reduction cycle of riboflavin's isoalloxazine moiety using one or two electron transfer accompanied with a proton addition or abstraction.[158] 112

Scheme 4- 2 Proposed mechanism for the degradation of Ca-EDTA chelate from the electron donation from excited state riboflavin. 114

Scheme 4- 3 Proposed possible first steps in EDTA degradation by electron transfer which accounts for formaldehyde formation 118

Scheme B- 1 Photoreduction of AQS-2 155

Scheme B- 2 Photoreduction of AQS-1,5 156

Scheme B- 3 Photoreduction of AQS-2,6 156

List of Abbreviations

AQS-2	Anthraquinone-2-sulfonic acid
AQDS-2,6	Anthraquinone-2,6-disulfonic acid
AQDS-1,5	Anthraquinone-1,5-disulfonic acid
cOMCA	cis-ortho-methoxy-cinnamic acid
CPC	*o*-Cresolphthalein Complexone
CTAB	Cetyl trimethylammonium bromide
CTAOH	Cetyltrimethylammonium hydroxide
EDDA	Ethylenediamine-*N,N'*-diacetic acid
EDTA	Ethylenediaminetetraacetic acid
h	Planck's constant
hv	Energy of a photon
HOMO	Highest Occupied Molecular Orbital
ISC	Intersystem crossing
LUMO	Lowest Unoccupied Molecular Orbital
M	Molarity. ($mol \bullet L^{-1}$)
M_r	Molar Mass
NOE	Nuclear Overhauser Effect
NOESY	NOE SpectroscopY
mCA	meta-methoxycinnamic acid
mCoum	meta-hydroxycinnamic acid
NMR	nuclear magnetic resonance

pCoum	para-hydroxycinnamic acid
PET	Photoinduced Electron Transfer
OMCA	Ortho-methoxy-cinnamic acid
S_0	Singlet ground-state
S_1*	Excited-state singlet, first energy level
S_n*	Excited-state singlet, any excited level
SET	Single electron transfer
STD	standard
RB	Riboflavin
RBTA	Riboflavin tetraacetate
	2',3',4',5'-tetraacetylriboflavin
T_1*	Excited-state triplet, first energy level
T_n*	Excited-state triplet, any energy level
tCA	Trans-cinnamic acid
tOMCA	Trans-ortho-methoxy-cinnamic acid
v	frequency

Chapter 1: Introduction

1.1 Research introduction and significance

Intelligent “smart” materials respond to stimuli and affect changes in their environment. In our work we look at systems that will change their rheological properties such as, viscosity, when a phototrigger is applied. These versatile materials have many valuable uses including: microfluidics devices,[1-2] encapsulation of bacteria and living eukaryotic cells,[3-4] tissue engineering,[5] 3-D bioprinting,[6-7] pharmaceutical drug release systems,[8-11] and medical procedures.[12]

While several response-trigger materials have been developed from triggers such as electromagnetism, pH, temperature and pressure, the use of light as a trigger has some key advantages. Light allows for nanometer levels of spatial resolution based on the light source. Unlike other stimuli, light can be used with exact temporal control having minimal lag between trigger and reaction. Most photochemical reactions occur in time scales below that of heat or chemically induced ones. The ease and safety of light sources also provides an added advantage to using it as a trigger.[13]

Our research combines organic photochemistry with the engineering principles of rheology in the study of photorheological fluids (PR). Photorheological fluids are those substances that can transition from a free-flowing sol state to a highly viscous gel state or in reverse by a light trigger. The two photochemical processes presented in this thesis show they can affect changes in

the rheological properties of their respective systems through two different photochemical pathways – electron transfer and photoisomerization. We will use readily available materials that are cost efficient and which we believe can expand the use of photochemistry in material science.

1.2 Photochemistry Background

Molecules are constantly in motion, existing in different vibrational energy states and, depending on the absorption of energy, can exist in different electronic states. The parts of the molecule that can absorb photons are called chromophores. Chromophores are chemical moieties such as conjugated pi systems that, unlike other types of chemical structures, absorb specific wavelengths of light (energy) and then undergo processes to release that energy. A molecule before the absorption of light is said to be at its ground state (S_0), or its lowest energy state. After the photon has been absorbed the molecule is now in the excited state, something which is commonly designated by an asterisk (*). There are several excited states that a molecule could theoretically reach and then several pathways to release that energy.

The absorption of a photon leads to several concurrent energetic and electronic changes. The molecule's electronic structure, or electron configuration, changes upon the absorption of light, (Figure 1-1). An electron from the ground state, S_0, after the absorption of light ($h\nu$) will be promoted to a higher energy level becoming an unpaired electron. Notice that the direction of the photon (or spin) stays exactly as it had been in the ground state. This is called the first excited state

singlet, $^{*}S_1$. The electron moved from the highest occupied molecular orbital (HOMO) up into the lowest unoccupied molecular orbital (LUMO).

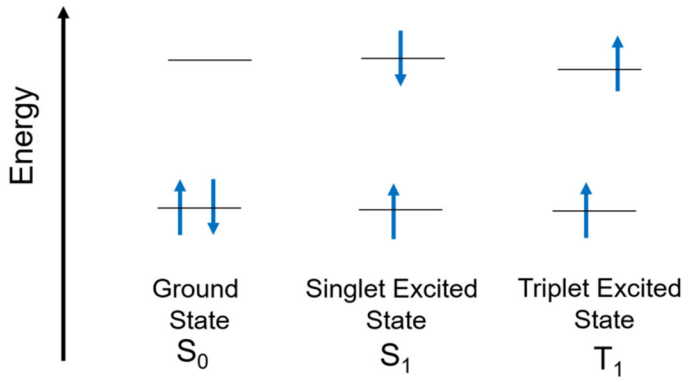


Figure 1- 1 Diagram describing the ground state, singlet excited state and triplet state electron spins and energy levels characterizing each.

The S_1 singlet is not the only possible excited state or electronic configuration. The excited state electron can undergo an intersystem crossing, ISC, into an excited triple state, $^{*}T_1$. In this process, the spin of the singlet changes direction and is considered a spin-forbidden process.

Key to photochemistry is that once the molecule is in the excited state it is considered its own distinct species different from the ground state and having its own unique chemical and physical properties.[14] These new properties include changes in pKa, redox potentials and energy. This can lead to unique chemical pathways that the excited molecule has access to that are unavailable at the ground state leading to novel reactions.

Once a molecule absorbs light it can go through one of the following competitive processes: (1) a radiative release of energy (2) nonradiative release of energy, and (3) photoreactions. The first two are photophysical processes that

will be covered in this section, while the photoreactions applied in our research in later sections. The Jablonski diagram (Figure 2) clearly illustrates the radiative, light producing, and nonradiative pathways to release the excited state energy gained by the absorption of the photon. The first step necessary for a change in electronic state is for the absorption of a photon of light. The actual electron orientations in their orbitals were shown previously in Figure 1. This figure can now be expanded to include the photophysical processes that can lead to the electron going back to the ground state (Figure 1-2). The solid blue arrow going upwards indicates photon absorption to different excited states of the molecule. Each lecule, depending on its structure, can absorb only certain quantized amount of energy, to move to a certain vibrational and electronic excited state.

The higher the state the more energy the molecule absorbs, something that will then need to be released through one photophysical process or another shown in Figure 1-2. Once at the excited state, there are several mechanisms in place for the molecule to lose its energy. The green solid arrow is a radiative release of light known as fluorescence. For fluorescence to occur the molecule is either at the lowest excited state, or it must go through a nonradiative process called internal conversion (IC) to reach the lowest excited state S_1. At this point, it then releases the excess energy as fluorescent light, known as Kasha's rule. It should be noted that while rare, there are exceptions to Kasha's rule but those are not dealt within our study. As stated, the excited molecule can also go through a nonradiative event called an internal conversion. In an internal conversion the molecule loses the

excess energy as heat or molecular movement but does not change its electronic state. Instead, it moves to an isoenergetic vibrational state.

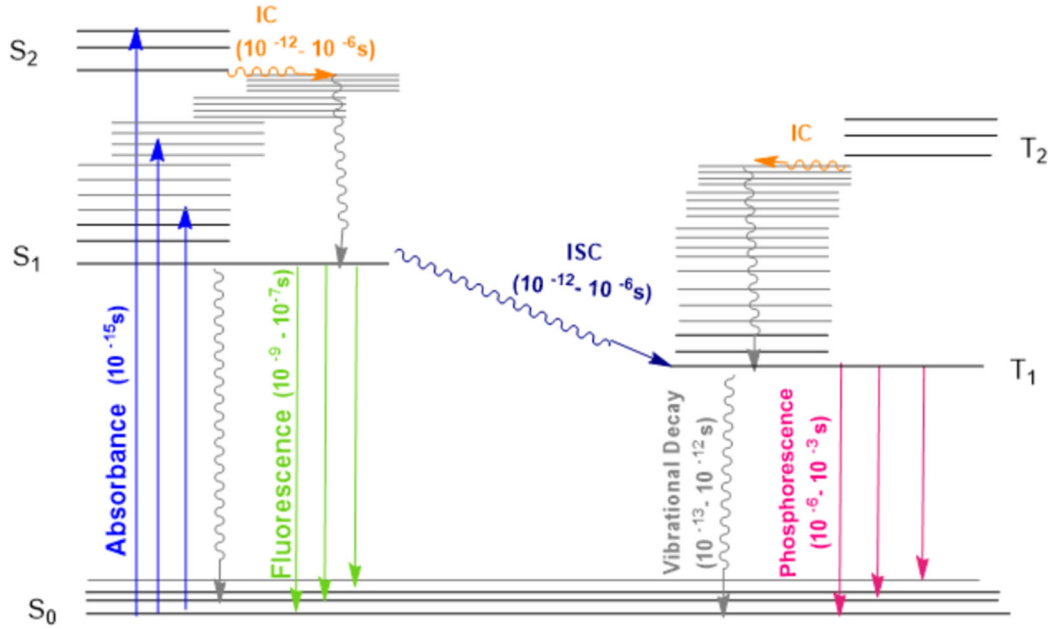


Figure 1- 2 Jablonski diagram describing photon absorption and subsequent intramolecular excited state processes[15] .

Another possibility is that the molecule goes from the S_1 state to the S_0 state without any light release as shown by a wavy grey arrow. The three arrows show a loss of energy by the molecule through a nonradiative process through a redistribution of the energy in the excited structure. The electronic energy is redistributed over many vibrational modes, but the electronic state (singlet or triplet) does not change. In contrast, an intersystem crossing (ISC), wavy blue line, indicates an isoenergetic change that also changes the electronic state of the molecule by either going from a singlet to a triplet or triplet to singlet.

In another process the singlet excited state electron will change its spin, to differ from the singlet state. These triplet states are lower in energy and usually

longer lived than S_1. Depending on what energy level the triplet state is in it can drop down to a lower triplet energy state through another IC, or it can ISC again into a nonradiative loss of energy into the S_0 state. Radiative energy loss is possible, through phosphorescence, (purple arrow in Figure 2), but with a few exceptions, it cannot occur unless the molecule is immobile such as in very low temperatures.[16]

Another important factor in these photophysical processes is their time scale. In photochemical processes the time scales are very short, as absorption of an electron occurs almost instantaneously (10^{-16}-10^{-14} s).[17] When compared to the time of nuclear movement necessary for chemical reaction pathways (10^{-13}-10^{-12}s) photochemical processes can out compete them based on timescale.[18] Time scale accounts for the Franck-Condon principle which states that because the electronic transitions occur faster than nuclear movement, absorption is vertical on the Jablonski diagrams. This means that absorption occurs before any changes in the molecular structure of the ground state.

Molecules have a specific absorption spectrum based on the photochemical principles previously discussed. A plot of a molecule's absorption as a function of wavelength is its UV/vis spectrum. These plots are generated based on Beer's law.[18]

$$\log [I_0/I] = \mathrm{A} \tag{1.1}$$

$$\mathrm{A} = \varepsilon \bullet b \bullet c \tag{1.2}$$

The factors associated with absorbance, A, are: I_0 the intensity of the incident light, I Intensity of transmitted light, b pathlength in cm, c concentration in mol/L and ε the molar extinction coefficient in $M^{-1}cm^{-1}$. Absorption spectra are based on a molecules chromophore region, the functional groups that absorb the UV/vis light. Absorption spectra are used to help identify molecules and can also indicate if a change has occurred in the chromophore region of the molecules as the UV/vis spectra would also change. Also, since all photochemical reactions occur after the absorption of light, knowing not only the wavelength which a molecule absorbs, but also the efficiency in which it does so will be important factors when conducting photochemical reactions.

1.3 Photoisomerization

One of the photoreactions that certain molecules can undergo after the absorption of light is photoisomerization. This involves the changing of geometry or bonding in molecules triggered by absorption of light to create an isomer of the compound. Common examples include the interconversion of E/Z alkenes or ring opening and ring closing of molecules.[19] Isomers are differentiated by each molecule having differing physical and chemical characteristics. Figure 1-3 presents examples of molecules that go through photoisomerization such as azobenzenes, stilbenes, and spiropyrans.[20, 21,22] Stilbene and azobenzene create *E* and *Z* alkene isomers while spiropyrans create rings after isomerization.

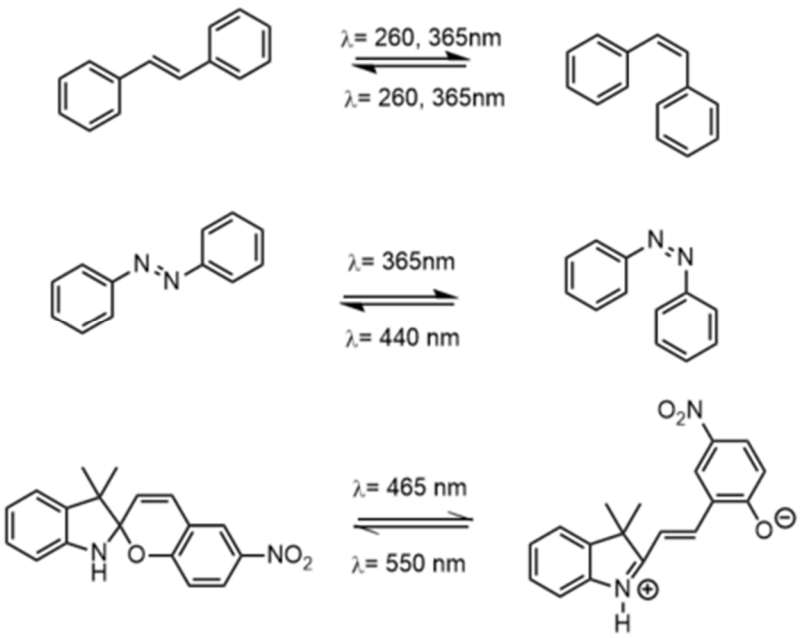


Figure 1- 3 Photoisomerization of stilbene, azobenzene and spiropyran at different corresponding wavelengths.

When a molecule absorbs light, besides electronic changes, there can also be changes in the geometry of the molecule (Figure 1-3). The excited state molecule commonly has differing structural properties than the ground state including a preferred geometry. This leads to the opportunity for a photoisomerization reaction to occur in the excited state. Figure 1-4 is a simplified schematic theoretical energy surface in a diabatic photoisomerization reaction. Just like in the Jablonski diagram, we see absorption of light from the S_0 ground state into an S_1 excited state. The black lines for the two states are reaction coordinates that indicate the progression of the reaction. The molecules is first excited into one potential energy configuration, and then undergoes a change in geometry until it reaches a minimum in energy.

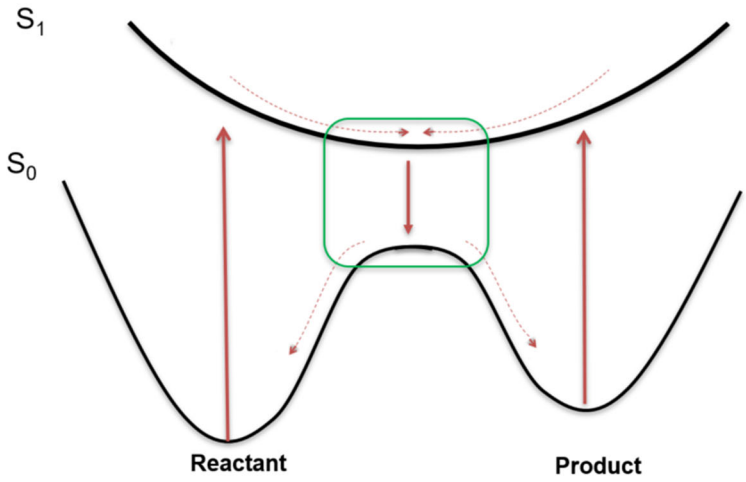


Figure 1- 4 Generalized schematic of a surface diagram with two potential energy surfaces in a photoreaction such as photoisomerization adapted from reference [18, 23, 24]

In favorable photoisomerization reaction this minimum of the excited state would have a small energy gap with a ground state maximum. This area of the diagram is called a conical intersection and is shown in the green box. In productive photoisomerization reactions the electron would jump into the ground state maximum. This conical intersection is a point at which a change in geometry in the excited state can be transferred into the ground state as only the electronic state would change. A productive reaction would then lead to the change of geometry that would change the molecule into its isomer while an unproductive one would have the molecule revert to the original reactant geometry. Nonproductive reactions include a reactant reaching the excited state but then releasing the energy gained from photon absorption through a nonradiative pathway before any photochemistry can occur. If the product can also absorb light then the reverse reaction could occur. Reverse reactions depend on both the difference in stability

between reactant and product, as well as the wavelength and absorption efficiency of each isomer.

Photoisomerization can be thought of in two steps the excitation of the reactant isomer into the excited state then the excited state into the product isomer. The following reaction equations describe the photoisomerization process:[20, 23, 25]

$$R \underset{k_{rR}}{\overset{\varepsilon_R I}{\rightleftharpoons}} R^* \xrightarrow{k_P} P \tag{1.3}$$

Where R is the reactant isomer, R^* is the excited state of the reactant isomer, ε_R is the molar absorption coefficient of reactant isomer, P is the product isomer, and I is light intensity. The rate constant $\varepsilon_R I$ corresponds to the transformation of the reactant isomer into its excited state. The rate constant considers the efficiency of photon absorption of the reactant molecule at a particular wavelength. After the reactant isomer is excited another rate constant is needed, k_P, to describe the rate of the excited state converting into the product isomer. As mentioned previously the excited state can also revert to the ground state which is shown through the rate constant kr_P. If the product isomer also absorbs light the reverse reaction can be described in a similar manner as follows:

$$P \underset{k_{rP}}{\overset{\varepsilon_P I}{\rightleftharpoons}} P^* \xrightarrow{k_R} R \tag{1.4}$$

A few other factors must be true for these two equations to fully describe the competing processes in a photoisomerization. First, these rate variables would be sufficient so long as there is no fluorescence, phosphorescence or significant

thermal isomerization at the temperature being studied. If only one significant method of relaxation occurs, then kr_P is the only rate constant necessary. We can express the time-dependent changes in isomer concentration at the location the solution is being irradiated as follows: [20, 23, 25]

$$\frac{\partial[R]}{\partial t} = -\varepsilon_R\, I[R] + k_{rR}\,[R^*] + k_P[P^*] \tag{1.5}$$

$$\frac{\partial[R^*]}{\partial t} = \varepsilon_R\, I[R] - k_{rR}\,[R^*] - k_R[R^*] \tag{1.6}$$

$$\frac{\partial[P]}{\partial t} = -\varepsilon_P\, I[P] + k_{rP}\,[P^*] + k_R[R^*] \tag{1.7}$$

$$\frac{\partial[P^*]}{\partial t} = \varepsilon_P\, I[P] - k_{rP}\,[P^*] - k_P[P^*] \tag{1.8}$$

It should be noted that diffusion is neglected as this is a unimolecular reaction and diffusion's time scale is much longer than that in the photoreaction. At some point, after a period of irradiation, the solution will reach a photostationary state.[18] The photostationary state is a point at which the ratio of isomers stays constant. This state is very similar to thermodynamic equilibrium except that the concentrations of each isomer would not coincide with thermodynamic equilibrium because they are governed by different variables. The photostationary phase can be described through equation 1.9.[18, 23]

$$\frac{[P]}{[R]} = \frac{\varepsilon_R \Phi_R}{\varepsilon_P \Phi_P} \tag{1.9}$$

In this equation we see that the interconversion from reactant isomer to product isomer using irradiation at a single wavelength would depend on each isomer's efficiency of absorption ε and the quantum yield of interconversion. If the wavelength changes then the photostationary proportions would also change dependent on these factors. In this way it is possible in some systems to find wavelengths in which one isomer absorbs energy more efficiently than the other. A highly studied example is that of stilbene (Figure 1-3). Both isomers absorb in the 300 nm range (specifically at 313 nm), with the *trans* to *cis* process having a quantum yield of $\Phi = 0.5$, while the cis to trans has $\Phi = 0.35$. At this wavelength, the photostationary state favors higher concentrations of the *cis* isomer with 93% yield.[13] Thermal isomerization on the other hand favors the *trans* alkene since it is more stable. Photochemical reactions can also be tuned to create the preferred alkene if the two isomers have distinct wavelengths that they absorb at, like azobenzene (Figure 1-3). This basic understanding of photoisomerization is useful in creating intelligent materials, as will be seen later in our research.

1.4 Photoinduced Electron Transfer

The second photochemical reaction studied for intelligent material design is photoelectron transfer (PET). In this type of photoreaction an electron transfers from one species to another after the trigger of light absorption occurs. These types of reactions are not rare but observed in natural pathways such as the photosynthetic processes of plants. There has been extensive research into

applications of PET for solar energy capture[26],molecular devices[27], photobiocatalysis[28] and organic synthetic methods[29].

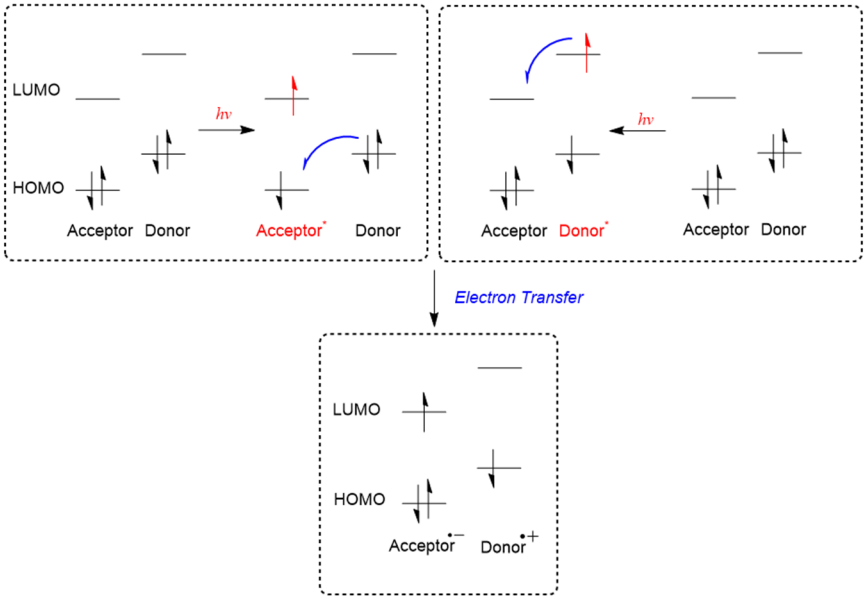


Figure 1- 5 Schematic representation of photoinduced electron transfer.

In PET, like all photochemical reactions, the starting step is the absorption of light. A key distinction in the case of PET is that there are two pathways that can create the conditions for an electron to transfer. Either the donor molecule or the acceptor molecule can be excited (Figure 1-5). A single electron transfer (SET) then occurs which creates a radical cation and a radical anion. In the case of excitation of the acceptor (the oxidizing agent), a half-filled orbital is created that accepts an electron from the HOMO of the ground state donor. The other option is that excitation of the donor (reducing agent) creates a high energy electron that donates into the LUMO of the acceptor. In this way, excitation by light can create molecules that are better oxidants and reductants than their ground state species.

A way to predict the success of an electron transfer (ET) reaction is to calculate the free energy change, ΔG_{ET}. The Rehm-Weller equation (1.10) is used to approximate this in PET[30,31]:

$$\Delta G_{ET} = 23.06(\, E^{D}_{ox} - E^{A}_{red} - S) - E_{00} \tag{1.10}$$

The free energy change of the electron transfer reaction is described in terms of the ground state oxidation potential of the donor E^{D}_{ox}, and the reduction potential of the acceptor E^{A}_{red}. The excited state energy of the singlet or triplet involved in the electron transfer is shown by E_{00}. The equation term S, is a coulomb electrostatic term that in polar solvents is negligible and can be excluded.[32] At the ground state a redox reaction that is endothermic with a $\Delta G_{ET} > 1$ could change after the addition of the photon energy. After electron absorption the reaction can become exothermic so that $\Delta G_{ET} < 1$. This means ET reactions that are thermodynamically impossible in the ground state would be possible through excited state chemistry.

In these PET reactions the photosensitizer is either reduced or oxidized depending on the pathway taken. A photosensitizer is a molecule that absorbs a photon of light and then causes a photophysical or photochemical change in another chemical species. If the photosensitizer returns back to its original redox state and can perform more than one photoreaction cycle, it has also been called a photocatalyst.[33]

1.5 Self-Assembly of Surfactants

Part of our study explores how the interactions at the molecular level affect the macroscopic property of a solution, specifically its rheology. By triggering a photochemical reaction, we can affect changes in these interactions. A key factor of these systems is the ability of the components to self-assemble. Self-assembly is a cooperative process that is driven by the need to prevent an increase in free energy that develops at higher surfactant concentrations due to unfavorable alkyl chain/water contacts, also called the hydrophobic effect.[34] A surfactant molecule typically has two groups attached together one end that is a water-soluble head group and the other which is the hydrophobic tail group.[35] Upon reaching a threshold concentration, termed the critical micelle concentration (CMC), surfactant molecules associate into spherical micelles. Above the CMC surfactants can display more complex morphologies.[34,36]

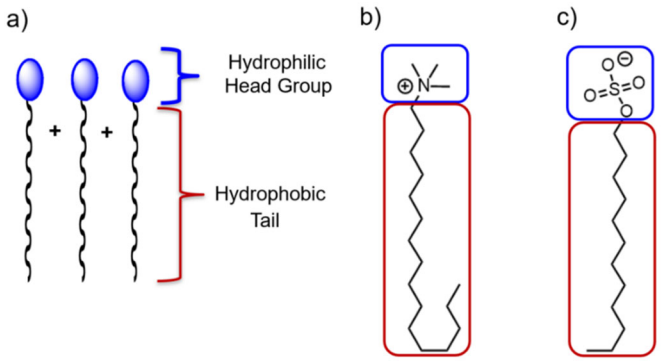


Figure 1- 6 a) General diagram of surfactant molecule b) cetyltrimethylammonium cationic surfactant and c) dodecyl sulfate anionic surfactant. [36]

The aggregate structure formed by surfactant molecules can have a strong influence on the rheological properties of a solution (Figure 1-6). It is therefore important to understand and control the molecular interactions that induce the sol

to gel transitions.[36] The geometry of the surfactant, its charge, and concentration as well as environmental conditions such as temperature, ionic strength, salt concentrations, and additives concentration all influence the size and shape of aggregate structures.[37] A useful tool, to predict probable geometry of micelles formed by surfactants is the surfactant packing parameter, P, given by equation 1.11.[37]

$$P = v/a_0 l \tag{1.11}$$

In equation 1.11 v and l are the volume and length, respectively, of the hydrophobic moiety and a_0 is the optimal surface area occupied by one surfactant molecule at the micelle-water interface. Figure 6 highlights some of the possible geometries as a function of P. A spherical or spheroidal shape is predicted for the micellular aggregate when P ≤ 1/3. At 1/3 ≤ P ≥1/2, the micelles tend to elongate into cylindrical, rodlike shapes. As the packing parameter increases toward 1/2, the cylindrical shape increases in length and micelles transform from rod-like to worm-like (thread-like).

While both rod and wormlike micelles have a cylindrical shape, only worm-like micelles are long and flexible. They wormlike micelles will entangle to form transient networks, similar to flexible polymers.[37,38] These entangled systems increase the viscosity and elasticity of the bulk solution. The existence of wormlike micelles has been confirmed by electron microscopy, light and neutron scattering, as well as NMR experiments.[39] The packing parameter can be used to understand and predict changes in micelle shape, it can therefore be correlated to macroscopic viscosity changes, since increase in viscosity indicates wormlike micelles.

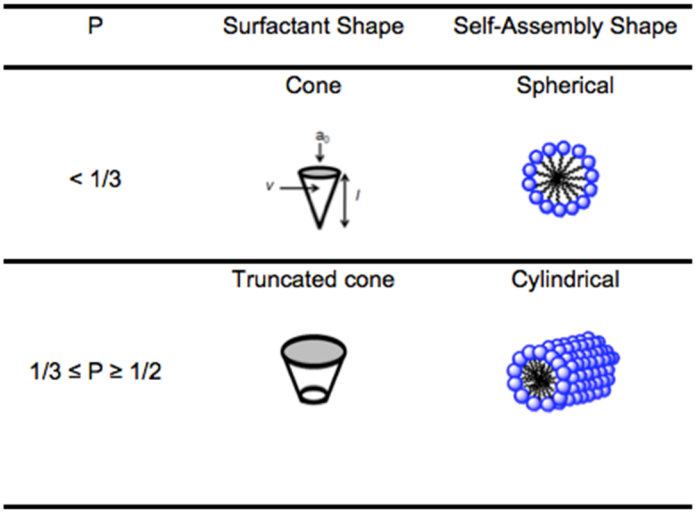


Figure 1- 7 Surfactant self-assemblies as a relationship to P[34,37]

The packing parameter is a useful tool that helps explain viscosity changes and has been very valuable in studies of additive binding. It should be kept in mind that while it is a good model there are some limitations since packing of surfactants is also dependent on other factors besides geometry. Even though there are several factors that affect aggregate shape and size; the focus of this discussion is on addition of small organic molecules which can be modified through photochemical processes.

1.6 Rheological Measurements Background

Rheology is the study of the flow and subsequent deformation behavior of matter.[40-41] When a substance is placed under stress, it will undergo a characteristic deformation. This deformation can be seen qualitatively, or quantitative measurements can be taken. Both types of methods will be used in our work to examine changes in rheology after illumination with light. Qualitative

methods include visual confirmation of gel formation or tipping tests. Complex fluids, like the ones we study, have characteristics that are both viscous and elastic, so they are called viscoelastic. Rheological measurements are taken to quantify the deformation based on the amount of stress placed on the material. These measurements can be performed under steady state or dynamic shear. Correlations can then be made between the microscopic structure of the material and the macroscopic flow changes.[42]

$$\eta = \frac{\sigma}{\dot{\gamma}} \tag{1.12}$$

In steady shear measurements it is the viscosity of the sample that is being measured. Viscosity η ,the ability of a substance to flow, can be calculated from the ratio of the shear stress and shear rate (1.12).[43] In these measurements the sample will have a constant shear rate $\dot{\gamma}$. Shear rate is the change of the strain over the change in time. Strain is the displacement x over the height of the sample as depicted in Figure 1-8. The response of the material to the shear is measured as shear-stress σ. Shear stress accounts for the Force, F, applied over an area, A (Figure 1-8).

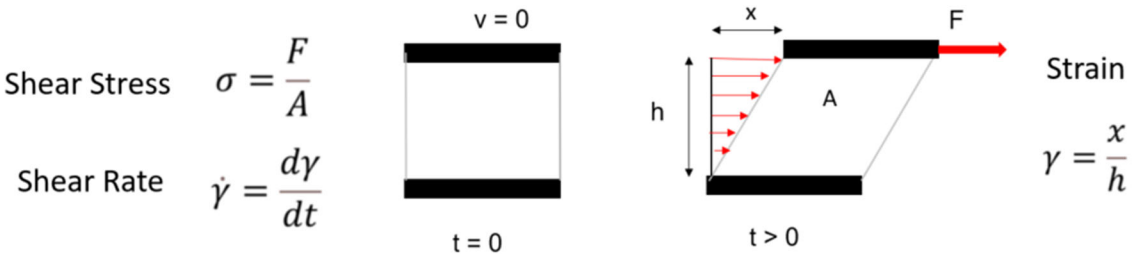


Figure 1- 8 Diagram of relationship between strain, shear stress and shear rate.[41]

Once the apparent viscosity is calculated a flow curve for the material can be constructed by plotting viscosity versus shear rate using equation 1.12. These flow curves can describe the behavior of the material and whether the fluid shows Newtonian behavior. A Newtonian fluid has predictable linear behavior between the shear stress as related to the shear rate and the viscosity is independent of the shear rate. Some materials on the other hand behave this way only at lower shear rates, something which is designated the Newtonian region of their flow curve. In this region you would get the zero-shear viscosity η_0 in the limit of $\dot{\gamma} \to 0$.[44] Rheological measurements are mainly done in this linear viscoelastic region (LVER) where the applied stresses will not cause a structural breakdown of the material's macromolecular structure.[45] This makes sure we are measuring the microstructural properties of our material as if at rest and not when the structure changes or yields. If outside this region it would be hard to correlate microstructural properties to the rheological measurements as the structure itself would have changed due to the yielding to stress applied.

In dynamic or oscillatory shear rheological measurements a sinusoidal strain is applied to the sample as described in equation 1.13. The maximum applied deformation or strain amplitude is γ_0 and the frequency of oscillation is ω.

$$\gamma = \gamma_0 \sin(\omega t) \tag{1.13}$$

The sample response will be in the form of sinusoidal stress described by equation 1.14 where δ is the phase angle relative to the strain waveform.

$$\sigma = \sigma_0 \sin(\omega t + \delta) \tag{1.14}$$

The wave from equation 1.14 can then be separated into two components combined using trigonometric identities to the following equation 1.15:

$$\sigma = \sigma_0 \cos(\delta) \sin(\omega t) + \sigma_0 \sin(\delta) \cos(\omega t) \tag{1.15}$$

Equation 1.15 is rewritten with two material functions introduces G' the elastic modulus and G'' the is the viscous modulus.[46]

$$\sigma = \gamma_0 [G' \sin(\omega t) + G''(\omega) \cos(\omega t)] \tag{1.16}$$

The G' elastic modulus provides information about the elastic nature of the material. The elastic modulus is also called the storage modulus as it implies the storage of the original form, or the solid nature. This component is said to be in-phase of the stress. The G'' viscous modulus shows the materials fluid or liquid characteristics. It is also called the loss modulus and refers to the out-of-phase component of the stress that would cause the deformation. For these two functions to be meaningful the measurements must be taken in LVE regime where the stress is linear to the strain. Both G'' and G' will be functions of the frequency ω and independent of strain.

These values are then used to create a dynamic mechanical spectrum of the material. The spectrum is a plot of G'' and G' as a function of the frequency ω plotted on a double-log scale. This plot is the key to showing the signature of the microstructure and the timed response. With it we can then make correlations between the structure and rheological behavior of the material.

Between steady and dynamic rheology, the dynamic measurements enable the characterization of the material without its ultimate disruption or destruction. Steady shear measurements apply strain until the material yields to indicate where the LVER is located or whether the material is purely Newtonian, which is not the case in most complex materials. We can then correlate the static microstructures in a material with the dynamic measurements and the flow-induced ones from the steady shear.

Chapter 2: Elucidation of Binding Characteristics between CTAB and Cinnamic Acid Derivatives that Change Solution Rheology upon Photoisomerization.

2.1 Introduction

Recently there has been interest in the development of smart materials that change their solution characteristics with light stimuli. These smart systems self-assemble into nanostructures ranging from spherical micelles, rodlike to wormlike micelles then change when the trigger is applied.[47] These nanostructures impart different viscosity or rheological properties to the solution (Figure 7) . Photorheological fluids (PR) are those that can transition from a free flowing sol state to a highly viscous gel state with specific wavelengths of light.[48] Photorheological materials have various applications including as microfluidic valves,[49] drug delivery,[50] medical materials,[50] microelectronic mechanical systems (MEMs) devices and sensors.[51] The advantages of using light as a stimulus are the spatial precision and wavelength specificity of photochemical reactions.[52]

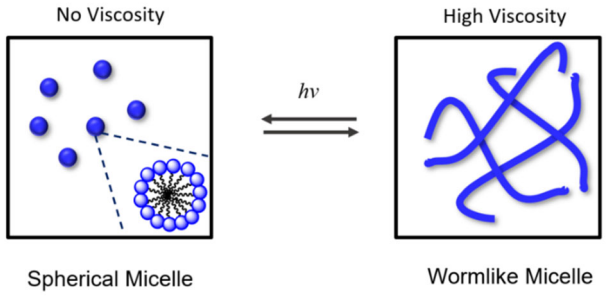


Figure 2- 1 Diagram of transition from spherical micelles to wormlike micelles triggered by light.

Our work into intelligent photorheological materials focuses on the molecular interactions that affect the viscosity of the bulk solution and how photoisomerization changes those interactions. Recently Ketner et. al. have combined cetyltrimethylammonium bromide (CTAB) with trans-orthomethoxycinnamic acid (tOMCA) in aqueous media to produce a photorheological fluid that can transition from a sol to a gel irreversibly with irradiation of UV light.[51] In an effort to make photorheological fluids more accessible to other groups, easily affordable materials were used, as previous examples required synthesis.[53] Ketner et al. hypothesized that the trans to cis isomerization of ortho-methoxycinnamic acid was the cause of a gel to sol transition seen in the CTAB system.[51] While the cis to trans change has now been proven, the exact interactions that change upon isomerization to cause the loss of viscosity are still being characterized.[54]

In our lab Borak et al. created a system that required one wavelength for deprotection of the cinnamic acid, which caused an increase of viscosity in the CTAB surfactant system, and another wavelength to bring about cis isomerization to cis, thus reducing the viscosity, a phenomena called photothinning.[55] Herein, will study the molecular interactions of the cinnamic acid derivatives in Figure 2-2 with CTAB.

The mechanism of sol to gel transitions in solutions is still an area of investigation in colloidal chemistry as it is not completely clear how some organic aromatic additives induce larger structural changes in the CTAB micelles at a molecular level and thus to bulk solution viscosity. We will look further into the

intermolecular interactions that cause the changes in rheology upon photoisomerization by studying the systems before and after photolysis. The CTAB surfactant concentration will be kept constant at 20 mM at which concentration CTAB cannot form wormlike micelles without the help of an additive. Any changes in viscosity will therefore are attributed to the interactions with the aromatic additives.

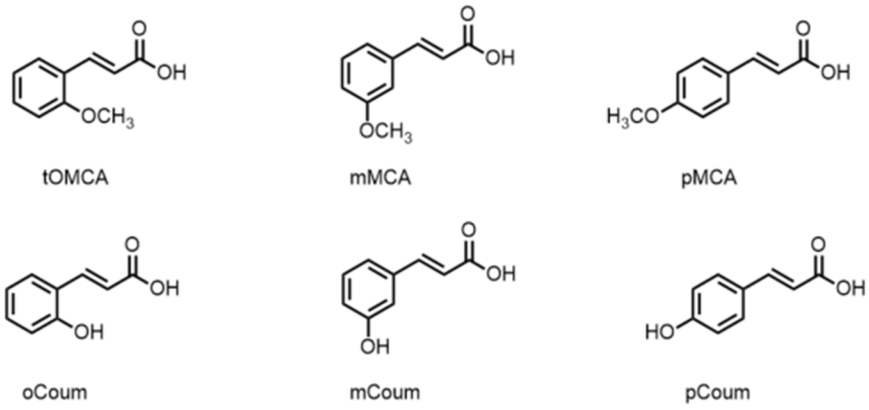


Figure 2- 2 Coumarate derivatives and methoxy-cinnamic acid derivatives used in our isomerization studies as additives and the abbreviations.

The cinnamic acid derivatives have placement of either a hydroxy group or a methoxy group in ortho, meta, or para positions in respect to the alkenyl carboxylate group to identify structural features that encourage rheological changes. The results will show that the ortho and meta placements create the largest change in viscosity.

Though cinnamic acid derivatives are known to photoisomerize under UV light, our experiments will explicitly demonstrate that the photoprocess occurring in the system is the isomerization when rheological changes occur through ^{1}H NMR characterization. Titration studies with cinnamic acid derivatives in CTAB will

clarify orientational binding occurring when we compare the chemical shift changes of free cinnamic acid derivatives versus when added into CTAB solutions. The binding orientation of the different surfactants will either promote or hinder the formation of wormlike micelles. There is precedence for the orientational binding of aromatic compounds in CTAB through the shielding and deshielding of protons in the aromatic region of a molecule. Previously Bachofer and Turbitt studied that orientational binding of substituted benzoate with CTAB by ^{1}H NMR.[56] Their results did indicate that depending on the substitution location and type of functional group the benzoate ions would have different shifts on protons depending on how the molecule oriented in the micelle. More recently, T Liu et al. [57] studied the orientation of cinnamic acid and methoxy-cinnamic acid derivatives in cetyltrimethylammonium hydroxide (CTABOH). Our work will investigate a larger group of cinnamic acid derivatives to further elucidate the binding between surfactant and additive molecule.

We will show how changing the attachments to the benzene ring changes how the derivative interacts to the CTAB surfactant causing differing results in viscosity. Both 1D and 2D 1H NMR experiments will elucidate interactions at a molecular level, while rheological studies will show that viscosity changes occur when the interactions are favorable and will not when unfavorable. B3LYP calculations were added to further 3D modeling of the interactions between CTAB and the cinnamic acid derivatives. Finally, an orientational model for all the cinnamic acid derivatives will be presented. And a model of the interactions between tOMCA and cOMCA will be presented that will explain how the different

interactions hinder or help the formation of wormlike micelles and therefore viscosity of the solution.

2.2 Experimental Section

2.2.1 Materials:

CTAB purity was greater than 98% as per manufacturer specifications, purchased from Sigma-Aldrich and used without any further purification. The *trans*-OMCA form was purchased from Acros chemical and the *cis*-OMCA form from TCI. All other photoactive additives were purchased from Sigma Aldrich and used without further purification. All samples were prepared with ddH_2O for rheological and photolysis studies. In the NMR studies D_2O, 99.95% from Cambridge Isotopes was used and NaOD added to dissolve the photoactive additives.

CTAB solutions studies were stirred and heated for a minimum of 3 hours to assure complete dissolution. The solutions were subsequently stored in a 298 K water bath to avoid precipitation overnight and were allowed to equilibrate. These were subsequently mixed with additive solutions to reach the final desired concentration. pH results were taken on a Fisher Scientific *Accumet* Semimicro Size Glass Combination Electrode, pH 0-14. Sample pH was 8 - 9.

2.2.2 Photolysis Studies:

Samples were photolyzed in Rayonet RMR-100, 8 bulb, 253.7 nm UV light, circular set-up was the light source for all photolysis studies. Samples were prepared according to the molarity desired. Samples containing CTAB were 20

mM in all photolysis samples. The 1 cm pathlength quartz cuvettes were placed inside the Rayonet RMR-100. During each time interval 600 µl aliquots were removed from the cuvette and placed in NMR tubes for characterization. For rheology photolysis samples a quartz test tube was used instead of a cuvette and large 10 mL amounts were photolyzed for 5 to 6 hrs.

2.2.3 Titration Methodology:

A stock solution of 50mM CTAB and 50 mM additive was made in D_2O. Samples had 1- 1.5 equivalents of NaOD added to the cinnamic acid derivative stock solution to deprotonate the carboxylate and allow the compound to dissolve in D_2O. A dilution series was set up then a corresponding amount of water and additive stock solution was added to reach a volume of 1 ml and the needed molarity of additive. The concentration of CTAB always stayed constant at 20 mM in all titration samples and additive concentrations were varied.

2.2.5 Rheological Studies Methodology:

Steady state and dynamic rheological experiments were performed on an AR2000, TA Instruments Newark DE, stress-controlled rheometer. Samples were run at 298 K on a cone-and-plate geometry set to 40 mm diameter, 2-degree cone angle. For samples that were too fluid a couette geometry, rotor of radius 14 mm, height 42 mm, and cup radius 15 mm was used. The linear viscoelastic regime of each additive sample was obtained by dynamic stress-sweep experiments. The dynamic frequency spectra were obtained in this regime if it existed in each sample.

2.2.4 NMR Spectroscopy Methodology:

The one and two dimensional ^{1}H NMR spectra were obtained on a Bruker 600 MHz spectrometer using a BBI probe. All ^{1}H NMR solutions were made with deuterium oxide, at 298 K-300 K depending on CTAB concentration and peak resolution. All water signals were set to 4.80 ppm as a standard for comparison, and water suppression studies used a corrected reference signal.

2.3 Results and Discussion:

Our investigations looked at various number of cinnamic acid derivatives in CTAB for binding interactions that lead to increase in viscosity and the subsequent interruption of binding through photoisomerization. Names and the abbreviations used for each one used in the study in Table 2-1.

Table 2- 1 Name and abbreviation of additives used in study

Name	Abbreviation
trans-ortho-methoxycinnamic acid	tOMCA
cis-ortho-methoxycinnamic acid	cOMCA
trans-meta-methoxycinnamic acid	mMCA
trans-para-methoxycinnamic acid	pMCA
ortho-coumarate *trans*-2-hydroxycinnamic acid	oCoum
meta-Coumarate, *trans*-3-hydroxycinnamic acid	mCoum
para-coumarate, *trans*-4-hydroxycinnamic acid	pCoum

2.3.1 Steady state and Dynamic Rheological Measurements

Rheological data for tOMCA and cOMCA is readily available at high CTAB concentrations above 30 mM but we choose to do our study at 20 mM CTAB since at this concentration, CTAB cannot create wormlike micelles without the help of additives but is still above the critical micelle concentration (CMC = $9x10^{-5}$ M in water).[58] Therefore, any change in the rheological properties of the solution would be cause by the addition of the cinnamic acid derivative. We performed steady state and dynamic state rheology on each of the additives before and after UV photolysis at 20 mM CTAB. All rheological experiments were done in the Raghavan lab at the University of Maryland in the Chemical Engineering Department with the help of Hyuntaek Oh.

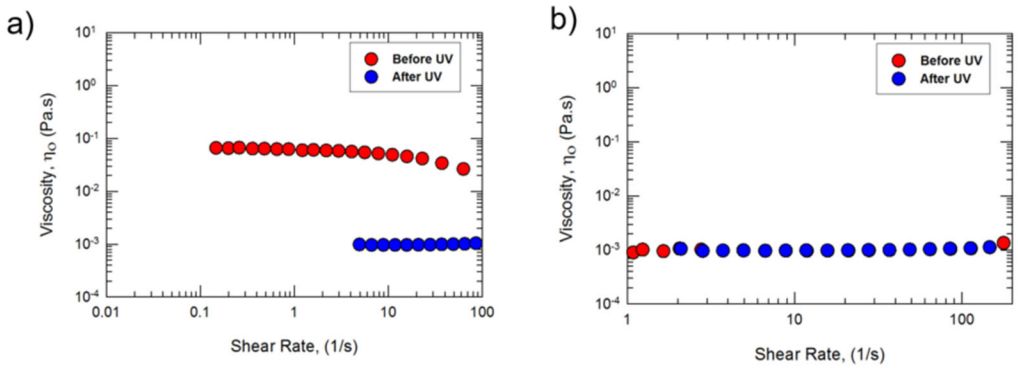


Figure 2- 3 Steady state rheology of 20 mM CTAB and 20 mM additive before and after 5 hr photolysis a) tOMCA b) cOMCA

The results for the steady state rheological measurements for tOMCA and cOMCA can be seen in Figure 2-3. They show that at 20 mM CTAB and 20 mM tOMCA there is some viscosity in the sample before photolysis as seen by the shear-thinning behavior of the solution. This behavior is a plateau in the viscosity at low shear rates and then followed by a decrease in viscosity at higher shear

rates. After 60 minutes in a Rayonet with 254 nm bulbs, the viscosity of the sample decreased until it was closer to water, as well as, there was no shear-thinning seen, but instead mostly Newtonian behavior. This means that samples showed negligible shear rate-dependence. These results are consistent, if at lower CTAB concentrations, with what has been previously reported by Ketner et al.[51] In comparison and as expected, the cOMCA sample in the same conditions showed no viscosity before or after photolysis.

Dynamic or oscillatory shear rheological measurements were also performed on the samples to further examine the structure of the fluids. The results for 20 mM CTAB in the presence of 20 mM cOMCA or tOMCA before and after photolysis can be found in Figure 2-4. These are plots of the elastic modulus *G'* and the viscous modulus *G"* as a function of the angular frequency ω. For Maxwell fluids both moduli will vary with frequency based on the following equations where τ_m is the relaxation time:[59-60]

$$G'(\omega) = G\,\frac{(\omega\tau_m)^2}{1+(\omega\tau_m)^2} \tag{2.1}$$

$$G''(\omega) = G\,\frac{\omega\tau_m}{1+(\omega\tau_m)^2} \tag{2.2}$$

The relationship between the viscous and elastic modulus of complex fluids can give us information on the nanostructures found in the solution. In the case of our cOMCA sample there is no *G'* curve. This indicates that this sample does not have strong characteristics of a solid and would not have any wormlike micelles or entanglements found in this solution. This type of sample would be closer to water

with no structures to give it viscosity. These results match well with the steady state rheology measurements.

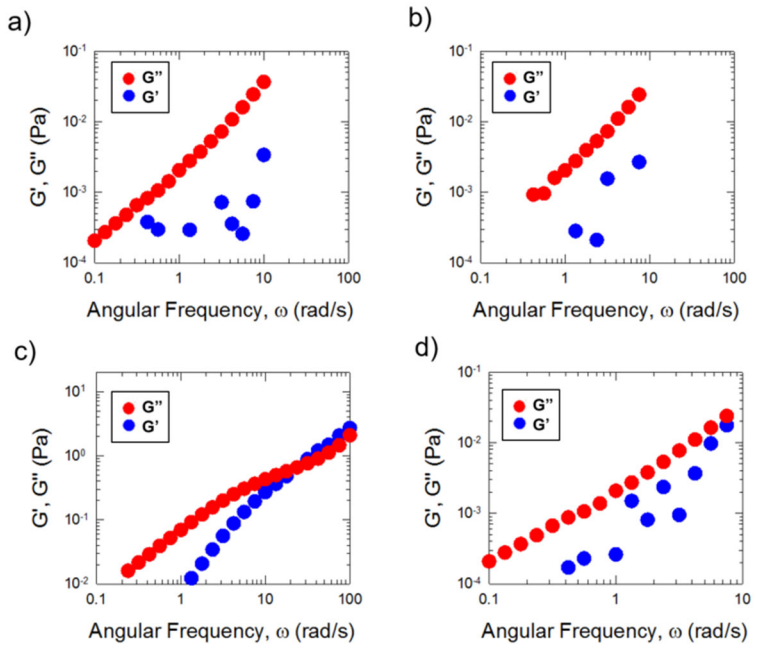


Figure 2- 4 Dynamic rheology a) cisOMCA preUV b) cisOMCA postUV c) tOMCA preUV and d) tOMCA postUV.

The tOMCA results found in Figure 2-4c do show both viscous and elastic curves. While the curves are not sharp enough to fit into a Maxwell curve there is qualitative data that can be obtained. The tOMCA sample before irradiation shows viscoelastic response, like those of wormlike micelles, though not completely. It matches viscoelastic behavior by having the *G'>G",* elastic behavior, at high frequencies and *G'<G"*, viscous behavior, at lower frequencies with an intersection of both curves. What is missing is a *G'* plateau, which can be found in higher viscosity samples with wormlike micelles. After photolysis the *G'* curve is gone showing a purely viscous response.

These results also match those previously done on tOMCA and CTAB by Ketner, which leads us to have confidence that the binding interactions that we study at lower concentrations will be those that will lead to those found at higher concentrations, letting us create a model of these interactions.

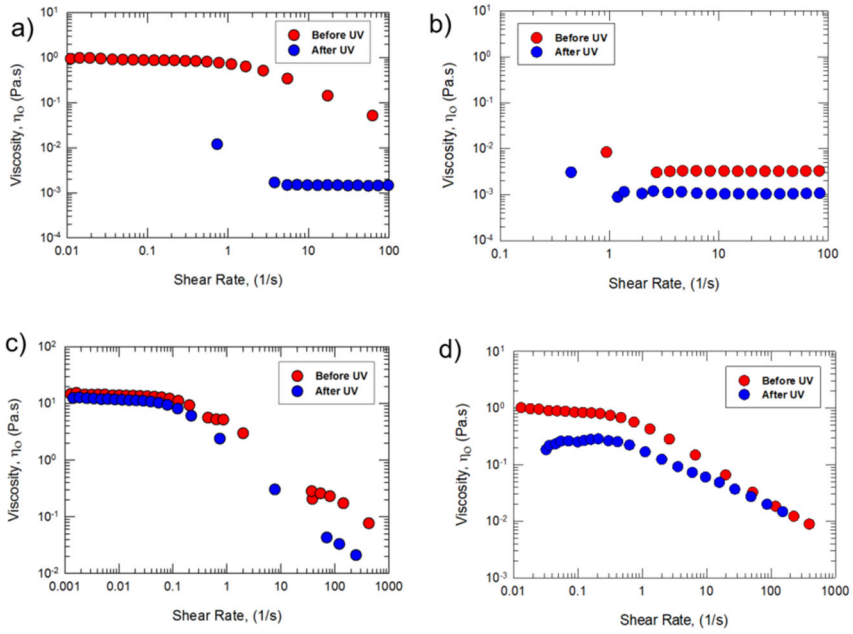


Figure 2- 5 Steady state rheology 20 mM CTAB to 20 mM additive. Pre and post photolysis on a Rayonet 254nm. a) mMCA b) pMCA c) oCOUM and d) mCOUM

The steady state pre and post photolysis results for the remaining additives can be found in Figure 2-5. These results show some interesting trends. All the samples except pMCA show shear thinning at 20 mM CTAB and 20 mM additive. After photolysis the mMCA demonstrates a viscosity loss. The loss coincides with three levels of magnitude from 10^{0} to 10^{-3}. While the oCoum sample shows no loss of viscosity after photolysis. The mCoum sample shows a small loss of viscosity and the photolyzed sample still shows shear thinning. It is also interesting to note that the apparent viscosity of mMCA is higher at 20 mM than that of tOMCA.

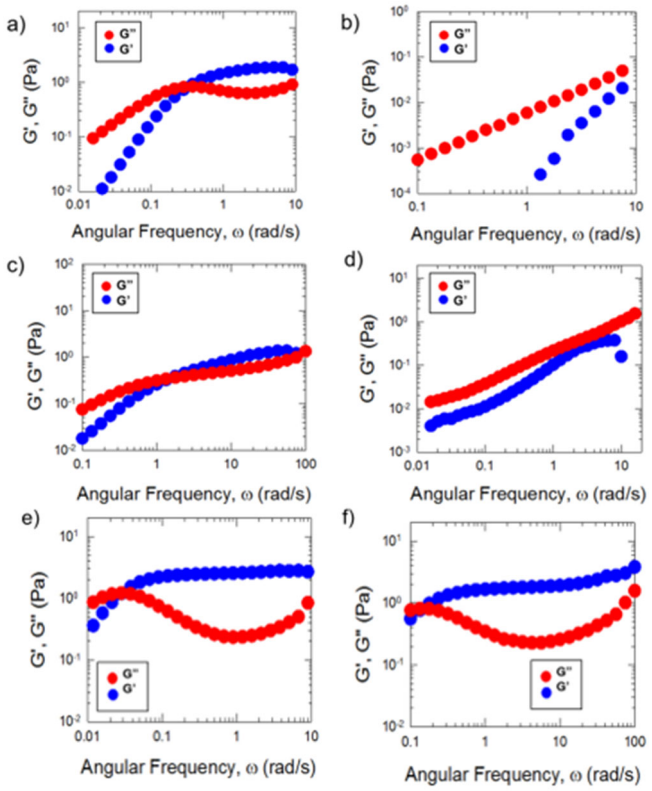


Figure 2- 6 Dynamic Rheology of 20 mM CTAB: 20 mM additive. Post UV with Rayonet 254 nm. a) mMCA preUV b) mMCA post UV c) mCOUM preUV d) mCOUM post UV e) oCOUM preUV f) oCOUM postUV

The dynamic rheology measurements for mMCA, mCoum and oCoum follow the viscoelastic characteristics of samples with wormlike micelle formation (Figure 2-6). The sample for mMCA, unlike tOMCA, even includes a *G'* plateau that, along with the other previously described characteristics, indicates the presence of wormlike micelles and entanglements that create viscoelastic behavior. After photolysis the mMCA sample shows only viscous behavior with loss of *G'* and *G"* curve intersection and *G*' plateau. The sample of mCoum shows the loss of elastic behavior with the G" curve being higher than that of G', though they are still close if no intersection. The curve for oCoum shows an intersection that moves toward a lower frequency, but there is now loss of curve

shape. The samples of pMCA did not show any *G*' behavior before or after photolysis like cOMCA (data not shown).

From this data we can postulate that oCoum has the highest ability to create viscous wormlike solutions as, at these low concentrations it shows not only the highest apparent viscosity, but also a dynamic rheological measurements indicative of more entangled worm like micelle formation. This additive also shows a low change in viscosity through photolysis which we will discuss in the photolysis section.

Our results indicate that at these lower CTAB concentrations certain additive molecular structures are more likely to increase viscosity than others. We could predict from our data that at higher CTAB and additive concentrations, the mMCA would be second to oCoum in viscosity changes but that pCoum would not be able to form very viscous samples. Our predictions are confirmed by a paper recently published by ZH Yan et al.[61] Our 1D and 2D NMR and binding model data will coincide with their work but offer a more thorough explanation at the molecular level.

2.3.2 1-D ^{1}H NMR titrations studies of additives in CTAB

The solutions of tOMCA have been shown to increase in viscosity as more additive is added, while the photoisomerization of tOMCA to cOMCA caused the reduction in viscosity. Therefore, the binding patterns in tOMCA with CTAB would show binding that is constructive so as to increase in viscosity, while the binding of cOMCA would show binding that is destructive to viscosity. Titration ^{1}H NMR

studies were performed to characterize the binding of the additives to CTAB and the subsequent changes in binding as the ratio of additive to CTAB is increased until the rheology changes.

Surfactant systems rely on self-assembly through non-covalent binding interactions of the components in the system. Changes in concentrations of additive will therefore cause, depending on the additive structure, a change in morphology of the system at high enough concentrations. To ensure that our readings are at an equilibrated morphology all samples were sonicated, mixed for a minimum of 48 hours in a warm bath, then left to stand in the NMR tubes before any readings were taken.

NMR chemical shifts are sensitive to a proton's chemical environment such as: hydrogen bonding, electric fields, conformation and ring currents.[62] If the environment (proximity of neighboring groups/atoms) changes so will the chemical shift. An upfield shift, ppm decreasing, is described as a proton becoming more shielded. Whereas, a downfield shift, ppm is increasing as a protons becomes more deshielded.[63] Studies into surfactant gel systems, using ^{1}H NMR have been previously employed to elucidate the molecular interactions between surfactant and additive based on chemical shift changes.[56, 64-67]

The titration of tOMCA in 20 mM CTAB can be found in Figure 2-7. The tOMCA protons all shift upfield or toward a lower ppm value when compared to the control sample of only 2 mM tOMCA in D_2O. The aromatic protons H4, H5, H6 show the largest shielding in CTAB. As more additive was added, the proton signals continued to shift until they started to broaden at the to 20 mM tOMCA

concentrations (Figure 2-7e). At the 1:1 ratio of additive to surfactant the proton signals are at the broadest but also the viscosity of the sample is higher than at the 2 mM, which was completely liquid, indicating a change in the morphology of the solution. Already it was described how the dynamic rheology of the sample indicated wormlike micelle characteristics. This coincides with previous observations that broadening of peaks indicates formation of larger aggregates in surfactant systems.[57, 68]

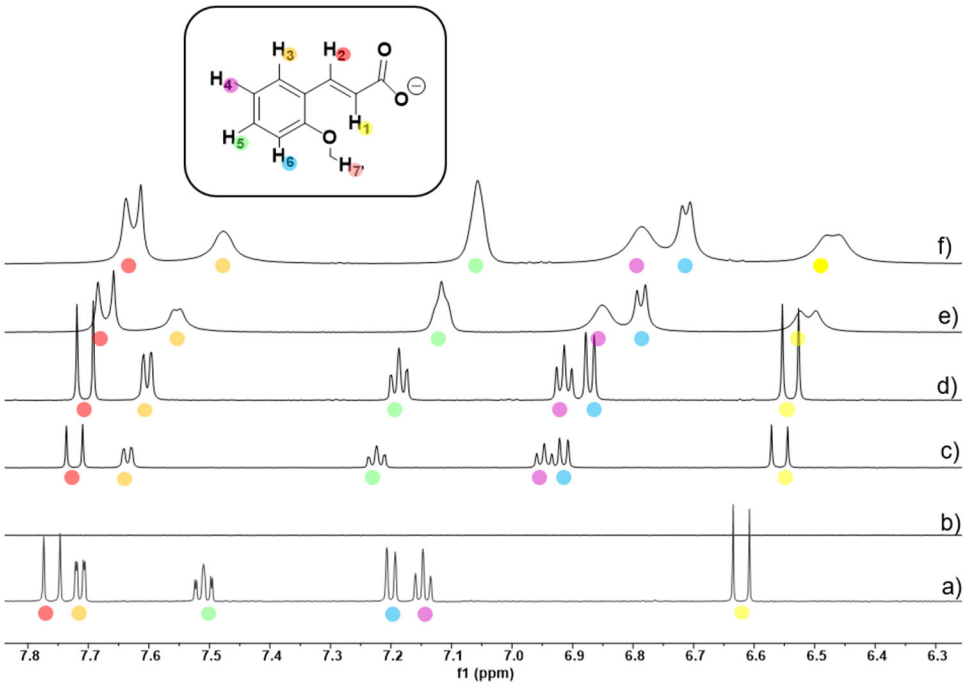


Figure 2- 7 Conjugated region of additive tOMCA at various amounts in 20 mM CTAB titration a) 2 mM tOMCA b) 20mM CTAB c) 2 mM tOMCA:CTAB d) 5 mM tOMCA:CTAB e)10 mM tOMCA:CTAB f) 20 mM tOMCA:CTAB

Protons that had the least overall change in chemical shift from being in the water were H1 and H2, those that are on the alkene and nearest to the carboxylate group. Since the carboxylate group is charged, it would most likely want to be

nearest to the ammonium headgroup and the water interface. Another interesting change is the switching of H6 becoming more shielded than H4. This could mean there is now an orientational preference for the H6 side to be toward the shielding environment of the micelle core. We further propose that the shielding effect is too large to indicate just the presence of the additive in the aliphatic region of the micelle. Instead, there may be some orientational interaction or at the very least proximity to other aromatic molecules inside the micelle. Further discussion will be presented in the NOESY section.

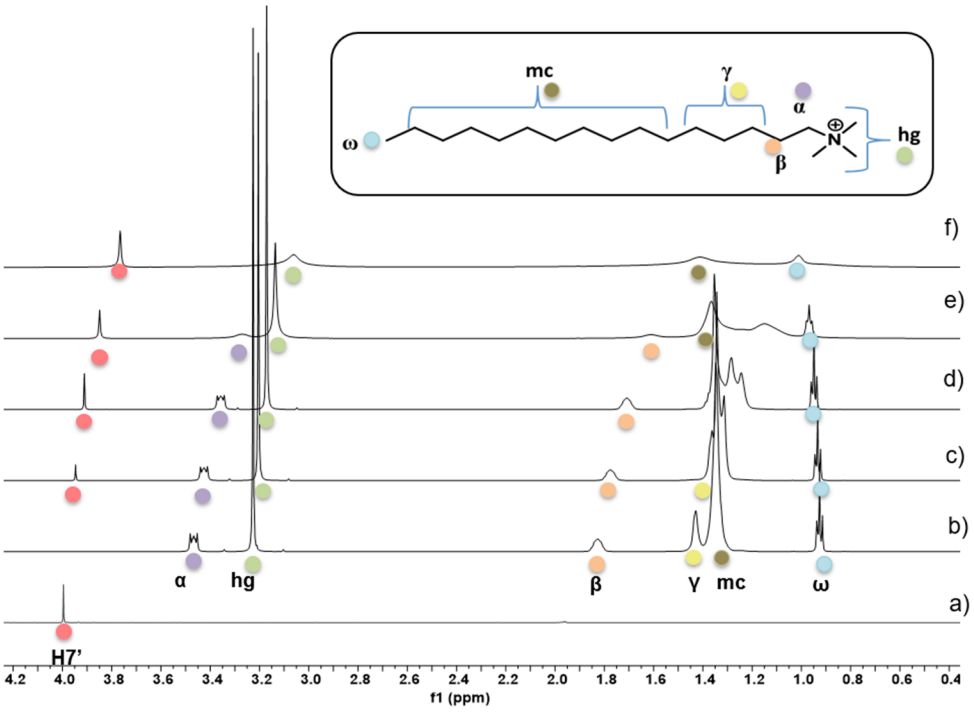


Figure 2- 8 CTAB region of H-NMR at various amounts of tOMCA in 20 mM CTAB a) 2 mM tOMCA b) 20mM CTAB c) 2 mM tOMCA:CTAB d) 5 mM tOMCA:CTAB e) 10 mM tOMCA:CTAB f) 20 mM tOMCA:CTAB

The CTAB region of the spectra also shows shifting upfield especially the β and γ protons (Figure 2-8). As more tOMCA is added the main chain signal, which

totals 10 protons starts to differentiate. This is an indication that some of the protons in the main chain are experiencing differing chemical environments, and are longer in solely exposed to the aliphatic tails of other surfactants. The main chain signal (mc) also becomes, overall, more shielded. The γ proton signal becomes shielded and is lost into the main chain signal, perhaps becoming the new signal the shows up to the right of the main chain signal at higher additive ratios. The aromatic region of the additives being closer to these main chain protons would explain both the chemical shift and the new proton signals. This is especially important as protons in the CTAB micelle are already in the hydrophobic, shielded environment, so any change is primarily due to the insertion of the additive.

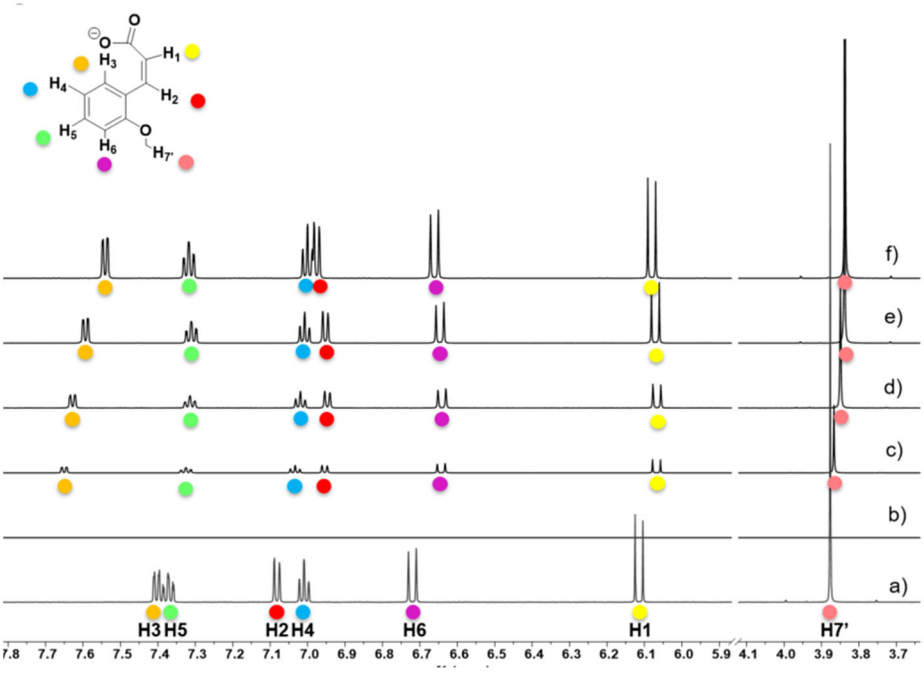


Figure 2- 9 Substituent NMR Signals cOMCA in 20mM a) 2 mM cOMCA:CTAB b) 20mM CTAB c) 2 mM cOMCA:CTAB d) 5 mM cOMCA:CTAB e)10 mM cOMCA:CTAB f) 20 mM cOMCA:CTAB

There is also a slight deshielding (Δδ = 0.09) to the omega signal, which could indicate it has some contact with the tOMCA also. A full list of all chemical shifts and chemical shift changes can be found in Appendix A. These observations would indicate that the additives have intercalated deeper into the micelle than previously proposed. Aromatic systems create an anisotropic induced magnetic field due to the pi electrons. Depending if a proton is near the region of the aromatic ring that aligns (deshields) or opposes (shields) the applied magnetic field there will be different effects on the surfactant chain. Any change in the ω protons would indicate the tOMCA molecules are intercalated beyond the headgroup into the hydrophobic core of the micelle.

In contrast cOMCA has a different chemical shift pattern from tOMCA which can explain its inability to produce viscosity changes (Figure 2-9). The cOMCA protons H3 and H4 show deshielding Δδ of 0.25 and 0.03 respectively at 2 mM concentration. This is a large difference with H3 clearly being the closest to the ammonium group. In contrast the H6 proton is highly shielded (Δδ = 0.56 at 2 mM), while H1, H2, H5, and H7 protons show slight shielding up to 10 mM concentration. At 20 mM additive and 20 mM CTAB protons H1, H2 H6 start to move downfield, reversing a trend that did not occur in tOMCA. This could mean that the cOMCA molecules have saturated their interaction with CTAB and are now free in solution.

The CTAB region of the cOMCA titrations shows very little change until 20 mM of cOMCA is added, but the change does not include broadening of the signals like with the tOMCA spectra (Figure 2-10). One significant change is the loss of the γ into the main chain as it becomes more shielded, which we are presenting

as the aromatic group of cOMCA being inserted into the outer layer of the micelle. The shielding affect to the CTAB head group, which would indicate the electrostatic interactions with other CTAB molecules is reduced also indicates that cOMCA is near the headgroup. An explanation could be that although cOMCA is in a different isomeric geometry it will still have a negative carboxylate group at pH 9 which will act as a counter ion to the positively charged ammonium group. But the lack of shielding or major chemical shift changes of main chain protons indicates that the interactions are isolated to the outer part of the micelle and not deeper into the micelle core. This is a large difference in comparison to the trans isomer.

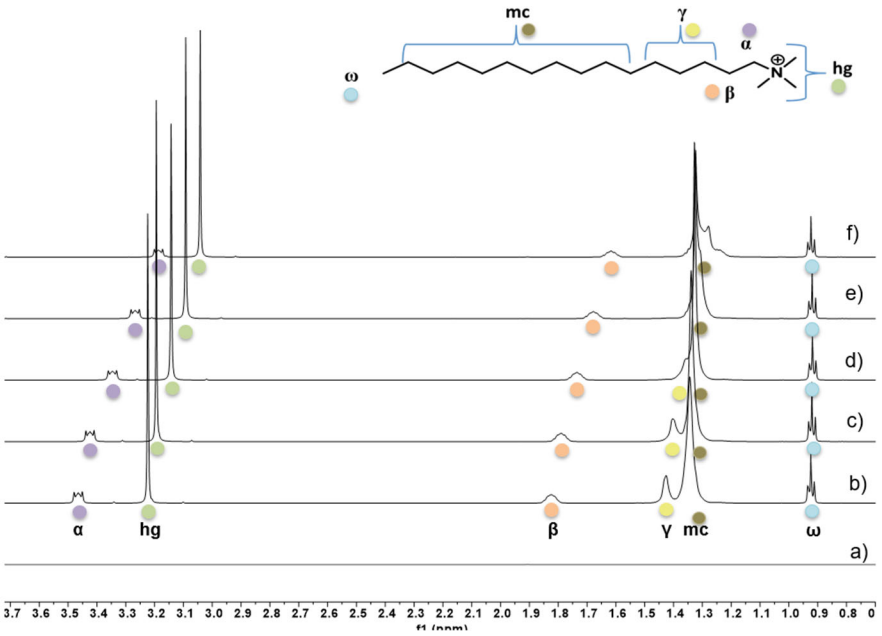


Figure 2- 10 CTAB region NMR Signals cOMCA in 20mM a) 2 mM cOMCA:CTAB b) 20mM CTAB c) 1:10 , 2 mM cOMCA:CTAB d) 1:4, , 5 mM cOMCA:CTAB e) 1:2 ,10 mM cOMCA:CTAB f) 1:1, 20 mM cOMCA:CTAB

Titration NMR experiments were also conducted on the other additives which can be found in Appendix A along with a table of all the chemical shift data. To further analyze the differences in binding chemical shift changes were

calculated for all the peaks at all the titration concentrations. The shift difference for each proton was graphed versus concentration of additive. The chemical shift change was given a color code and a diagram made of the shift changes for each additive (Figure 2-11 to 2-13).

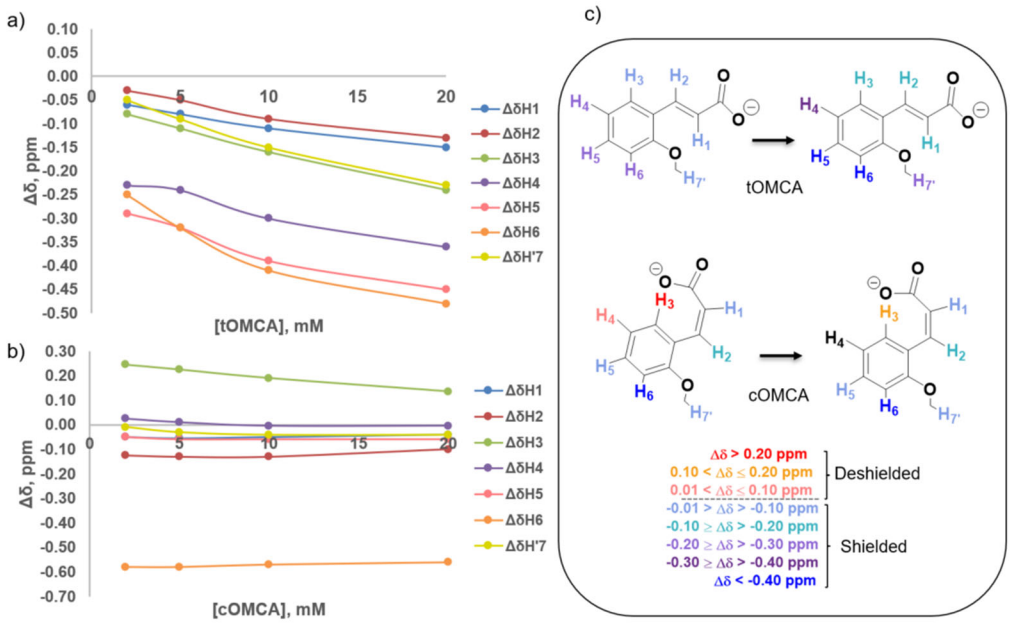


Figure 2- 11 Chemical shift difference graph versus concentration a) tOMCA b) cOMCA and c) a visual representation of the chemical shift difference starting with the difference between 2mM additive 0 mM CTAB to 2mM 20 mM CTAB. The second figure is 2mM additive to 20 mM additive 20 mM CTAB

A clear pattern in chemical shift changes appears from the graphs and diagrams for tOMCA and cOMCA (Figure 11). The shift changes for tOMCA protons H6 and H5 at 2 mM start negative (shielded) but become more negative until they reach 20 mM (Δδ < -0.4 ppm). None of the protons show a positive chemical shift change which may indicate more of the additives are fully enveloped into the shielded environment of the micelle aliphatic region. In contrast the isomer cOMCA has two deshielded protons, H3 and H4. A key to identifying the orientation of the cOMCA is the H6 proton having Δδ = -0.6 ppm. This proton is

shielded and stays shielded changing very little as more cOMCA is added. It can be inferred that this proton stays the furthest from deshielding environments such as the positively charged ammonium head group and the D_2O solvent.

The cOMCA proton H3 is deshielded with the $\Delta\delta$ = 0.25 ppm. H3 is on the other side of the cOMCA molecule than the H6 shielded proton indicating a strong directional difference in chemical shift change. These distinctive differences between the two isomer's chemical shift changes suggest specific orientational alignments in the micelle. More evidence to these orientational differences will be given in the NOESY section.

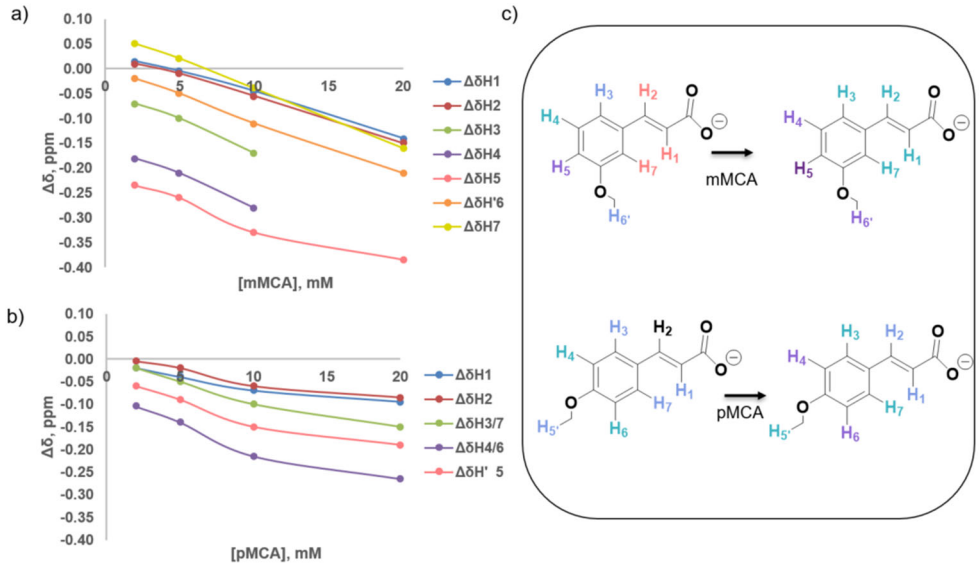


Figure 2- 12 Chemical shift difference graph versus concentration a) mMCA b) pMCA and c) a visual representation of the shift magnitude and direction by color coding

The chemical shift change graphs for mMCA and pMCA can be found in Figure 18. The first data points of 2 mM in 20 mM CTAB for mMCA show that three protons H1, H2 and H7 were deshielded. This would indicate that the carboxylate side of the molecule is more exposed to the ammonium head. The

protons on the bottom aromatic part of the molecule become more shielded with H5 having the largest change at Δδ = -0.39. Protons H3 and H4 become one broad signal by and cannot be differentiated at 20 mM so no data points are shown (Appendix A). This shifting is pattern is similar to tOMCA in that all protons become shielded as the concentration is increased. These two additives also produce wormlike micelle behavior in their rheology at 20 mM CTAB, indicating the importance of continued intercalation into the micelle of more additives to wormlike formation.

The pMCA derivative results also show that all protons are more shielded at the first data point except for H2 that shows no difference between being in CTAB and in D_2O (Figure 2-12). The chemical shift changes for pMCA are not as large in mMCA and there is some directional preference for H1 and H2 protons to be toward the ammonium group as they are the least shielded. At our concentrations of pMCA to CTAB no wormlike micelle behavior was seen but with these shift results it could be possible at higher concentrations.

Next, we analyzed the coumarate additives chemical shift changes with the results found in Figure 2-13. For oCoum the chemical shift changes show that both the H6 and H2 proton are deshielded (Figure 2-13). The H2 proton does not become shielded, not even at 20 mM CTAB indicating that it stays in a deshielding environment. H6 is interesting that it is also deshielded, but this could be because it is near the hydroxy group that would want to be near the polar area of the solution. All other protons on oCoum are shielded and continue to become more shielded with larger concentrations of additive.

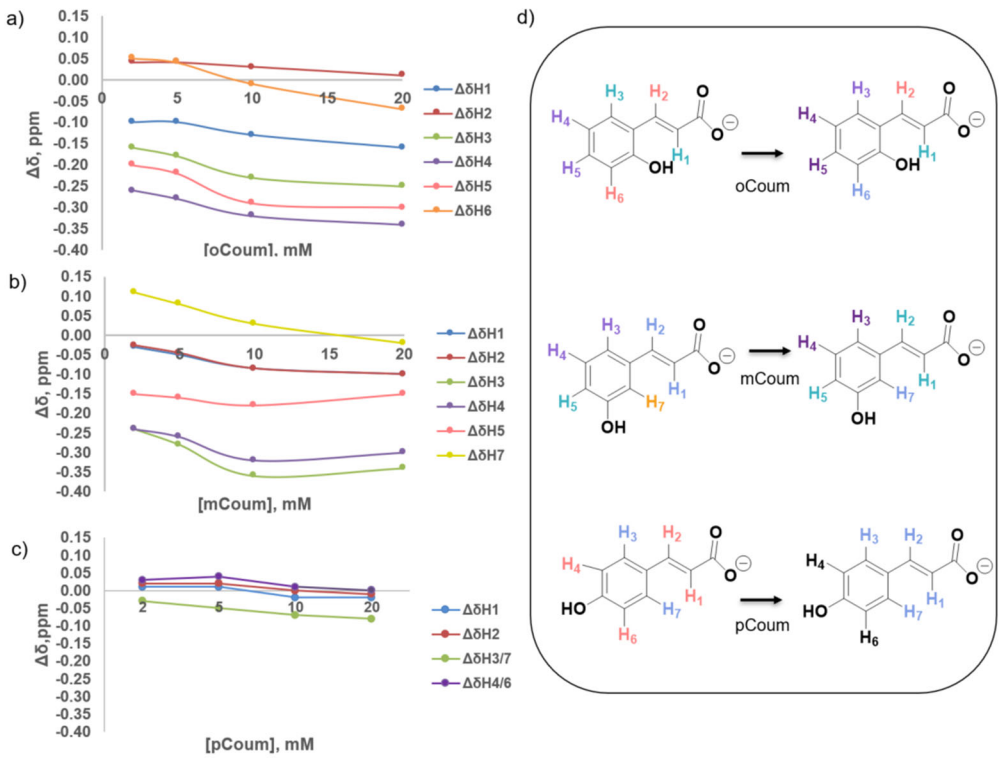


Figure 2- 13 Chemical shift difference graph versus concentration a) oCoum b) mCoum c) pCoum and d) a visual representation of the shift magnitude and direction by color coding.

For mCoum the only deshielded proton was H7 which is between the hydroxy and the alkenyl carboxylate group (Figure 2-13b). This pattern would make sense as both the hydroxy and carboxylate groups would want to be near polar head group of CTAB. Interesting though is that H1 and H2 do not show any deshielding, even though they are not very shielded at less than Δδ <-0.05. The most shielded protons are H3 and H4 indicating this part of the molecule would spend the most time or bind the strongest to the hydrophobic shielding part of the micelles.

The chemical shift changes of additive pCoum can be found in Figure 19c. This additive when tested did not give changes in viscosity at 20 mM CTAB 20 mM

additive. The chemical shift changes for pCoum show a beginning deshielding on both sides of the molecule H1, H2 protons and H4, and H6 protons. This could indicate that both sides of the molecule want to be near the polar interface and ammonium head group. At 20 mM additive and surfactant only H1, H2, H3, H7 are even slightly shielded while H6 and H4 which were deshielded now have zero chemical shift change versus free 10 mM pCoum. This may imply that pCoum orients both the hydroxy and carboxylate groups toward the ammonium ion. The additive could as a mixture of both orientations. Both oCoum and mCoum showed viscoelastic behavior at 20 mM CTAB and 20 mM so their binding patterns would indicate productive binding, while pCoum, which did not form wormlike micelles, would indicate unproductive binding patterns.

2.3.3 Photolysis studies of CTAB and Additives:

Photolysis studies were performed and proton NMRs taken to confirm the conformational change of the cinnamic acid derivatives in water and with CTAB present. Cinnamate derivatives trans to cis conversion has been reported previously including the tOMCA to cOMCA through UV Vis spectra [51] and ^{1}H NMR[69] in water. Recently an ^{1}HNMR of tOMCA in cetyltrimethylammonium hydroxide (CTAOH) after photolysis was reported by T. Liu et al.[57] We will provide photolysis data that compares the derivative in CTAB versus in D_2O of the cinnamic acid derivatives with proton designations.

Photolysis of the samples were analyzed through comparison of unphotolyzed sample vs photolyzed sample ^{1}H NMR. They were then used to

assess molecular changes after photolysis. We observed that the appearance of the cis isomer of the cinnamic acid derivatives coincided with the lowering of rheology for most the cinnamic acid derivatives. Exceptions included pCoum that showed no viscosity in either isomeric conformation or in oCoum which creates two photoproducts. The change in molecular interactions between the cis isomer and CTAB therefore affects the morphology of the surfactant and subsequently the viscosity. All samples were photolyzed in a Rayonet with 254 nm bulbs in a the ^{1}H NMR tubes.

First photolysis of tOMCA in water were used to confirm the isomerization and identify peaks as seen in Figure 2-14d-c. The ^{1}H NMR spectra showed the appearance of new peaks which all correspond to the cOMCA isomer after 30 minutes of UV irradiation and the reduction of tOMCA peak area. Integration of the peaks and comparison between starting material peak area show a 27% conversion. All new protons in the aromatic region were accounted for but cOMCA H2 proton was not identified because it would overlap with the tOMCA t4 signal in D_2O. The reverse experiment where cOMCA was irradiated also gave isomerization of the product. The cOMCA peaks were integrated to show a 20% conversion in 30 minutes. From the integration analysis our samples were not

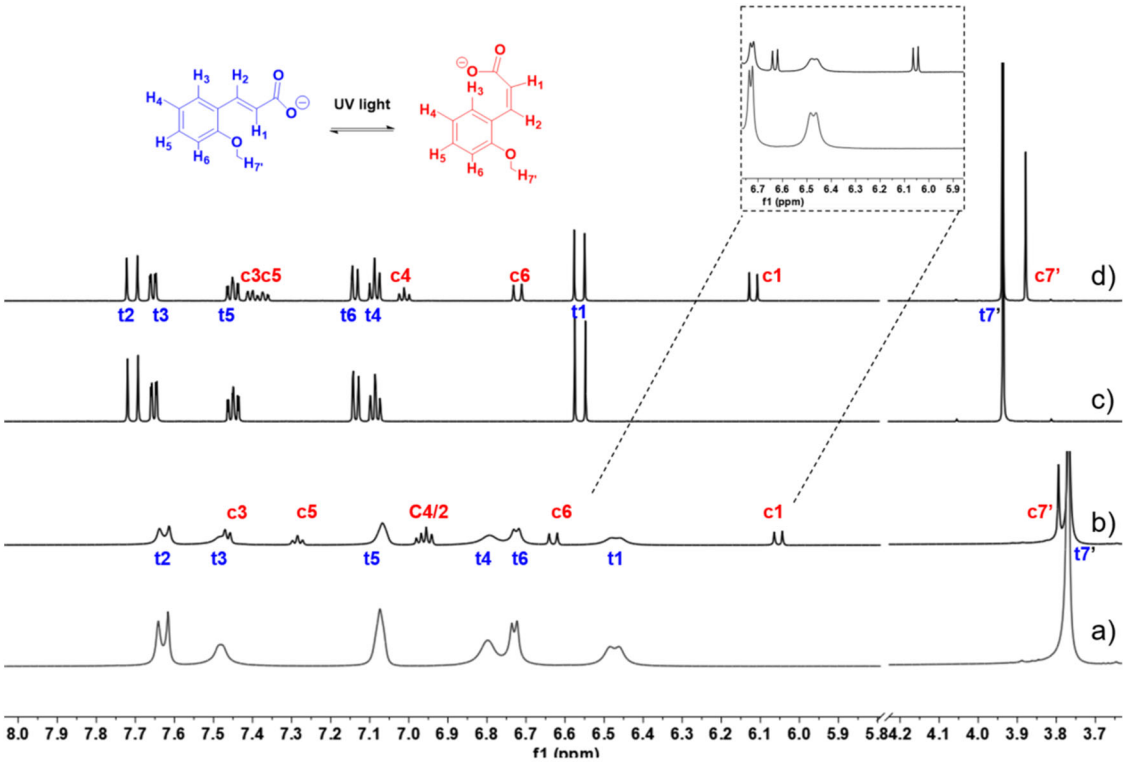


Figure 2- 14 Photolysis of tOMCA, 254 nm Rayonet a) 20 mM tOMCA, 20mM CTAB b) 30 min UV, 20 mM tOMCA, 20mM CTAB c) 20 mM tOMCA D_2O d) 30 min UV, 20 mM tOMCA

photolyzed long enough to reach the photostationary state at which the concentrations of each isomer would have reached a maximum and stayed stable.

Photolysis of 20 mM tOMCA in 20 mM CTAB was also performed with results found in Figure 2-14a-b. All new peaks were able to be identified as belonging to cOMCA with no dimerization products detected. The cOMCA signals show little to no broadening when compared to the tOMCA signals in CTAB. This observation would suggest that the cOMCA molecules are not part of the wormlike micelles. There was the slight shifting of protons signals for cOMCA in CTAB versus free cOMCA when the signals are compared between Figure 2-14b and Figure 2-14d results. The shifting demonstrates the same pattern as the titration

results of cOMCA in 20 mM CTAB. This would coincide with the theory that when cOMCA is created its binding is not as strong as tOMCA so it would relocate into the solvent or near the solvent interface of the micelle.

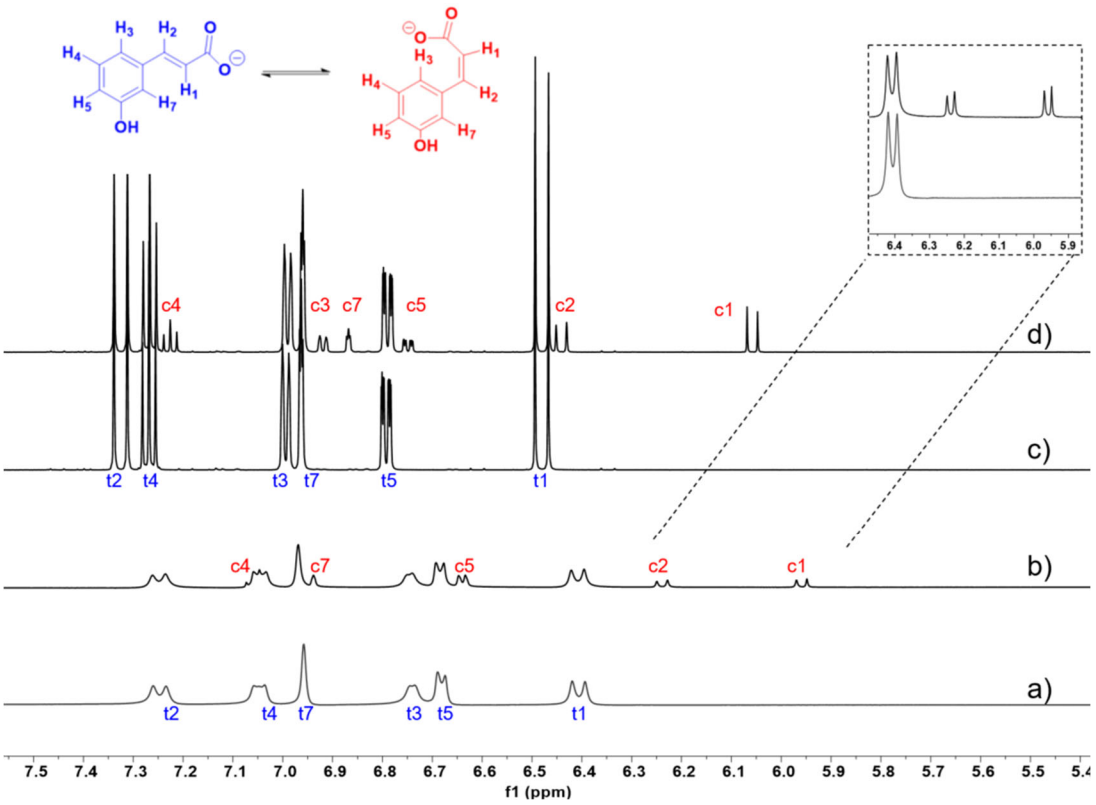


Figure 2- 15 Photolysis^{1}H NMR studies of mCoum at 298 K. Photolysis with Rayonet 254 a) 20 mM mCoum, 20 mM CTAB b) 20 mM mCoum, 20 mM CTAB photolysis 60 min c) 20 mM mCoum D_2O d) 20 mM mCoum 60 min photolysis.

The integration was more difficult for the CTAB samples because of the broadening of signals which made the results less accurate so they were not reported. While not a surprising finding it does confirm that in our conditions isomerization is occurring and that as this is the only molecular change it is the isomerization of tOMCA into its cis form is occurring and the new cOMCA molecules are presenting the same chemical shift change pattern from the titration studies.

The results from the photolysis of mMCA and pMCA can be found in Appendix A. Both show isomerization in D_2O without any dimerization or side photoproducts present. All isomer signals can be identified in both spectra.The *cis*-mMCA signals, like cOMCA, show up sharply in contrast to the *trans*-mMCA spetra containing CTAB after photolysis.

The results of mCoum photolysis clearly indicate the formation of the cis isomer peaks after photolysis in both water and CTAB solutions (Figure 2-15). Similarly, to the photolysis of tOMCA, the *cis*-mCoum isomer peaks are straight but there is a slight broadening. Closer magnification of the *cis*-mMCA (insert Figure 2-15) shows that the signals are slightly broadened. This is now a chance to compare the *cis*-mCoum shifting patterns between in D_2O and CTAB. When the two are compared c1, c2, c5, c4 are shielded when in CTAB but c7 is deshielded. These results for the *cis*-mCoum follow the *trans*-mCoum titration chemical shift results. The shifts are small when compared to the chemical shift changes of the mCoum though, so the *cis*-mCoum may still not bind as strongly.

The oCoum samples presented extra peaks not corresponding to the cis isomer Figure 2-16. These peaks correspond to the photoproduct coumarin. This is notable because oCoum sample rheology did not lessen much after photolysis. The coumarin peaks are present in the 20 mM oCoum 20 mM CTAB photolysis NMR solutions as shown in Appendix A. Finally, pCoum does not show broadening of the trans isomer signals in CTAB also shows that cis isomers peaks do not broaden. The shift of the protons in CTAB versus D_2O is slight for both isomers.

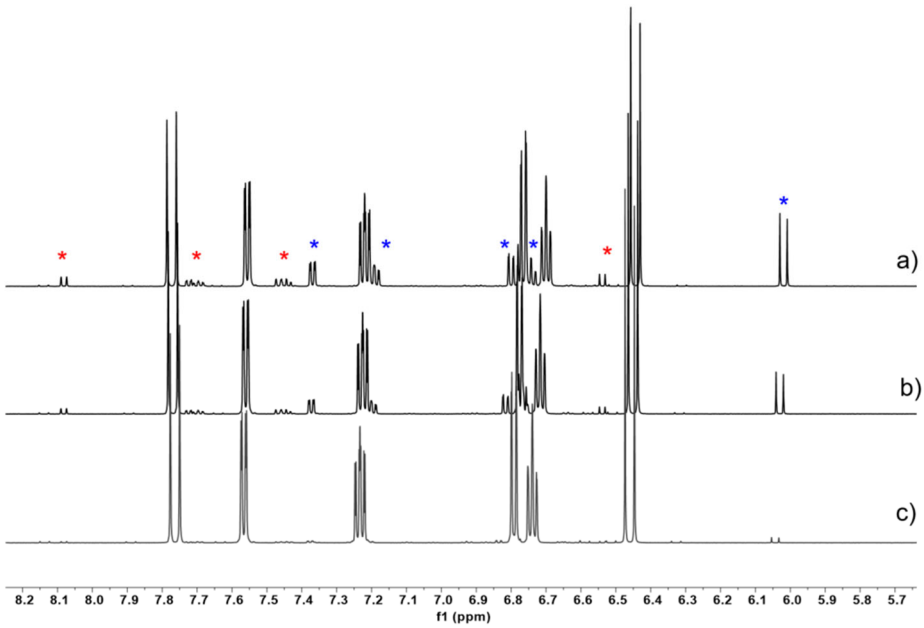


Figure 2- 16 Photolysis of 20mM oCoum at 254 nm in a Rayonet a) 0 min b) 30 min c) 60min. Red asterisks indicate coumarin proton signals. Blue asterisks denote cis-ortho-coumarate signals

The photolysis studies indicate that tOMCA to cOMCA have the largest difference in chemical shift patterns when in CTAB. The cis isomers of mMCA, mCoum and pCoum all followed the general pattern of the trans isomer but to a lower extent. The oCoum sample was the only cinnamic acid derivative that showed a photoproduct other than its isomer.

2.3.4 Two-Dimensional NOESY of additives with CTAB surfactant

Further identification of the additive surfactant interaction were done by using ^{1}H-^{1}H 2D NOESY on select cinnamic acid derivatives. 2D NOESY spectra identify protons who produce a nuclear Overhauser effect or NOE. The NOEs are a through-space alteration of signal intensity that can only occur between protons whose distances are no larger than 5 angstroms.[70-71] The NOESY signals are

detected as cross peaks between the two spectra and while usually of different phases (shown as different colors) for large molecules, though for intermolecular NOEs can be in the same phase.[72-73] Intermolecular 2D NOESY experiments have been done extensively in the characterization of polymers[74] and protein-ligand binding experiments.[73] In this manner we can understand more of the three-dimensional structure interactions between the additive and surfactant.

The NOESY experiments for all the additives were done at the 1:2 ratio of 10 mM tOMCA and 20 mM CTAB. While a 1:1 ratio was attempted the higher viscosity and saturation of the signals did not allow for distinctive signals to be acquired. Additionally, to identify the strongest interactions and increase the tumbling rate of the CTAB/additive complex in the slightly viscous solution the temperature had to be raised from 298 K to 303 K for the tOMCA samples. Control studies of tOMCA rheological samples at 303 K vs 298 K showed very little difference in both dynamic and steady state rheology. There was also no significant difference between ^{1}H NMR signal at the two temperatures. These two results gave confidence that the slight increase in temperature would not significantly alter the interaction between tOMCA and CTAB. Therefore, results at 303 K correlated to all other data gathered at 298 K.

The NOESY experiments for tOMCA in Figure 2-17 at 10 mM tOMCA 20 mM CTAB at 303 K. This concentration was chosen as it showed some broadening of peaks and in the CTAB chemical shift region indicating a morphological change of the micelle, as well as, the binding of the additive to CTAB. This sample was not highly viscous with visual inspection, unlike 20 mM CTAB. The 1:2 concentration

of additive to CTAB ensured that the additive signal would be strong enough to detect versus the CTAB signal while also ensuring that most additive molecules would be interacting with CTAB as it was in 50% excess. Cross peaks are emphasized for clarity with shapes and color coded. If there are corresponding crosspeaks on both sides of the NOESY the colors and shapes will match. In the 1D NMR reference spectra the protons in red are from tOMCA while the ones in black are from CTAB.

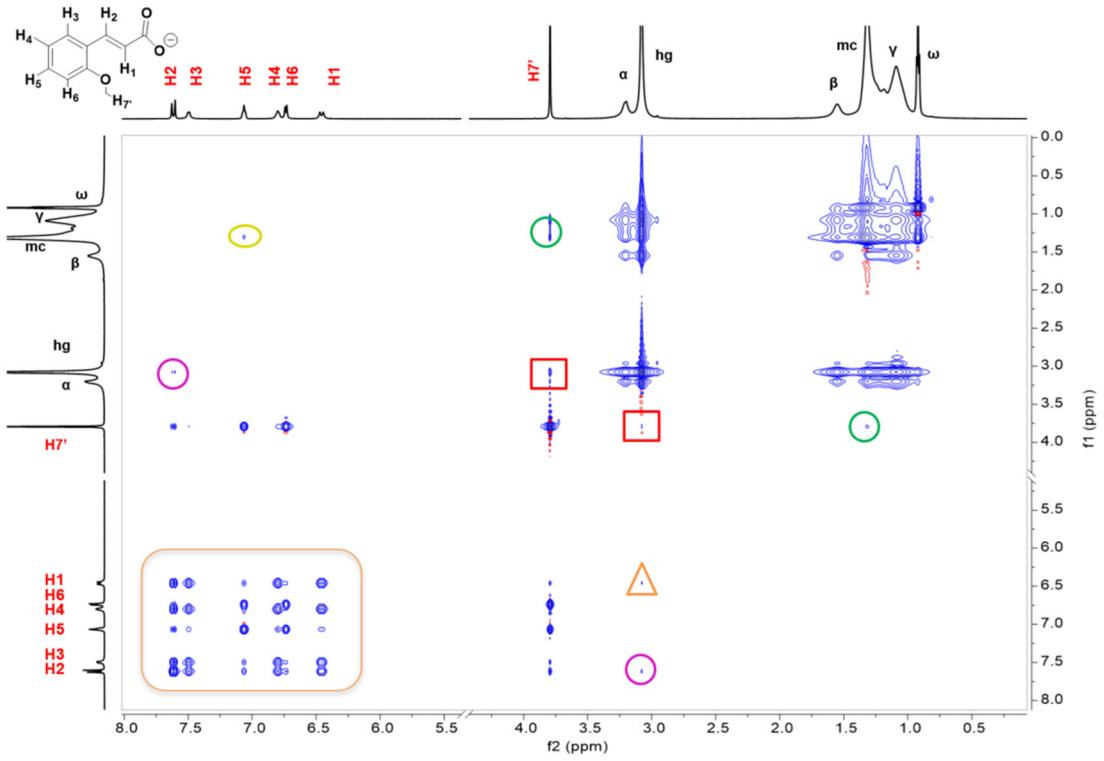


Figure 2- 17 ^{1}H-^{1}H 2D NOESY of 10 mM tOMCA 20 mM CTAB at 303 K, 600 MHz Bruker magnet with BBI probe, D_2O solvent. Strongest NOESY cross peak layer.

The spectra in Figure 2-17 clearly indicates crosspeaks between the CTAB headgroup (hg) and CTAB protons H2 and H7 on both sides of the spectra. While H1 has a crosspeak with the headgroup of CTAB but it is only seen on the hg proton side of the NMR. The main chain (mc) proton signal represents ten protons

in the middle CTAB region. The NOESY spectra indicates that H5 and H7 are within in the micelle hydrophobic region but not the exact proton in the hydrophobic tail. This shows an orientational preference in the interaction between the tOMCA and CTAB when only the strongest NOE signals are taken into account.

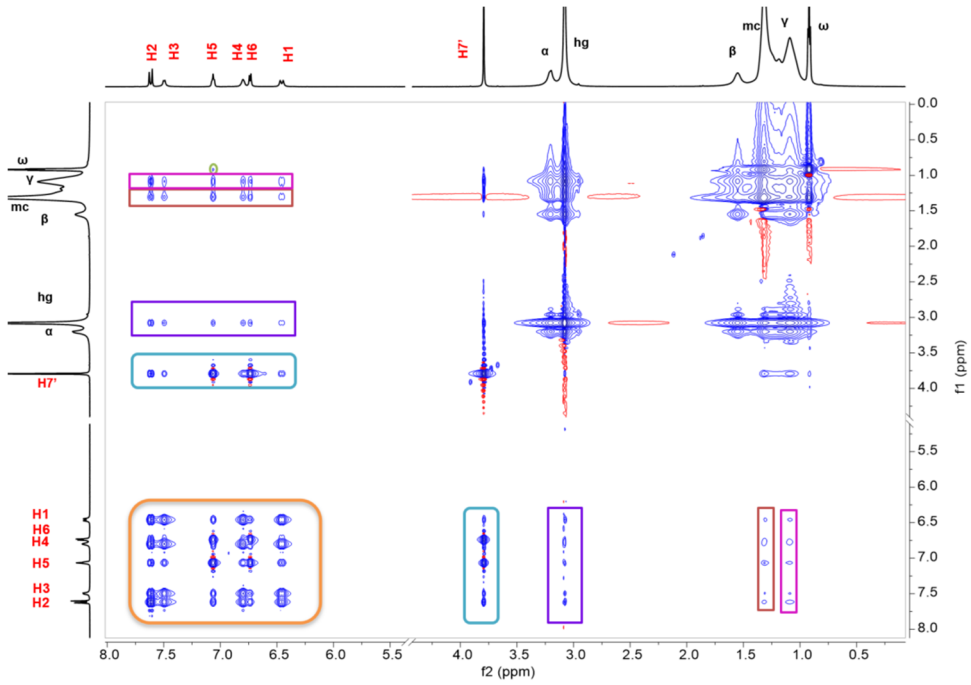


Figure 2- 18 H-^{1}H 2D NOESY of 10 mM tOMCA 20 mM CTAB at 303 K, 600 MHZ Bruker magnet with BBI probe, D_2O solvent.

We have previously showed the first crosspeaks that appeared in the NOESY to avoid spin diffusion effects and to find the strongest NOEs. The further expansion of the NOE spectra can be found in Figure 2-18 as a comparison. The additional NOE signals could be valid and not just noise from spin-diffusion or conformational changes. Specifically, there are two areas of interest 1) the additional crosspeaks between CTAB and all the tOMCA protons 2) the increased homo-dimeric signals in the tOMCA region.

The presence of NOEs between CTAB and all tOMCA protons could imply that molecules of tOMCA are intercalating deeper into the micelle than previously reported. A small crosspeak can even be seen between H5 and the ω inner micelle proton in CTAB. Another difference that supports further intercalation is the appearance of an NOE crosspeaks between tOMCA protons and the new unassigned proton signals that developed to the right of the CTAB headgroup. These protons signals are more shielded and likely the γ protons that continually became shielded with the addition of more tOMCA in the titration studies. The γ protons are located between the head group and main chain. Therefore, if tOMCA were intercalating then an NOE between these protons and tOMCA would be expected. While these NOEs are not necessarily conclusive, it is additional evidence that tOMCA intercalates further into the micelle than the headgroup.

The large orange square on the NOESY spectra in Figure 2-17 and 2-18 is expanded in Figure 2-19 but with only the first and strongest signals being shown. This orange boxed area indicates interesting possible intermolecular interactions between tOMCA molecules. While some of these crosspeaks could be considered intramolecular, the proton crosspeaks that are too far to reasonably give intramolecular NOEs have been boxed and if a matching crosspeak occurs given the same color. In the spectra the only way that protons like H2 and H4 could form crosspeaks is if two molecules of the additive were oriented such that these were no greater than 5 angstroms apart. In total there are three possible intermolecular cross peaks H2-H4, H1-H4, H1-H3. The H7-H2 crosspeak could in theory be intramolecular but is not very strong giving some possibility that it is intermolecular.

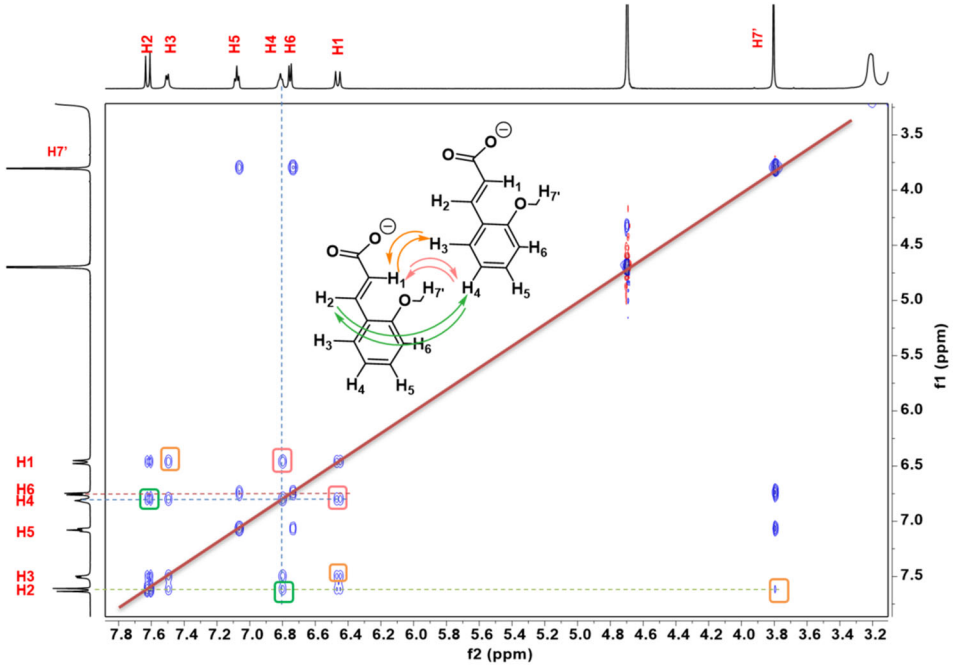


Figure 2- 19 Subset of the ^{1}H-^{1}H 2D NOESY focusing on the strongest NOESY signals for the tOMCA aromatic proton section. Sample was of 10 mM tOMCA 20 mM CTAB at 303 K, 600 MHZ Bruker magnet with BBI probe, D_2O solvent

These results would indicate that molecules of tOMCA are close inside the micelle, perhaps even interacting homo-dimerically. Close interactions between the aromatic additives would also explain the continued increase in shielding seen of tOMCA protons in the titration studies. The increased shielding could be explained by the proximity of aromatic ring currents as more additive molecules are added, along with, an increased presence inside the micelle.

Interaction of aromatic regions such as π- π stacking are known to occur in supramolecular chemistry. The possibility of these interactions in tOMCA was mentioned by Baglioni et al[54] though the 2D NOESY crosspeaks for tOMCA were not explained or any distinctive orientational data possible as they used 1:1 ratios of additive to surfactant. Another 2D NOESY spectra of tOMCA in a different

surfactant system reported the same intermolecular crosspeak pattern in the tOMCA region though π- π stacking was not mentioned.[75] While we cannot rule out π- π stacking the analysis of the strongest NOESY signals in the aromatic proton region as seen in Figure 2-19 indicate that the intermolecular crosspeaks seen are more likely π-anion interactions with the methoxy groups opposite to each other. The orientation of the carboxylate anion next to the aromatic ring currents has been thoroughly investigated in protein chemistry[76] and would better explain the specific intermolecular NOE signals seen in the NOESY spectra. We believe we are the first to introduce this concept and find evidence of its occurrence inside of micelles with cinnamic acid derivatives in a surfactant system.

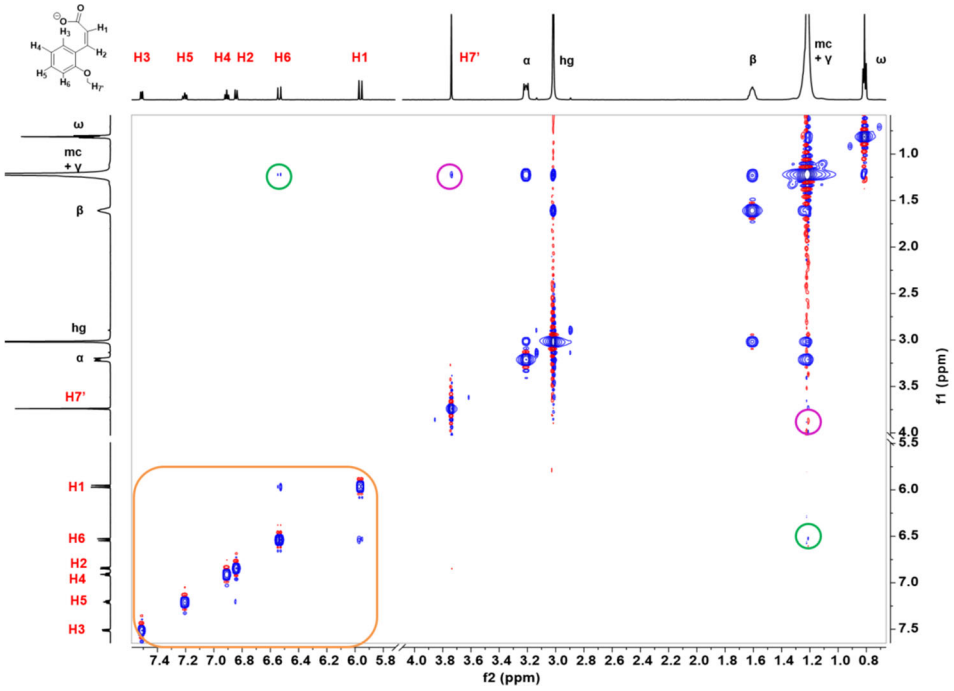


Figure 2- 20 ^{1}H-^{1}H 2D NOESY of 10 mM cOMCA 20 mM CTAB at 298 K, 600 MHZ Bruker magnet with 5 mm BBI probe, D2O solvent. Strongest NOESY cross peak layer

In contrast, cOMCA which shows no increase in viscosity when added to CTAB shows a markedly different NOESY spectrum as seen in Figure 2-20. The first difference is that crosspeaks in the cOMCA and CTAB were much harder to find indicating that binding between the additive and CTAB may not be as strong. This goes along with the titration studies where the cOMCA proton become shielded then quickly plateaued showing only slight shift changes after the initial 2:20 cOMCA to CTAB sample. The two protons that showed intermolecular NOEs were H7' and H6 with the main chain but this result could also indicate an NOE with γ. The γ became part of the main chain as more additives was added. Additionally, the orange boxed area of the cOMCA to cOMCA does not show as many crosspeaks as tOMCA. This could be explained by the conformational difference in cOMCA not favoring the same stacking interactions.

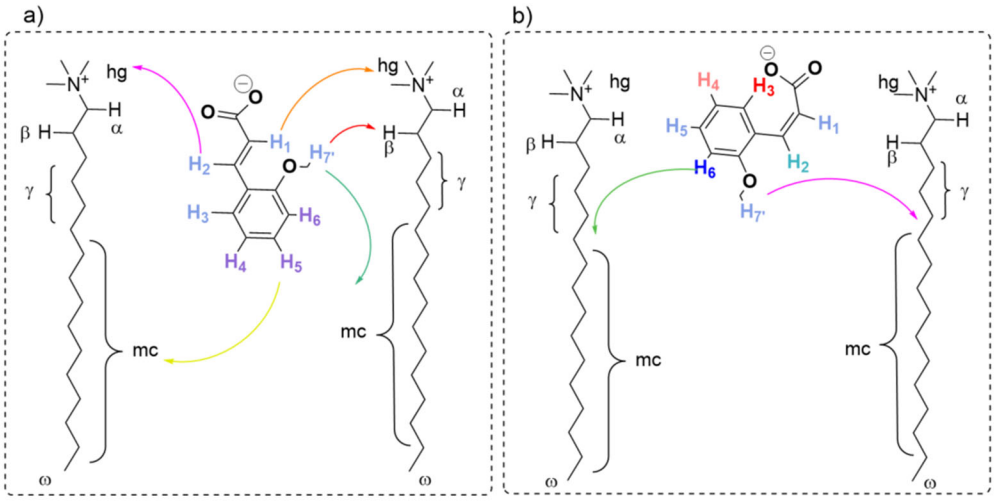


Figure 2- 21 Diagram illustrating the strongest NOESY signals Is for tOMCA and cOMCA.

Using the information from the 2D NOESY spectra of both isomers and the data from the titration studies a model was formed for the additive interactions with

CTAB (Figure 2-21). The diagram illustrates the strongest NOESY signals and chemical shifts superimposed onto an orientational model of the additive. The NOESY intermolecular results are in agreement with the orientational implications of the titration studies between additive and surfactant.

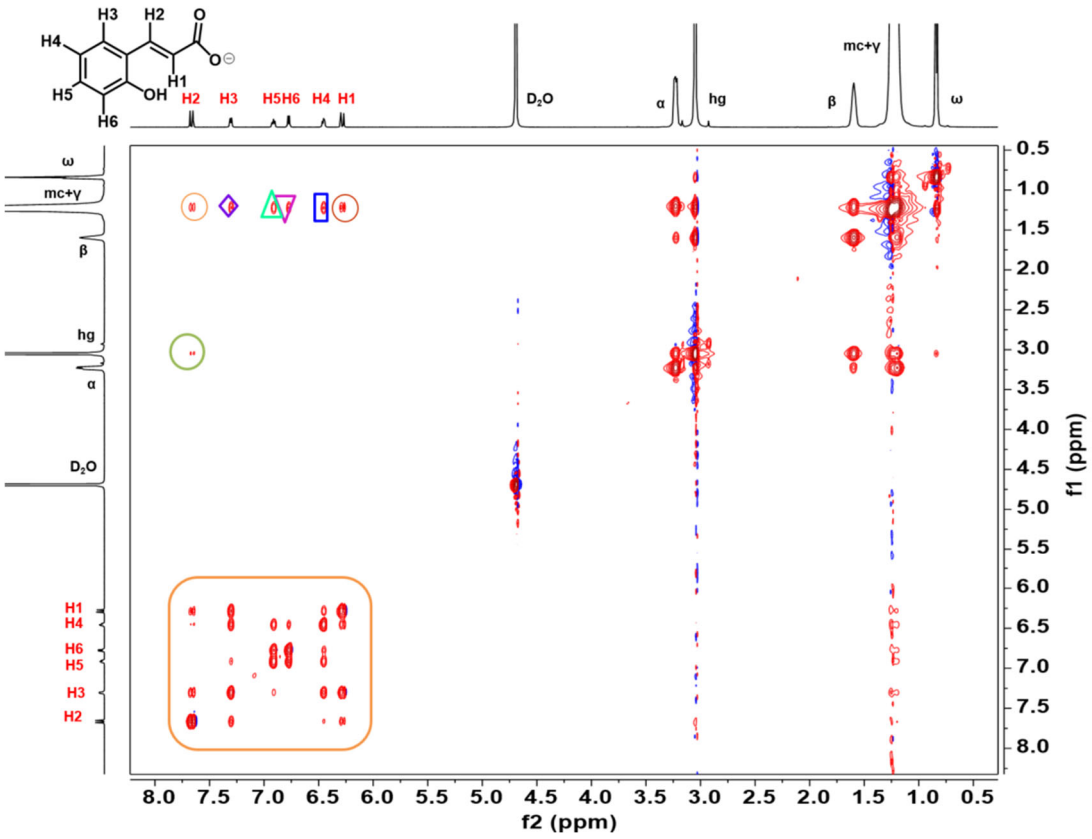


Figure 2- 22 ^{1}H-^{1}H 2D NOESY of 5 mM oCoum 20 mM CTAB at 298 K, 600 MHZ Bruker magnet with BBI probe, D2O solvent. Strongest NOESY crosspeak layer.

2D NOESY spectra were also taken for the hydroxy cinnamic acids. Figure 2-22 presents the results of 5 mM oCoum in 20 mM CTAB at 298 K. The derivative oCoum induces one of the largest rheological changes in CTAB so when trying to perform NOESY experiments a lower ratio of additive to surfactant was necessary. Even at this lower concentration intermolecular NOEs can still be identified between oCoum and CTAB. All the protons have NOEs with the mc + γ CTAB

signal. Another signal that is interesting is the crosspeak between the head group and H2 which would show a directional binding in the CTAB micelle.

The oCoum derivative also shows some possible intermolecular NOEs, even at this lower concentration of additive. The ratio is 1:5 means there are less oCoum molecules present and this data less likely to show intermolecular NOEs. Most of the peaks can be explain by the conformational change of the alkene towards the aromatic ring. The hydroxy group in the ortho position is less bulky than the methoxy, therefore, it would be expected that oCoum would have less barrier to rotation of the alkene group on the benzene. More investigations would need to be done to identify if the oCoum molecules are in close contact.

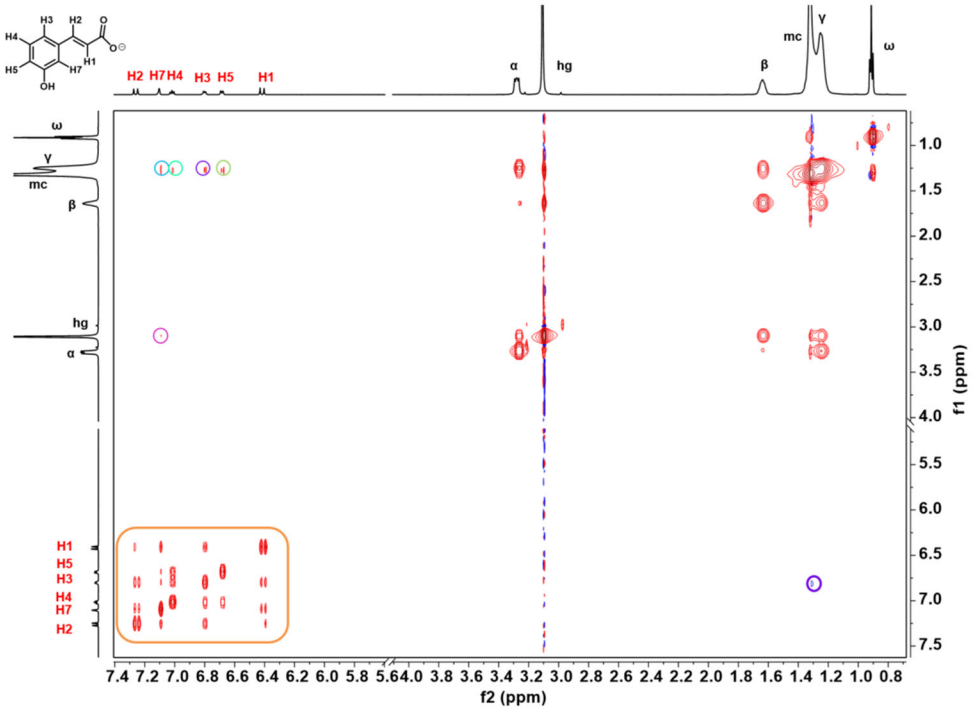


Figure 2- 23^{1}H-^{1}H 2D NOESY of 5 mM mCoum 20 mM CTAB at 298 K, 600 MHZ Bruker magnet with BBI probe, D2O solvent. Strongest NOESY cross peak layer.

The mCoum additive also creates a high viscosity so the NOESY spectra was taken at 5 mM additive to 20 mM CTAB as seen in Figure 2-23. Proton H7 has crosspeaks with the mc+ γ and the head group. This would indicate that there is an intercalation where the H7 is close to the headgroup. The aromatic protons H4, H3, H5 have crosspeaks with the mc + γ set of signals. These signals may implicate that the hydroxy group on the benzene may have some deprotonation. While NaOD was added to the equivalent concentration of mCoum it could be possible that some of the hydroxy group is deprotonated as the pKa of the coumarate hydroxy group is calculated close to 9.7 [77] and the pH of our solutions are basic close to pH = 9. While that may be true it does not change that the binding pattern showed in our conditions creates a viscous solution as presented in our rheological data.

Also, the titration study clearly indicates that the mCoum molecules will intercalate into the CTAB micelle as the chemical shifts for the CTAB protons become shielded and there is a large change in the γ proton (Appendix A). The 2D NOESY for the 10 mM mCoum and 20 mM CTAB at 303 K can be found in Appendix A. The cross section of aromatic protons is the same as with tOMCA. While this does not mean there is intercalation in a particular orientation, it perhaps would indicate proximity of mCoum molecules possibly in a homo-dimeric fashion. Further studies would be necessary to elucidate the exact nature of the interactions.

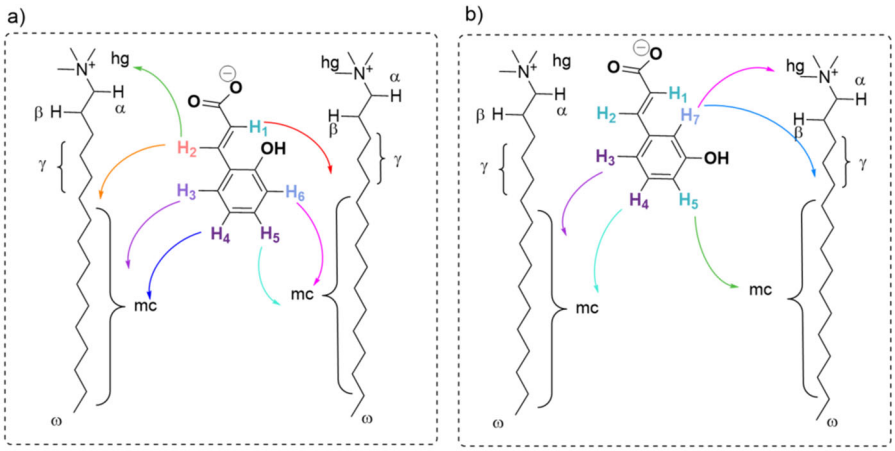


Figure 2- 24 Diagram illustrating the NOESY signals Is for a) oCoum and b) mCoum.

Using the information from the strongest peaks in the NOESY spectrums of oCoum and mCoum a diagram was made of the NOESY interactions in Figure 2-24. While the oCoum shows large chemical shifts that match the NOESY information the orientation of mCoum does not explain the chemical shift difference seen in the titration as well as it did for tOMCA and cOMCA. Another possibility is the hydrogen bonding ability that the hydroxy group gives the molecule may affect its interaction with the D_2O solvent, other coumarate derivatives and the ammonium headgroup differently than the methoxy derivatives. As mentioned, before it could also be possible that the hydroxy group is deprotonated therefore competing with the carboxylate group to orient toward the ammonium head group.

Even with a less accurate match there is still a pattern present that shows protons furthest from the carboxylate group are the most shielded, thereby indicating they are found closer to the main chain protons. The protons that are closer to either the carboxylate or the hydroxy group get shielded less or in the case of oCoum H2 proton are deshielded indicating they are closer to the

ammonium head group or the solvent interface. Also, like tOMCA both show the possibility of intermolecular interactions between derivative molecules inside the micelle or that they pack close together in the present morphology.

The 2D NOESY of 10 mM pCoum in 20 mM CTAB at 298 K can be found in Figure 2-26. The NOESY was very clean with very little noise as there was no viscosity to the sample. Since the molecule is symmetrical there are less aromatic signals. The protons for H3/7 and H4/6 both have crosspeaks with the headgroup, a main chain proton that has not shifted and a main chain proton that shifted upfield possibly one of the protons in the γ group designation.

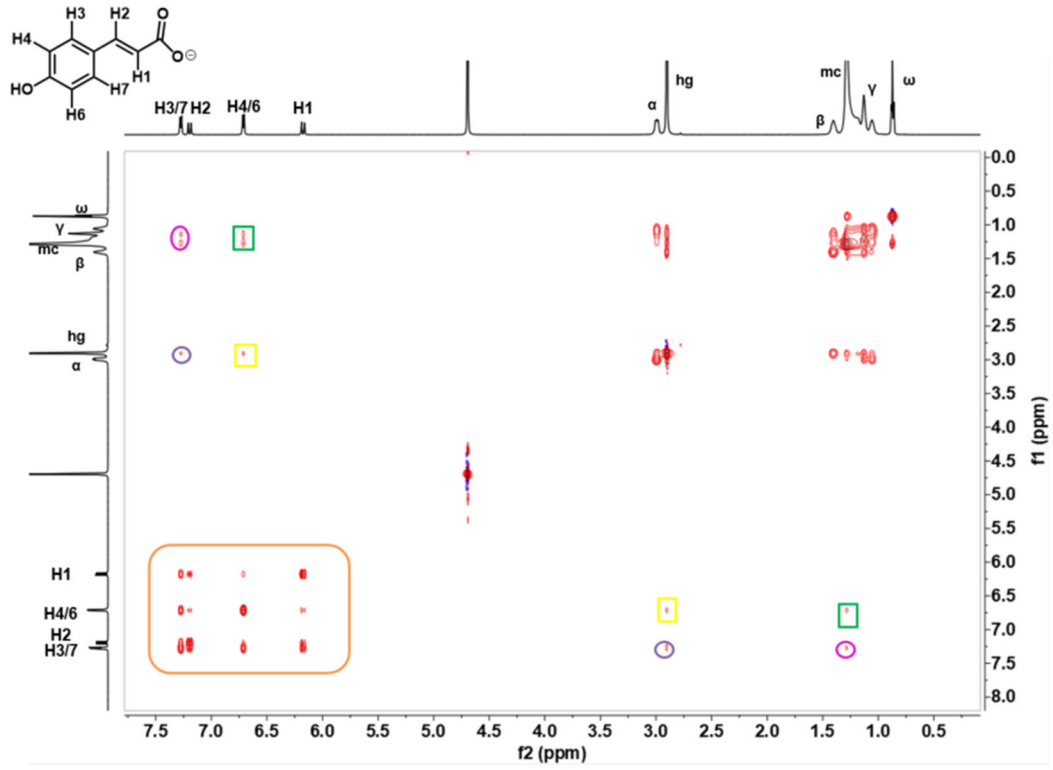


Figure 2- 25 ^{1}H-^{1}H 2D NOESY of 10 mM pCoum 20 mM CTAB at 298 K, 600 MHZ Bruker magnet with BBI probe, D2O solvent. Strongest NOESY cross peak layer.

The pCoum derivative had no viscosity change when added to 20 mM CTAB. The titration studies showed only a small shielding effect in chemical shift change when the additive was added to CTAB with any change then being stable even after more pCoum was added. Therefore, the lack of intermolecular NOE is to be expected if our theory is correct that there is directional binding that is productive or unproductive to rheological changes.

The diagram in Figure 2-26 illustrates the possible orientation of the pCoum molecule with respect to the CTAB surfactant molecule. The NOESY data does not differentiate between the two orientations but with the titration chemical shift changes it is possible that the orientation shown in Figure 2-26b could predominate as this would better explain the small upfield chemical shift change of the H1,H2, H3 and H7 protons.

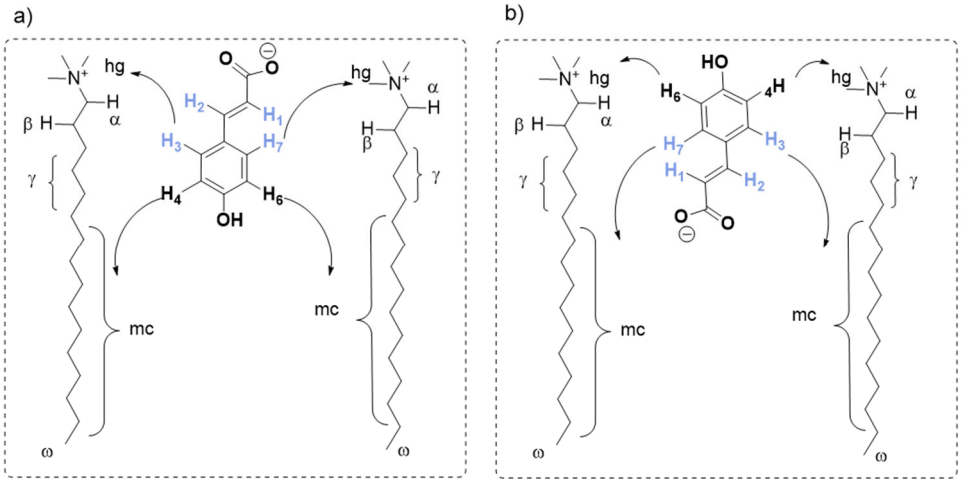


Figure 2- 26 Diagram illustrating the NOESY signals ls for a) pCoum orientation with the carboxylate toward the headgroup and b) pCoum orientation with the hydroxy group toward the ammonium head group.

As stated, our samples are close to the pKa of the hydroxy groups attached to the aromatic ring, which could mean it is deprotonated. Another possibility is

that the hydroxy group participates with hydrogen bonding with the D_2O and therefore prefers that orientation.

2.3.4 B3LYP Calculations

In order to take into account the effect of molecular geometry between changes between the cis and trans isomers, DFT-B3LYP/6-31+G(d,p) calculations were done for both compounds using Gaussian. The results for cOMCA and tOMCA are shown in Figure 2-27. The 3D structure of these isomers shows that the tOMCA isomer prefers a planar conformation of the whole molecule. In contrast the cis isomer of OMCA seen on the right in Figure 33 indicates that the carboxylate is out of the plane from the phenyl ring creating a kinked structure. This lack of planarity could account for the different binding patterns between the cOMCA versus the tOMCA. These results are in line with modeling of the two isomers previously performed.[78]

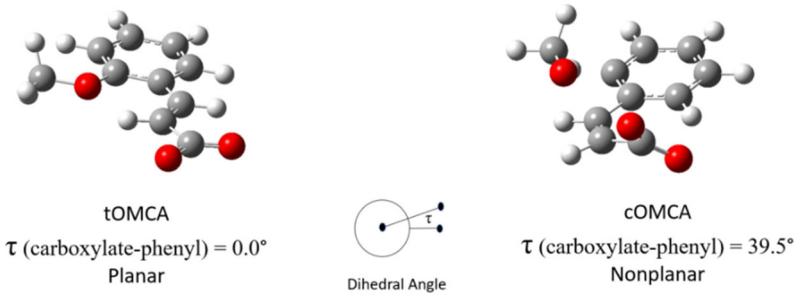


Figure 2- 27 DFT-B3LYP/6-31+G(d,p) 3-D molecule and dihedral angles for cis and trans OMCA isomers.

The carboxylate being out of plane would change the binding of the additive to the surfactant molecule as it acted as a counter ion, therefore changing the geometry of interaction with the CTAB. This change in geometry would have

impacts on the packing parameters of the CTAB molecules and as a consequence the rheology of the sample. We found some binding of cOMCA to CTAB so it could still reduce the electrostatic repulsion between the surfactant's ammonium headgroup, but it did not increase viscosity. This shows that the reduction of the repulsion is not the only intermolecular interaction occurring between cOMCA and the CTAB surfactant. The planar geometry of tOMCA would allow it to intercalate in a flat orientation. Nevertheless, the cOMCA main difference is the lack of planarity. It would seem to indicate that the binding patterns are disrupted by the cis geometry and it is also key to the rheological changes.

In Figure 2-28 the calculations for other additive molecules studied can be seen. The calculations show that all the trans isomers are expected to be planar without exception. The cis isomers do have some differences. For the oCoum the orientations of the carboxylate groups shows that it prefers to be bent toward the hydroxy group indicating the possibility of hydrogen bonding between the two groups. This hydrogen bonding reduces the out of plane geometry of the carboxylate group when compared to the other cis isomers. This tethering of the carboxylate group could also help explain the smaller reduction in viscosity after UV irradiation of the oCoum CTAB, along with the coumarin side product produced through photolysis. In a recent study done by ZH Yan et al.[61] where they studied CTAB and coumaric acid derivatives for formation of light-regulated wormlike micelles at much higher concentrations of CTAB showed the same results. Their data reported that oCoum, while causing an increase in viscosity of samples, did not create as large a reduction of its viscosity in either of the surfactants when

photolyzed. Our data clearly shows an explanation for the lack of viscosity change whether it is the creation of coumarin or the tethering of the carboxylate, and also shows the same results at a lower CTAB concentration.

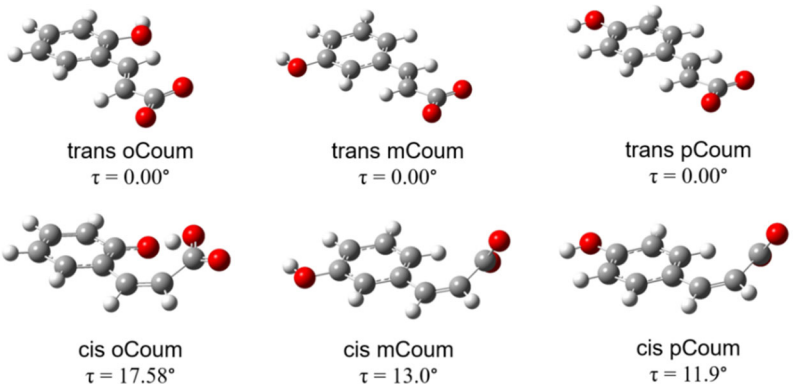


Figure 2- 28 DFT-B3LYP/6-31+G(d,p) 3-D molecular model with alkenyl to phenyl dihedral angles of cis and trans isomers for listed derivatives.

In contrast to oCoum the mCoum additive showed a marked reduction in viscosity when it was photolyzed. The cis-mCoum molecular model in Figure 2-28 shows the same carboxylate out of plane geometry as cOMCA. In both cases the trans geometry caused viscosity to increase in CTAB samples when added, while the addition to UV light lead to the creation of the cis isomer lowered the viscosity. This would indicate that in these samples the main differences between the two isomers is what causes the change in viscosity. Therefore, the 3D geometry of the additive is vital to the viscosity changes. Specifically, the carboxylate group being out of plane is the biggest difference between the two isomers.

2.3.5 Model of molecular interactions in CTAB micelles

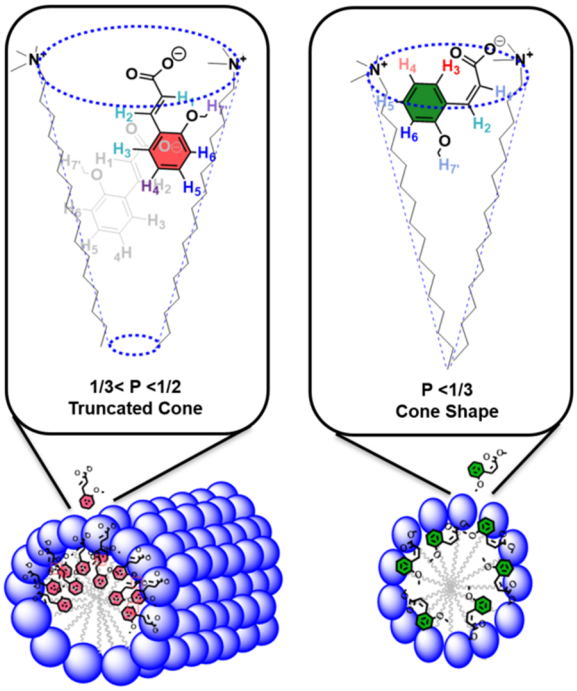


Figure 2- 29 Molecular model detailing the different interactions of tOMCA and cOMCA with CTAB that leads to the difference in packing parameter.

Using the packing parameter as a basis for morphology changes in surfactant systems we applied the data obtained in our study to produce a model that describes the molecular interactions between CTAB and the ortho methoxy cinnamic acid isomers that explain the changes in rheology both additives produce. The model we are proposing for tOMCA and cOMCA in CTAB surfactant can be found in Figure 2-29. This model has major differences with previous models other labs have proposed. Molecular models for tOMCA in CTAB,[79] other cinnamic acid derivatives in CTAB,[54, 78] or cinnamic acid derivatives with other surfactant systems [79, 69, 75] have been documented. Our lab has also previously proposed a molecular model describing the interactions between CTAB and cinnamic acid.[55]

We propose three major differences : 1) the cis isomer does intercalate into the micelle and orients in a perpendicular fashion 2) tOMCA intercalates into the core micelle region and 3) we propose close interactions between tOMCA additive molecules, most likely π-anion stacking.

First our model explains why the creation of cOMCA, which intercalate into the micelle, causes a loss viscosity. We have, unequivocally, shown that it is incorrect to state that cOMCA does not intercalate or bind into the micelle. It does intercalate with the head group region possibly with the γ protons. We are the first to provide significant evidence of cOMCA binding patterns in CTAB. The titration studies clearly show that it is the H4 and H3 aromatic protons that are deshielded and therefore most likely to be near the ammonium charged headgroup. The protons on the other side of the cOMCA are all shielded indicating that they would be further away from the water interface and ammonium headgroup, showing agreement with the *cis*-conformation shown. This orientation, in terms of packing parameters ($P = v/a_0 l$), encourages micelle formation by increasing the a_0 variable of the equation therefore lowering the packing parameter value. This would favor the cone shape geometry that induces micelles.

Additionally, after photolysis of tOMCA the newly formed cOMCA had the same chemical shift change as the protons in the cOMCA titration studies correlating to the 20 mM ppm; they were in the same pattern. 2D NOESY experiments further corroborated our model with indications of intermolecular NOEs between cOMCA and mc + γ CTAB protons.

Therefore, our model proposed that when tOMCA is photoisomerized viscosity goes down not only because of loss of tOMCA but also because of the intercalation of cOMCA. The binding pattern of cOMCA promotes spherical micelles for two-fold reasons: 1) it binds perpendicularly to the CTAB molecules near the head group 2) it does not go deep into the micelle core and therefore cannot add to the volume in the packing parameter. These two factors would favor the packing parameter being $p<1/3$ or spherical.

The binding of tOMCA indicates that it intercalates into the micelle core in close proximity within the micelle to other tOMCA molecules. From our model addition of tOMCA molecules into the micelle core would increase the volume of the micelle inducing a truncated cone geometry that forms the worm-like micelles. The added possibility of anion-π stacking could also explain why the wormlike micelles are formed at so low CTAB concentrations, as they would bring added stability beyond reducing electrostatic repulsion between CTAB headgroups. We provided evidence of this possible interaction as seen through the crosspeaks in the 2D NOESY spectrums, as well as the shielding of protons in the titration studies. The with the linear geometry of the trans isomers would also allow for the aromatic interactions to occur.

2.4 Conclusion

Interest in smart materials that can produce changes through stimuli, especially phototriggered systems, continue to grow. To create better photosensitive surfactant systems an understanding of the molecular interactions

favoring and hindering viscosity is key to optimizing existing systems and directing the creation of new intelligent materials specific characteristics.

We have provided new evidence through 1D ^{1}H NMR titration studies of both the tOMCA and cOMCA, as well as other cinnamic acid derivatives, in CTAB about the molecular interactions within the system that helps or hinders, the creation of wormlike micelles. Photolysis studies produced evidence of the conversion of the trans isomers into the cis isomers for all additives. Though oCoum was notable in that it also produced the side product coumarin.

^{1}H-^{1}H 2D NOESY experiments further defined the structure of the additive surfactant interactions in 3D space. These studies indicated which protons where found closest to different CTAB regions providing further evidence of a likely orientation in the micelle. From these studies orientational models were produced that showed tOMCA, mMCA, oCoum, and mCoum molecules having similar orientation of the carboxylate toward the ammonium head group. It showed that with each addition of additive all these molecules showed continual deshielding until the protons in CTAB and the aromatic region broadened indicating a morphology change.

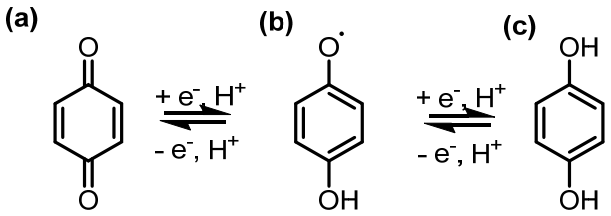
Preliminary evidence of intermolecular interactions between tOMCA molecules inside the micelle was presented. The 2D NOESY detected crosspeaks between the additives, showing close intermolecular distances between the additive molecules in the trans isomers. These NOEs were not detected in the cOMCA isomers. We postulated that the aromatic region of one additive and carboxylate anions region of another were detected possibly interacting through

π-anion stacking. More work should be done to define these interactions of additives more clearly within the micelle.

Finally, molecular modeling clearly indicated a change in geometry that explains why the cis isomers would need to bind in the pattern seen in our titration studies. This change would also explain why no intermolecular NOEs were found between cOMCA molecules. We hope that this new information will better inform the creation of new phototriggered intelligent materials.

Chapter 3: Release of Calcium Through Disruption of EDTA Chelator Binding by Anthraquinone Sensitizers Electron Donation.

3.1 Introduction

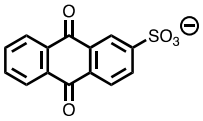
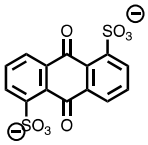
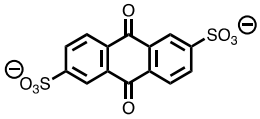


Scheme 3- 1 Quinone one-electron reduction from a) oxidized quinone to b) semiquinone and then to fully reduced c) hydroquinone

Quinones are a ubiquitous class of biomolecules found in living cells and organic materials, especially in plants where they take part in redox signaling and oxidative phosphorylation.[80] They contain a chemical moiety consisting of two ketones and two double bonds conjugated with each other in a cyclohexane ring structure (Scheme 2a). Quinones can cycle between three redox states Scheme 2: a) oxidized, b) radical semiquinone and c) a fully reduced hydroquinone. One useful property is that they can act as photosensitizers, molecules that absorb light then cause a photochemical reaction to occur. While there are many photochemical uses, previous research interest includes their role in dissolved organic matter (DOM) natural water systems, organic synthesis and uses in photodynamic therapy (PDT) of tumors.[81] Their ability to act as photosensitizers and the availability of their reactive moieties in nature made them sensible choices in our own studies.

Our research used the following three water soluble quinone derivatives: 2-anthraquinone sulfonate (2-AQS), 2,6-anthraquinone disulfonate (2,6-AQDS) and 1,5-anthraquinone disulfonate (1,5-AQDS). These anthraquinones were examined as possible electron transfer sensitizers for the degradation of the calcium chelator ethylenediaminetetraacetic acid (EDTA). The biocompatibility of the quinone moiety and higher solubility of sulfonic acid derivatization made these compounds promising candidates to act as photo-oxidants in aqueous solutions. General photophysical properties of the anthraquinones sensitizers used in our study can be found in Table 2.

Table 3- 1 Photophysical properties of anthraquinone derivatives used in this study**

Sensitizer	ID	λ_{max} (nm)	E_{red}[a] (V)	E_T[b] (eV)	$\tau_{triplet}$ (ns)	ε ($M^{-1}s^{-1}$)
	2-AQS	330[82]	-0.38[83]	2.68[84]	15[85]	5200[82]
	1,5-AQDS	326[86]	-0.50 [83]	2.36[87]	135[88]	3800[89]
	2,6-AQDS	326[90]	-0.31[83]	2.68[91]		5200[90]

** All reported values are in predominantly aqueous media, pH=7 unless otherwise stated. [a] $-E°$(MIM$^-$),V(NHE) for one electron transfer.[b] E_T Is the triplet energy of the excited state anthraquinone.

Quinones can act as photo-oxidants through electron transfer reactions. Photoinduced electron transfer (Figure 3-1) starts with the sensitizer's absorption of light. This photon absorption then causes the molecule to reach its excited state

which confers a change in oxidation potentials. This makes the electron transfer more favorable. The donor or the acceptor can be the sensitized molecule depending on the location of the chromophore. When quinones absorb light they accept an electron from compatible reductants. Previous electron transfer research with anthraquinones include studies on their ability to initiate polymerization of vinyl polymers,[92-94] H-atom abstraction mechanisms to form anthraquinol AQH_2 ,[86-95] electron transfer from thymine [96] and hindered amines.[88, 97]

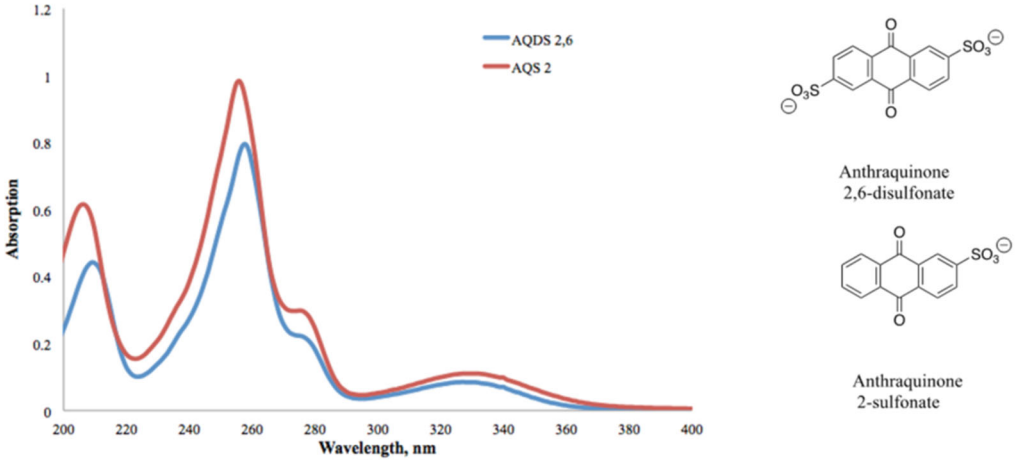


Figure 3- 1 Absorption spectrum for sensitizer anthraquinone 2,6-disulfonate and anthraquinone 2- sulfonate.

We are proposing that an electron transfer from the EDTA chelator to the anthraquinone will lead to the release of the divalent ion captured by the chelator. The process of EDTA degradation after the accepting electrons has been previously researched and is known to occur.[98-102] The release of calcium is useful in both biological and engineering applications. Calcium is a vital secondary messenger in biological systems and its controlled release has been used to study

muscle contractions, cell apoptosis, and as a useful trigger for rheology changes in such biopolymers such as alginate and pectin. To our knowledge, this is the first time anthraquinones have been used to degrade EDTA and then subsequently release calcium.

The interactions of calcium with materials such as alginate can lead to changes in the rheology of the solution, or its ability to flow. Changes in rheology have been explored for the creation of intelligent systems that react to stimulus and can be controlled precisely.[103] Besides these applications biological release of calcium has been used to examine many biological processes in detail such as neuron firing, enzyme function and electrochemical potentials outside cells.[104-105] Therefore, it is useful to control the amount of calcium that is available to a system. These changes in a system, through the addition or entrapment of varying ions such as calcium have been studied and are or particular interest to our research.

Our study will use affordable and commercially available materials to release calcium using light as a trigger. It was considered important that the materials used in this study were easily accessible to create a robust system that can be studied and possibly be used as a way of studying it in a wide range of applications. In the mechanistic process a sensitizer will first absorb light, changing its electronic oxidative potentials. The sensitizer in its excited state then accepts an electron from the chelator thereby becoming reduced. Once the chelator is oxidized it degrades thereby releasing the calcium. We will demonstrate the release of calcium through a calcium assay and degradation of the chelator. NMR

studies will also show the degradation of the EDTA. Application of the system to alginate hydrogels will be limited to external addition of alginate to a photolyzed solution. We will show the ability of our sensitizer to degrade EDTA and release enough calcium to form an alginate bead when it is added to the photolyzed solution.

3.2 Materials and methods

Photolysis materials including anthraquinone-2-sulfonic acid sodium salt, anthraquinone-2,6-disulfonic acid, anthraquinone-1,5-disulfonic acid and sodium alginate from brown algae were purchased from Sigma Aldrich and used without further purification. Calcium analysis chemicals: dye *o*-Cresolphthalein Complexone (CPC) and diethylamine were bought in analytical grade from Aldrich.

3.2.1 Photolysis of samples

Samples were photolyzed at 254nm and 350 nm using a Rayonet Photoreactor from the Southern New England Ultraviolet Company. Polychromatic wavelength photolysis at other wavelengths were done on a 150 W Hg-Xe medium pressure lamp, using cut off filters as indicated in the results section Table 3-2. The solutions were 1 mL in volume with a concentration of Ca-EDTA that ranged from 2.5mM to 25 mM in deionized water (pH 5-7). Anthraquinone sensitizers were added from 0.5 to 5 mM in the photolysis solutions. Alginate gels were prepared by % weight followed by sonication.

3.2.2 Calcium Dye Assay

A modified spectrophotometric dye method using *o*-Cresolphthalein Complexone (CPC) was used in our study to determine the amounts of calcium released (Figure 3-2).[106,107] The working dye solution was made by adding 1 mL concentrated HCl to 40 mg of CPC. The dissolved CPC was then transferred into a 1 L volumetric flask. To the CPC 100 mL of dimethyl sulfoxide and 2.5 g of 8-hydroxyquinoline were added.

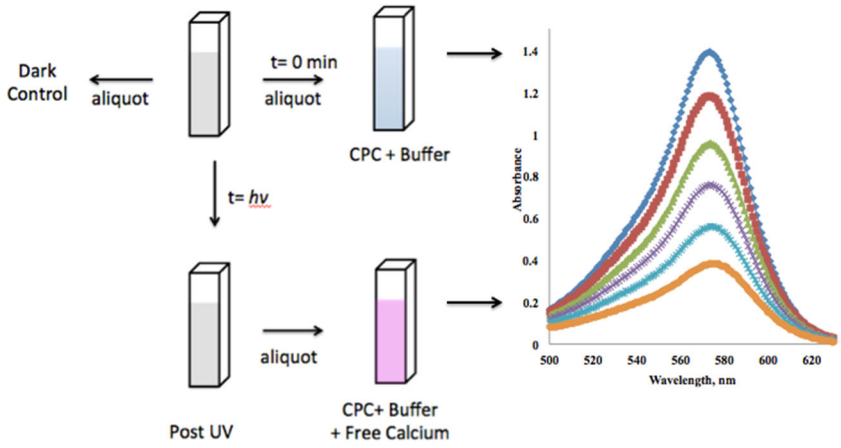


Figure 3- 2 Modified CPC Calcium assay steps for determination of photolysis calcium concentration.

The solution was mixed until dissolved and then diluted to volume with deionized water. The DEA buffer was made by adding 40 mL of diethylamine into a 1 L volumetric flasks. Then 0.5 g of potassium cyanide is added and dissolved with deionized water until the 1 L volumetric flask mark.

The assay involved adding 1 mL of CPC working solution, then 1 mL of diethylamine buffer solution (DEA), and 1 mL of water to make calcium testing solution. Once the solution was mixed by inversion, a UV-Vis at 575 nm was taken to serve as a blank. To the calcium testing solution, a 20 µL amount of test sample

was added, mixed by inversion and then UV-Vis measured at 575 nm to serve as the experimental. A calibration curve was then used to determine molar concentration. Experiments also had dark controls to confirm no reactions occurred without the light trigger; none of the dark controls showed calcium release. Experimental error calculations and testing of assay can be found in Appendix B, including precision and accuracy calculations.

3.2.3 1-Dimensional ^{1}H-NMR

Spectra were taken in deuterium oxide solvent, at 298 K and without spinning. All water signals were suppressed using standard Bruker water suppression program zgesgp. This is a solvent suppression with double pulse field gradient spin echo. Each spectrum had 32 scans, 2 s relaxation delay, and a receiver gain of 1625.

3.2.4 Instrumentation

All UV-Vis spectra were taken on a Shimadzu UV-1800. 1-D ^{1}H-NMR spectra were obtained on a Bruker 400 MHz spectrometer with a BBI probe.

3.3 Results and Discussions

The absorption spectra of the anthraquinones (Figure 15) indicates wavelength maximum around the 250 nm and 330 nm range. We took advantage of both absorptions, with preference toward the more biologically relevant higher wavelength region. The photophysical characteristics of the sensitizers can be found in the Table 2. The spectral range also influenced our use of calcium

analysis dye and the method by which we finally adapted the assay. Our assay had to be able to withstand any interference from the absorption of the dyes in the 400 nm range, and so we chose to go with CPC, whose absorbance maximum was 575 nm for our assay.[108] This also allowed for testing at different time points from the same photolysis mixture, creating a time course of calcium release based on the same sample mixture. Full details can be found in the Methods section 3.2.2.

The testing of the reliability of our assay including calibration curves, accuracy and reproducibility can be found in Appendix 3-1. Errors became apparent if the mixture of CPC, DEA and deionized water was mixed more than 5 minutes before the aliquot was added. Calibration curves were used and their linearity tested before use each week of testing. LINEST error calculations showed errors in the slope of 0.06 and 0.04 for the intercept in the example given, which is indicative of the other calibration curves. Errors in calcium determination did not exceed 10% and averaged 5% in most calcium concentrations. Once we established our calcium assay would work with our photolysis mixture, we proceeded to test our calcium system.

3.3.1 Calcium Release Experiments:

Our system showed that calcium was released at both 254 nm and 340 nm light (Table 3-2). While anthraquinones do have absorptions above 340 nm, our testing at those wavelengths with cutoffs on the Xe-Hg lamp did not show any detectable calcium release. Based on our wavelength range, the highest calcium

release was at the 254 nm. These results were not unexpected as the absorption is higher at that wavelength maximum, though it had been hoped that our system would be able to be used in the visible wavelength range, as it is more biologically relevant.

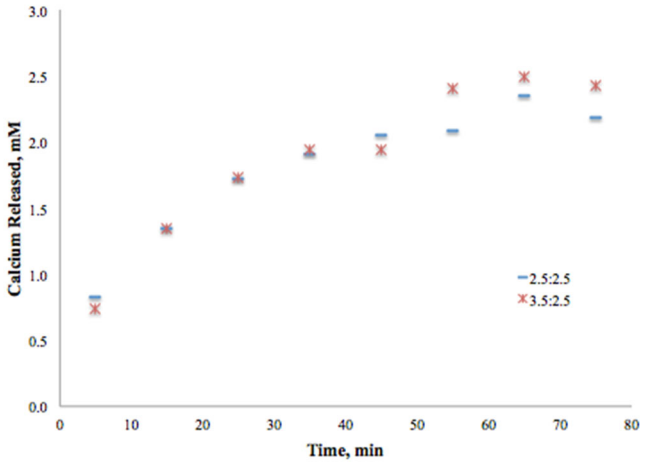


Figure 3- 3 Variable AQS-2 Sensitizer to Ca-EDTA ratios. All solutions contained fixed 2.5 mM Ca-EDTA, photolysis at 350nm, Rayonet.

In the testing of our system false positives were a concern or interference of photolysis products with our system. To further expand our understanding, we tested the maximum calcium the system would detect and if that value, was consistent with the maximum amount found in the solution as compared to the sensitizer. In one case, the sensitizer was present in the same amount as the Ca-EDTA; in the other, the sensitizer was above the amount of Ca-EDTA while keeping all other variables constant, (Figure 3-3). In both cases, the maximum calcium released did not exceed the initial 2.5 mM added pre-photolysis. The increase in calcium concentration continued until it reached the max 2.49 mM at 60 minutes. Of note is that in both cases the release followed the same rate release

progression, even though the sensitizer amounts varied. This could be within our error calculations, or there could be some dependence on the Ca-EDTA concentration for the release of calcium. This dependence on both starting compounds is true of most biomolecular reaction systems.

Our results also depend on the reaction not occurring when light was absent. This is important as anthraquinones can act as oxidants without light activation in certain systems. In each case, a small aliquot of solution was left in an area without light during the photolysis (the dark control). When the photolysis experiment was carried out, it was tested for calcium release and compared to the original t = 0 sample. In all cases there was no calcium release found in the dark controls.

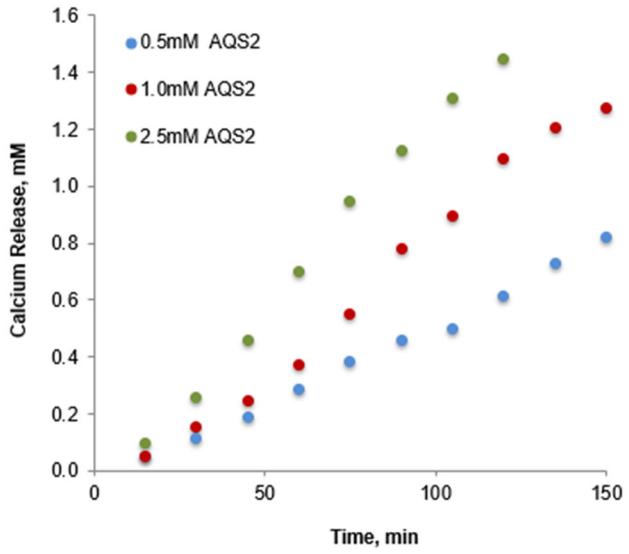


Figure 3- 4 Variable AQS-2 concentrations in 25 mM Ca-EDTA, 340 nm with cut-off filter, Hg-Xe lamp

A dependence on sensitizer concentration was found during calcium release (Figure 3-4). Testing of variable amounts of sensitizer, while keeping the amount of Ca-EDTA at 25 mM, indicated that anthraquinones released close to 1:1 stoichiometric amounts of calcium to sensitizer. Though calcium was released at close to stoichiometric amounts to the sensitizer during the time recorded, there were also cases when more calcium was released.

Figure 3-4 shows calcium release of AQS-2 at varying amounts of sensitizer while the Ca-EDTA concentration was held constant at 25 mM. The release follows a linear increase with time at the 340 nm filter cut off. There were notable exceptions of extended photolysis allowing larger amount of calcium to be released, something that will be discussed later. A comparison of all three anthraquinone sensitizer at the same 2.5 mM concentration in 25 mM Ca-EDTA mixture can be found in Figure 3-5. The results demonstrate that AQS2 and AQDS1,5 are stronger sensitizers in our parameters.

When comparing the three anthraquinone sulfonates at 254 nm photolysis it was evident that 2-AQS and 2,6-AQDS acted as stronger sensitizers than 1,5-AQDS (Figure 3-5). While all three have similar wavelength maxima, 1,5-AQDS does not have a strong phosphorescence, something reported by Loeff et. al.[87] This indicates that the conversion to the triplet state is low, causing it to be a much weaker sensitizer and photo-oxidizer than the other two anthraquinones. Another possibility which is mentioned by Moore et al[91] is that these weaker sensitizers took part in self-quenching. Additionally, as reported herein (Table 3-1), the molar absorptivity of 1,5-AQDS is much lower, making it much less efficient at absorbing

photons and starting the photochemical redox reaction. Table 3-2 shows key results of calcium release varying different variables including wavelength, sensitizer concentration, and Ca-EDTA concentration.

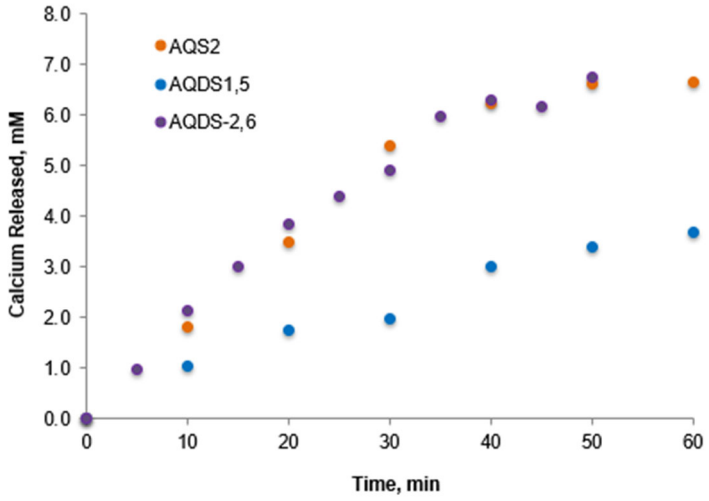


Figure 3- 5 Photolysis at 254 nm light measuring for calcium release. Ca-EDTA concentration was at 25 mM. Each sensitizer used was at 2.5 mM

As stated, the photoelectron transfer reaction we believe is occurring when EDTA donates an electron to the excited state of anthraquinones, an event which oxidizes the EDTA and reduces the anthraquinones. Once the reaction occurs the anthraquinone will abstract a proton and be partially reduced. It can then again accept another electron when it is excited again, turning into the completely reduced form, as seen in previous studies.[109] Once they are in this reduced form, they can no longer take part in the degradation of EDTA and release of calcium. We believe this was occurring in our samples. We believe the efficiency of the catalytic cycle is limiting the amount of calcium released. In other words, we reached a limit to the recycling and therefore calcium release because the sensitizer stayed in its reduced form.

Table 3- 2 Key Calcium release results with varying Sensitizer and Ca-EDTA concentrations

Sensitizer	[Sensitizer] (mM)	[Ca-EDTA] (mM)	λ (nm)	Time (min)	Released Ca^{2+} (mM)
2-AQS	2.5	25	254	60	6.4
2-AQS	5.0	25	254	60	5.3
2-AQS	0.5	25	340	60	0.3
2-AQS	1.0	25	340	60	0.4
2-AQS	2.5	25	340	60	0.7
2-AQS	2.5	2.5	350	60	2.1
2-AQS	2.5	3.5	350	60	2.4
2-AQS	3.5	2.5	350	60	2.4
1,5-AQDS	2.5	25	254	60	3.7
1,5-AQDS	2.5	25	394	60	0.0
1,5-AQDS	2.5	25	440	60	0.0
2,6-AQDS	2.5	25	254	50	5.1
2,6-AQDS	5.0	25	254	60	3.4
2,6-AQDS	2.5	25	440	60	0.0

To test this hypothesis, we took absorption spectra of the photolysis solution before and after photolysis in which calcium was released. Figure 3-6 shows the results of one of those experiments. As can be seen the AQS-2 solution changes color and wavelength absorption shifting toward red, indicating an increase in conjugation of the system. The change can be attributed to the AQS-2 form of the molecule being reduced into the AH_2QS form. A new λ_{max} looks to be forming from 330 to 380 nm, which fits perfectly to previously reported results of the absorption maximum of the reduced form of AQS-2.[86, 110] There was no reversal of the color change therefore, we can surmise that the reverse reaction was no longer occurring.

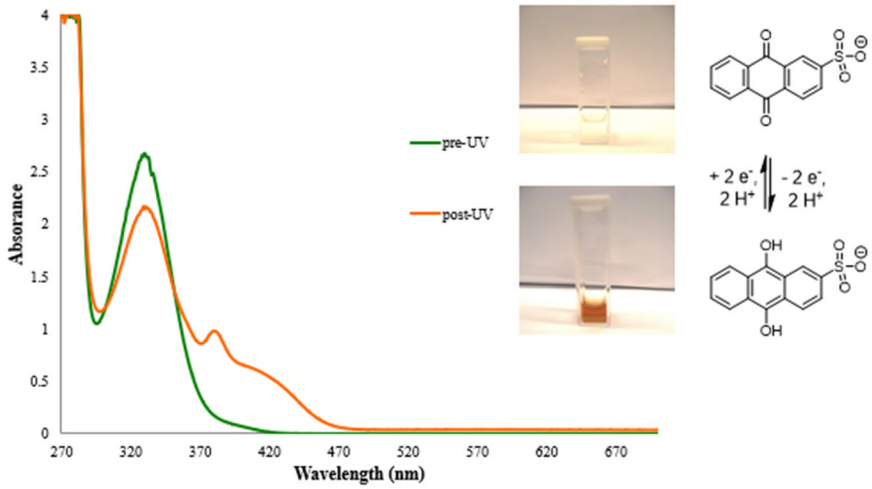
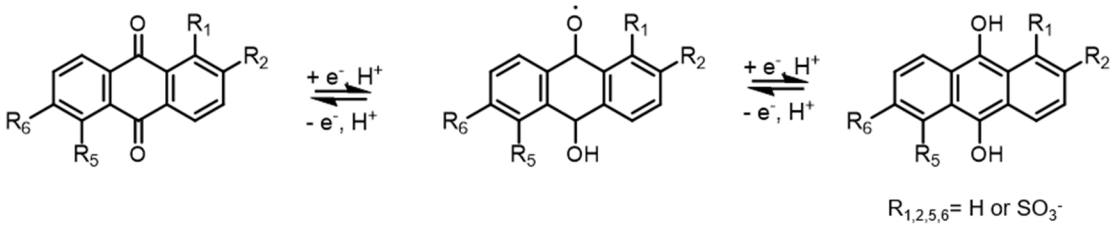


Figure 3- 6 Absorption spectra of the oxidized/reduced form of AQS2. Reaction conditions are as follows: AQS-2 = 0.5 M in Ca-EDTA= 25 mM, Xe-Hg Full Spectrum, Nitrogen Purge, 0.2 mM Ca release after 60min.

For anthraquinones there has been reported catalytic cycle leading back to the oxidized form. In the case of AQS-2 it was shown that in the presence of oxygen, the sensitizer can be reoxidized back to its original form. The photocatalytic has been studied previously and is reported to occur in similar conditions .[111,112] In these previous studies it has been shown that anthraquinones will most likely react in their triplet state with a substrate that donates an electron. Scheme 3 shows that catalytic cycle that has been reported. [113,114] This possible recycling of the anthraquinones made them a good choice for the photocatalysis of the EDTA degradation reaction and the release of calcium, in our attempts to create a photocatalytic system. But while we have shown above stoichiometric release of calcium we do not have, in some cases, a release much higher than 1:1 stoichiometric ratio.



Scheme 3- 2 Anthraquinone 1 electron and 2 electron reduction/oxidation

In order to investigate our system more closely, we conducted experiments to see if oxygen was indeed necessary for the release of calcium. This would indicate at least partial reoxidation was occurring, allowing for there to be a catalytic cycle. In this portion of the study, we ran photolysis experiments at consistent 2.5 mM AQS-2 concentrations and 25 mM Ca-EDTA using 340 nm cut-off filters on a 150 W Hg-Xe medium pressure lamp. Figure 3-7 indicates the results of one of those studies where there is a much lower calcium release in the absence of oxygen than there is under nitrogen or argon. This indicates that oxygen is necessary for significant amounts of calcium to be released. An interesting result of this study is that not even stoichiometric amounts of calcium were released under nitrogen and argon atmosphere.

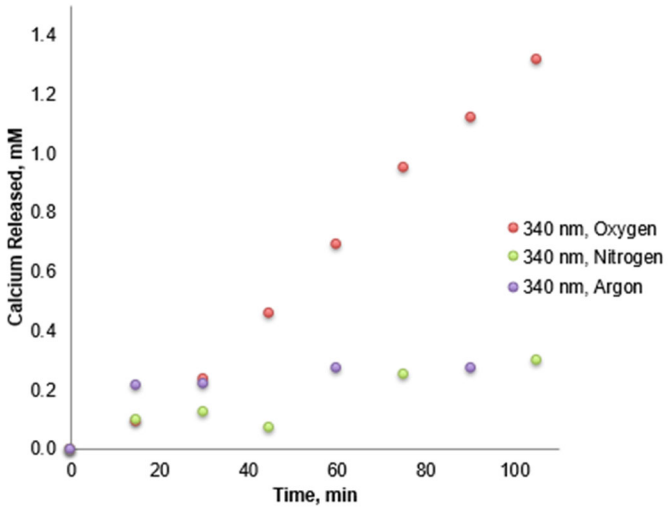


Figure 3- 7 Photolysis under Anaerobic and Aerobic conditions. Solutions consisted of 2.5 mM AQS2 sensitizer and 25mM Ca-EDTA at pH=7

Without oxygen small amounts of calcium are released, less than the 1:1 sensitizer to calcium amounts. This contrasts the stoichiometric amounts and slightly larger amount of calcium reported in Table 3-2. The graph shows the effect of the addition of oxygen to the solution (increases in calcium released). The lack of oxygen causes a substoichiometric amount of calcium to be released. These results indicate that at least one reoxidation event must occur to the quinone sensitizer (Scheme 3) for the release of calcium to even reach 1:1 stoichiometry.

Further studies have to be done to clarify whether the reoxidation event is a full two electron reoxidation back to the quinone or if a one electron transfer to the semiquinone occurs reversibly more than once. Another possibility is that EDTA needs to donate more than one electron for the degradation to reach a point that calcium is released or that there may be a back transfer reaction of the electron. What is clear is that the presence of oxygen is necessary for stoichiometric and above stoichiometric release of calcium to occur.

3.3.2 ^{1}H Nuclear Magnetic Resonance Results:

Nuclear magnetic resonance was applied to our photolysis experiment so as to identify redox forms of the anthraquinones and the degradation of EDTA. The experiments qualitatively showed the appearance of the reduced form of anthraquinones and the loss of the oxidized proton peaks as the Ca-EDTA signals disappeared. Peaks were assigned from previously reported assignments or those that were theoretically calculated.[115,116] Further analysis was attempted using external calibration signal in a co-axial tube for quantitative NMR (qNMR) but only a relative concentration was able to be calculated as all the necessary variables were not met for the calibration standard to make our calculations truly pass quantitation standards.

The NMR spectra of all solutions show the anthraquinone signals in the 7.5-9 ppm region and the Ca-EDTA signals in the 3.5-4.1ppm region. This is fortunate, as there is no overlap in signals between the two molecules in our system. This allowed for the two to be distinguishable from each other. Another advantage of the wide frequency difference between the sensitizer and EDTA signals, is that degradation and reduction products, for the most part, fell within the same ranges as the original material with no overlap. The chemical shifts for the degradation products in the anthraquinone region and the Ca-EDTA region for each of the sensitizers can be seen in Figure 3-8.

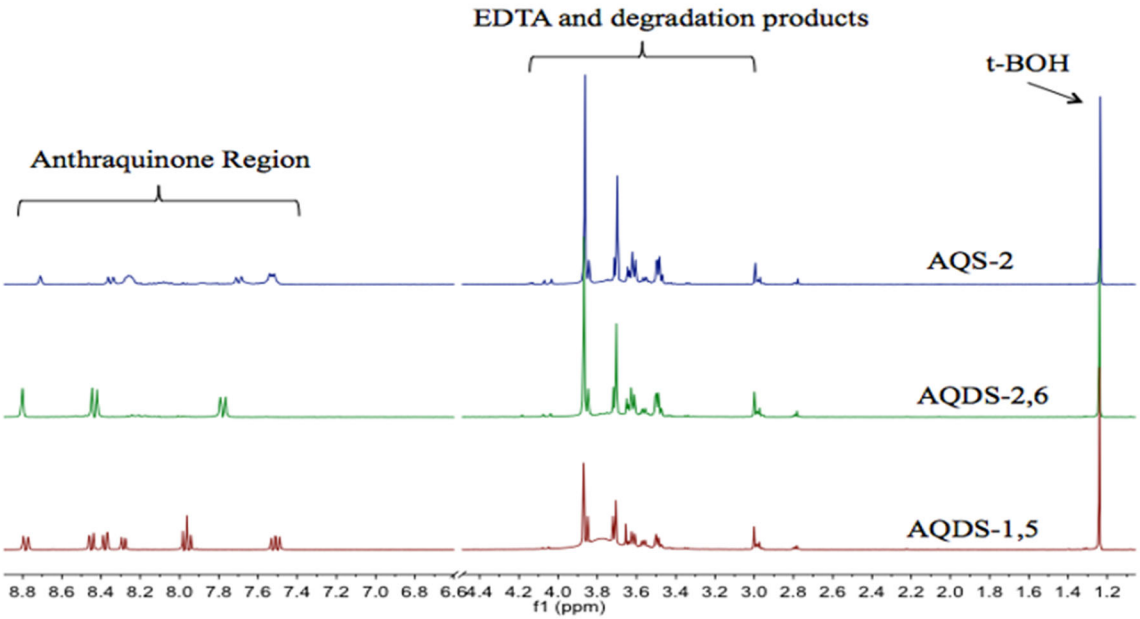


Figure 3- 8 Anthraquinone H NMR, in D2O, 298K, 20 min photolysis at 350nm. 2.0 mM sensitizer, [Ca-EDTA] was set at 10 mM.

The post 350 nm photolysis ^{1}H-NMR spectra for the three anthraquinone derivatives (Figure 3-9) all show the same EDTA degradation pattern and the formation of the reduced form of the sensitizer. When comparing all the spectra at the end of the 20 minutes at 350 nm photolysis, in both AQS-2 and AQS-2,6, there was complete reduction, while AQS-1,5 still contained the original oxidized reactant. AQDS-1,5 has been predicted and shown to be the weakest oxidizer in previous studies so these results of incomplete reduction are consistent with previous research.[87]

Analysis of the AQS-2 photolysis time course spectra shows a disappearance of the original signals in the aromatic region, 7.5-9 ppm, as the photolysis progresses, Figure 3-9. Then new signals which are still in the same

aromatic region but shifted in respect to the originals are the aromatic protons in the reduced form of the anthraquinones.

After 20 minutes, there are none of the original signals and only the new set of aromatic signals between 7.4 - 8.8 ppm that do not overlap with the previous AQS-2 oxidized signals are left. Each new signal corresponds to the predicted proton signals of AH_2QS-2 (the reduced form as indicated in Figure 3-9). These reduction products would indicate that an electron transfer event is occurring with the anthraquinones.

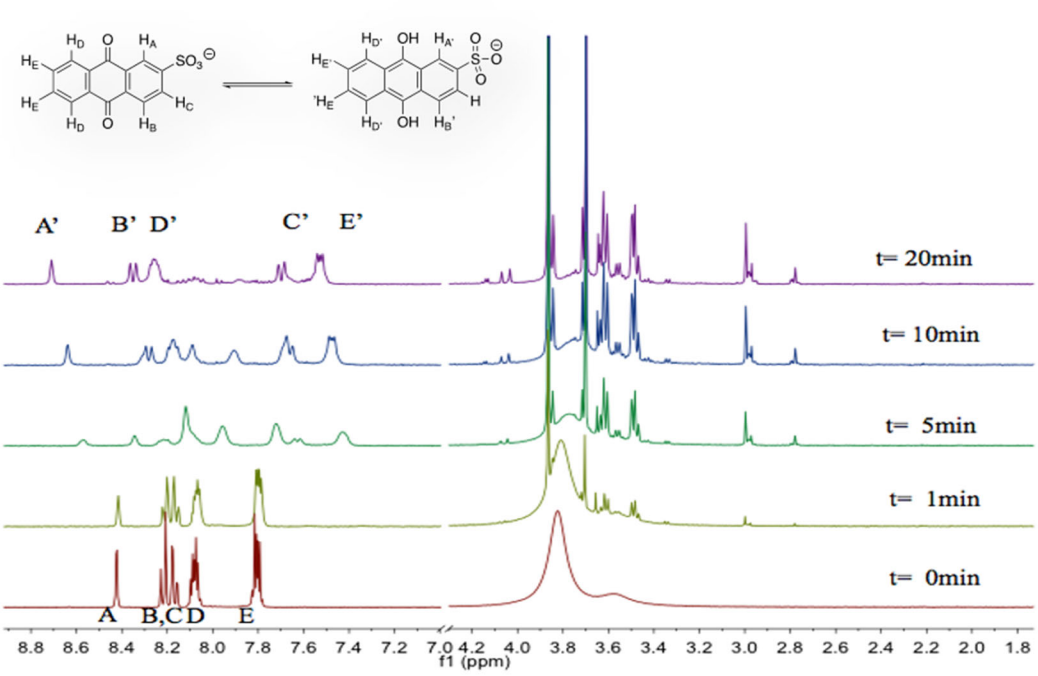


Figure 3- 9 AQS-2 ^{1}H-NMR photolysis time course. Solution contained 20 mM AQS-2, 10mM Ca-EDTA. 350nm photolysis lamp.

The spectra were further investigated through the relative quantification of sensitizer and Ca-EDTA. This was assessed using a co-axial technique where ^{1}H-NMR signals were integrated and compared to the known standard in the co-axial.

Since the ^{1}H-NMR resonance areas are directly proportional to the number of nuclei responsible for that signal the following equations can be applied:

$$I_x \alpha N_x \quad (3.1)$$

$$I_x = K_s \bullet N_x \quad (3.2)$$

In the formula (3.1) I is the integrated area under the curve of the corresponding NMR signal, N_X is the relative number of spins, of the ^{1}H protons which cause the resonance. Ks is the spectrometer constant and remains the same for all resonances in an NMR sequence if the same acquisition parameters are used. This variable therefore cancels out. The acquisition parameters must be closely matched as Ks is affected by the pulse excitation, repetition time (should be 5 times that of T1, spin lattice relaxation) and the broad-bank decoupling. Broad bank decoupling causes inherent distortion in intensity due to the Nuclear Overhauser Effect (NOE). Please refer to Appendix B for table of parameters used during experiments. If all these parameters are taken at a controlled molar ratio (MX/MY), then X and Y can be calculated by employing the following expression.[117]

$$\frac{M_{\mathrm{X}}}{M_{\mathrm{Y}}} = \frac{I_{\mathrm{X}}}{I_{\mathrm{Y}}} \cdot \frac{N_{\mathrm{Y}}}{N_{\mathrm{X}}} \quad (3.3)$$

In equation (3.3) there is no Ks because it should all be the same for all the resonances as acquisition parameters were kept the same. Similarly, the fraction of compound A in a mixture of Z components can also be calculated using formula:

$$\frac{M_{\mathrm{A}}}{\sum_{i=1}^{Z} n_i} = \frac{I_{\mathrm{A}} N_{\mathrm{A}}}{\sum_{i=1}^{Z} \frac{I_{\mathrm{i}}}{N_{\mathrm{i}}}} \cdot 100\% \quad (3.4)$$

Our choice of co-axial reference was tert-butyl alcohol, which has a strong 9 proton signal resonance at 1.24 ppm. The chemical shift for tert-butyl alcohol was attained versus tetramethyl silane (TMS) (Appendix B). Photolysis experiments on this standard were done to assure that degradation would not occur during photolysis. Using expression (3.3) and the known amount of our co-axial reference tert-butyl alcohol, we were able to arrive at estimations, or relative concentrations of sensitizer available at the beginning of the experiment and how much of it was oxidized and reduced by the end of our photolysis. Table 3-3 gives a summary of results. Examples of the integration calculations and table of all integrations for every sensitizer can be found in Appendix B.

Table 3- 3 Relative Average Concentration Results from NMR photolysis time course in mM and percentage calculations

	Oxidized		Reduced				
	0 min	20 min	0 min	20 min	Oxidized	Reduced	Unknown
[AQS2]	2.15	0.18	0.03	1.59	8%	74%	18%
[AQDS 2,6]	2.33	0.22	0.02	2.11	9%	91%	0%
[AQDS 1,5]	1.91	0.96	0.03	0.84	50%	44%	6%

Calculations of concentrations are averages of the relative concentration given for each separate proton. Some signals did slightly overlap from the oxidized to reduced form, specifically for AQS-2. These signals that overlapped did not give reliable quantitation amounts. Also, there is a loss of 18% in AQS-2 indicating that a side reaction was taking place creating another form that is not accounted for in our calculations.

The conversion rate for each AQS-2, AQDS-2,6 and AQDS-1,5 are 74%, 91%, and 44% respectively. These results match the fact that AQDS-1,5 released

the least amount of calcium, perhaps indicating that this failure to reduce is the probable cause for low calcium release. Low level of reduction would indicate a small amount of EDTA degradation. AQS-2 and AQDS-2,6 show a much higher amount of reduction and release of calcium as previously reported in Table 3-2 photolysis studies. This ability to be reduced correlates with the higher amounts of calcium release.

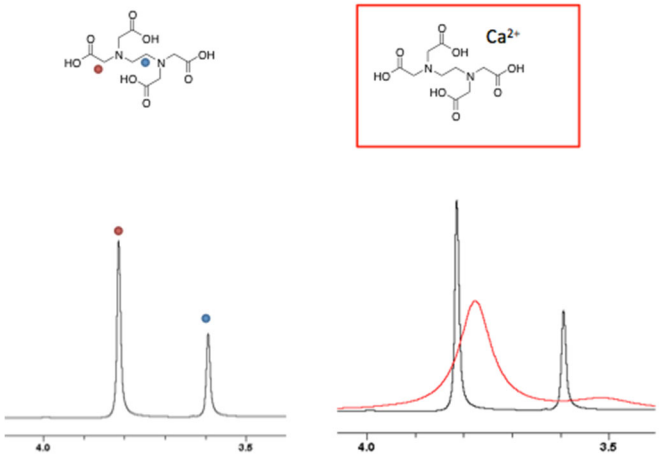


Figure 3- 10 ^{1}H NMR of EDTA and of Ca-EDTA causing the broadening of NMR signal.

It was not possible to get accurate Ca-EDTA signals because of the broadening of the signal (Figure 3-10). The EDTA signals have been broadened by a weak binding with the divalent calcium ion. Based on the pkA of the EDTA carboxylic moieties, the calcium ion would exchange in and out of the –COOH/-COO^{-} causing the chemical environment of the EDTA protons to change and chelation to vary. This change is slow enough to cause the averaging of the proton signals to show a broadening affect.

While quantitation was not possible in these experiments for EDTA degradation, it can be seen that degradation products appear in the 25-minute photolysis when the broadening is no longer evident. Future work could focus on setting a higher pH to eliminate broadening and allow for comparison of original EDTA concentration and final EDTA concentration. Another experiment to conduct would be to just have the EDTA present without the calcium so that their binding is not a variable.

3.3.3 Alginate Results:

Once we proved that calcium was being released through the addition of light to our system we focused on changing the rheological properties of a solution. We wanted to create a photorheological system that upon the addition of light triggered the creation of solid structures. The ability to retain a shape is an important characteristic in microfluidics and drug release applications. We therefore choose a naturally occurring alginate, a polysaccharide that is widely used in biological and engineering applications. Alginate is a repeating polymer of guluronic and mannuronic sugar monomers in varying ratios (Figure 3-11).. When an alginate solution is exposed to calcium it forms box-like structures around the cation, causing the viscosity to increase. If enough calcium and alginate are present a hydrogel forms with definite shape.

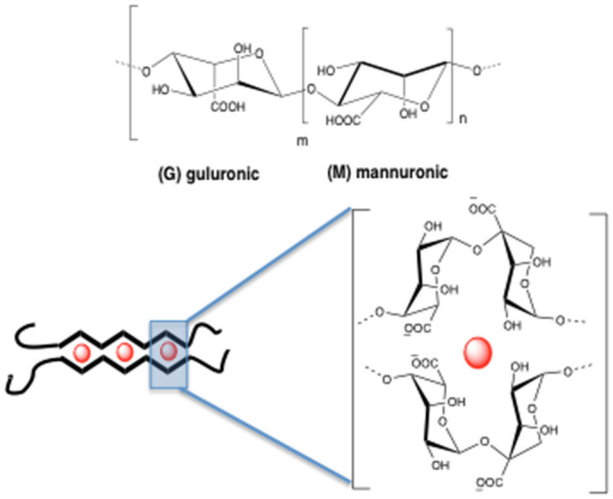


Figure 3- 11 Diagram of alginate monomers and their box-like arrangement with a second monomer when a divalent ion is added, leading to the formation of gels

Two different alginates were tested, and we had success with BioA alginate obtained from Sigma Aldrich. Varying concentrations of alginate % by mass to water were examined (1% to 3%). In Figure 3-12c shows an experimental run which shows the formation of clear circular alginate structures in the post-photolysis mixture. The 3% alginate solution was added dropwise into the photolysis solution of anthraquinone 2,6 and Ca-EDTA. Control experiments were done through the same procedure of a drop-wise addition of the alginate to water and a Ca-EDTA solution that had not been photolyzed at the same concentration as the photolysis mixture of 25 mM. Figure 3-12 shows that the only alginate to hold a shape was the one is the photolysis mixture. After photolysis the solution was tested, and the molar concentration shown to have risen to 6.63 mM after photolysis. The green color is a contrast dye added so that the clear structures could be seen. While adding alginate after photolysis did create solid structures, if photolysis was done with the alginate present, the solutions became less

viscous. This indicates possible degradation of the alginate which could be caused by its interaction with the anthraquinone sensitizers.

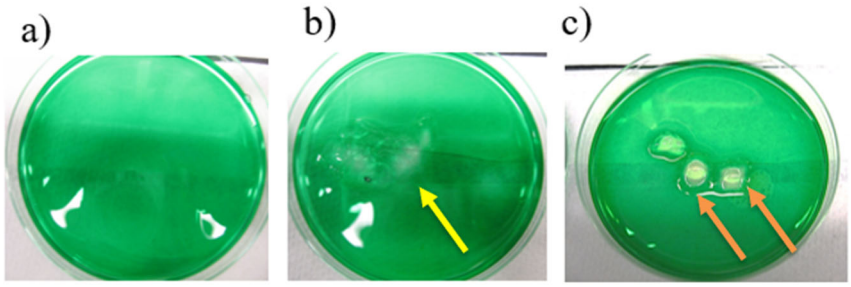


Figure 3- 12 Gelation of alginate by calcium from photolysis solution. Each solution had drops of 3% by weight BioA Alginate added. a) water control b) Ca-EDTA control c) photolysis of AQDS-2,6 with 254 nm Rayonet. The solution consisted of 10 mM AQDS-2,6 , 25 mM Ca-EDTA .

3.5 Conclusion

Our study has shown that a newly developed photo-triggered calcium release system is possible with Ca-EDTA and anthraquinones as electron transfer sensitizers. This was possible with easily accessible and affordable materials, and so realized our goal of increasing the availability of photocatalyzed systems for study. The sensitizers showed limitations in their inability to release calcium above the 350 nm range of light into the visible range. While they can absorb in the 300 nm range, the most calcium was released when 254 nm light was used with an increase above 1:1 stoichiometric release to about a 2:1 ratio calcium to sensitizer concentrations.

The NMR experiments clearly showed the transformation of the anthraquinones into their reduced form by not only their signals, but also a relative

quantitation of the amount of sensitizer reduced. Both AQS-2 and AQDS-2,6 showed high reduction rates after 20 minutes of photolysis, reaching 74% and 91% conversion respectively attained through qNMR techniques. AQDS-1,5 was only half converted into its reduced form, providing evidence for a possible reason of its low calcium release. EDTA degradation was shown qualitatively through the loss of NMR signal, but quantitation was not possible because of signal broadening.

Applying this system to the natural polymer alginate showed that enough calcium was being released in the photolysis system to allow alginate to gel into a definite shape. A limitation was that the photolysis was not done in-situ with the alginate, as those studies created a reduction in viscosity. Future studies will focus on advancing the system into the visible range, as well as finding a method to allow in-situ gelation.

Chapter 4 Visible Light Initiated Release of Calcium Ions through Photochemical Electron Transfer Reactions.[118]

4.1. Introduction

Calcium ions play key roles in numerous processes having physiological, environmental, and technological significance. For example, Ca^{2+} controls several cellular functions including muscle contraction, the secretion of neurotransmitters and hormones, wound healing and even cell death.[105, 119-120] Besides their importance in biology, calcium ions have also seen increasing utilization in the engineering of responsive biopolymers such as alginate gels. These calcium sensitive gels have applications ranging from microfluidic devices to the, encapsulation of cells to facilitate drug delivery.[121-129] For these reasons, there has been significant interest in developing new methods for the precise delivery of Ca^{2+} in various contexts.[105, 119-134]

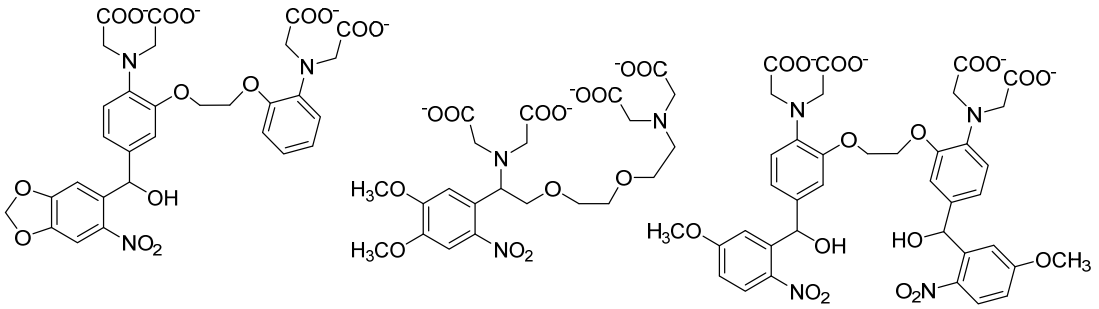


Figure 4- 1 Examples of previously synthesized photolabile calcium cages nitr-5 Tsien[127] lab, DM-nitrophen by Ellis-Davies[135] lab and nitr-T a more recent addition by the del Campol ab[122]

Photochemical control of a reaction has several key advantages. It allows for the generation of spatially and temporally defined concentrations of ions without

direct contact with the system. These characteristics, in turn, enable calcium ions to be used in photo-patterning applications as well as in physiological studies.[121-123] [131] To this end there has been a considerable amount of research into the synthesis and study of “caged calcium” compounds.[105] [127-130] Caged calcium compounds refer to molecules where Ca^{2+} is sequestered by a chelating group whose affinity can be lowered through a photochemical mechanism.[126] Key examples of synthesized calcium cages include nitr-5 by the Tsien group, DM-nitrophen developed by Kaplan and Ellis-Davis whose calcium binding diminishes with the addition of light, and nitr-T a more recent addition that expands on the BAPTA based calcium cages which can be seen in Figure 4-1.[122, 127-129] More recently, Agarwal et al. have demonstrated calcium release with visible light using a nitroaromatic photoremovable protecting group.[130]

While there are many advantages to these cages which have been used in calcium release at the cellular level, they are expensive and require multistep synthesis to produce. These light triggered release systems of calcium still have areas that could be further improved.[105,134] For example, it would be desirable to continue to expand the extent these that systems respond to visible wavelength something which would preclude the negative side effects of UV irradiation on cellular material such as DNA and tissue damage. Likewise, the ability to release Ca^{2+} with inexpensive and biocompatible reagents could increase the use of this technology by bringing into a more attainable cost range. To this end we have previously shown (Chapter 3) that anthraquinone derivatives could degrade EDTA and release calcium. The limitations of our previous work to this point are close to

stoichiometric need for the sensitizer and an absorption range that releases the most calcium in the UV 254 nm light range.

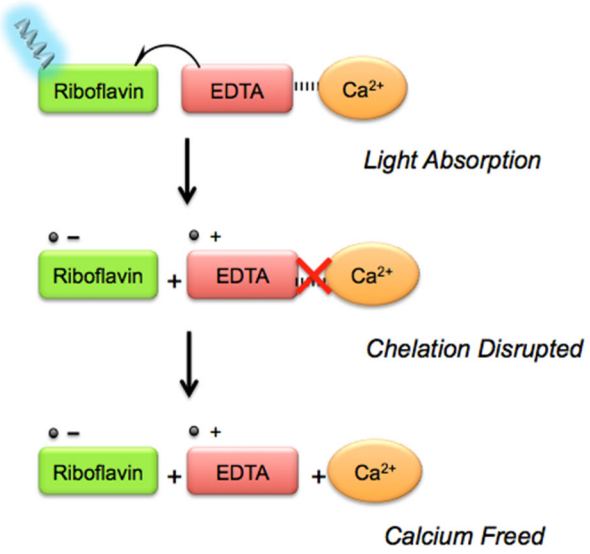


Figure 4- 2 Depiction of photocatalyzed calcium release system used in our study

We present studies using riboflavin and a derivative to expand the wavelength used in our calcium release system into the visible range. The general process of our system wherein the riboflavin absorbs the blue light photon causing a large enough redox potential change that allows for the electron transfer from EDTA, is shown in Figure 4-2. Riboflavin is a part of the larger flavin group of molecules containing the 7,8-dimethyl-10-alkylisoalloxazine chromophore moiety. Flavins are pervasive in nature taking part in many naturally processes such as the generation of light by bacterial luciferase and DNA repair by photolyase. In biology riboflavin is better known as vitamin B_2, a coenzyme involved in biochemical redox reactions in humans. It's compatibility in biological systems, availability and relatively affordable cost made it a good candidate for our system.

The degradation of EDTA is similar to our laboratory's previous success in releasing carboxylate ions through photoinduced electron transfer.[136] In these reactions light is absorbed by the redox active chromophore which then causes an excited-state oxidation or reduction. After the electron is transferred, the desired event, such as removal of a protecting group or the release of the desired species, is achieved.

What follows are descriptions of the experiments we have undertaken to demonstrate an extension of this concept to the release of Ca^{2+}. We predicted that the EDTA would also react in a similar manner, thereby releasing calcium in detectable amounts. Specifically, it is shown that photolysis of oxidizing photosensitizers, by flavin derivatives, can trigger the degradation of EDTA bound to calcium ions. This can rapidly generate millimolar concentrations of free Ca^{2+} with the advantage of being a 1000-fold release compared to photosensitizer concentration. Studies at different pH levels and photolysis wavelengths affected the amount of calcium released. Our system was then applied to photochemically generate alginate hydrogels.

4.2 Materials and Methods

4.2.1 Materials

Riboflavin, anthraquinone-2-sulfonic acid sodium salt, and sodium alginate from brown algae were purchased from Sigma Aldrich and used without further

purification. Riboflavin tetraacetate was synthesized as described in the following sections.

The 1.0 M standard calcium and EDTA solutions were bought from Fischer. The calcium and EDTA working standards were made using serial dilution methods with volumetric flasks. Specific pH level was adjusted using NaOH and HCl.

4.2.2 Chemical Synthesis and Characterization

Synthesis of 2',3',4',5'-tetraacetylriboflavin was based on a previous procedure in which riboflavin is first suspended in acetic anhydride, and then sulfuric acid added to initiate the reaction. Stirring was continued at 80°C under nitrogen for one hour.[137] The cooled solution was neutralized with 0.8 M $NaHCO_3$, extracted three times with CH_2Cl_2 layer wand washed in cold water three times. The CH_2CH_2 layer was dried with anhydrous $MgSO_4$, filtered and evaporated. ^1H NMR signals matched those in the paper. Spectra can be found in Appendix C.

4.2.3 Photolysis of Samples

Samples were photolyzed at 350 nm using a Rayonet Photoreactor from the Southern New England Ultraviolet Company. Polychromatic wavelength photolysis at other wavelengths were done on a 150 W Hg-Xe medium pressure lamp, using cut off filters as indicated in Table 2. The solutions were 1 mL in volume with a concentration of Ca-EDTA that ranged from 2.5 mM to 25 mM in deionized water (pH 6.5-7.3). Riboflavin concentrations were kept below 50 μM to avoid self-

association. Visible-light alginate gels were prepared by photolysis with a 1 W, 447 nm CW diode laser.

4.2.4 Calcium Assay

A modified spectrophotometric dye method using o-Cresolphthalein Complexone (CPC) was used in our study to determine the amounts of calcium released.[106] The working dye solution was made by adding 1 mL 38% HCl to 40 mg of CPC. The dissolved CPC is transferred into a 1 L volumetric flask by washing with deionized water. To the CPC 100 mL of dimethyl sulfoxide and 2.5 g of 8-hydroxyquinoline were added. The solution was mixed until dissolved and then diluted to volume with deionized water. The DEA buffer was made by adding 40 mL of diethylamine into a 1 L volumetric flasks. Then 0.5 g of potassium cyanide was added and dissolved with deionized water until the 1 L volumetric flask mark was reached.

The assay involved adding 1 mL of CPC working solution, 1 mL of diethylamine buffer solution (DEA), and 1 mL of water to make calcium testing solution. Once the solution was mixed by inversion, a UV-Vis at 575 nm was taken to serve as a control. To the calcium testing solution, a 20 µL amount of test sample was added, mixed by inversion and the UV-Vis measured at 575 nm to serve as the experimental. The difference in absorbance at 575 nm was then compared to a calibration curve to determine molar concentration. Further information can be found in Chapter 3 methods.

4.2.5 Quantum Yield

Quantum yields were determined as follows: solutions containing 25 mM Ca-EDTA and 9.0 ± 0.5 μM Riboflavin were irradiated using the output from a 1000 W Hg-Xe lamp that was passed through a monochromator set to 366 ± 10 nm. Calcium concentrations at various times were determined using the CPC assay at the intensity (I_0) above. The lamp output was calibrated using ferrioxalate actinometry as described by Hatchard and Parker.[138] In order to ensure that R did not vary significantly throughout the sample, photolysis was carried out under optically thin conditions wherein the Abs 366 was held at 0.1. The apparent quantum yield was

$$\phi = \frac{R_{Ca^{2+}}}{R_{EX}} = \frac{\left(Rate\,calcium\,release\right)}{\left(Rate\,of\,excitation\right)} \tag{4.1}$$

$$R_{EX} = I_0(1 - 10^{-A}) \tag{4.2}$$

determined using equations 1 and 2.

4.2.6 Laser Flash Photolysis

Laser flash photolysis experiments were performed using a Nd:YAG laser pump beam source with a Continuum Surelite II-10 capable of 266, 532, or 355 nm pulses between 5-7 ns. A LeCroy 350 MHz digital oscilloscope was used to observe all waveforms. The samples were prepared so that their relative absorbance was between 0.75 and 1.5 at the excitation wavelength, 355 nm. The probe beam was a 350 W Xenon arc lamp. The samples were loaded into a 1 cm quartz cuvette and were purged with pure N_2 for 10 mins in the solution and an

additional 5 minutes in the headspace. Samples were flowed continuously thorough out the experiment to avoid build-up of photoproducts.

4.2.7 Peroxide testing:

Peroxide testing was performed using Quantofix semi-quantitative peroxide test strips. Since we did not want to contaminate the solution, 10 µl were removed and placed on the strip gradient area at the designated time intervals.

4.2.8 1-Dimensional Co-axial ^{1}H-NMR

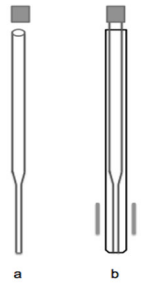


Figure 4- 3 Coaxial NMR set up a) the coaxial tube b) the coaxial tube in NMR tube before being placed in NMR, the lines show area where signal is collected.

^{1}H NMR spectra were taken in deuterium oxide solvent, at 298K and without spinning. All water signals were suppressed using standard Bruker water suppression program zgesgp with double pulse field gradient spin echo. Typical parameters for the spectra are listed in Appendix C. The co-axial 1-D ^{1}H-NMR spectra in this study were obtained on a Bruker 600 MHz spectrometer with a BBI probe. Figure 4-3 illustrates the NMR co-axial insert used for the quantitative NMR experiments.

4.2.9 Instrumentation

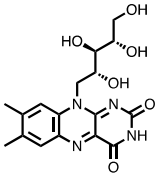
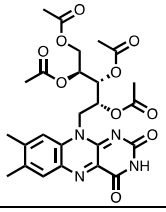
All fluorescence experiments were performed using a Hitachi F-4500 fluorescence spectrophotometer. All UV-Vis spectra were taken on a Shimadzu UV-1800 and pH was measured with a Mettler pH meter. ^{1}H-NMR spectra were taken on a Bruker 600 MHz or 400 MHz.

4.3 Results and Discussion

Several previous studies have established that flavins have a photocatalytic ability to oxidize different substrates including benzyl alcohols,[139] benzyl amines,[140] amino acids,[141,142] indoles,[143] unsaturated lipids,[144] and amines,[140,145,146]. Secondary amines such as EDTA, have been shown to be electron donors and can therefore be photo-oxidize by flavins. EDTA donation of electrons then leads to decomposition, primarily through decarboxylation events.[98, 147-149] There are studies that have paired EDTA and riboflavin to monitor either the degradation of EDTA or riboflavin. Nevertheless, none of these studies investigated the possibility of releasing calcium through this electron transfer process or the necessary conditions to apply the process to rheological studies.

We hypothesized that photolysis of Ca-EDTA complexes by flavins would initiate similar chemistry to what our lab had previously observed and the resulting dismantling of the EDTA chelator, in turn, release the chelated ions in large enough amounts as to then cause a rheological change in our alginate solutions. Table 4-1 shows the sensitizers employed in this study along with some key photophysical parameters of Riboflavin (RB) and its tetraacetate derivative (RBTA).

Table 4- 1 Key photophysical properties of flavin sensitizers.

Sensitizer		λ_{max} (nm)	E_{red} (V)	$\tau_{singlet}$ (ns)	$\tau_{triplet}$ (ns)	ε ($M^{-1}s^{-1}$)
	RB	450[150]	-0.507[151]	2.3[17]	19[17]	12200[150]
	RBTA	445	-1.18[151]	23.8[151]	-	8600

Both flavins have a large absorbance max in the 400 nm range and cannot readily be differentiated by their UV VIS spectra, though RB has a higher absorptivity coefficient than RBTA, making it a more efficient photocatalyst. Another difference is the lifetime of their reactive intermediates, with RBTA having a longer-lived singlet at 23.8 ns and only 2.3 ns for RB. The RB triplet has a longer lifetime at 19 ns, while there was none listed for RBTA at the time of writing. We chose RBTA as it has been shown to be a photocatalyst in the oxidation of aldehydes,[152] aniline derivatives,[153] benzyl alcohols,[154] and is more photostable than RB.[155] To our knowledge there has been no studies of RBTA photo-oxidizing EDTA and the subsequent release of calcium.

4.3.1 Calcium Release

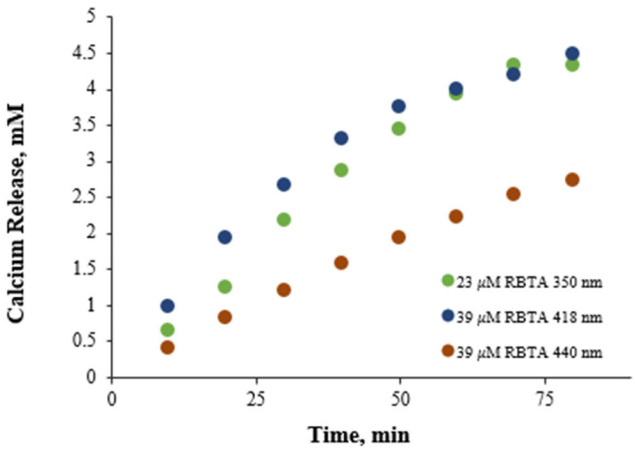


Figure 4- 4 Photorelease of calcium from EDTA with RBTA using various light sources. Initial [Ca-EDTA]=25mM in water (pH 6.5-7.3)[118]

Our first calcium release results show that like our previous anthraquinone studies there was a typical time-dependence of Ca^{2+} photorelease as shown in Figure 4-4. The graph shows the RBTA sensitized release of calcium based on the wavelength at pH 6.5-7.3. The higher energy wavelengths, 350 nm and 418 nm released the most calcium. This is even true when less RBTA was used at the 350 nm wavelength compared to photolysis at 418 and 440 nm.

The release of calcium with RBTA is larger than any of the anthraquinones. At 440 nm and 39 μM concentration of RBTA, while there was 16 μM difference compared with 350 nm. The release of calcium 1000-fold higher than the sensitizer concentration with RBTA was employed. The maximum calcium release was reached at both 418 and 350 nm for RBTA at a concentration of 4.5 mM with a micromolar concentration of sensitizer added. Table 4-2 lists yields of free Ca^{2+} along with the amount and identity of the sensitizer, photolysis wavelengths and

times. Aqueous solutions containing 25 mM Ca-EDTA complex (pH 6.5-7.3) were used and varying amounts of sensitizer were then tested.

Table 4- 2 Photolytic release of Ca^{2+} with various sensitizers at differing wavelengths

Sensitizer	[Sensitizer] (mM)	[Ca-EDTA] (mM)	λ (nm)	Time (min)	Released Ca2+ (mM)
RBTA	0.02	25	350 [a]	60	3.9
RBTA	0.02	25	Broadband [b]	60	3.7
RBTA	0.02	25	Broadband [b]	120	4.9
RB	0.035	25	> 370 [c]	60	4.3
RB	0.035	25	> 418 [c]	60	4.0
RB	0.035	25	> 440 [c]	60	2.1

[a] Photolyzed using a 35 W, 12-bulb Rayonet photoreactor
[b] Unfiltered light from a 150 W Hg-Xe lamp
[c] Light from 150 W Hg-Xe lamp filtered with 370, 418 and 440 nm high pass filters

Each air-equilibrated solution was exposed to light at 350 nm in a Rayonet photoreactor, or to filtered (>390 nm, >420 nm, >450 nm) light from a Hg-Xe arc lamp. The yield of free Ca^{2+} was determined spectrophotometrically by adding aliquots from the photolyzed sample to an analysis solution containing the spectrophotometric dye, *o*-cresolphthalein complexone (CPC) as explained in the Methods section.

Concentrations of Ca^{2+} were evaluated using the absorbance of 575 nm compared with a calibration curve. While RBTA has the highest release at 4.9 mM with broadband light excitation for 120 min, RB still releases in the 4 mM calcium

range in the 400 nm excitation range and in half the time, which makes it useful for calcium release in the visible range. Further experiments into light efficiency of calcium release could be done to further our understanding of the difference of both these sensitizers ability to degrade EDTA and release calcium.

4.3.2 Quantum Yields of Calcium Release:

In addition to chemical yields, the utility of a photorelease system also depends on the quantum yield of the reaction. Quantum yields (Φ) are used to quantify how many reactions occur per unit of light absorbed. It is commonly calculated by dividing number of moles of product by the number of photons absorbed in simple reactions. The number of photons absorbed can be difficult to attain instead, so instead the calculation is based on incident light absorbed by the sample. These formulas can be found in the methods section.

$$\Phi = \phi_r \phi_q = \phi_r \frac{k_q[CaEDTA]}{k_q[CaEDTA] + k_s} \qquad (4.3)$$

We determined these values using ferrioxalate actinometry methods previously reported and adapted to the available apparatus.[156,157] When we tested Ca-EDTA (concentration 20 mM) with RBTA (9 μM), the quantum yield was determined to be 0.31 ± 0.03. In the current experiment, the key photochemical step is a bimolecular electron transfer reaction from Ca-EDTA to excited sensitizer, and as such any observed quantum yield will be a product of quenching efficiency(ϕ_q) and the efficiency of the oxidative electron transfer reaction (ϕ_r)as described in equation (4.3). Thus, the quantum yield determined under these

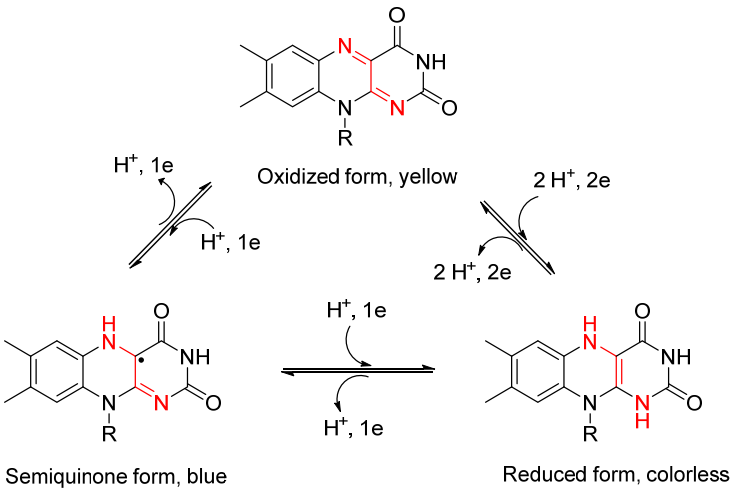
conditions is a lower limit of what might be achieved under higher Ca-EDTA concentrations, or if the sensitizer and the chelator were linked to one another. Though this is to be expected in a bimolecular reaction where the rate is determined not only by the absorption of the photon, but also by the concentrations of sensitizer and chelator. Calculations can be found in Appendix C.

Using the quantum yield we can also calculate the quantum efficiency of our reaction. Under steady-state illumination conditions, the overall rate of Ca^{2+} production depends on the intensity of the light source, the molar absorptivity of the sensitizer (ε) and the quantum yield for release (ϕ). The product of the latter two terms, the photochemical efficiency ($\varepsilon \times \phi$), can be used to characterize the effective release rate at a given light intensity. The value for the current system of $\varepsilon \times \phi = 2700\ M^{-1}cm^{-1}$ demonstrates that RBTA/Ca-EDTA can produce calcium ions at a rates comparable to previously characterized systems.[105] Under pulsed illumination conditions, the relevant consideration would be the rate-limiting step in the formation of free Ca^{2+} following light absorption. Additional mechanistic studies will be aimed at determining that rate constant.

4.3.3 Reoxidation of Sensitizer:

As mentioned previously, in contrast to anthraquinones, when the flavin derivatives, RBTA and RB, were employed ca. 1000-fold concentration, then free Ca^{2+} was released relative to the sensitizer added. This suggests that either the reduced flavin can recycle back to its original form and/or any by-products of the sensitizer retain photooxidative ability. Previous work into the photochemistry of

flavins has shown their ability to go through a photochemical cycle that is illustrated in Scheme 4. One of the most common electron acceptors in the reoxidation of riboflavin is oxygen. We therefore wanted to test whether our system was going through re-oxidation of the flavin sensitizer by testing its dependence of oxygen availability.



Scheme 4- 1 The reversible oxidation-reduction cycle of riboflavin's isoalloxazine moiety using one or two electron transfer accompanied with a proton addition or abstraction.[158]

In this set of experiments, we took UV-Vis spectra of our solutions before and after photolysis to measure the amount of riboflavin that was still oxidized. The reduced form of riboflavin (Scheme 4-1) no longer has the large conjugation between the three rings and therefore loses its 445 nm max. All cuvettes were sealed to make sure that there was no entrance of oxygen into the sample during photolysis. Samples either contained oxygen or were purged with nitrogen or argon gas before hand. Results are illustrated by the UV-Vis absorption spectra in Figure 4-5. In these experiments riboflavin (40 μM) was photolyzed in the presence of Ca-EDTA (12.5 mM).

Photolysis of the solution with an unfiltered Xe-Hg lamp light for 5 minutes resulted in diminishment of the flavin absorption band at 445 nm, consistent with the known photoreduction to the corresponding dihydroflavin derivative.[158-161] When the resulting solution was allowed to stand under conditions of air equilibration, the 445 nm band returned, thus indicating the return of the fully oxidized riboflavin.

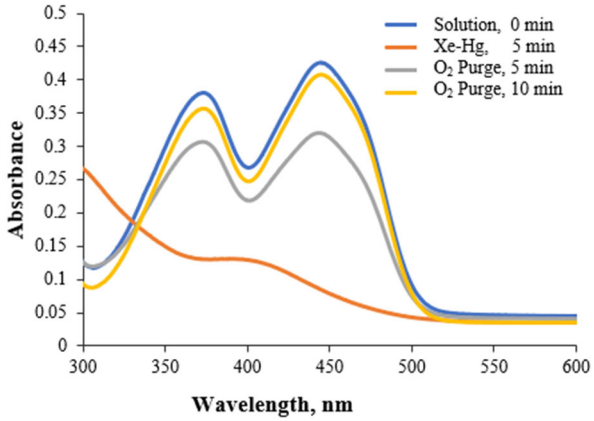
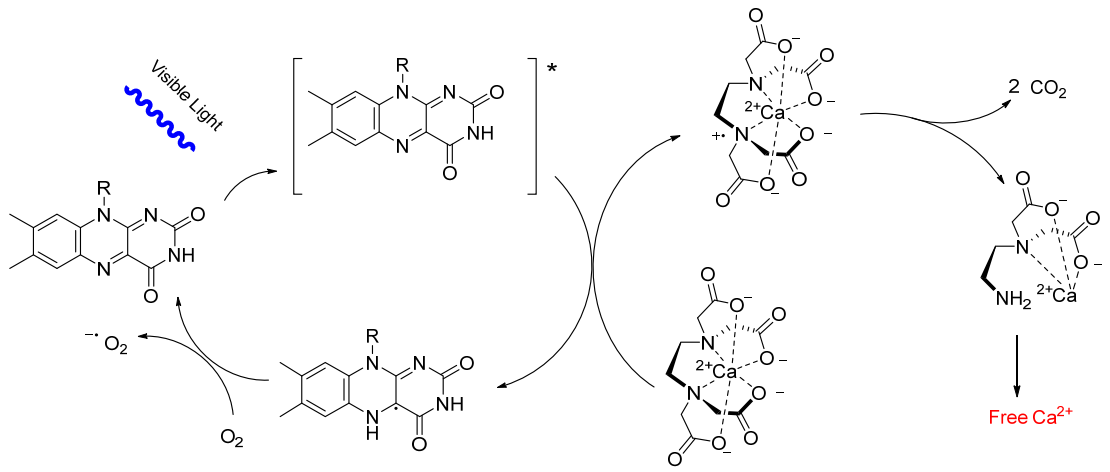


Figure 4- 5 Change in absorbance of sample containing [Ca-EDTA]= 12.5mM, [RB]= 40 μM. Spectra were taken before photolysis, after exposure to an unfiltered Xe-Hg lamp, and then after purging the solution with oxygen for 5 to 10 minutes.[118]

For riboflavin to fully re-oxidize the solution had to be left in the dark for 10 minutes, wherein the flavin absorption recovered to 98.4±0.5% of its original value. Similar experiments with RBTA produced a 100.1 ± 0.5% recovery of the original absorbance. On this basis, we conclude that air oxidation of the dihyrdoflavin to flavin allows these sensitizers to be recycled and used in sub-stoichiometric amounts. While we cannot completely rule out peroxide production could contribute to some of the degradation, we ran experiments to test peroxide production and found no significant amount of peroxide produced. We will further

investigate riboflavin degradation in a later section to further understand the mechanism of our system.

4.3.4 Laser Flash Photolysis and Fluorescence



Scheme 4- 2 Proposed mechanism for the degradation of Ca-EDTA chelate from the electron donation from excited state riboflavin.

Our proposed mechanism for Ca^{2+} photorelease as seen in Scheme 4-2 is consistent with literature precedents for EDTA electron transfer photochemistry as well as the observations from our experiments described herein. It has been previously documented that RB can photooxidize EDTA by an electron transfer event. This event has been shown to occur twice as described in Enns et al.[162] and further elaborated in Armstrong et al.[163] The Armstrong study shows that donation of an electron causes a decarboxylation sequence to happen, and the work in our laboratory with photoremovable protecting groups further shows a decarboxylation event occurring after electron transfer.

After absorption of a photon, singlet flavin abstracts an electron from EDTA which subsequently degrades, resulting in the loss of its ability to chelate calcium

subsequently releasing free Ca^{2+}. The reduced riboflavin can return to its original form after reoxidation with oxygen, thus completing the cycle and allowing the reaction to be done with substoichiometric amounts of sensitizer. We reported studies that have shown that RB will not release measurable amounts of calcium under conditions of nitrogen and the exclusion of oxygen supporting our proposed photocatalytic cycle. The 1000-fold release of calcium is therefore explained through the reoxidation of riboflavin after it is reduced by EDTA and is shown in our proposed mechanism (Scheme 4-2).

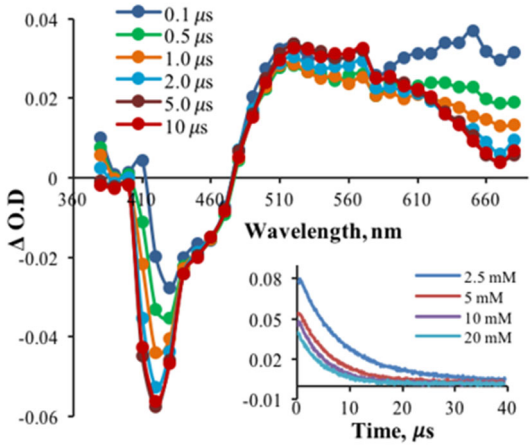


Figure 4- 6 LFP and Quenching Transient absorption spectrum of RB (123 μM) with 2.5 mM Ca-EDTA in phosphate buffered water (pH= 7.4). Waveforms at 660 nm with increasing [Ca-EDTA] are shown in the inset.[118]

We now present further evidence of the electron transfer event through fluorescence quenching and laser flash photolysis (LFP) experiments. In our experiments, illustrated in Figure 4-6, a pulsed laser photolysis (355 nm, 5-7 ns, 5-10 mJ) of RB with Ca-EDTA in aqueous solution produces the transient UV-Vis spectrum that includes a broad absorption near 660 nm, a sharp long-lived maximum near 510 nm and a negative bleaching signal at 420 nm. These signals

have been reported previously in a paper published in our lab and the spectrum taken in collaboration with a graduate student in the lab.[118] The negative signal is caused by depletion of ground-state RB and, the short-lived absorbance at ca. 660 nm is attributed to the triplet state of RB.[164] The long-lived 510 nm peak is the flavin radical derived from oxidation of EDTA.

The result of adding Ca-EDTA is illustrated in the inset which shows the response of the signal at 660 nm to increasing concentrations of Ca-EDTA. Here, we find the Ca-EDTA decreases the initial triplet intensity but has negligible effect on the decay rate of the triplet. We would expect that if the triplet was reacting the decay rate would change. On this basis we concluded the Ca-EDTA reacts with the excited singlet state of RB, but not the triplet in our experiments in contrast to other studies in riboflavin reductions. [147-148, 165]

Further evidence of the singlet being involved in the electron transfer reaction was derived from fluorescence quenching experiments done by another graduate student in our lab and published.[118] Fluorescence quenching experiments (Figure 4-7), which, combined with previously reported lifetime for the excited state (RB*) given in Table 4-1, provided a k_q value of 5.7×10^9 $M^{-1}s^{-1}$. Fluorescence is the release of excited state energy from the singlet state. Quenching it would mean that the singlet state population is being depleted.[166-169] The singlet state is reached by excited molecules first before the triplet state, therefore if it is being depleted by the presence of EDTA then that is strong evidence that the electron transfer is singlet state mediated.

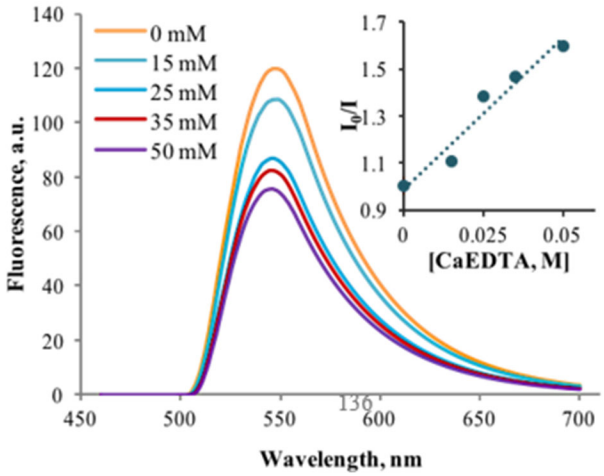
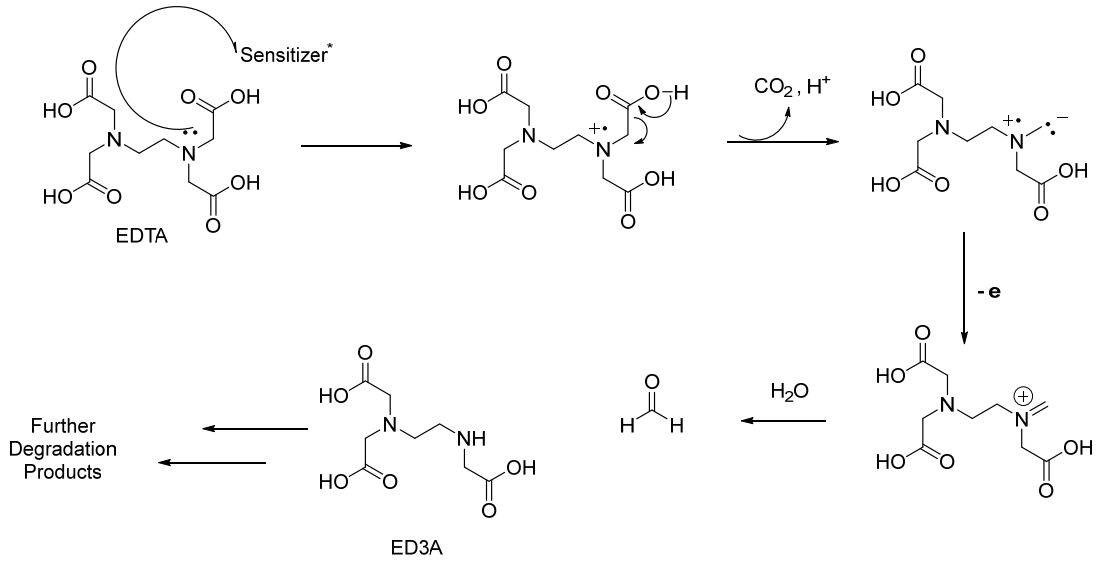


Figure 4-7 Fluorescence quenching (λ_{ex} = 320 nm) of RB with varying concentrations of Ca-EDTA in water (pH = 6.8). Fluorescence quenching (inset) measured at 547 nm.[118]

4.3.5 Experiments on EDTA degradation:

The photocatalytic mechanism for the excitation of our sensitizer, subsequent electron transfer to EDTA, and then re-oxidation with oxygen was provided in Scheme 4-2. We now provide a possible mechanism for the decarboxylation of EDTA after an electron transfer to the flavin sensitizer in Scheme 4-3. ^{1}H NMR evidence of the degradation of EDTA and the subsequent formation of formate was found at pH = 4 and pH = 7. Previous degradation studies have measured EDTA degradation indirectly through total organic carbon analysis (TOC)[102] and recently more directly through gas chromatography-mass spectrometry (GC-MS).[170] We present, to our knowledge, the first qualitative and quantitative ^{1}H NMR evidence of EDTA degradation.



Scheme 4- 3 Proposed possible first steps in EDTA degradation by electron transfer which accounts for formaldehyde formation

Our mechanism proposes that the excited state sensitizer abstracts one electron from the Ca-EDTA complex. After the abstraction the resulting aminium radical decarboxylates providing an alpha-amino radical, which we expect would be further oxidized by ground state sensitizer, providing an iminium ion (Scheme 4-3). The decarboxylation of aminium radicals has been explored extensively.[171-173] Under aqueous conditions the iminium ion would hydrolyze, producing ED3A and formaldehyde. The former would suffer similar oxidation hydrolysis reaction, forming mixtures of EDDA isomers and, ultimately ethylene diamine. A byproduct of this reaction would be the formation of formaldehyde, that would then undergo a disproportionation or self oxidation-reduction to create formic acid, which would be deprotonated to formate.

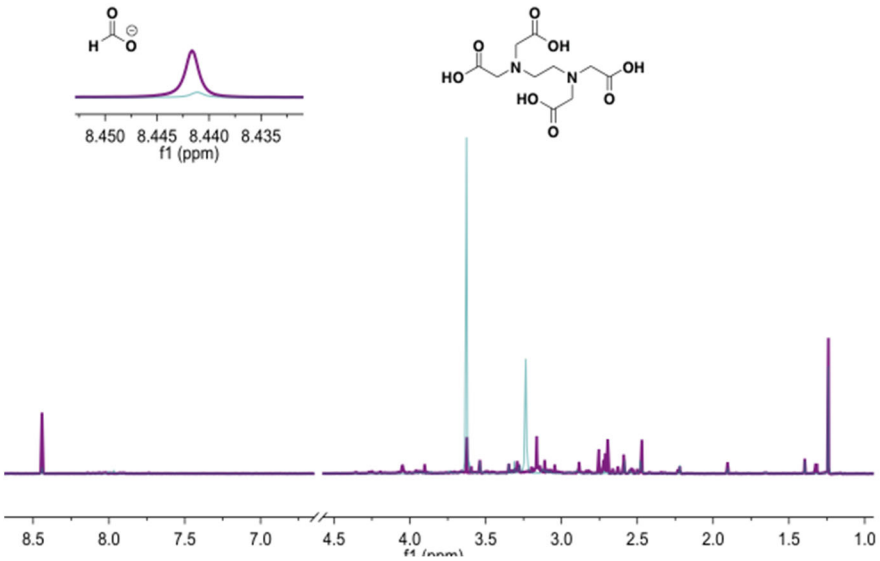


Figure 4- 8 Stacked ^{1}H NMR of pre (blue) and post (red) photolysis of a solution containing 75 µM Riboflavin , 1.5 mM EDTA, at pH 7.3. Photolysis wavelength was 447 nm for 60min. The magnified window shows the formation of formate after photolysis

Analysis of the photolysis solutions using ^{1}H NMR spectroscopy showed a complex mixture of signals characteristic of EDTA degradation and the production of formate. The signal for formate was found in our photolysis spectra at 8.4 ppm at pH 7.3 experiments, which is consistent with previous reports on the photooxidative degradation of EDTA (Fig 4-8). [98, 147-149]

Next, co-axial ^{1}H NMR experiments were performed in the absence of the calcium ion at 4. These control experiments were to confirm that EDTA would be degraded in by flavin in our experimental the conditions. The spectra for the photolysis of RB and EDTA at pH 4 (Figure 4-9) displays a decrease in the EDTA signals and an increase in formate signal. The spectra clearly indicates the degradation of EDTA.

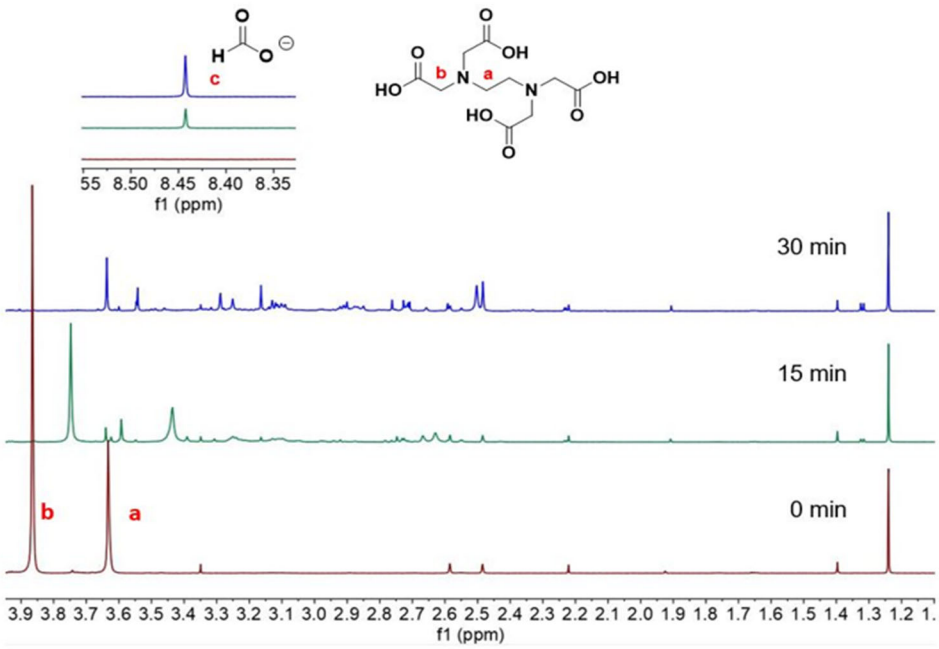


Figure 4- 9 Stacked 1H NMR of pre (red), 15 min (green) and 30 min (blue) photolysis of a solution containing 50 µM Riboflavin, 1.0 mM EDTA, at pH 4.3. Photolysis at 447 nm.

It appears that most of the EDTA has been degraded though we were unable to identify specific degradation products other than formate. The riboflavin aromatic signals are also lost indicating its photoreduction. A possibility is that as degradation occurs in D_2O some signals could be lost if the degradation products abstract a proton from the solvent. These new compounds would have signals that are silent.

Following the qualitative confirmation of EDTA degradation we performed quantitative ^1H NMR methods described in Chapter 3. The signal at 1.2 ppm is for tert-butyl alcohol in the coaxial which was used as a standard for relative quantitation of compound concentrations. The spectra were integrated, and the

areas of the molecules compared to the standard in the co-axial tube to get relative quantities.

Table 4- 3 Relative quantitation results from the 50 μM RB, 1mM EDTA, pH = 4.3, 447 nm photolysis.

Time	EDTA-C		EDTA-N		Formate
(min)	(uM)	% Left	(uM)	% Left	(uM)
0	907	100%	1030	100%	12
15	92	10%	414	40%	110
30	62	7%	91	9%	236

The concentrations of EDTA after the photolysis time points were divided by those at t = 0 then multiplied by 100 to get a percentage remaining. While for formate we report the relative amount calculated to have been produced. The results from these calculations can be found in Table 4-3. The results indicate that about 90% of the EDTA is being degraded while there is an over 200% increase in formate. If our mechanism is correct and one formate is formed when one EDTA carboxylate group leaves, then we can infer that the extra formate could be formed from decarboxylation of the byproducts of the first EDTA decarboxylation.

Next, we photolyzed EDTA with the calcium ion present. The photolysis of a solution with 1 mM of Ca-EDTA at pH 7.3 shows a quartet at 3.1 ppm and the singlet 2.5 ppm which were identified as Ca-EDTA bounded complex (Figure 4-10). The comparison of the pre and post NMR spectra shows the reduction in the signal after photolysis but not the complete degradation of EDTA which coincides with our calcium release results. The insert of the 8.4 ppm region the formate signal increases as the Ca-EDTA signal is degraded.The smaller peaks in the 2-4 ppm

are thought to be unidentified degradation products of EDTA or the ribose section of the RB sensitizer.

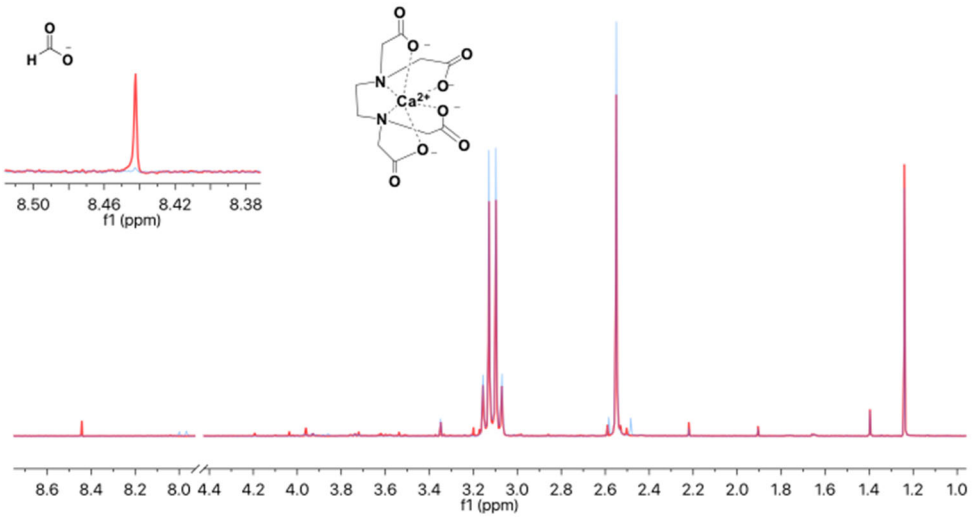


Figure 4- 10 ^{1}H NMR of pre (blue) and post (red) photolysis of a solution containing 75 µM Riboflavin, 1 mM Ca-EDTA, at pH 7.3. Photolysis wavelength was 447 nm for 30min using a 1 W, CW diode laser. The magnified window shows the appearance of formate after photolysis.

Photolysis of Ca-EDTA at acidic pH created a broad peak that would not allow for accurate integration. While we could not integrate, the spectra does show qualitative reduction of EDTA concentration (Appendix C). Future work would provide further describes the mechanism of EDTA degradation in more detail.

RBTA also produced degradation of EDTA. The ^{1}H NMR spectra for Ca-EDTA and RBTA can be found in Figure 4-11. The pH of the solution was acidic creating a broad peak for the Ca-EDTA signal. As the solution is photolyzed the broad signal, indicating the chelation of the calcium ion and EDTA disappears leaving unidentified degradation products.

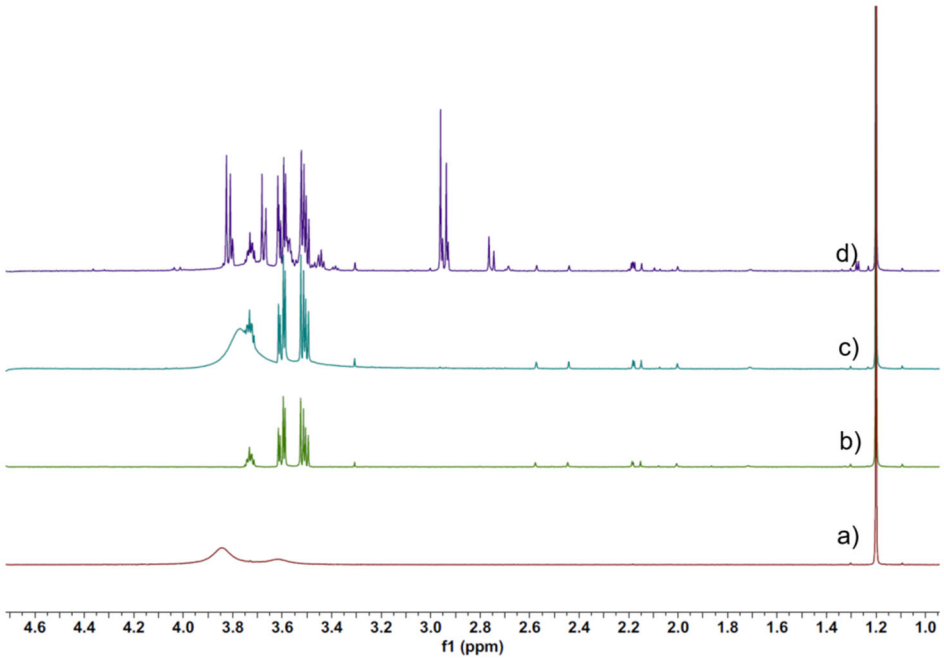


Figure 4- 11 ^{1}H NMR at pH= 4 of a) Ca-EDTA b) RBTA c) pre UV solution of RBTA (2.1 μM) and Ca-EDTA (10mM) solution in H_2O/D_2O d) 40 min photolysis with a Hg lamp with a 360 nm cutoff filter of c.

4.3.6 Effect of pH and wavelength on the amount of calcium released

Our process would ideally be applied to biological systems, which unless are occurring in specialized organelles whose pH can range from 2 to 8, maintain a biological pH around 7. Therefore, we investigated how pH and wavelength affected calcium release. The pH level that was tested ranged from 4 to 7. Also, the visible light range is best suited for biological systems of live cells so we studied if there was any difference between the calcium release at different wavelengths.

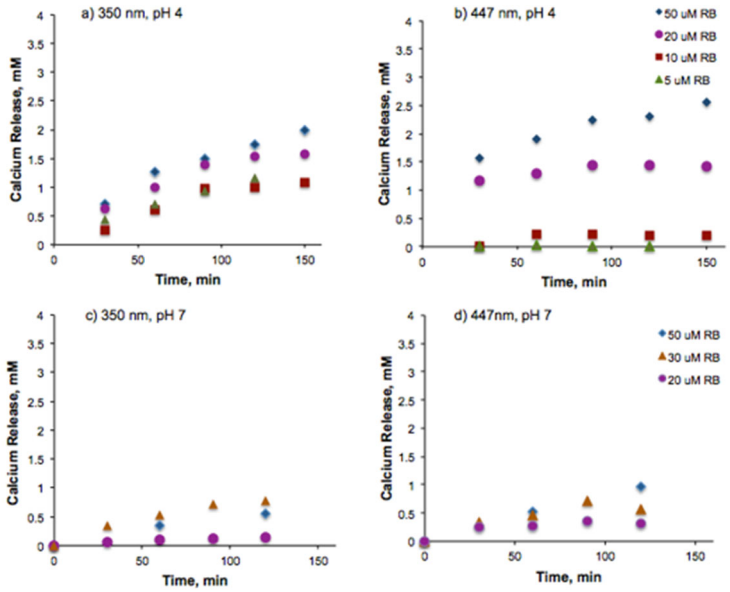


Figure 4- 12 Photolysis solutions at 5 mM Ca-EDTA while varying wavelength, pH and riboflavin concentrations to identify factors that have the largest effect on calcium release. a) 350 nm , pH 4 wand 5 µM riboflavin. b) 447 nm , pH 4 riboflavin. c) 350 nm, pH 7.

Results for the testing of pH on calcium release can be seen in Figure 4-13. The results show that more calcium is released at pH = 4 versus pH = 7 overall. Also, because of the variation in binding constant K_{sp} of EDTA to the calcium ions at the two differing pH each calcium sample taken was adjusted to consider the unbound calcium detected at time 0 by subtracting the initial absorption before photolysis of sample to the proceeding samples. Therefore, the higher calcium release readings were not because of EDTA's weaker binding to calcium at lower pH. An example of a control reading can be found in Appendix C.

The variation in concentration in our investigation also optimized the amount of flavin that could be present. These parameters consider the solubility of

riboflavin and possible self-quenching/aggregation range. The solubility of riboflavin has been reported as 12 mg per 100 ml at 27.5 C or 318 *μM* [174]. Fritz et al suggest that possible self-quenching of riboflavin somewhere in the range of 40-80 μ*M* (pH 7) [175]. Therefore, our samples go no higher than *50 μM*.

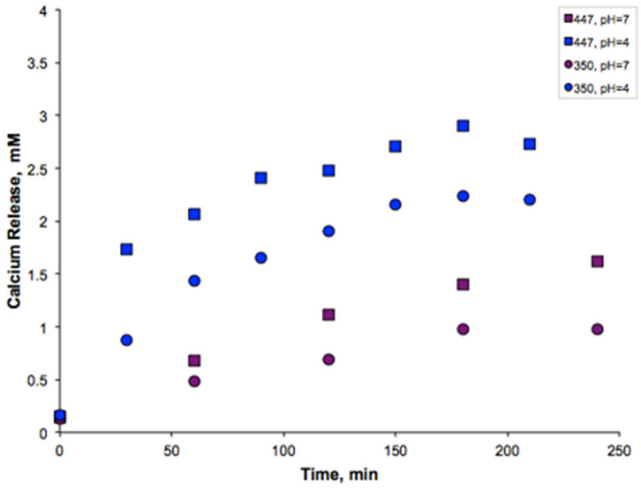


Figure 4- 13 Photolysis of 5 mM Ca-EDTA with 50 μM Riboflavin for photolysis wavelength of 447 and 350 at pH 4 and pH 7.

When light sources were compared regardless of pH or flavin concentration the diode light source at 447 released the most calcium of all other conditions (Figure 4-14). It should also be noted that even though the 447 lamp was the most calcium released the more important factor was pH since the pH 4 350 nm released more calcium than any of the pH 7 at any light source. It can then be inferred that the availability of protons is crucial for calcium release in our system. The most likely possibility for the pH being a large factor in calcium release could be the availability of protons is necessary for the reoxidation cycle of the sensitizers

Table 4- 4 Sample data for 180 min of photolysis at varying starting pH and wavelengths of Photolysis µM sensitizer and 5 mM Ca-EDTA.

Sample	UV	pH Start	pH End	Calcium (mM)	Calcium Released
1	447	4.1	8.2	2.90	58%
2	447	7.4	8.4	1.41	28%
3	350	4.1	7.8	2.23	45%
4	350	7.4	8.2	0.98	20%

Another consideration is if the pH changes with photolysis. During calcium release experiments the pH was taken before and after photolysis. Table 4-4 lists the data for each set of results at 180 mins. In all samples tested the pH increases, with a max of around pH 8. Since EDTA binds more strongly to the calcium ion at higher pH this means that our previous results that showed pH 4 released more calcium were not because of the change in binding. If this was the case you would expect less calcium to be free when the pH increases. These pH studies are preliminary and future work could more closely identify the mechanistic reason for the difference in calcium release.

4.3.7 Experiments on the effect of pH and wavelength on amount of Sensitizer degradation:

Previously we reported that when a photolysis solution with riboflavin sensitizer was purged with nitrogen, the amount of calcium released when this was done reduced to the point it was no longer detectable. When oxygen was reintroduced into the solution, there was an increase in the oxidized signal of riboflavin again. We deduced this was because the reoxidation of the flavin derivatives allowed for more than one electron transfer event. Reoxidation is not

limitless though. In this study we further our understanding of the system by investigating what is happening to the sensitizer during the calcium release process.

There are documented pathways to degradation that compete with reoxidation and therefore hinder the recycling of the sensitizers. The degradation products of riboflavin have been extensively studied by such groups as Ahmad et al. [165, 176-179] Figure 4-15 lists the major products that have been identified for the photoreduction and photoaddition of riboflavin in aqueous solution.[177]

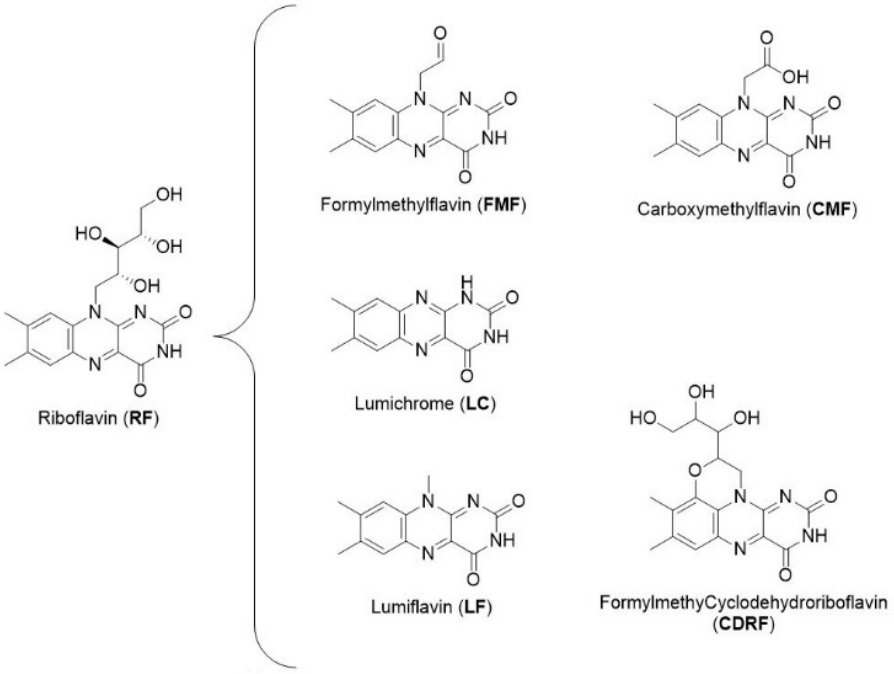


Figure 4- 14 Possible degradation products from the photolysis of RF with Ca-EDTA

We studied the degradation process through the changes in the UV/Vis spectra of the solution in acidic and neutral pH at visible and UV photolysis wavelengths. Each sample had the same amount of riboflavin and Ca-EDTA, 50 μM and 5 mM, respectively. The identification of the products will be qualitative

though based on the multicomponent spectrometric method developed by Ahmad et al.[180]

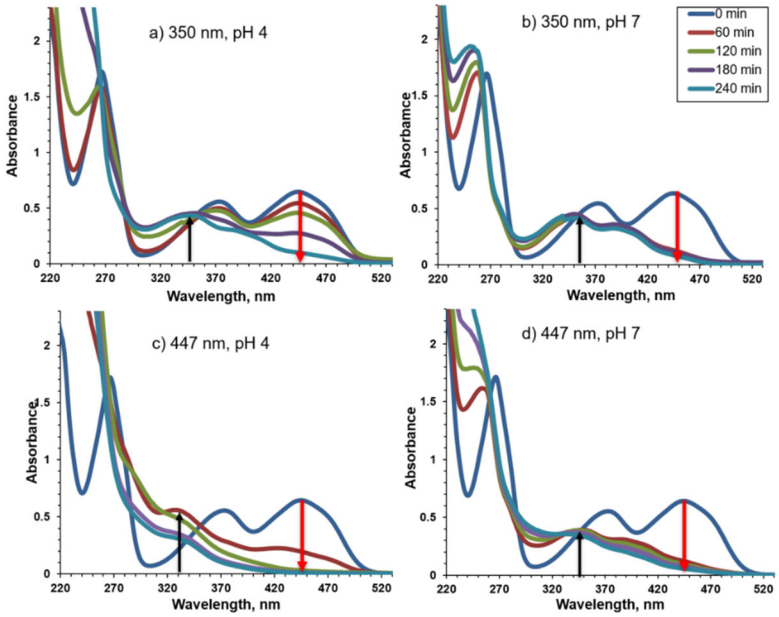


Figure 4- 15 Riboflavin degradation UV-Vis at various times, wavelengths and pH as stated on graph. Riboflavin was at 50 µM, Ca-EDTA at 5 mM.

The UV/Vis spectra in Figure 62 were taken simultaneously as the calcium release studies shown in section 4.3.6 where pH and wavelength were considered. All the spectra have a loss of the absorption band at 445 nm indicated by the red arrow (Figure 4-16). This indicates that the RB is being degraded because none of the possible degradation products have an absorption max in the 445 nm range.[177, 181] The pH 7 samples lose their 445 nm absorption band the fastest with it being completely gone in the first 60 minutes. For pH 4 the 350 nm lamp keeps the band until the 240 min time point. The increase of the 350-360 nm region indicates the formation of lumichrome (LC) through a photoreduction pathway while the smaller increase in 410 nm indicates the cyclization of RB into CDRF through a photoaddition in the pH 7 samples. The pH 4 samples have almost no

increase in the 410 nm band at 447 photolysis but the LC band is present. These results indicate that there is a difference in the photoreduction pathway of RB at the different pH and photolysis wavelength used. These may explain the difference in calcium release at the two pHs but more research into why exactly that happens would have to be done.

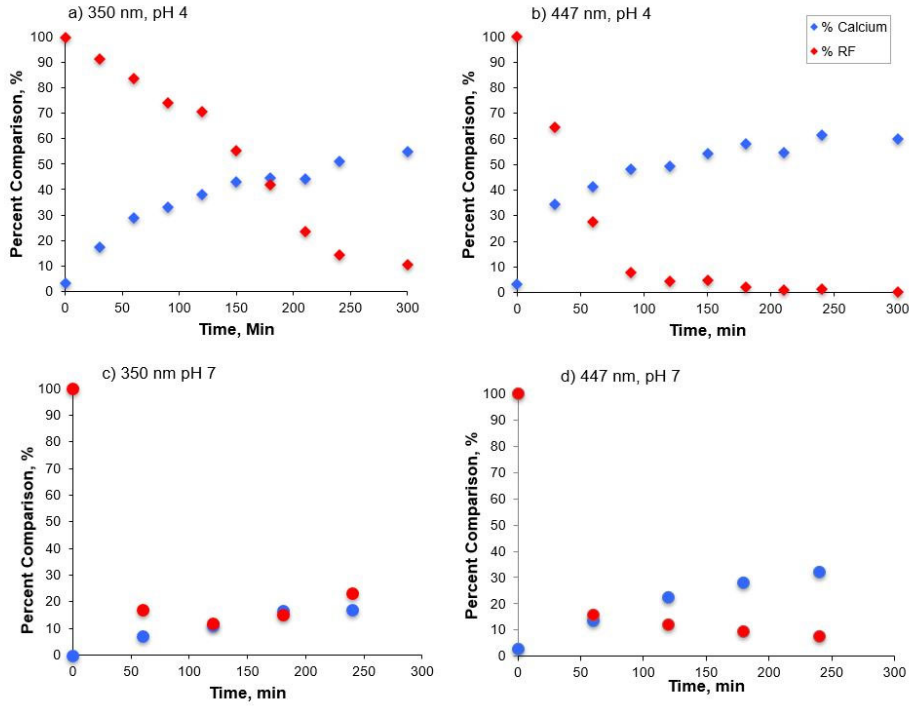


Figure 4- 16 Comparison of percent calcium release and percent depletion of RB versus time. Each mixture contained 50 µM RB, 5 mM CaEDTA, a) and b) are pH= 4, c) and d) pH= 7.3; RF concentration was based on the loss of 445 nm molar wavelength and use of beer's law.

A graphical comparison of the RB degradation versus calcium release shows a pattern in the loss of RF and the release of calcium (Figure 4-17). The percentage loss of RB coincides with a plateauing of the release of calcium. The loss in RB is much steeper at pH 7 so the calcium release is much lower. The ability of flavin to reoxidize and not degrade seems to be an important factor in the

release of calcium. Though it cannot be excluded that some of the photoproducts could in theory also take part in electron transfer, most are less soluble in water than RB so this would require further research.

4.3.8 Alginate Gelation Experiments

Alginate experiments were also conducted with RBTA, RB and Ca-EDTA. At neutral or acidic pH demonstrated that when photolyzed at 350 or 447 nm the alginate gels would produce a photothinning effect. Meaning that the alginate of 2%-3% by weight that had gel properties would become completely liquid.

To verify that the current system was capable of delivering a useful concentration of free Ca^{2+} we photolyzed the Ca-RBTA separately from the alginate. Then the 2 % alginate was added to see if a gel would form. The results in Figure 4-19 indicate that a gel formed from the calcium released when compared to the dark control but this was only done as a spot test

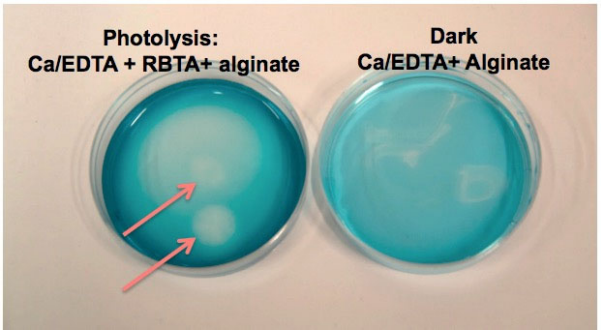


Figure 4- 17 Ca-EDTA 20 mM, 20 µM RBTA, 60 min photolysis solution. 2% by weight alginate was added to the solution to both solutions.

Another graduate student in our lab was able to produce free standing gels by photolyzing RB, Ca-EDTA, alginate gels at a basic pH (pH = 9.3) in vitro. His gelation work is reported in our published paper.[118] At this basic pH whatever is causing photothinning of the gel at lower pH was avoided. More research would need to be done to understand the implications of those results.

4.4 Conclusion

Experiments described herein demonstrate that visible light triggered photorelease of calcium ions in up to millimolar concentrations can be accomplished using inexpensive and biocompatible reagents. Using riboflavin, it is possible to carry out release of calcium in a photocatalytic manner using substoichiometric amounts of the flavin sensitizer.

The photocatalytic mechanism for this reaction was shown to be electron transfer that was dependent on the presence of oxygen and the degradation of EDTA through decarboxylation. The efficiency of the reaction was shown to be comparable to other calcium release reactions reported indicating its competitiveness with other systems. There was a pH dependence that indicated acidic solutions could release more calcium than neutral ones. Further inquiry showed that the degradation of RB a contributing factor to the difference in calcium release.

Finally, it has been shown that this photochemically generated free calcium can be used to trigger gelation in alginate solutions. Future studies will (a) explore extension of this method to other chelating agents and metals (b) examine

additional applications of the current system, and (c) develop linked sensitizer-chelator systems that can be used in biological systems.

Chapter 5 Conclusion and Future work

Our studies focused on investigating intelligent materials that responded to light through two different photochemical pathways; photoisomerization and photoinduced electron transfer. These photorheological materials whose viscosity can be tuned through light have received considerable interest. Light is an economical and green catalyst that can be easily utilized in a laboratory setting.

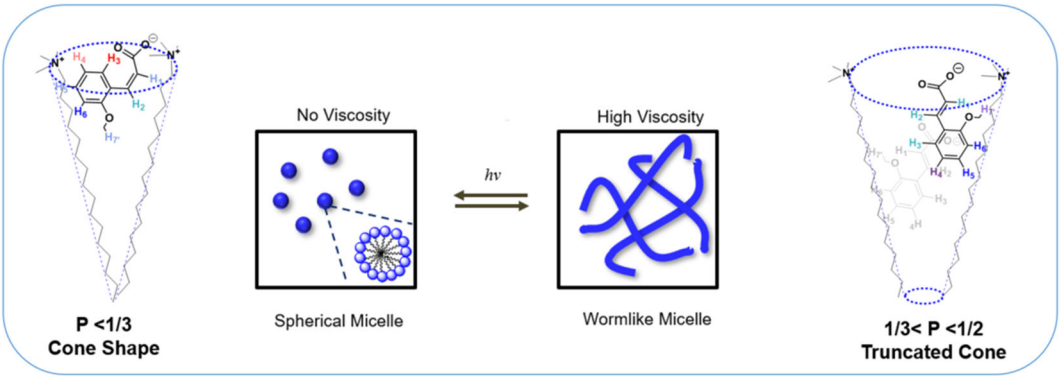


Figure 5- 1 Molecular interactions in cinnamic acid derivative isomers and CTAB. Visualization of morphology change

The first system studied the photoisomerization of six cinnamic acid derivatives in solutions with CTAB surfactants. The molecular change from trans to cis isomers caused the rheology of the solution to change by lowering its viscosity. These changes were due to the different intermolecular interactions that each isomer created with the CTAB surfactant molecules (Figure 5-1). The interactions between most trans isomers created favorable conditions for the micelles to elongate into wormlike micelles causing the viscosity of the solution to increase. Exceptions were the para isomers. Photoisomerization into the cis conformation then removed the favorable interactions thereby reducing the

viscosity of the solution. It was shown that the cis isomer oriented itself differently by being wedged closer to the head groups in a perpendicular manner. These changes decreased the packing parameter thereby favoring spherical micelles over wormlike micelles and therefore the viscosity lessened.

The orientation of tOMCA also alluded to the possibility of some interaction between other tOMCA molecules inside the micelle. The proximity of protons identified through 2D NOESY experiments and the titration studies indicated possible aromatic π interactions which we are proposing are anion- π (Figure 5-2). Further research would help give more definitive evidence as to whether the aromatic interactions are occurring and how much that contributes energetically to the formation of the wormlike micelles. It is important to understand the molecular interactions that lead to the bulk properties of materials so that it can inform the design of new intelligent materials.

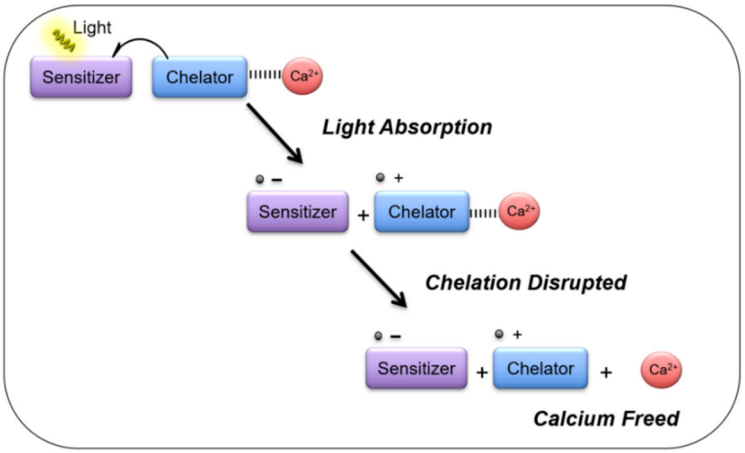


Figure 5- 2 Depiction of photoinduced electron transfer by sensitizer and calcium release.

The release of calcium was produced with the use of anthraquinone and flavin derivative sensitizers at the UV and visible light spectrum respectively.

Characterizing the photochemical process, it was shown that a photoinduced electron transfer occurred whereupon the sensitizer absorbed light and the EDTA donated an electron to the sensitizer (Figure 66). The calcium was sequestered in an EDTA and the electron donation commenced the degradation of EDTA through decarboxylation breaking the chelation. We provided direct proof of the EDTA degradation and subsequent calcium release. The anthraquinones produced approximate stoichiometric calcium while the flavin derivatives acted at substoichiometric amounts. The calcium release from the flavins was 1000-fold. The quantum efficiency of the flavin sensitizer promoted release of calcium was on par with commercially available molecules.

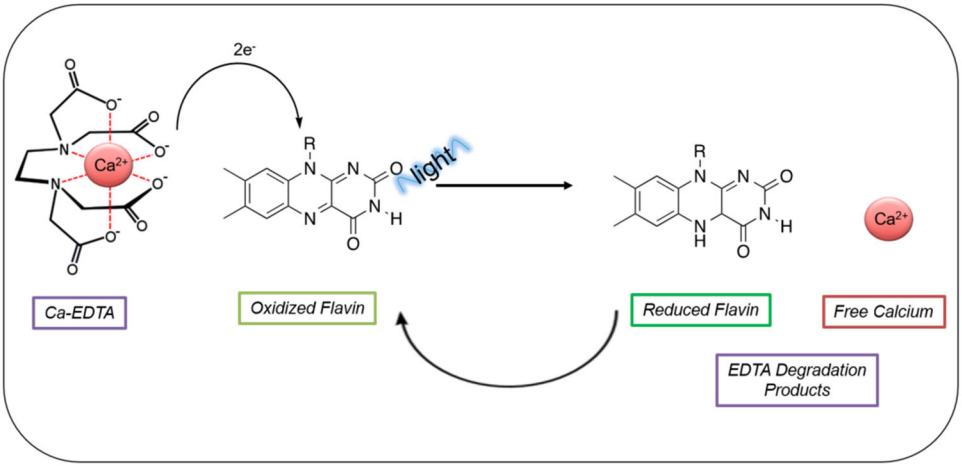


Figure 5- 3 Visualization of Ca-EDTA degradation through photoinduced electron transfer reaction leading to the release of calcium

The flavins ability to release above stoichiometric amounts of calcium was shown to be because of the photocatalytic processes whereupon the flavin reoxidizes and is able to participate again in photoinduced electron transfer(Figure 5-3). We further studied how pH, concentration of sensitizer and wavelength affected the release of calcium in the flavin system. We were able to release

enough calcium to create gels, *in vitro* at very high pH or when the solution and alginate were mixed after photolysis. Both these studies use economical, green chemistry that could lead to an increase in the efficiency in intelligent material design and to influence future work in photorheological research.

Appendix A: Supporting Information for Photoisomerization of Cinnamic Acid Derivatives in CTAB

Table A- 1 Parameters for acquisition of ^{1}H NMR in Bruker 600 Mhz spectrometer, BBI prode

NMR:	600MHz	**P1**	10.3-14.5 usec
solvent	D2O	**PL1**	2db
NS	32-16	**SF**	600MHz
D1	2-4sec	**SWH**	8000-9600 Hz
DS	0-2	**PROBHD**	5mm BBI 1H/D
AQ	2.5-2.9sec		
Temp	298K		
Pulse Prog	zg30		
Receiver Gain	180-300		

Table A- 2 Parameters for acquisition of ^{1}H NMR in Bruker 400 Mhz spectrometer, BBI probe

NMR:	400MHz	**P1**	12.00usec
solvent	D2O	**PL1**	3.00dB
NS	32	**SF**	400Mhz
D1	2	**SWH**	5995 Hz
DS	4	**PROBHD**	5 mm BBI
AQ	1.5sec		
Temp	298K		
Pulse Prog	zgesgp		
Receiver Gain	180-322		

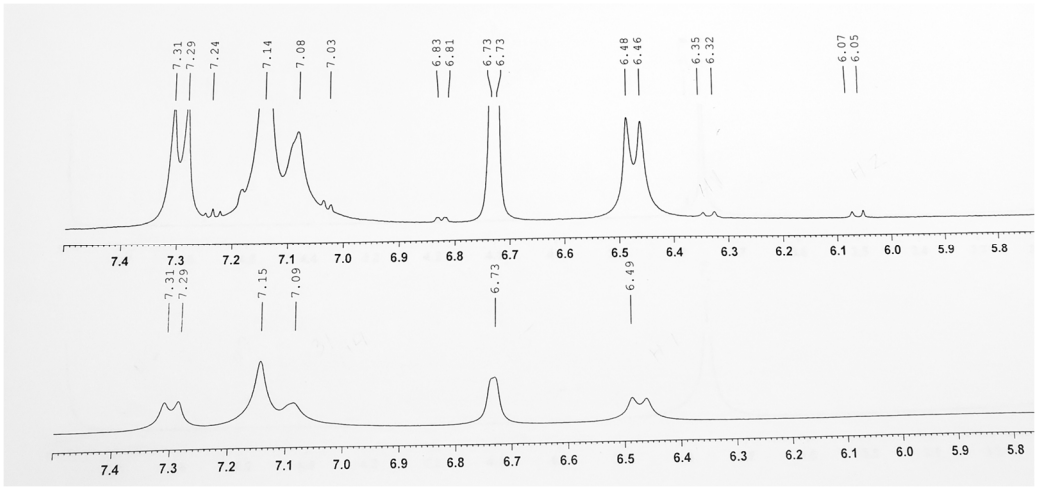


Figure A- 1 ^{1}H NMR spectra of 10 mM MCA, 20 mM CTAB in D_2O, 298 K. Photolysis with Rayonet 254 nm bottom 0 min and top 60 min.

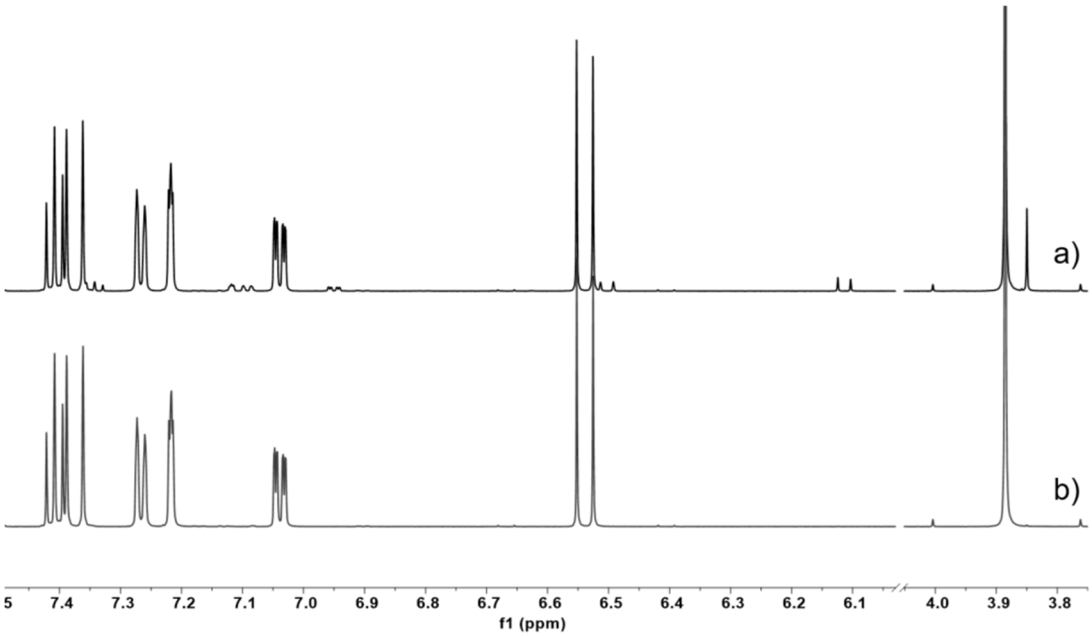


Figure A- 2 ^{1}H NMR spectra of 10 mM MCA in D_2O, 298 K. Photolysis with Rayonet 254 nm a) 60 min b) 0 min

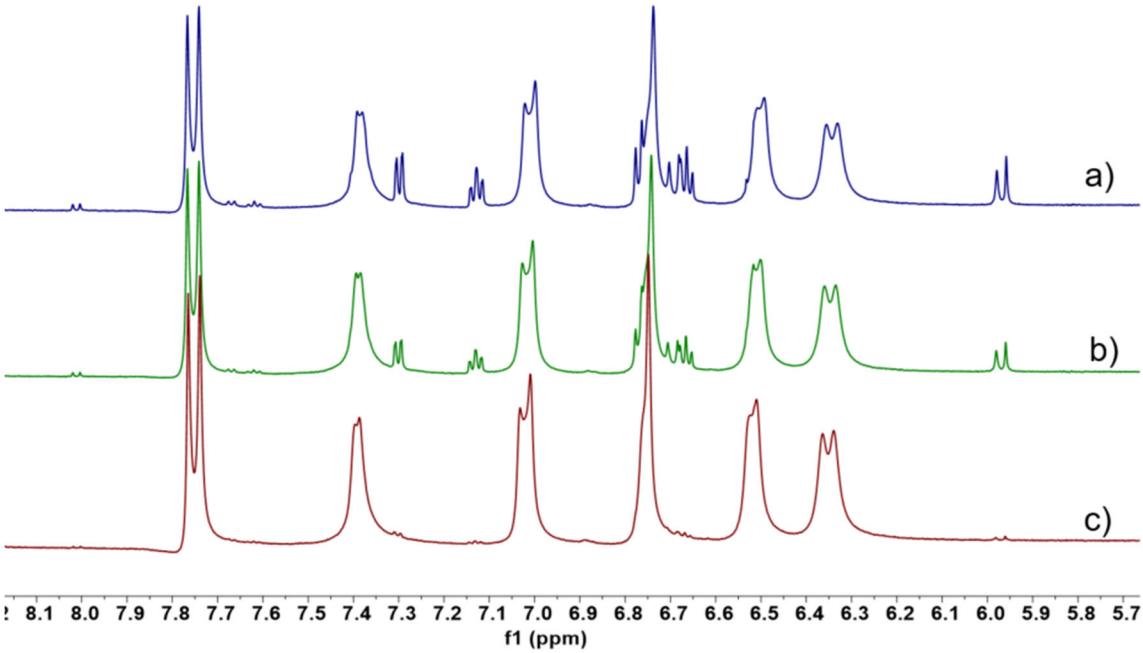


Figure A- 3 4 ^{1}H NMR spectra of 20 mM oCoum 20mM CTAB in D_2O, 298 K. Photolysis with Rayonet 254 nm a) 60 min b) 30 min c) 0 min

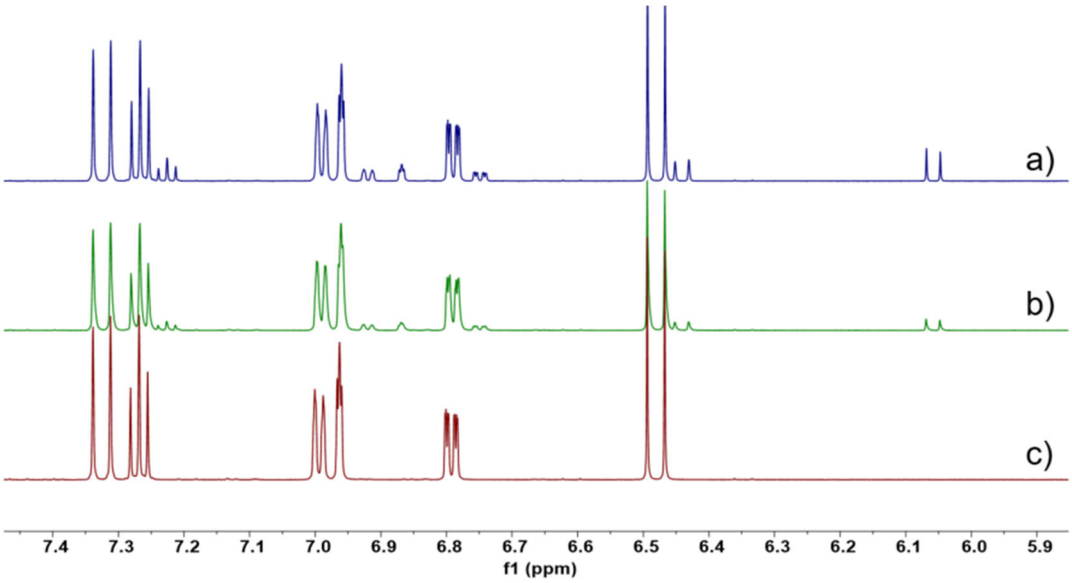


Figure A- 5 6 ^{1}H NMR spectra of 20 mCoum in D_2O, 298 K. Photolysis with Rayonet 254 nm a) 60 min b) 30 min c) 0 min

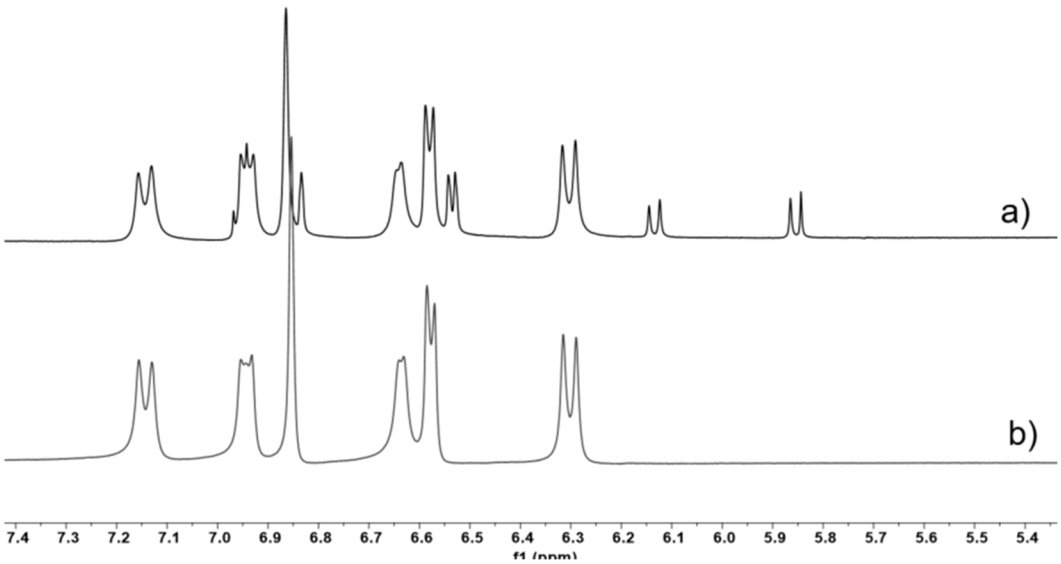


Figure A- 7 ^{1}H NMR spectra of 20 mCoum 20 mM CTAB in D_2O, 298 K. Photolysis with Rayonet 254 nm a) 60 min b) 0 min

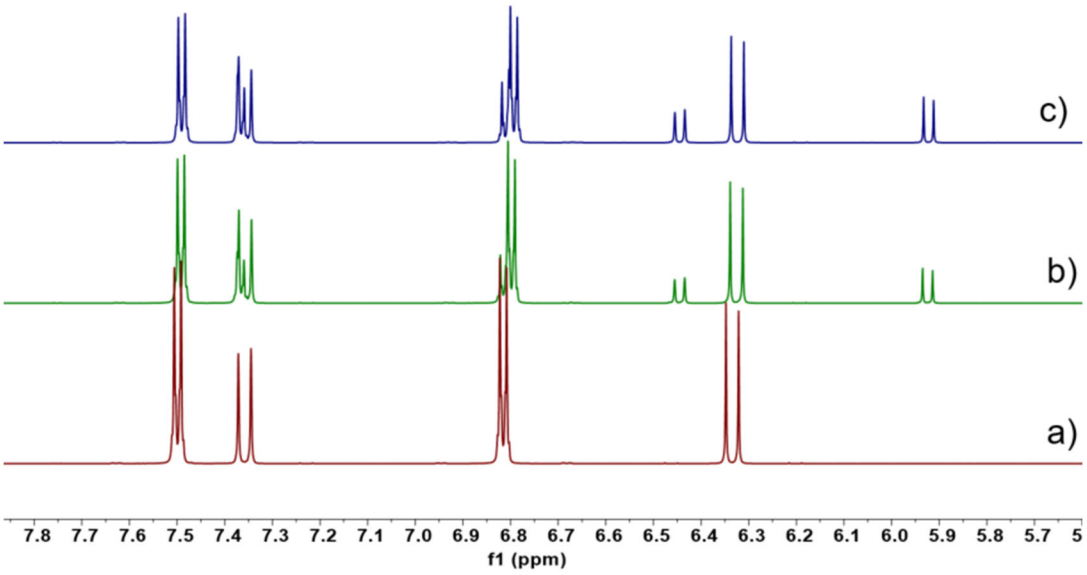


Figure A- 8 ^{1}H NMR spectra of 20 pCoum in D_2O, 298 K. Photolysis with Rayonet 254 nm a) 0 min b) 30 min c) 60 min.

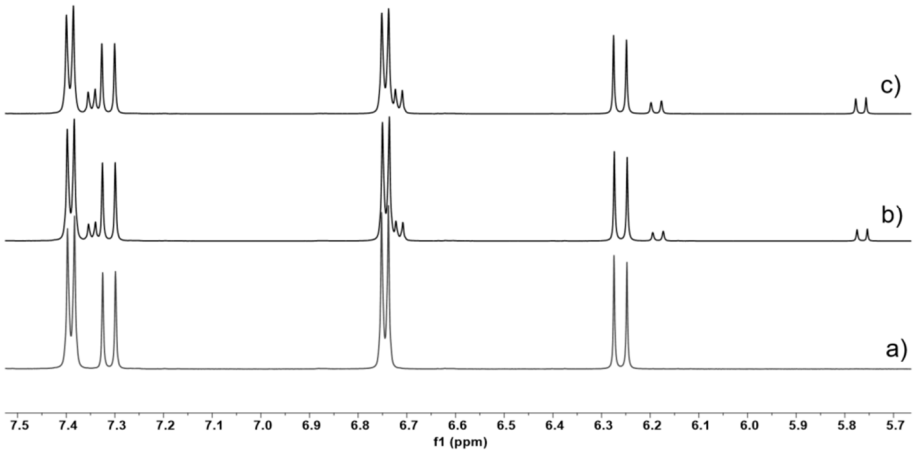


Figure A- 9 ^{1}H NMR spectra of 20 pCoum 20 mM CTAB in D_2O, 298 K. Photolysis with Rayonet 254 nm a) 0 min b) 20 min c) 30 min

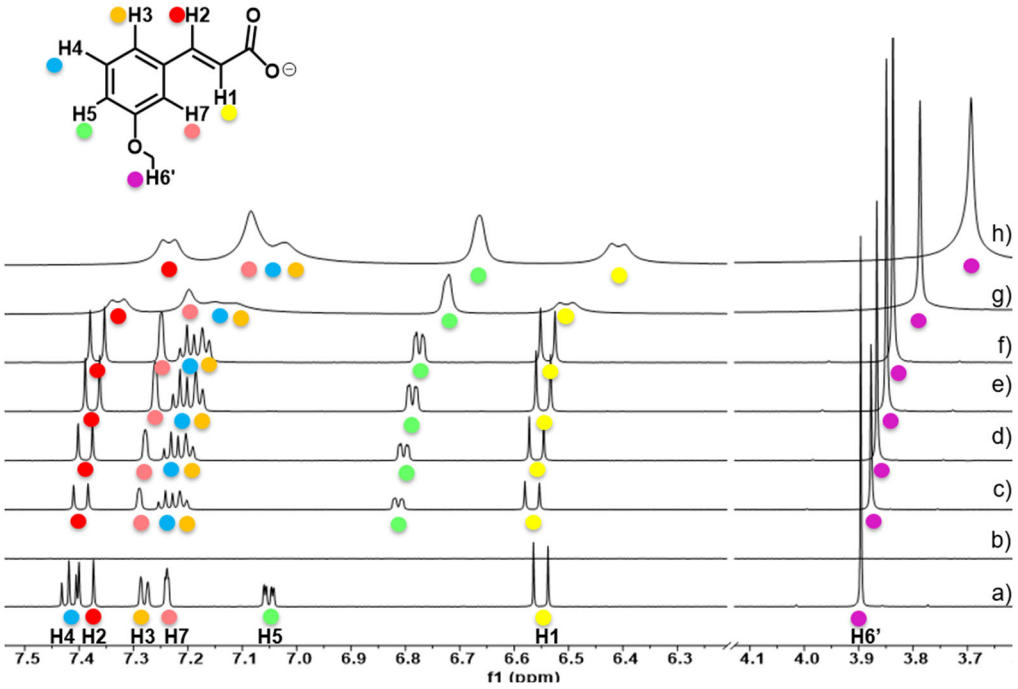


Figure A- 10 Aromatic chemical shift region of mMCA. ^{1}H NMR spectra, Bruker 600 MHz , 298 K a) 2 mM mMCA control b) 20 mM CTAB control c) 2 mM mMCA d) 3 mM mMCA e) 5 mM mMCA f) 6 mM mMCA g) 10 mM MCA h) 20 mM mMCA to 20 mM CTAB.

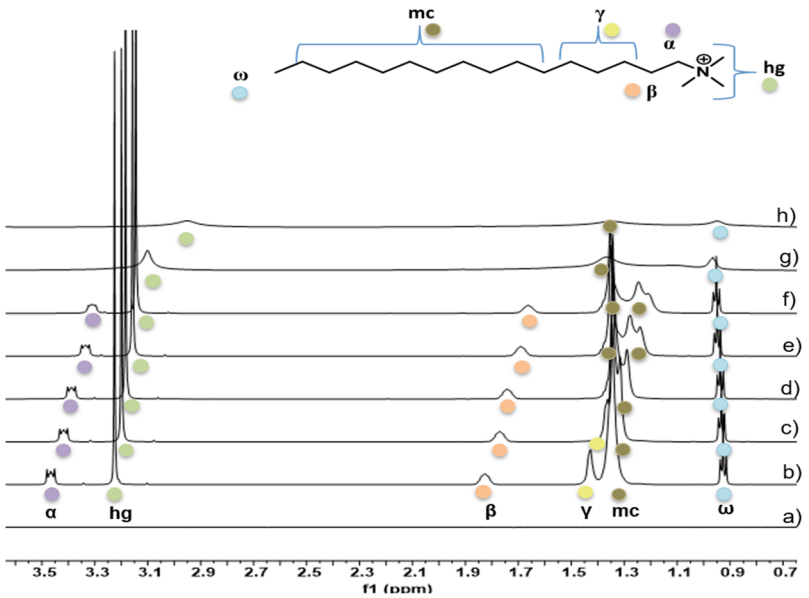


Figure A- 11 CTAB chemical shift region of mMCA. ^{1}H NMR spectra, Bruker 600 MHz , 298 K a) 2 mM mMCA control b) 20 mM CTAB control c) 2 mM mMCA d) 3 mM mMCA e) 5 mM mMCA f) 6 mM mMCA g) 10 mM MCA h) 20 mM mMCA to 20 mM CTAB.

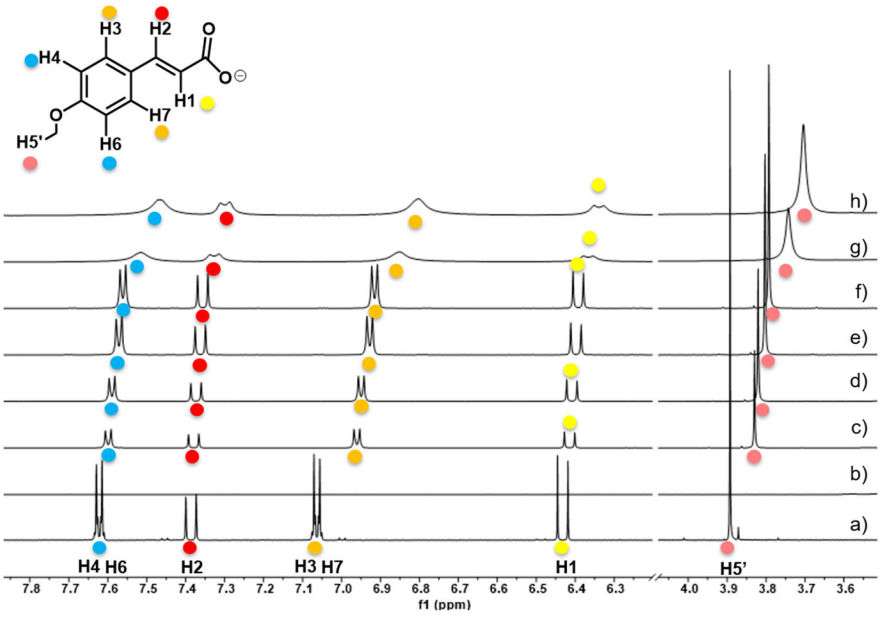


Figure A- 12 Aromatic chemical shift region ^{1}H NMR spectra of pMCA. Bruker 600 MHz , 298 K a) 2 mM pMCA control b) 20 mM CTAB control c) 2 mM pMCA d) 3 mM pMCA e) 5 mM pMCA f) 6 mM pMCA g) 10 mM pMCA h) 20 mM pMCA to 20 mM CTAB.

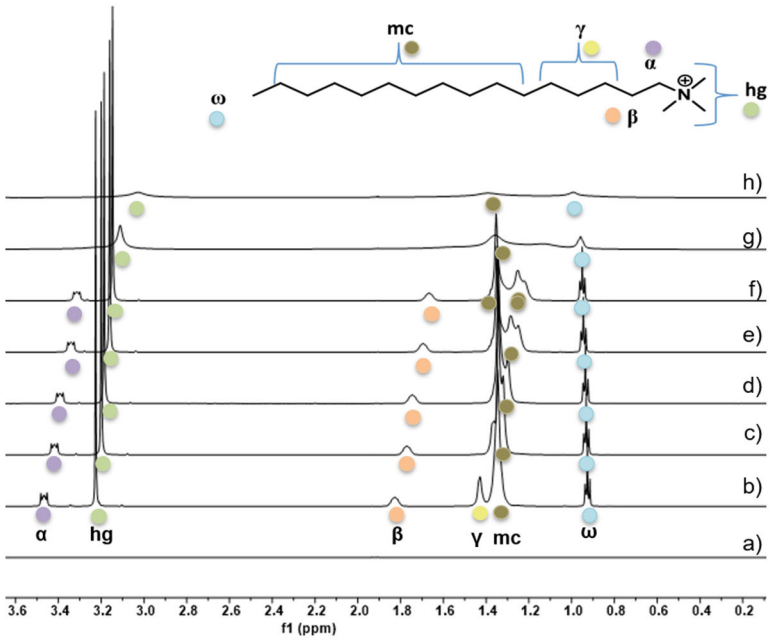


Figure A- 13 CTAB chemical shift region of ^{1}H NMR spectra of pMCA. Bruker 600 MHz , 298 K a) 2 mM pMCA control b) 20 mM CTAB control c) 2 mM pMCA d) 3 mM pMCA e) 5 mM pMCA f) 6 mM pMCA g) 10 mM pMCA h) 20 mM pMCA to 20 mM CTAB.

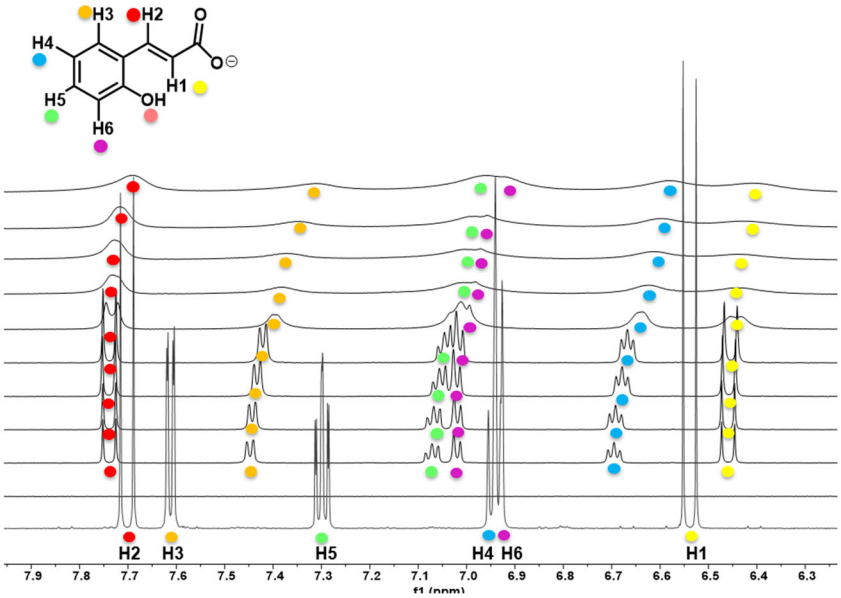


Figure A- 14 Aromatic chemical shift region ^{1}H NMR spectra of oCoum. Bruker 600 MHz , 298 K a) 10 mM oCoum control b) 20 mM CTAB control c) 2 mM oCoum d) 3 oCoum mM e) 4 mM oCoum f) 5 mM oCoum g) 6 mM oCoum h) 7 mM oCoum i) 8 mM oCoum j) 10 mM oCoum k) 15 mM oCoum to 20 mM CTAB

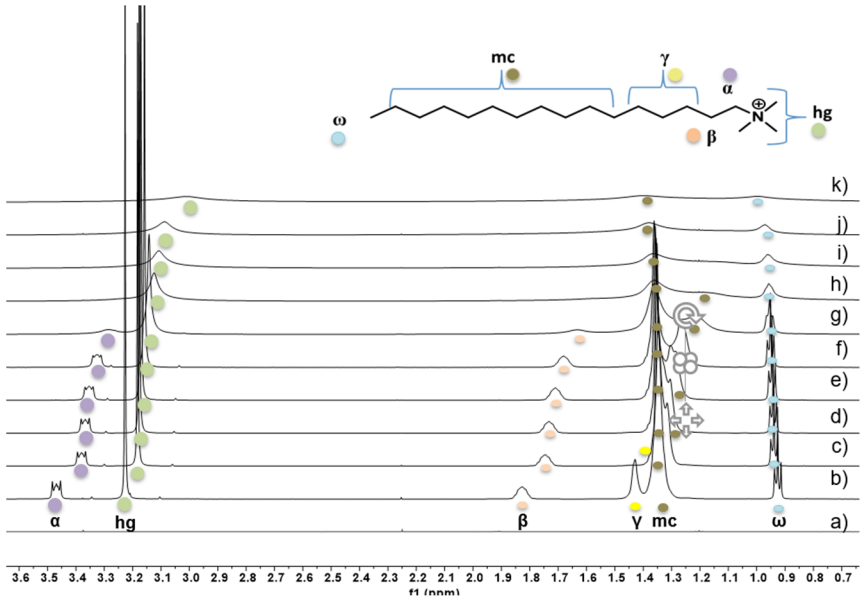


Figure A- 15 CTAB chemical shift region ^{1}H NMR spectra of oCoum. Bruker 600 MHz , 298 K a) 10 mM oCoum control b) 20 mM CTAB control c) 2 mM oCoum d) 3 oCoum mM e) 4 mM oCoum f) 5 mM oCoum g) 6 mM oCoum h) 7 mM oCoum i) 8 mM oCoum j) 10 mM oCoum k) 15 mM oCoum to 20 mM CTAB

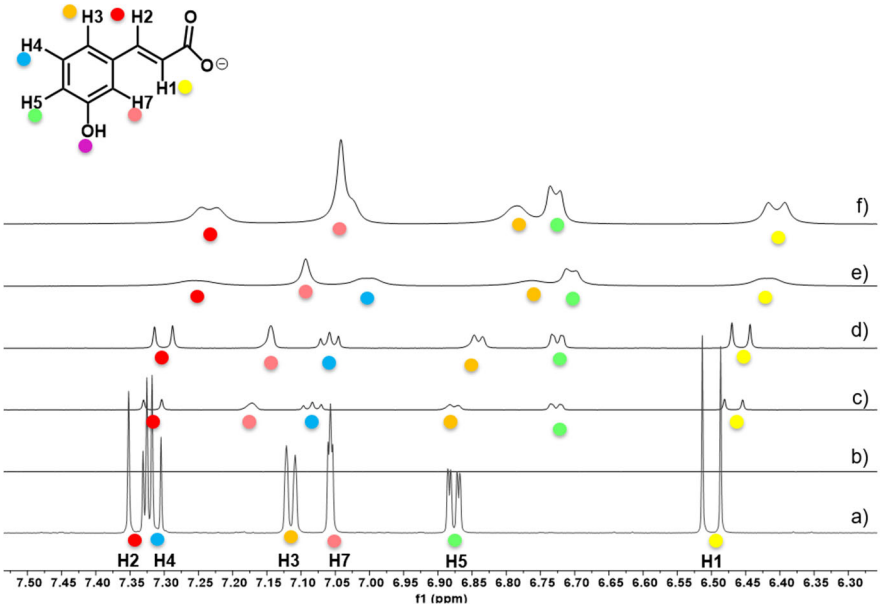


Figure A- 16 Aromatic chemical shift region ^{1}H NMR spectra of mCoum. Bruker 600 MHz , 298 K. a) 10 mM mCoum control b) 20 mM CTAB control c) 2 mM mCoum d) 5 mM mCoum e) 10 mM mCoum f) 20 mM mCoum in 20mMCTAB

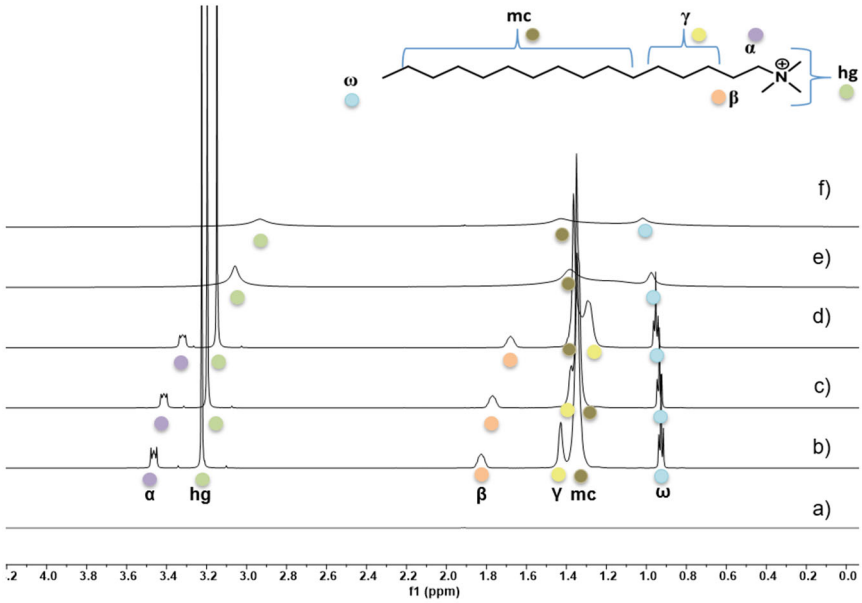


Figure A- 17 CTAB chemical shift region ^{1}H NMR spectra of mCoum. Bruker 600 MHz , 298 K.a) 10 mM mCoum control b) 20 mM CTAB control c) 2 mM mCoum d) 5 mM mCoum e) 10 mM mCoum f) 20 mM mCoum in 20mMCTAB

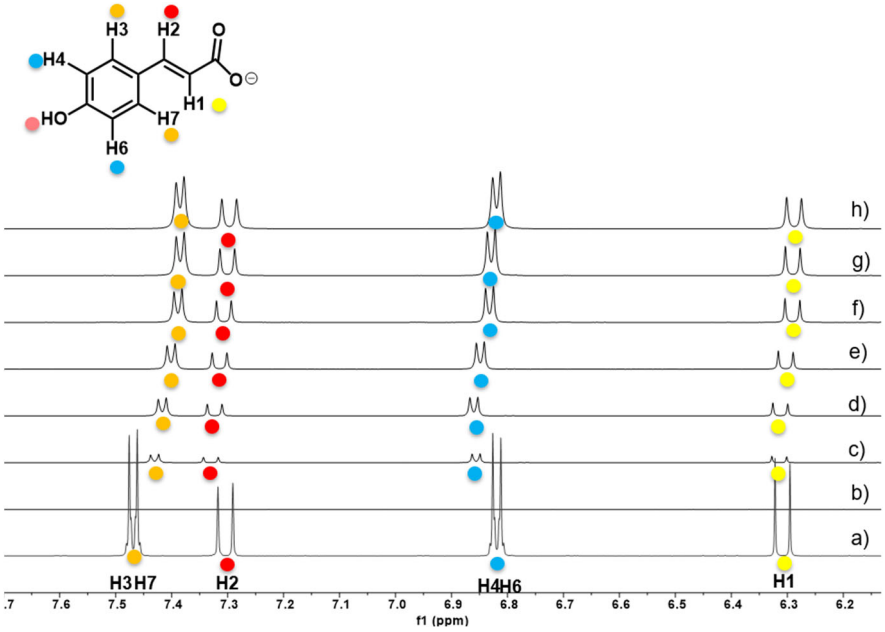


Figure A- 18 Aromatic chemical shift region ^{1}H NMR spectra of pCoum. Bruker 600 MHz , 298 K a) 10 mM pCoum control b) 10 mM CTAB control c) 2 mM pCoum d) 5

mM pCoum e) 8 mM pCoum f) 10 mM pCoum g) 15 mM pCoum h) 20 mM pCoum in 20mMCTAB

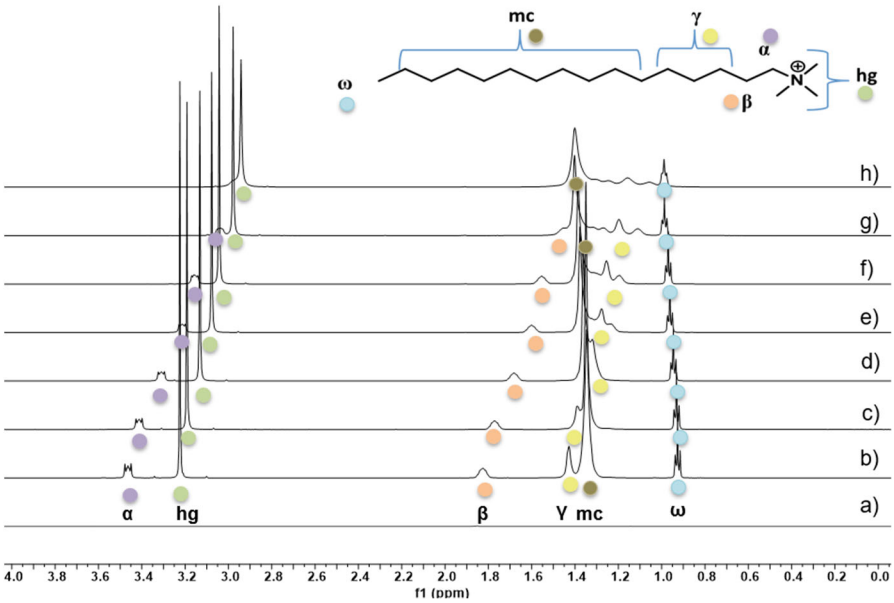


Figure A- 19 CTAB chemical shift region ^{1}H NMR spectra of pCoum. Bruker 600 MHz , 298 K a) 10 mM pCoum control b) 10 mM CTAB control c) 2 mM pCoum d) 5 mM pCoum e) 8 mM pCoum f) 10 mM pCoum g) 15 mM pCoum h) 20 mM pCoum in 20mMCTAB

Table A- 3 Titration study chemical shifts (ppm) of aromatic protons

[tOMCA]	H1	H2	H3	H4	H5	H6	H'7
2mM Control	6.63	7.77	7.72	7.15	7.51	7.20	4.00
2mM/20mMCTAB	6.57	7.74	7.64	6.92	7.22	6.95	3.95
5mM/20mMCTAB	6.55	7.72	7.61	6.91	7.19	6.88	3.91
10mM/20mMCTAB	6.52	7.68	7.56	6.85	7.12	6.79	3.85
20mM/20mMCTAB	6.48	7.64	7.48	6.79	7.06	6.72	3.77
[cOMCA]	H1	H2	H3	H4	H5	H6	H'7
10 mM Control	6.12	7.08	7.41	7.01	7.38	7.22	3.88
2mM/20mMCTAB	6.07	6.96	7.65	7.04	7.33	6.64	3.87
5mM/20mMCTAB	6.07	6.95	7.63	7.02	7.32	6.64	3.85
10mM/20mMCTAB	6.07	6.95	7.60	7.01	7.32	6.65	3.84
20mM/20mMCTAB	6.08	6.98	7.54	7.01	7.32	6.66	3.84
[mMCA]	H1	H2	H3	H4	H5	H'6	H7
2mM Control	6.55	7.39	7.28	7.42	7.05	3.90	7.24
2mM/20mMCTAB	6.57	7.40	7.21	7.24	6.82	3.88	7.29
5mM/20mMCTAB	6.55	7.38	7.18	7.21	6.79	3.85	7.26
10mM/20mMCTAB	6.51	7.33	7.11	7.14	6.72	3.79	7.20
20mM/20mMCTAB	6.41	7.24	—	—	6.67	3.69	7.08
[pMCA]	H1	H2	H3/7	H4/6	H'5		
2mM Control	6.44	7.39	7.62	7.07	3.89		
2mM/20mMCTAB	6.42	7.38	7.60	6.96	3.83		
5mM/20mMCTAB	6.40	7.37	7.57	6.93	3.80		
10mM/20mMCTAB	6.37	7.33	7.52	6.85	3.74		
20mM/20mMCTAB	6.34	7.30	7.47	6.80	3.70		
[oCOUM]	H1	H2	H3	H4	H5	H6	H'7
10mM Control	6.51	7.72	7.59	6.87	7.27	6.88	N/A
2mM/20mMCTAB	6.41	7.76	7.43	6.61	7.07	6.93	
5mM/20mMCTAB	6.41	7.76	7.41	6.59	7.05	6.92	
10mM/20mMCTAB	6.38	7.75	7.36	6.55	6.98	6.87	
20mM/20mMCTAB	6.35	7.73	7.34	6.53	6.97	6.81	
[mCOUM]	H1	H2	H3	H4	H5	H'6	H7
10mM Control	6.50	7.34	7.12	7.32	6.88	N/A	7.06
2mM/20mMCTAB	6.47	7.32	6.88	7.08	6.73	N/A	7.17
5mM/20mMCTAB	6.45	7.30	6.84	7.06	6.72	N/A	7.14
10mM/20mMCTAB	6.42	7.26	6.76	7.00	6.70	N/A	7.09
20mM/20mMCTAB	6.40	7.24	6.78	7.02	6.73	N/A	7.04
[pCOUM]	H1	H2	H3/7	H4/6	H'5		
2mM Control	6.37	7.37	7.53	6.87	—		
2mM/20mMCTAB	6.31	7.34	7.43	6.85	—		
5mM/20mMCTAB	6.30	7.33	7.41	6.84	—		

10mM/20mMCTAB	6.29	7.31	7.39	6.82	—
20mM/20mMCTAB	6.29	7.31	7.40	6.82	—

Table A- 4 Titration study chemical shifts change (Δ ppm) of aromatic protons

[tOMCA]	ΔδH1	ΔδH2	ΔδH3	ΔδH4	ΔδH5	ΔδH6	ΔδH'7
1:10	-0.06	-0.03	-0.08	-0.23	-0.29	-0.25	-0.05
1:04	-0.08	-0.05	-0.11	-0.24	-0.32	-0.32	-0.09
1:02	-0.11	-0.09	-0.16	-0.3	-0.39	-0.41	-0.15
1:01	-0.15	-0.13	-0.24	-0.36	-0.45	-0.48	-0.23
[cOMCA]							
1:10	-0.05	-0.13	0.25	0.03	-0.05	-0.58	-0.01
1:04	-0.05	-0.13	0.23	0.01	-0.06	-0.58	-0.03
1:02	-0.05	-0.13	0.19	0.00	-0.06	-0.57	-0.04
1:01	-0.04	-0.10	0.14	0.00	-0.06	-0.56	-0.04
[mMCA]	**ΔδH1**	**ΔδH2**	**ΔδH3**	**ΔδH4**	**ΔδH5**	**ΔδH'6**	**ΔδH7**
1:10	0.02	0.01	-0.07	-0.18	-0.23	-0.02	0.05
1:04	0.00	-0.01	-0.10	-0.21	-0.26	-0.05	0.02
1:02	-0.04	-0.05	-0.17	-0.28	-0.33	-0.11	-0.04
1:01	-0.14	-0.15	—	—	-0.39	-0.21	-0.16
[pMCA]	**ΔδH1**	**ΔδH2**	**ΔδH3/7**	**ΔδH4/6**	**ΔδH' 5**		
1:10	-0.02	0.00	-0.02	-0.11	-0.06		
1:04	-0.04	-0.02	-0.05	-0.14	-0.09		
1:02	-0.07	-0.06	-0.10	-0.22	-0.15		
1:01	-0.09	-0.09	-0.15	-0.27	-0.19		
[oCOUM]	**ΔδH1**	**ΔδH2**	**ΔδH3**	**ΔδH4**	**ΔδH5**	**ΔδH6**	**ΔδH'7**
1:10	-0.10	0.04	-0.16	-0.26	-0.20	0.05	—
1:04	-0.10	0.04	-0.18	-0.28	-0.22	0.04	—
1:02	-0.13	0.03	-0.23	-0.32	-0.29	-0.01	—
1:01	-0.16	0.01	-0.25	-0.34	-0.30	-0.07	—
[mCOUM]	**ΔδH1**	**ΔδH2**	**ΔδH3**	**ΔδH4**	**ΔδH5**	**ΔδH'6**	**ΔδH7**
1:10	-0.03	-0.02	-0.24	-0.24	-0.15	—	0.11
1:04	-0.05	-0.04	-0.28	-0.26	-0.16	—	0.08
1:02	-0.09	-0.09	-0.36	-0.32	-0.18	—	0.03
1:01	-0.10	-0.10	-0.34	-0.30	-0.15	—	-0.02
[pCOUM]	**ΔδH1**	**ΔδH2**	**ΔδH3/7**	**ΔδH4/6**	**ΔδH' 5**		
1:10	0.01	0.02	-0.03	0.03	—		
1:04	0.01	0.02	-0.05	0.04	—		
1:02	-0.02	0.00	-0.07	0.01	—		
1:01	-0.02	-0.01	-0.08	0.00	—		

Table A- 5 Titration study chemical shifts (ppm) of CTAB protons

[tOMCA]	hg	α	β	γ	mc	ω
20mM CTAB	3.23	3.47	1.82	1.43	1.34	0.92
2mM/20mMCTAB	3.2	3.42	1.77	1.36	1.34	0.93
5mM/20mMCTAB	3.17	3.35	1.71	n/a	1.35	0.95
**10mM/20mMCTAB	3.14	3.27	1.6	n/a	1.37	0.97
**20mM/20mMCTAB	3.06	n/a	n/a	n/a	1.41	1.01
[cOMCA]	**hg**	**α**	**β**	**γ**	**mc**	**ω**
20mM CTAB	3.22	3.47	1.82	1.43	1.34	0.92
2mM/20mMCTAB	3.19	3.42	1.79	1.4	1.34	0.92
5mM/20mMCTAB	3.14	3.35	1.73	1.36	1.33	0.92
10mM/20mMCTAB	3.09	3.27	1.68	n/a	1.32	0.92
20mM/20mMCTAB	3.04	3.19	1.62	n/a	1.32	0.92
[mMCA]	**hg**	**α**	**β**	**γ**	**mc**	**ω**
20mM CTAB	3.22	3.47	1.82	1.43	1.34	0.92
2mM/20mMCTAB	3.2	3.42	1.77	1.36	1.34	0.93
5mM/20mMCTAB	3.16	3.34	1.69	n/a	1.35	0.95
**10mM/20mMCTAB	3.1	n/a	n/a	n/a	1.37	0.97
**20mM/20mMCTAB	n/a	n/a	n/a	n/a	n/a	n/a
[pMCA]	**hg**	**α**	**β**	**γ**	**mc**	**ω**
20mM CTAB	3.22	3.47	1.82	1.43	1.34	0.92
2mM/20mMCTAB	3.2	3.42	1.77	1.37	1.34	0.93
5mM/20mMCTAB	3.16	3.34	1.7	n/a	1.35	0.95
**10mM/20mMCTAB	3.11	n/a	n/a	n/a	1.36	0.96
**20mM/20mMCTAB	3.03	n/a	n/a	n/a	1.39	0.99
[oCOUM]	**hg**	**α**	**β**	**γ**	**mc**	**ω**
20mM Control	3.23	3.47	1.82	1.43	1.35	0.92
2mM/20mMCTAB	3.19	3.4	1.77	1.37	1.35	0.93
5mM/20mMCTAB	3.15	3.33	1.69	n/a	1.35	0.95
**10mM/20mMCTAB	3.1	n/a	n/a	n/a	1.37	0.95
**20mM/20mMCTAB	2.99	n/a	n/a	n/a	1.4	0.99
[mCOUM]	**hg**	**α**	**β**	**γ**	**mc**	**ω**
20mM Control	3.22	3.46	1.83	1.42	1.34	0.93
2mM/20mMCTAB	3.2	3.41	1.77	1.38	1.35	0.93
5mM/20mMCTAB	3.15	3.32	1.68	n/a	1.36	0.95
**10mM/20mMCTAB	n/a	3.06	n/a	n/a	1.38	0.98
**20mM/20mMCTAB	2.93	n/a	n/a	n/a	1.43	1.02
[pCOUM]	**hg**	**α**	**β**	**γ**	**mc**	**ω**
20mM Control	3.23	3.47	1.83	1.43	1.35	0.92
2mM/20mMCTAB	3.19	3.4	1.77	1.39	1.35	0.94
5mM/20mMCTAB	3.11	3.27	1.66	n/a	1.37	0.95

10mM/20mMCTAB	3	3.1	1.51	n/a	1.39	0.98
20mM/20mMCTAB	2.98	2.94	n/a	n/a	1.41	1.00

Table A- 6 Titration study chemical shifts change (Δ ppm) of CTAB protons

[tOMCA]	hg	α	β	γ	mc	ω
2mM/20mMCTAB	-0.03	-0.05	-0.05	-0.07	0	0.01
5mM/20mMCTAB	-0.06	-0.12	-0.11	n/a	0.01	0.03
10mM/20mMCTAB	-0.09	-0.2	-0.22	n/a	0.03	0.05
20mM/20mMCTAB	-0.17	n/a	n/a	n/a	0.07	0.09
[cOMCA]	**hg**	**α**	**β**	**γ**	**mc**	**ω**
2mM/20mMCTAB	-0.03	-0.05	-0.03	-0.03	0	0
5mM/20mMCTAB	-0.08	-0.12	-0.09	-0.07	-0.01	0
10mM/20mMCTAB	-0.13	-0.2	-0.14	n/a	-0.02	0
20mM/20mMCTAB	-0.18	-0.28	-0.2	n/a	-0.02	0
[mMCA]	**hg**	**α**	**β**	**γ**	**mc**	**ω**
2mM/20mMCTAB	-0.02	-0.05	-0.05	-0.07	0	0.01
5mM/20mMCTAB	-0.06	-0.13	-0.13	n/a	0.01	0.03
10mM/20mMCTAB	-0.12	n/a	n/a	n/a	0.03	0.05
20mM/20mMCTAB	n/a	n/a	n/a	n/a	n/a	n/a
[pMCA]	**hg**	**α**	**β**	**γ**	**mc**	**ω**
2mM/20mMCTAB	-0.02	-0.05	-0.05	-0.06	0	0.01
5mM/20mMCTAB	-0.06	-0.13	-0.12	n/a	0.01	0.03
10mM/20mMCTAB	-0.11	n/a	n/a	n/a	0.02	0.04
20mM/20mMCTAB	-0.19	n/a	n/a	n/a	0.05	0.07
[oCOUM]	**hg**	**α**	**β**	**γ**	**mc**	**ω**
2mM/20mMCTAB	-0.04	-0.07	-0.05	-0.06	0	0.01
5mM/20mMCTAB	-0.08	-0.14	-0.13	n/a	0	0.03
10mM/20mMCTAB	-0.13	n/a	n/a	n/a	0.02	0.03
20mM/20mMCTAB	-0.24	n/a	n/a	n/a	0.05	0.07
[mCOUM]	**hg**	**α**	**β**	**γ**	**mc**	**ω**
2mM/20mMCTAB	-0.02	-0.05	-0.06	-0.04	0.01	0
5mM/20mMCTAB	-0.07	-0.14	-0.15	n/a	0.02	0.02
10mM/20mMCTAB	-0.22	-0.4	n/a	n/a	0.04	0.05
20mM/20mMCTAB	-0.29	n/a	n/a	n/a	0.09	0.09
[pCOUM]	**hg**	**α**	**β**	**γ**	**mc**	**ω**
2mM/20mMCTAB	-0.04	-0.07	-0.06	-0.04	0	0.02
5mM/20mMCTAB	-0.12	-0.2	-0.17	n/a	0.02	0.03
10mM/20mMCTAB	-0.23	-0.37	-0.32	n/a	0.04	0.06
20mM/20mMCTAB	-0.25	-0.53	n/a	n/a	0.06	0.08

Appendix B Supporting Information for Anthraquinone Ca-EDTA

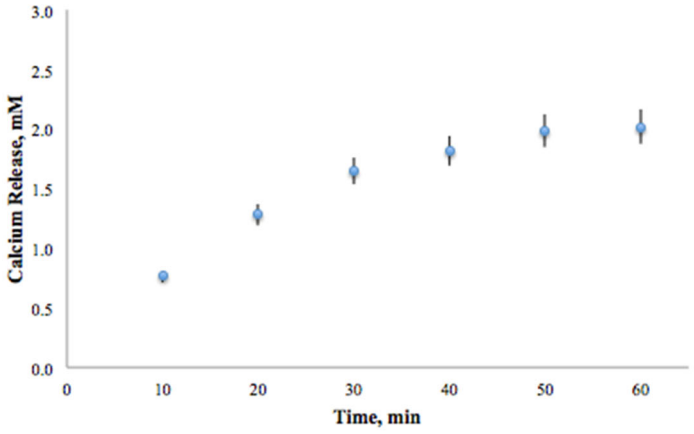
Example Error Calculations:

$$\text{STD Error} = (\text{STD})/\sqrt{n} \qquad \text{Exp. Error} = \frac{\text{Theoretical Value} - \text{Experimental Value}}{\text{Theoretical Value}}$$

$$\%\ \text{Error} = \frac{(\text{STD/mean})}{*100} \qquad \%\ \text{Exp. Error} = \frac{\text{Theoretical Value} - \text{Experimental Value}}{\text{Theoretical Value}} \times 100$$

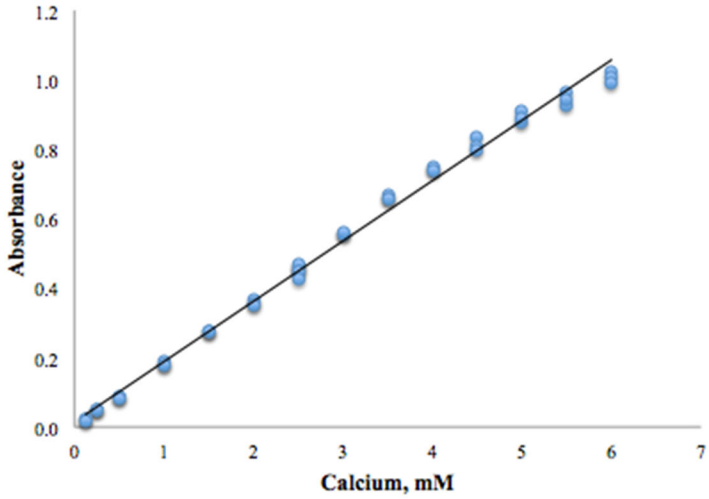
Table B-1 Sample standard error calculations for different repeated samples of 1 mM Ca^{2+}

	Corrected Abs		1mM Samples
s0	0.18	y = 0.1738x + 0.004	0.89
s1	0.18	y = 0.1738x + 0.004	0.88
s2	0.19	y = 0.1738x + 0.004	0.92
s3	0.19	y = 0.1738x + 0.004	0.93
Average	0.18	Average	0.91
STD Deviation	0.00	STD Deviation	0.02
STD Error	0.03	Exp Error	0.09
% Error	2.63	% Exp Error	9.45



Time	10	20	30	40	50	60	70
Average	0.76	1.28	1.65	1.82	1.99	2.02	2.28
STD Deviation	0.11	0.16	0.19	0.27	0.20	0.19	0.22
STD Error	0.06	0.10	0.11	0.15	0.12	0.11	0.13
Percent Error (%)	8.44	7.42	6.80	8.49	5.81	5.55	5.51

Figure B- 1 Sample error calculations and percent error for calcium release used in quantum yields



LINEST			
slope	5.72	-0.07	intercept
error	0.06	0.04	error
R-squared	0.99	0.14	STD of y

Figure B- 2 Calibration Curve Error Calculations using LINEST linearity test

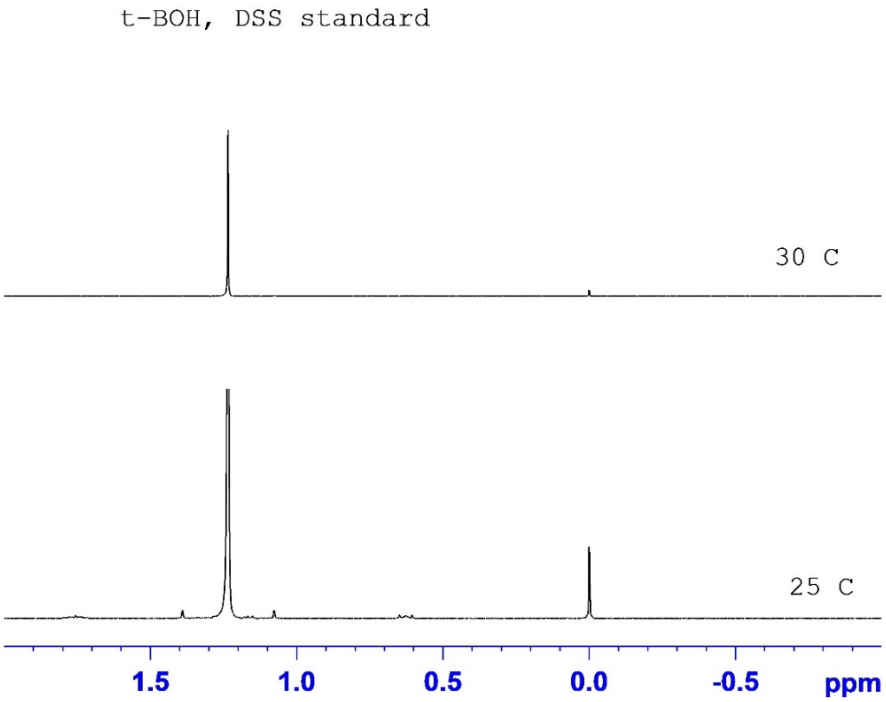


Figure B- 3 ^{1}H NMR of *tert*-butyl alcohol with DSS standard at 298 K and 303 K

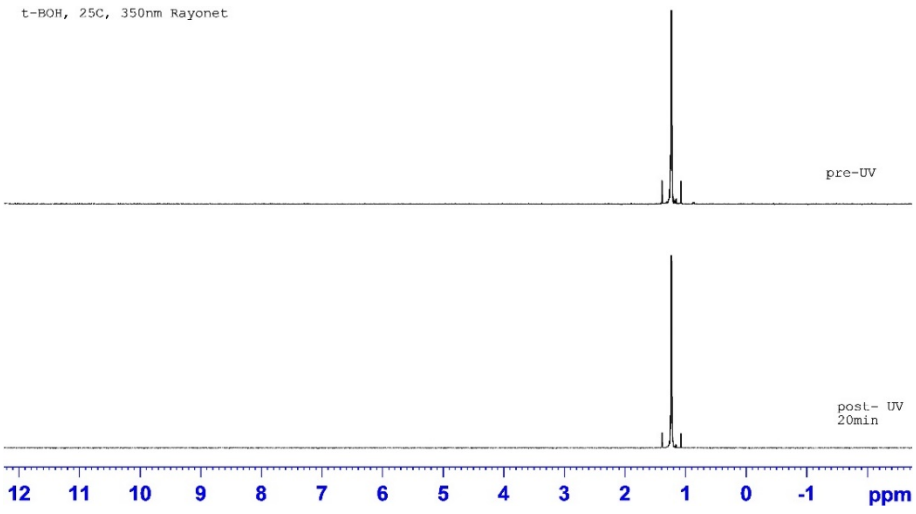


Figure B- 4 ^{1}H NMR of *tert*-butyl alcohol 254 nm Rayonet 20 min photolysis, 298 K

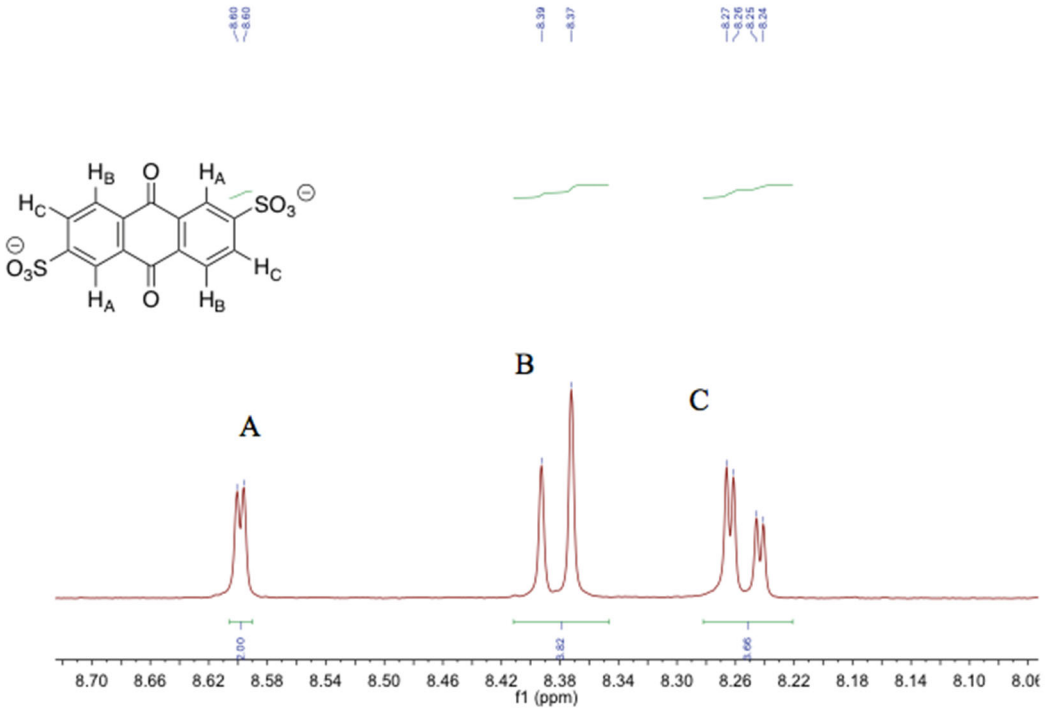


Figure B- 5 ^{1}H NMR spectra AQS-2, 2.5mM in D_2O, 298 K

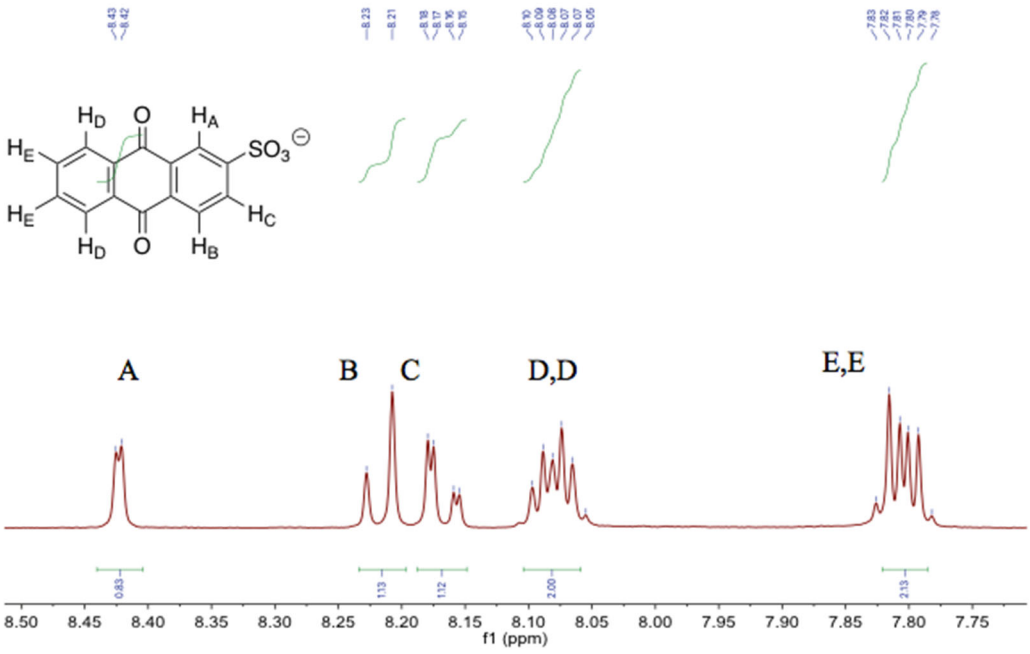


Figure B- 6 ^{1}H NMR spectra AQDS-1,5 2.5mM, in D_2O, 298 K

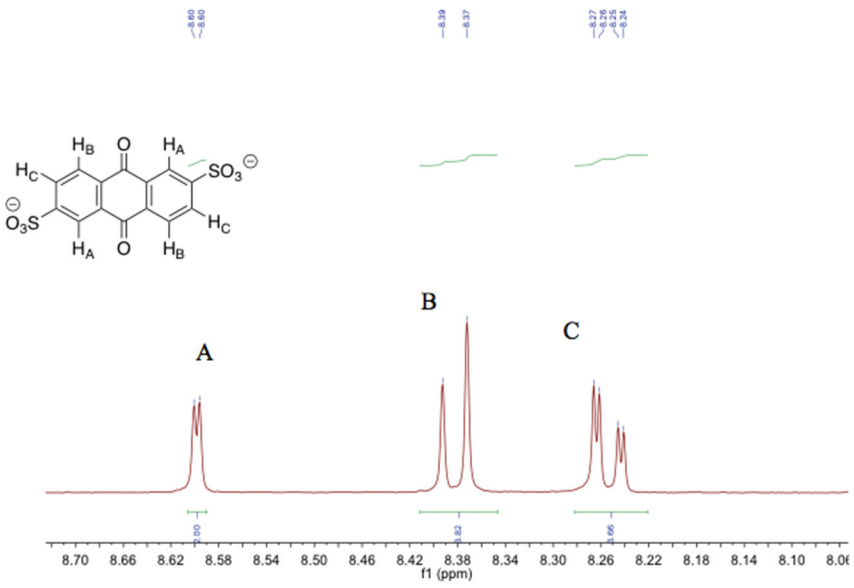
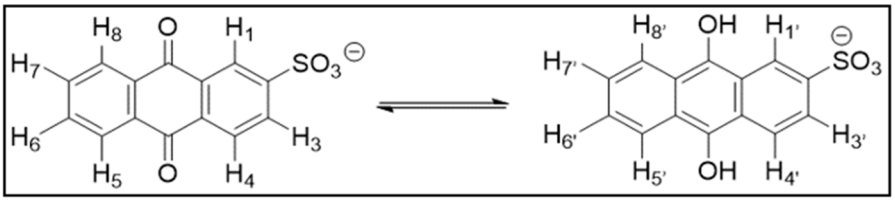
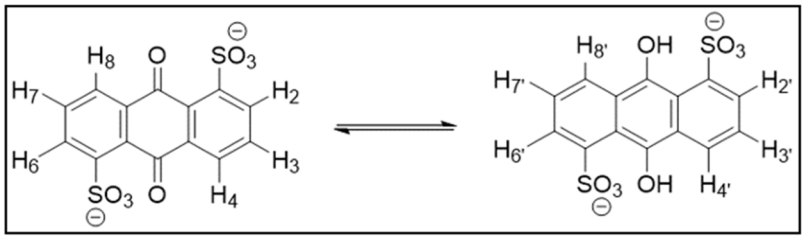


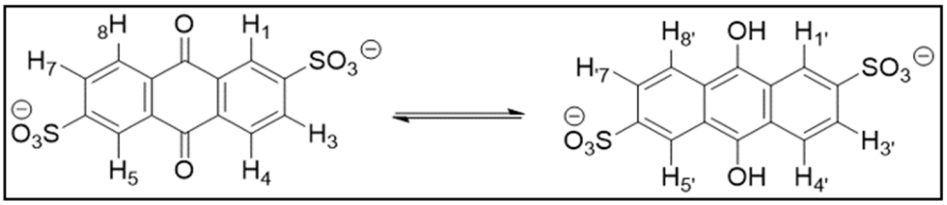
Figure B- 7 ^{1}H NMR spectra AQDS-2,6 2.5mM in D_2O, 298 K



Scheme B- 1 Photoreduction of AQS-2



Scheme B- 2 Photoreduction of AQS-1,5



Scheme B- 3 Photoreduction of AQS-2,6

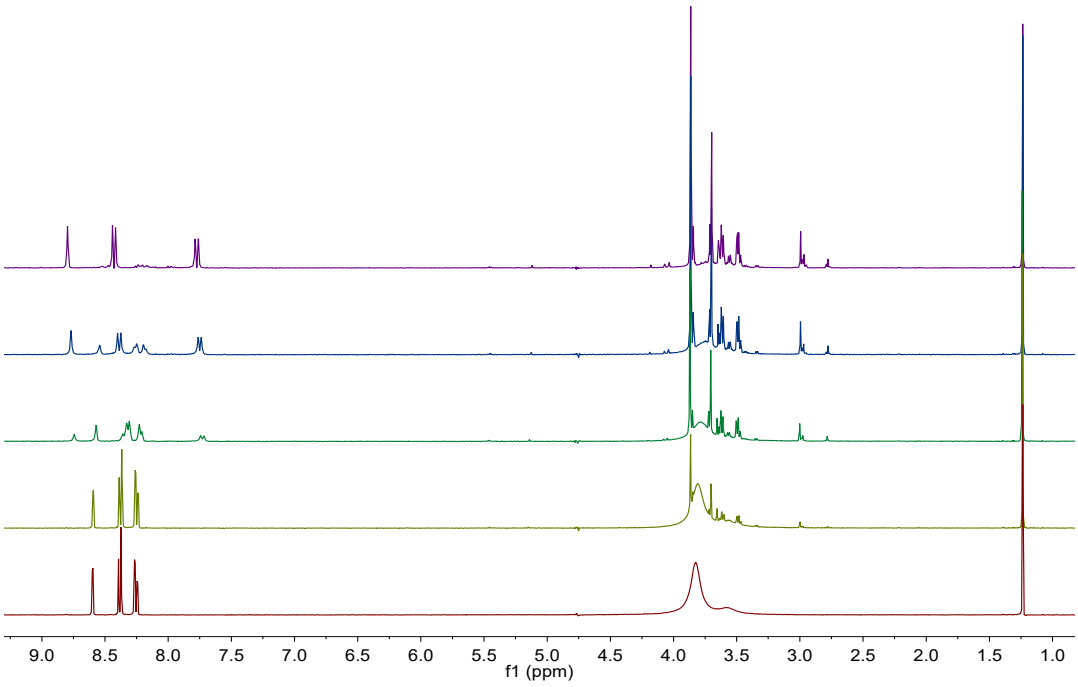


Figure B- 8 ^{1}H NMR spectra of 2.5mM AQDS-2,6 in10mM Ca-EDTA, 298 K. Photolysis Rayonet 350 nm. Times points bottom to top : 0, 1, 5, 10, 20 min

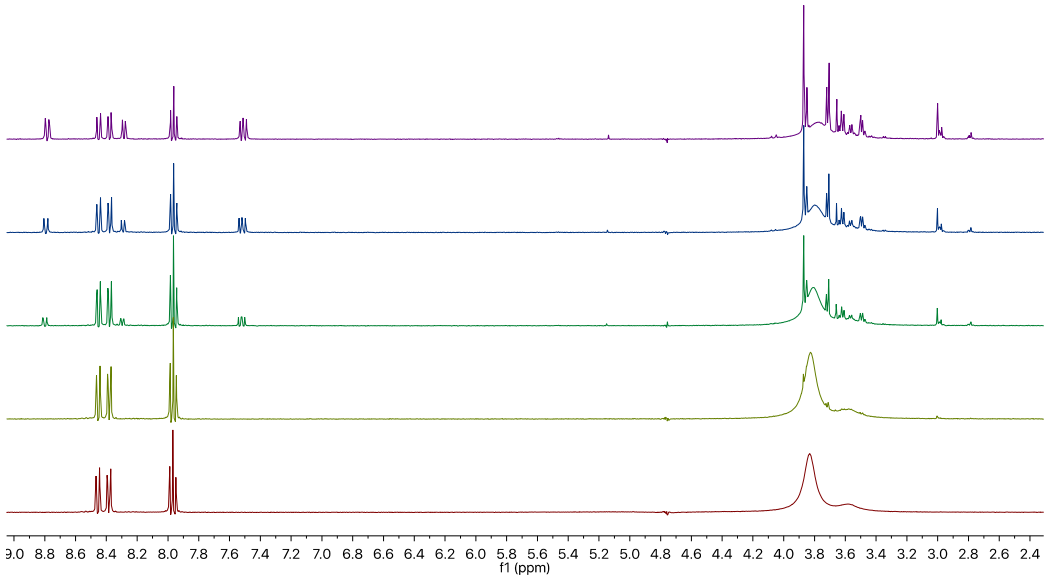


Figure B- 9 H NMR spectra of 2.5mM AQDS1,5 in10mM Ca-EDTA, 298 K. Photolysis Rayonet 350 nm. Times points bottom to top : 0, 1, 5, 10, 20 min

Sample Integration Method of Anthraquinone and EDTA signals :

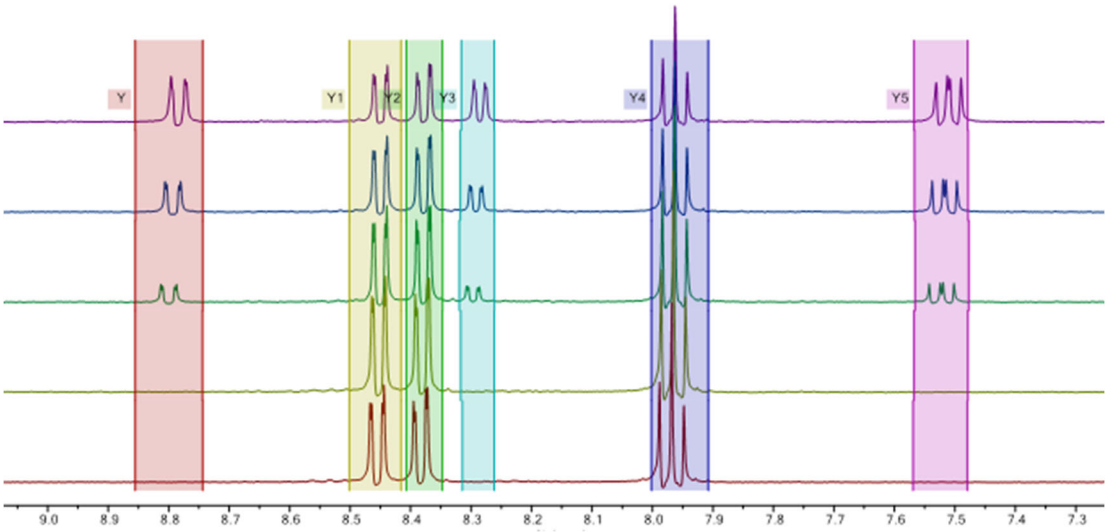


Figure B- 10 Sample integration figure of anthraquinone region

Conc X= (AreaUnknown/AreaSTD)*(ProtonsSTD/ProtonsX)*COncSTD

Table B- 1 Sample integration values for anthraquinone relative concentration calculations for photolysis time course

Time	Y(X)	Y'(X)	A'	Y1(X)	Y1'(X)	A	Y2(X)	Y2'(X)	B	Y3(X)	Y3'(X)	B'
	Integral(8.8			Integral(8.5			Integral(8.4			Integral(8.3		
min	55,8.744)	proton	mM	01,8.416)	proton	mM	07,8.347)	proton	mM	04,8.262)	proton	mM
0	348.031	2	0.03	25141.411	2	1.84	24469.702	2	1.79	624.178	2	0.05
1	696.725	2	0.04	30779.913	2	1.78	29858.103	2	1.73	707.625	2	0.04
5	4679.714	2	0.27	23771.431	2	1.39	24179.215	2	1.42	4978.052	2	0.29
10	8432.248	2	0.49	20197.315	2	1.19	20455.312	2	1.20	8071.512	2	0.47
20	14102.162	2	0.82	15259.861	2	0.89	15274.432	2	0.89	12398.432	2	0.72

Time	Y4(X)	Y4'(X)	C	Y5(X)	Y5'(X)	C'	Y8(X)		tBOH
	Integral(8.0			Integral(7.5			Integral(1.2		
min	02,7.908)	proton	mM	99,7.479)	proton	mM	68,1.174)	proton	mM
0	28706.826	2	2.10	62.589	2	0.00	32531.981	9	5.3
1	35769.976	2	2.07	74.47	2	0.00	41150.927	9	5.3
5	29786.251	2	1.75	5873.1	2	0.34	40674.378	9	5.3
10	25323.03	2	1.49	10359.321	2	0.61	40649.863	9	5.3
20	18701.235	2	1.09	16812.766	2	0.98	41054.362	9	5.3

Table B-3 ^{1}H NMR calculated relative concentrations for photolysis time course of 2.0 mM AQDS-2, 10mM Ca-EDTA, 5mMtBOH Coaxial, 350 nm Rayonet

AQS-2

Time	A_1	B_4	C_3	$D_{5,8}$	$E_{6,7}$	A_1'	B_4'	C_3'	$D_{5,8}$'	$E_{6,7}$'
min	mM	mM	mM	mM	mM	mM	mM	mM	mM	mM
0.00	1.68	2.30	2.24	2.13	2.42	0.00	—	0.03	0.07	0.01
1.00	1.01	2.05	1.98	1.84	2.28	0.03	—	0.06	—	—
5.00	0.73	—	—	1.27	1.32	0.59	—	1.03	—	1.01
10.00	—	—	—	0.70	—	1.03	1.45	0.00	1.70	1.91
20.00	0.07	—	0.22	—	0.24	1.07	1.64	1.86	1.58	1.82

Table B- 2 ^{1}H NMR calculated relative concentrations for photolysis time course of 2.0 mM AQDS-2,6 in 10mM Ca-EDTA, 5mMtBOH Coaxial, 350 nm Rayonet

AQDS-2,6

Time	$A_{1,5}$	$B_{4,8}$	$C_{3,7}$	$A'_{1,5}$	$B'_{4,8}$	$C'_{3,7}$
min	mM	mM	mM	mM	mM	mM
0.00	1.62	2.81	2.55	0.01	0.03	0.01
1.00	1.11	2.52	2.38	0.00	0.05	0.02
5.00	1.02	2.26	1.51	0.49	0.12	0.77
10.00	0.64	0.93	0.74	1.06	1.66	1.48
20.00	0.17	0.33	0.15	1.67	2.52	2.13

Table B- 3 ^{1}H NMR calculated relative concentrations for photolysis time course of 2.0 mM AQDS-1,5 in 10mM Ca-EDTA, 5 mM tBOH Coaxial, 350 nm Rayonet

AQDS-1,5

Time	$A_{4,8}$	$B_{2,6}$	$C_{3,7}$	$A_{4,8}'$	$B_{2,6}'$	$C_{3,7}'$
min	mM	mM	mM	mM	mM	mM
0.00	1.84	1.79	2.10	0.03	0.05	0.00
1.00	1.78	1.73	2.07	0.04	0.04	0.00
5.00	1.39	1.42	1.75	0.27	0.29	0.34
10.00	1.19	1.20	1.49	0.49	0.47	0.61
20.00	0.89	0.89	1.09	0.82	0.72	0.98

Appendix C Supporting Information for Riboflavin Ca-EDTA

1. Quantum Yield Calculations

Table C- 1 Table of Quantum yield calculation with standard error.

	mole calcium/L*s	Abs @366	1-10^-A	I * (1-10^-A)	Δϕ
1	4.50E-07	8.63E-02	1.80E-01	2.41E-06	0.19
2	5.32E-07	5.46E-02	1.18E-01	1.58E-06	0.34
3	8.08E-07	9.16E-02	1.90E-01	2.55E-06	0.32
4	8.15E-07	6.76E-02	1.44E-01	1.93E-06	0.42
5	7.25E-07	8.81E-02	1.84E-01	2.46E-06	0.29
6	7.68E-07	8.75E-02	1.82E-01	2.44E-06	0.31
7	8.23E-07	9.39E-02	1.94E-01	2.60E-06	0.32
				AVG	3.12E-01
				STD	6.93E-02
				STD Error	2.62E-02

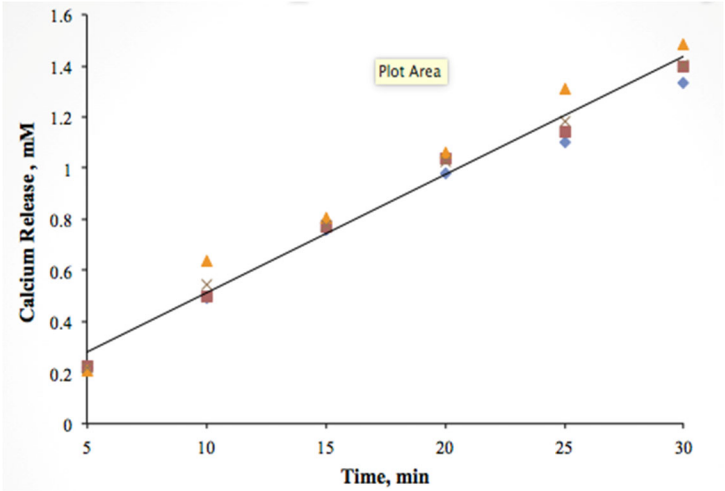


Figure C- 1 Graph of Calcium release experiments used in Quantum Yield Calculations overlapped for Error Calculation

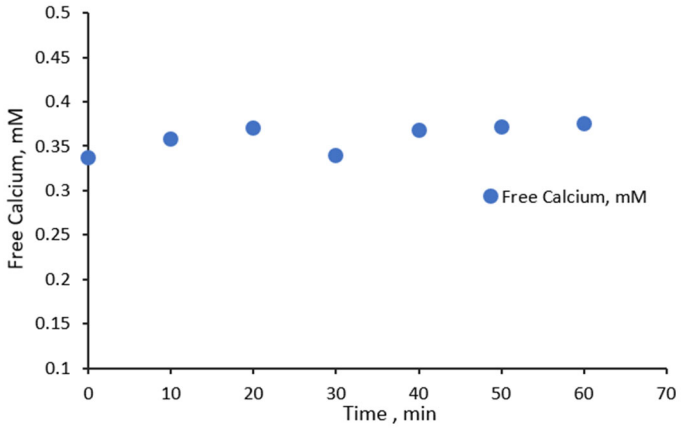


Figure C- 2 Control experiment illustrating the background level of free Ca^{2+} detected in our assay after photolysis (350 nm) for the given time in the absence of sensitizer.

Table C- 2 Table of ^{1}H NMR experiment parameters

Parameter	Value
Origin	Bruker BioSpin GmbH
Solvent	H2O+D2O
Temperature	298K
Pulse Sequence	zgesgp
Experiment	1D
Probe	5 mm BBI 1H
Number of Scans	128
Receiver Gain	2050
Relaxation Delay	2s
Pulse Width	9.57
Acquisition Time	2.0972s
Spectrometer Frequency	600.13
Spectral Width	7812.5
Nucleus	1H
Acquired Size	16384
Spectral Size	65536

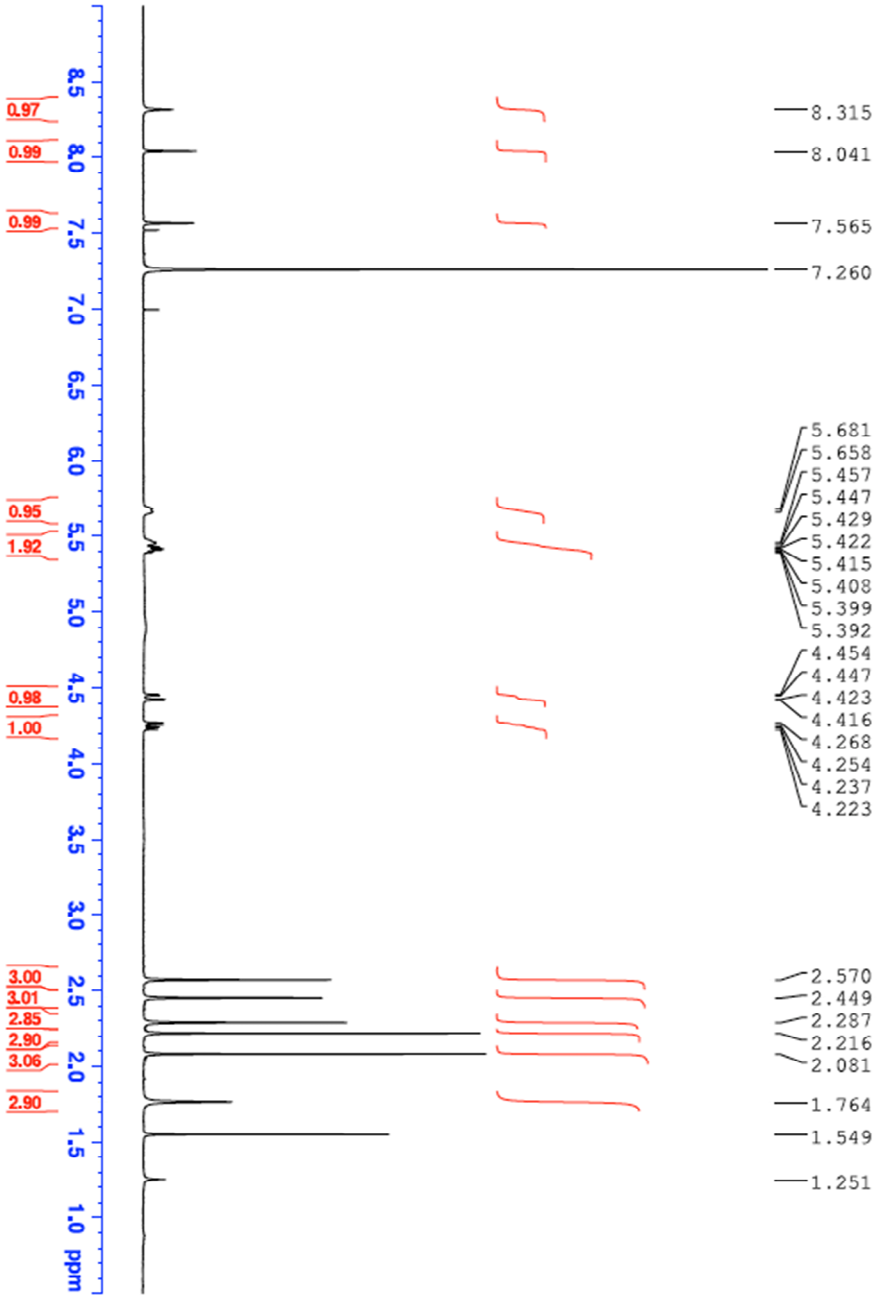


Figure C- 3 ^{1}H NMR spectrum of RBTA in CD_3Cl

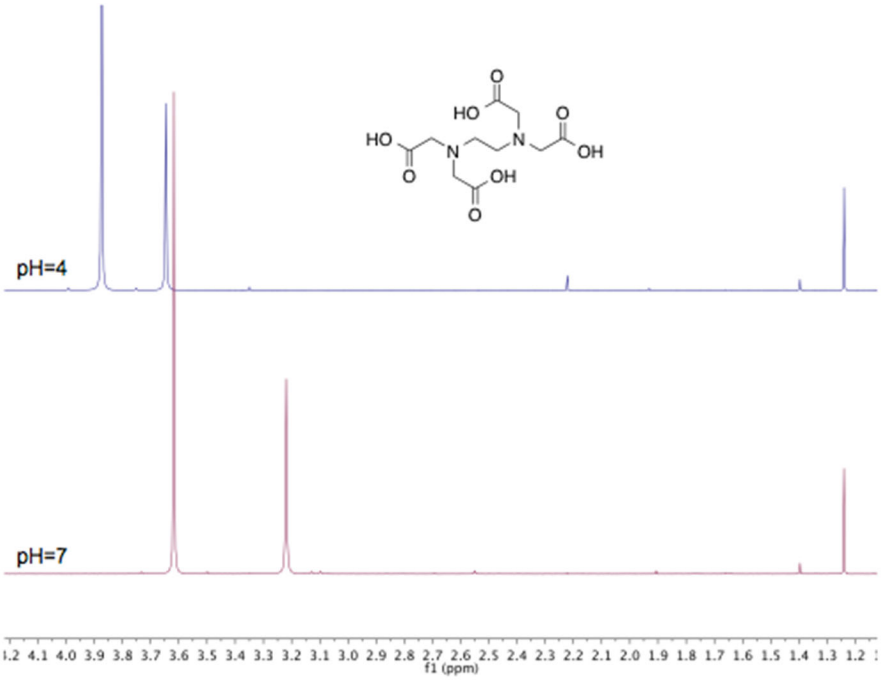


Figure C- 4 ^{1}H NMR or EDTA at acidic and neutral pH

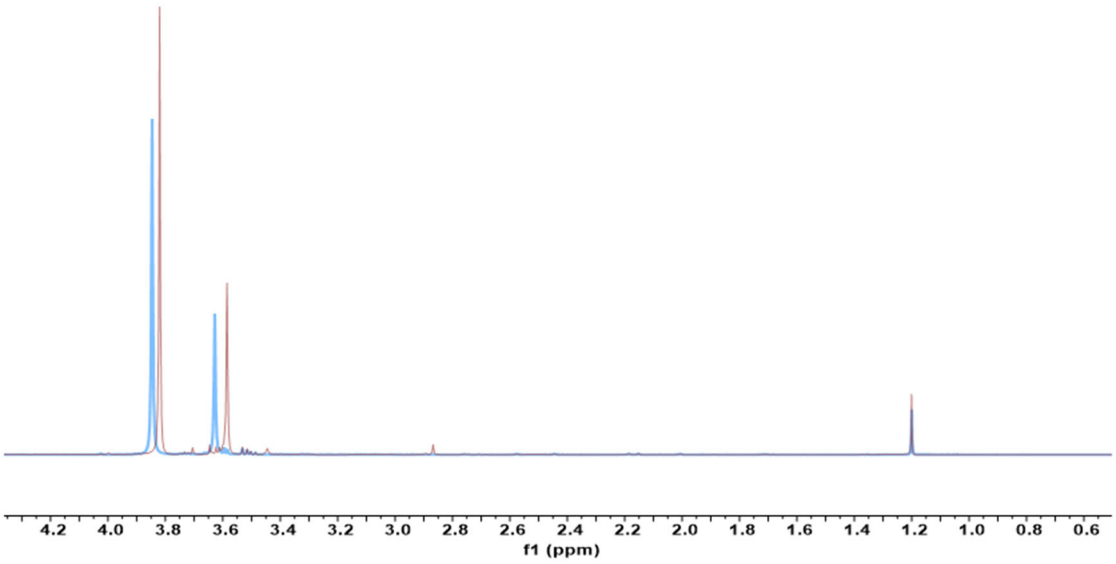


Figure C- 5 Photolysis of RBTA (2.1 μM) and EDTA (25mM) in H_2O/D_2O with a Hg lamp with a 360 nm cutoff filter. Photolysis for 40 minutes

Bibliography

1. Baigl Damien, D., Photo-actuation of liquids for light-driven microfluidics: state of the art and perspectives. *Lab on a Chip* **2012,** *12* (19), 3637-53.
2. Wu, J.; Gu, M., Microfluidic sensing: state of the art fabrication and detection techniques. *Journal of Biomedical Optics* **2011,** *16* (8).
3. Alkayyali, T. T.; Cameron, T.; Haltli, B.; Kerr, R. G.; Ahmadi, A., Microfluidic and cross-linking methods for encapsulation of living cells and bacteria - A review. *Analytica Chimica Acta* **2019,** *1053*, 1-21.
4. Zerobin, E.; Markovic, M.; Tomasikova, Z.; Qin, X. H.; Ret, D.; Steinbauer, P.; Kitzmuller, J.; Steiger, W.; Gruber, P.; Ovsianikov, A.; Liska, R.; Baudis, S., Hyaluronic acid vinyl esters: A toolbox toward controlling mechanical properties of hydrogels for 3D microfabrication. *Journal of Polymer Science* **2020,** *58* (9), 1288-1298.
5. Leijten, J.; Seo, J.; Yue, K.; Trujillo-de Santiago, G.; Tamayol, A.; Ruiz-Esparza, G. U.; Shin, S. R.; Sharifi, R.; Noshadi, I.; Álvarez, M. M.; Zhang, Y. S.; Khademhosseini, A., Spatially and temporally controlled hydrogels for tissue engineering. *Materials Science and Engineering: R: Reports* **2017,** *119*, 1-35.
6. Derakhshanfar, S.; Mbeleck, R.; Xu, K.; Zhang, X.; Zhong, W.; Xing, M., 3D bioprinting for biomedical devices and tissue engineering: A review of recent trends and advances. *Bioactive Materials* **2018,** *3* (2), 144-156.
7. Zhuang, P.; Sun, A. X.; An, J.; Chua, C. K.; Chew, S. Y., 3D neural tissue models: From spheroids to bioprinting. *Biomaterials* **2018,** *154*, 113-133.
8. Zhao, L.; Zhu, L.; Liu, F.; Liu, C.; Shan, D.; Wang, Q.; Zhang, C.; Li, J.; Liu, J.; Qu, X.; Yang, Z., pH triggered injectable amphiphilic hydrogel containing doxorubicin and paclitaxel. *International Journal of Pharmaceutics* **2011,** *410* (1-2), 83-91.
9. Dimatteo, R.; Darling, N. J.; Segura, T., In situ forming injectable hydrogels for drug delivery and wound repair. *Advanced Drug Delivery Reviews* **2018,** *127*, 167-184.
10. Li Wei, W.; Lin, J.; Wang, T.; Huang, P., Photo-triggered Drug Delivery Systems for Neuron-related Applications. *Current Medicinal chemistry* **2019,** *26* (8), 1406-1422.
11. Tao, Y.; Chan, H. F.; Shi, B. Y.; Li, M. Q.; Leong, K. W., Light: A Magical Tool for Controlled Drug Delivery. *Advanced Functional Materials* **2020,** *30* (49).
12. Poupart, O.; Schmocker, A.; Conti, R.; Moser, C.; Nuss, K. M.; Grutzmacher, H.; Mosimann, P. J.; Pioletti, D. P., In vitro Implementation of Photopolymerizable Hydrogels as a Potential Treatment of Intracranial Aneurysms. *Frontiers in Bioengineering and Biotechnology* **2020,** *8*.
13. Coyle, J. D., *Introduction to organic photochemistry*. Wiley: Chichester [West Sussex] ;, 1986.
14. Julliard, M.; Chanon, M., Photoelectrons-transfer catalysis - its connections with thermal and electrochemical analogs. *Chemical Reviews* **1983,** *83* (4), 425-506.
15. Klán, P., *Photochemistry of organic compounds from concepts to practice*. Chichester, U.K. : Wiley, 2009.: 2009.
16. Kavarnos, G. J., Fundamentals of photoinduced electron transfer. **1993**.

17. Murov, S. L.; Hug, G. L.; Carmichael, I., *Handbook of photochemistry*. 2nd ed., rev. and expanded / ed.; M. Dekker: New York :, 1993.
18. Anslyn, E. V.; Dougherty, D. A., *Modern physical organic chemistry*. University Science Books: Mill Valley, California, 2006.
19. Baroncini, M.; Groppi, J.; Corra, S.; Silvi, S.; Credi, A., Light-Responsive (Supra)Molecular Architectures: Recent Advances. *Advanced Optical Materials* **2019,** *7* (16).
20. Zimmerman, G.; Chow, L.-Y.; Paik, U.-J., The Photochemical Isomerization of Azobenzene1. *Journal of the American Chemical Society* **1958,** *80* (14), 3528-3531.
21. Bibal, B.; Mongin, C.; Bassani, D. M., Template effects and supramolecular control of photoreactions in solution. *Chemical Society Reviews* **2014,** *43* (12), 4179-4198.
22. Mukherjee, A.; Ghosh, S., Phototriggered Supramolecular Assembly. *ACS Omega* **2020,** *5* (50), 32140-32148.
23. Stranius, K.; Börjesson, K., Determining the Photoisomerization Quantum Yield of Photoswitchable Molecules in Solution and in the Solid State. *Scientific Reports* **2017,** *7* (1), 41145.
24. Kathan, M.; Hecht, S., Photoswitchable molecules as key ingredients to drive systems away from the global thermodynamic minimum. *Chemical Society Reviews* **2017,** *46* (18), 5536-5550.
25. Deshmukh, S.; Bromberg, L.; Smith, K. A.; Hatton, T. A., Photoresponsive Behavior of Amphiphilic Copolymers of Azobenzene and N,N-Dimethylacrylamide in Aqueous Solutions. *Langmuir* **2009,** *25* (6), 3459-3466.
26. Mattay, J., Photoinduced Electron Transfer I. Springer Berlin Heidelberg: Berlin, Heidelberg, 1990.
27. Ceroni, P.; Credi, A.; Venturi, M., Light to investigate (read) and operate (write) molecular devices and machines. *Chemical Society Reviews* **2014,** *43* (12), 4068-4083.
28. Lee, S. H.; Choi, D. S.; Kuk, S. K.; Park, C. B., Photobiocatalysis: Activating Redox Enzymes by Direct or Indirect Transfer of Photoinduced Electrons. *Angewandte Chemie-International Edition* **2018,** *57* (27), 7958-7985.
29. Dadashi-Silab, S.; Doran, S.; Yagci, Y., Photoinduced Electron Transfer Reactions for Macromolecular Syntheses. *Chemical Reviews* **2016,** *116* (17), 10212-10275.
30. Rehm, D.; Weller, A., Kinetics and mechanics of electron transfer during fluorescence quenching in acetonitrile. *Berichte Der Bunsen-Gesellschaft Fur Physikalische Chemie* **1969,** *73* (8-9), 834-&.
31. Rehm, D.; Weller, A., Kinetics of fluorescence quenching by electron and H-atom transfer. *Israel Journal of Chemistry* **1970,** *8* (2), 259-&.
32. Kavarnos, G. J., *Fundamentals of photoinduced electron transfer*. VCH Publishers: New York, NY, 1993.
33. Hoffmann, N., Chemical Photocatalysis. Edited by Burkhard König. *Angewandte Chemie International Edition* **2013,** *52* (44), 11456-11456.

34. Zana, R., Dynamics in Micellar Solutions of Surfactants. *Surfactant science series.* **2005,** *125*, 75-160.
35. Hassan, P. A.; Verma, G.; Ganguly, R., 1 - Soft Materials — Properties and Applications. In *Functional Materials*, Banerjee, S.; Tyagi, A. K., Eds. Elsevier: London, 2012; pp 1-59.
36. Trickett, K.; Eastoe, J., Surfactant-based gels. *Advances in Colloid and Interface Science* **2008,** *144* (1-2), 66-74.
37. Dreiss, C. A., Wormlike micelles: where do we stand? Recent developments, linear rheology and scattering techniques. *Soft Matter* **2007,** *3* (8), 956-970.
38. Lin, Z.; Cai, J. J.; Scriven, L. E.; Davis, H. T., Spherical-to-wormlike micelle transition in CTAB solutions. *Journal of Physical Chemistry* **1994,** *98* (23), 5984-5993.
39. Gonzalez, Y. I.; Kaler, E. W., Cryo-TEM studies of worm-like micellar solutions. *Current Opinion in Colloid & Interface Science* **2005,** *10* (5-6), 256-260.
40. Barnes, H. A.; Hutton, J. F.; Walters, K., *An introduction to rheology*. Elsevier Distributors for the U.S. and Canada, Elsevier Science Pub. Co.: Amsterdam ; New York, 1989.
41. Goodwin, J. W.; Hughes, R. W., Rheology for chemists : an introduction. 2nd ed. ed.; Royal Society of Chemistry: Cambridge, 2008.
42. Clausen, T. M.; Vinson, P. K.; Minter, J. R.; Davis, H. T.; Talmon, Y.; Miller, W. G., Viscoelastic micellar solutions- microscopy and rheology. *Journal of Physical Chemistry* **1992,** *96* (1), 474-484.
43. Macosko, C. W., Rheology : principles, measurements, and applications. VCH: New York, 1994.
44. Morrison, F. A., Understanding rheology. Oxford University Press: New York, 2001.
45. Malkin, A. I. A. k.; Isayev, A. I., Rheology : concepts, methods, and applications. 3rd edition. ed.; ChemTec Publishing: Toronto, 2017.
46. Janmey, P. A.; Georges, P. C.; Hvidt, S., Basic rheology for biologists. In *Cell Mechanics*, Wang, Y. L.; Discher, D. E., Eds. Elsevier Academic Press Inc: San Diego, 2007; Vol. 83, pp 3-27.
47. Dreiss, C. A., Wormlike Micelles: An Introduction. In *Wormlike Micelles: Advances in Systems, Characterisation and Applications*, Dreiss, C. A.; Feng, Y., Eds. 2017; Vol. 6, pp 1-8.
48. Wolff, T.; Emming, C. S.; Suck, T. A.; Vonbunau, G., Photorheological effectsin micellar solutions containing anthracene-derivatives - A rheological and static low-angle light-scattering study. *Journal of Physical Chemistry* **1989,** *93* (12), 4894-4898.
49. Aguilar, M. a. R.; Román, J. S., *Smart Polymers and Their Applications*. Woodhead Publishing: Burlington, 2014.
50. Wicaksono, G.; Djordjevic, I.; Shah, A. H.; Steele, T. W. J., Photorheology of bioadhesive dendrimer polycaprolactone composites. *Polymer Testing* **2019,** *80*.
51. Ketner, A. M.; Kumar, R.; Davies, T. S.; Elder, P. W.; Raghavan, S. R., A simple class of photorheological fluids: Surfactant solutions with viscosity tunable by light. *Journal of the American Chemical Society* **2007,** *129* (6), 1553-1559.

52. Turro, N. J.; Ramamurthy, V.; Scaiano, J. C., *Principles of molecular photochemistry : an introduction*. University Science Books: Sausalito, Calif. :, 2009.
53. Davies, T. S.; Ketner, A. M.; Raghavan, S. R., Self-assembly of surfactant vesicles that transform into viscoelastic wormlike micelles upon heating. *Journal of the American Chemical Society* **2006,** *128* (20), 6669-6675.
54. Baglioni, P.; Braccalenti, E.; Carretti, E.; Germani, R.; Goracci, L.; Savelli, G.; Tiecco, M., Surfactant-Based Photorheological Fluids: Effect of the Surfactant Structure. *Langmuir* **2009,** *25* (10), 5467-5475.
55. Borak, J. B.; Lee, H. Y.; Raghavan, S. R.; Falvey, D. E., Application of PET deprotection for orthogonal photocontrol of aqueous solution viscosity. *Chemical Communications* **2010,** *46* (47), 8983-8985.
56. Bachofer, S. J.; Simonis, U.; Nowicki, T. A., Orientational binding of substituted naphthoate counterions to the tetradecyltrimethyammonium bromide micellar interface. *Journal of Physical Chemistry* **1991,** *95* (1), 480-488.
57. Liu, T. Q.; Xue, F. F.; Yi, P.; Xia, Z. Y.; Bong, J. F.; Li, X. F., Structure-Property Relationship of Light-Responsive Wormlike Micelles Using Methoxycinnamate Derivatives as Light-Switchable Molecules. *Acta Physico-Chimica Sinica* **2020,** *36* (10).
58. Li, W.; Zhang, M.; Zhang, J.; Han, Y., Self-assembly of cetyl trimethylammonium bromide in ethanol-water mixtures. *Frontiers of Chemistry in China* **2006,** *1* (4), 438-442.
59. Koehler, R. D.; Raghavan, S. R.; Kaler, E. W., Microstructure and dynamics of wormlike micellar solutions formed by mixing cationic and anionic surfactants. *Journal of Physical Chemistry B* **2000,** *104* (47), 11035-11044.
60. Walker, L. M., Rheology and structure of worm-like micelles. *Current Opinion in Colloid & Interface Science* **2001,** *6* (5-6), 451-456.
61. Yan, Z. H.; Qian, F.; Sun, H. N.; Lu, X.; Li, Y.; Lv, H. B.; Dai, C. L.; Jiao, M. L., Study on the mechanism of the effect of coumaric acid with different hydroxyl substituent positions on constructing light-regulated wormlike micelles. *Journal of Molecular Liquids* **2020,** *315*.
62. Mulder, F. A. A.; Filatov, M., NMR chemical shift data and ab initio shielding calculations: emerging tools for protein structure determination. *Chemical Society Reviews* **2010,** *39* (2), 578-590.
63. Roggatz, C. C.; Lorch, M.; Benoit, D. M., Influence of Solvent Representation on Nuclear Shielding Calculations of Protonation States of Small Biological Molecules. *Journal of Chemical Theory and Computation* **2018,** *14* (5), 2684-2695.
64. Kreke, P. J.; Magid, L. J.; Gee, J. C., H-1 and C-13 NMR studies of mixed counterion, cetyltrimethylammonium bromide cetyltrimethylammonium dichlorobenzoate, surfactant solutions: The intercalation of aromatic counterions. *Langmuir* **1996,** *12* (3), 699-705.
65. Eriksson, J. C.; Gillberg, G., NMR-studies of solubilisation of aromatic compounds in cetyltrimethylammonium bromide solution 2. *Acta Chemica Scandinavica* **1966,** *20* (8), 2019-&.

66. Walker, F.; Isabettini, S.; Kuster, S.; Fischer, P.; Lutz-Bueno, V., Molecular interactions and the viscoelasticity of micellar aggregates. *Physics of Fluids* **2019,** *31* (8).
67. Bachofer, S. J.; Turbitt, R. M., The orientational binding of subtituted benzoate anions at the cetyltrimethyl ammonium bromide interface. *Journal of Colloid and Interface Science* **1990,** *135* (2), 325-334.
68. Oh, H.; Ketner, A. M.; Heymann, R.; Kesselman, E.; Danino, D.; Falvey, D. E.; Raghavan, S. R., A simple route to fluids with photo-switchable viscosities based on a reversible transition between vesicles and wormlike micelles. *Soft Matter* **2013,** *9* (20), 5025-5033.
69. Li, J.; Zhao, M. W.; Zhou, H. T.; Gao, H. J.; Zheng, L. Q., Photo-induced transformation of wormlike micelles to spherical micelles in aqueous solution. *Soft Matter* **2012,** *8* (30), 7858-7864.
70. Lambert, J. B., *Organic structural spectroscopy*. Prentice Hall: Upper Saddle River, N.J., 1998.
71. Lindon, J. C., Nuclear Magnetic Resonance Spectroscopy | Multidimensional NMR Spectroscopy☆. In *Encyclopedia of Analytical Science (Third Edition)*, Worsfold, P.; Poole, C.; Townshend, A.; Miró, M., Eds. Academic Press: Oxford, 2016; pp 248-256.
72. Claridge, T. D. W., High-resolution NMR techniques in organic chemistry. Third edition. ed.; Elsevier: Amsterdam ;, 2016.
73. Becker, B. A., Ligand–Protein Binding and Screening Using NMR Spectroscopy. In *Encyclopedia of Spectroscopy and Spectrometry (Third Edition)*, Lindon, J. C.; Tranter, G. E.; Koppenaal, D. W., Eds. Academic Press: Oxford, 2017; pp 579-585.
74. Bovey, F. A.; Mirau, P. A., 3 - The solution characterization of polymers. In *NMR of Polymers*, Bovey, F. A.; Mirau, P. A., Eds. Academic Press: San Diego, 1996; pp 155-241.
75. Tu, Y.; Chen, Q. Z.; Shang, Y. Z.; Teng, H. N.; Liu, H. L., Photoresponsive Behavior of Wormlike Micelles Constructed by Gemini Surfactant 12-3-12.2Br(-) and Different Cinnamate Derivatives. *Langmuir* **2019,** *35* (13), 4634-4645.
76. Lucas, X.; Bauzá, A.; Frontera, A.; Quiñonero, D., A thorough anion–π interaction study in biomolecules: on the importance of cooperativity effects. *Chemical Science* **2016,** *7* (2), 1038-1050.
77. Clinckspoor, K. J.; Ito, T. H.; Sabadini, E., A Rehage-Hoffmann rheological approach to worm-like micelles of C16TAB and ortho-hydroxycinnamate. *Colloid and Polymer Science* **2015,** *293* (11), 3267-3273.
78. Heerdt, G.; Tranca, I.; Markvoort, A. J.; Szyja, B. M.; Morgon, N. H.; Hensen, E. J. M., Photoisomerization induced scission of rod-like micelles unravelled with multiscale modeling. *Journal of Colloid and Interface Science* **2018,** *510*, 357-367.
79. Chu, Z.; Dreiss, C. A.; Feng, Y., Smart wormlike micelles. *Chemical Society Reviews* **2013,** *42* (17), 7174-7203.

80. Cory, R. M.; McKnight, D. M., Fluorescence spectroscopy reveals ubiquitous presence of oxidized and reduced quinones in dissolved organic matter. *Environmental Science & Technology* **2005,** *39* (21), 8142-8149.
81. Rajendran, M., Quinones as photosensitizer for photodynamic therapy: ROS generation, mechanism and detection methods. *Photodiagnosis and Photodynamic Therapy* **2016,** *13*, 175-187.
82. Liu, C.; Zachara, J. M.; Foster, N. S.; Strickland, J., Kinetics of reductive dissolution of hematite by bioreduced anthraquinone-2,6-disulfonate. *Environ. Sci. Technol.* **2007,** *41* (22), 7730-7735.
83. Loeff, I.; Rabani, J.; Treinin, A.; Linschitz, H., Charge transfer and reactivity of n.pi.* and .pi..pi.* organic triplets, including anthraquinonesulfonates, in interactions with inorganic anions: a comparative study based on classical Marcus theory. *Journal of the American Chemical Society* **1993,** *115* (20), 8933-8942.
84. Loeff, I.; Treinin, A.; Linschitz, H., Photochemistry of 9,10-Anthraquinone-2-sufonate in solution. 1. Intermediates and mechanism. *Journal of Physical Chemistry* **1983,** *87* (14), 2536-2544.
85. Loeff, I.; Treinin, A.; Linschitz, H., Photochemistry of 9,10-anthraquinone-2-sulfonate in solution. 1. Intermediates and mechanism. *The Journal of Physical Chemistry* **1983,** *87* (14), 2536-2544.
86. Cooper, H. R., Photoreduction of anthraquinone sulphonates in aqueous organic media. *Transactions of the Faraday Society* **1966,** *62* (526P), 2865-&.
87. Loeff, I.; Rabani, J.; Treinin, A.; Linschitz, H., Charge-transfer and reactivity of n-pi* and pi-pi* organic triplets, including anthraquinonesulfonates, in interactions with inorganic anions- A comparative-study based on classical Marcus theory. *Journal of the American Chemical Society* **1993,** *115* (20), 8933-8942.
88. Beckert, D.; Fessenden, R. W., Time-resolved ESR study of spin exchange processes in the photoreduction of 9,10-anthraquinone-1,5-disulfonate. *J. Phys. Chem.* **1996,** *100* (5), 1622-1629.
89. Cooper, H. R., Photoreduction of anthraquinone sulphonates in aqueous organic media. *Transactions of the Faraday Society* **1966,** *62* (0), 2865-2875.
90. Shi, Z.; Zachara, J. M.; Shi, L.; Wang, Z.; Moore, D. A.; Kennedy, D. W.; Fredrickson, J. K., Redox Reactions of Reduced Flavin Mononucleotide (FMN), Riboflavin (RBF), and Anthraquinone-2,6-disulfonate (AQDS) with Ferrihydrite and Lepidocrocite. *Environ. Sci. Technol.* **2012,** *46* (21), 11644-11652.
91. Moore, J. N.; Phillips, D.; Nakashima, N.; Yoshihara, K., Photophysics and photochemistry of sulfonated derivatives of 9,10-anthraquinone-strong versus weak sensitizers. *Journal of the Chemical Society-Faraday Transactions Ii* **1987,** *83*, 1487-1508.
92. Anwaruddin, Q.; Santappa, M., Anthraquinone sulfonates as photoinitiators of vinyl polymerization. *Journal of Polymer Science Part B-Polymer Letters* **1967,** *5* (5PB), 361-+.
93. Geuskens, G.; Etoc, A.; Di Michele, P., Surface modification of polymers - VII. Photochemical grafting of acrylamide and N-isopropylacrylamide onto polyethylene

initiated by anthraquinone-2-sulfonate adsorbed at the surface of the polymer. *European Polymer Journal* **2000,** *36* (2), 265-271.
94. Romero, N. A.; Nicewicz, D. A., Organic Photoredox Catalysis. *Chem. Rev.* **2016,** *116* (17), 10075-10166.
95. Phillips, G. O.; Worthing.Nw; McKellar, J. F.; Sharpe, R. R., Role of sodium 9,10-anthraquinone-2-sulphonate in photo-oxidation reactions. *Journal of the Chemical Society a -Inorganic Physical Theoretical* **1969,** (5), 767-&.
96. Geimer, J.; Beckert, D., Study of radical pairs generated by photoreduction of anthraquinone-2,6-disulfonic acid with thymine by Fourier transform electron paramagnetic resonance. *Chemical Physics Letters* **1998,** *288* (2-4), 449-458.
97. Gan, H.; Whitten, D. G., A sterically controlled recyclable system - reversible photoredox reactions between anthraquinone and hindered tertiary-amines. *Journal of the American Chemical Society* **1993,** *115* (18), 8031-8037.
98. Babay, P. A.; Emilio, C. A.; Ferreyra, R. E.; Gautier, E. A.; Gettar, R. T.; Litter, M. I., Kinetics and mechanisms of EDTA photocatalytic degradation with TiO2 under different experimental conditions. *International Journal of Photoenergy* **2001,** *3*.
99. Mansilla, H. D.; Bravo, C.; Ferreyra, R.; Litter, M. I.; Jardim, W. F.; Lizama, C.; Freer, J.; Fernandez, J., Photocatalytic EDTA degradation on suspended and immobilized TiO2. *J. Photochem. Photobiol. A-Chem.* **2006,** *181* (2-3), 188-194.
100. Liu, X.; Fan, J. H.; Ma, L. M., Oxidative Degradation of EDTA in Aqueous Solution by the Bimetallic Fe-Cu. *Water Air and Soil Pollution* **2013,** *224* (5).
101. Lockhart, H. B.; Blakeley, R. V., Aerobic Photodegradation of Fe(Iii)-(Ethylenedinitrilo)-Tetraacetate (Ferric Edta) - Implications for Natural-Waters. *Environmental Science & Technology* **1975,** *9* (12), 1035-1038.
102. Sorensen, M.; Zurell, S.; Frimmel, F. H., Degradation pathway of the photochemical oxidation of ethylenediaminetetraacetate (EDTA) in the UV/H2O2-process. *Acta Hydrochimica Et Hydrobiologica* **1998,** *26* (2), 109-115.
103. Flatau, A. B.; Chong, K. P., Dynamic smart material and structural systems. *Engineering Structures* **2002,** *24* (3), 261-270.
104. Ellis-Davies, G. C. R., Development and application of caged calcium. *Biophotonics, Pt A* **2003,** *360*, 226-238.
105. Ellis-Davies, G. C. R., Neurobiology with caged calcium. *Chemical Reviews* **2008,** *108* (5), 1603-1613.
106. Baginski, E. S.; Marie, S. S.; Clark, W. L.; Zak, B., Direct Microdetermination of Serum-Calcium. *Clinica Chimica Acta* **1973,** *46* (1), 49-54.
107. Corns, C. M.; Ludman, C. J., Some observations on the nature of the calcium-cresolphthalein complexone reaction and its relevance to the clinical laboratory. *Annals of Clinical Biochemistry* **1987,** *24*, 345-351.
108. Harris, W. E.; Kratochvil, B., *An introduction to chemical analysis*. Saunders College Pub.: Philadelphia, 1981.
109. Bechtold, T.; Burtscher, E.; Turcanu, A., Anthraquinones as mediators for the indirect cathodic reduction of dispersed organic dyestuffs. *Journal of Electroanalytical Chemistry* **1999,** *465* (1), 80-87.

110. Zhu, W.; Nan, Y.; Huang, T.; Wu, F., The Mechanism, Thermodynamic and Kinetic Characteristics of the Microbial Reduction of Goethite Mediated by Anthraquinone-2-Sulfonate. *Geomicrobiology Journal* **2013,** *30* (10), 928-940.
111. Guin, P. S.; Das, S.; Mandal, P. C., Electrochemical Reduction of Quinones in Different Media: A Review. *International Journal of Electrochemistry* **2011,** *2011*, 816202.
112. Batchelor-McAuley, C.; Li, Q.; Dapin, S. M.; Compton, R. G., Voltammetric Characterization of DNA Intercalators across the Full pH Range: Anthraquinone-2,6-disulfonate and Anthraquinone-2-sulfonate. *Journal of Physical Chemistry B* **2010,** *114* (11), 4094-4100.
113. Bedini, A.; De Laurentiis, E.; Sur, B.; Maurino, V.; Minero, C.; Brigante, M.; Mailhot, G.; Vione, D., Phototransformation of anthraquinone-2-sulphonate in aqueous solution. *Photochemical & Photobiological Sciences* **2012,** *11* (9), 1445-1453.
114. Maddigapu, P. R.; Minero, C.; Maurino, V.; Vione, D.; Brigante, M.; Mailhot, G., Enhancement by anthraquinone-2-sulphonate of the photonitration of phenol by nitrite: Implication for the photoproduction of nitrogen dioxide by coloured dissolved organic matter in surface waters. *Chemosphere* **2010,** *81* (11), 1401-1406.
115. Babenko, S. V.; Melnikov, A. R.; Tsentalovich, Y. P.; Kruppa, A. I., Exploring the reactivity of beta-cyclodextrin-encapsulated anthraquinone-2,6-disulfonate. *Journal of Inclusion Phenomena and Macrocyclic Chemistry* **2020,** *97* (1-2), 121-127.
116. Aquino, A. M.; Abelt, C. J.; Berger, K. L.; Darragh, C. M.; Kelley, S. E.; Cossette, M. V., Synthesis and photochemistry of some anthraquinone-substituted .beta.-cyclodextrins. *Journal of the American Chemical Society* **1990,** *112* (15), 5819-5824.
117. Bharti, S. K.; Roy, R., Quantitative H-1 NMR spectroscopy. *Trac-Trends in Analytical Chemistry* **2012,** *35*, 5-26.
118. Heymann, R. R.; Thum, M. D.; Hardee, A. L.; Falvey, D. E., Visible light initiated release of calcium ions through photochemical electron transfer reactions. *Photochem. Photobiol. Sci.* **2017,** *16* (6), 1003-1008.
119. Berridge, M. J., The AM and FM of calcium signalling. *Nature* **1997,** *386* (6627), 759-760.
120. Berridge, M. J.; Lipp, P.; Bootman, M. D., The versatility and universality of calcium signalling. *Nature Reviews Molecular Cell Biology* **2000,** *1* (1), 11-21.
121. Jakkampudi, S.; Abe, M.; Komori, N.; Takagi, R.; Furukawa, K.; Katan, C.; Sawada, W.; Takahashi, N.; Kasai, H., Design and Synthesis of a 4-Nitrobromobenzene Derivative Bearing an Ethylene Glycol Tetraacetic Acid Unit for a New Generation of Caged Calcium Compounds with Two-Photon Absorption Properties in the Near-IR Region and Their Application in Vivo. *ACS Omega* **2016,** *1* (2), 193-201.
122. Cui, J.; Gropeanu, R. A.; Stevens, D. R.; Rettig, J.; Campo, A. d., New Photolabile BAPTA-Based Ca2+ Cages with Improved Photorelease. *Journal of the American Chemical Society* **2012,** *134* (18), 7733-7740.
123. Chueh, B. H.; Zheng, Y.; Torisawa, Y. S.; Hsiao, A. Y.; Ge, C.; Hsiong, S.; Huebsch, N.; Franceschi, R.; Mooney, D. J.; Takayama, S., Patterning alginate hydrogels using

light-directed release of caged calcium in a microfluidic device. *Biomed Microdevices* **2010,** *12* (1), 145-51.
124. Asthana, A.; Ho Lee, K.; Kim, K. O.; Kim, D. M.; Kim, D. P., Rapid and cost-effective fabrication of selectively permeable calcium-alginate microfluidic device using "modified" embedded template method. *Biomicrofluidics* **2012,** *6* (1), 12821-128219.
125. Oh, H.; Lu, A. X.; Javvaji, V.; DeVoe, D. L.; Raghavan, S. R., Light-Directed Self-Assembly of Robust Alginate Gels at Precise Locations in Microfluidic Channels. *ACS Applied Materials & Interfaces* **2016,** *8* (27), 17529-17538.
126. Ellis-Davies, G. C. R., Caged compounds: photorelease technology for control of cellular chemistry and physiology. *Nature Methods* **2007,** *4* (8), 619-628.
127. Adams, S. R.; Kao, J. P. Y.; Grynkiewicz, G.; Minta, A.; Tsien, R. Y., Biologically Useful Chelators That Release Ca-2+ Upon Illumination. *Journal of the American Chemical Society* **1988,** *110* (10), 3212-3220.
128. Adams, S. R.; LevRam, V.; Tsien, R. Y., A new caged Ca2+, azid-1, is far more photosensitive than nitrobenzyl-based chelators. *Chemistry & Biology* **1997,** *4* (11), 867-878.
129. Kaplan, J. H.; Ellisdavies, G. C. R., Photolabile Chelators for the Rapid Photorelease of Divalent-Cations. *Proceedings of the National Academy of Sciences of the United States of America* **1988,** *85* (17), 6571-6575.
130. Agarwal, H. K.; Janicek, R.; Chi, S.-H.; Perry, J. W.; Niggli, E.; Ellis-Davies, G. C. R., Calcium Uncaging with Visible Light. *Journal of the American Chemical Society* **2016,** *138* (11), 3687-3693.
131. Javvaji, V.; Baradwaj, A. G.; Payne, G. F.; Raghavan, S. R., Light-activated ionic gelation of common biopolymers. *Langmuir* **2011,** *27* (20), 12591-6.
132. Lee, K. Y.; Mooney, D. J., Alginate: properties and biomedical applications. *Prog Polym Sci* **2012,** *37* (1), 106-126.
133. Higham, A. K.; Bonino, C. A.; Raghavan, S. R.; Khan, S. A., Photo-activated ionic gelation of alginate hydrogel: real-time rheological monitoring of the two-step crosslinking mechanism. *Soft Matter* **2014,** *10* (27), 4990-5002.
134. Bort, G.; Gallavardin, T.; Ogden, D.; Dalko, P. I., From One-Photon to Two-Photon Probes: "Caged" Compounds, Actuators, and Photoswitches. *Angewandte Chemie-International Edition* **2013,** *52* (17), 4526-4537.
135. Ellisdavies, G. C. R.; Kaplan, J. H., Nitrophenyl-Egta, a Photolabile Chelator That Selectively Binds Ca2+ with High-Affinity and Releases It Rapidly Upon Photolysis. *Proceedings of the National Academy of Sciences of the United States of America* **1994,** *91* (1), 187-191.
136. Borak, J. B.; Falvey, D. E., Ketocoumarin dyes as electron mediators for visible light induced carboxylate photorelease. *Photochemical & Photobiological Sciences* **2010,** *9* (6), 854-860.
137. Banekovich, C.; Ott, I.; Koch, T.; Matuszczak, B.; Gust, R., Synthesis and biological activities of novel dexibuprofen tetraacetylriboflavin conjugates. *Bioorganic & Medicinal Chemistry Letters* **2007,** *17* (3), 683-687.

138. Hatchard, C. G.; Parker, C. A., A New Sensitive Chemical Actinometer. II. Potassium Ferrioxalate as a Standard Chemical Actinometer. *Proceedings of the Royal Society of London. Series A. Mathematical and Physical Sciences* **1956,** *235* (1203), 518-536.
139. Megerle, U.; Wenninger, M.; Kutta, R. J.; Lechner, R.; Konig, B.; Dick, B.; Riedle, E., Unraveling the flavin-catalyzed photooxidation of benzylic alcohol with transient absorption spectroscopy from sub-pico- to microseconds. *Physical Chemistry Chemical Physics* **2011,** *13* (19), 8869-8880.
140. Kim, J. M.; Bogdan, M. A.; Mariano, P. S., Mechanistic analysis of the 3-methyllumiflavin-promoted oxidative deamination of benzylamine - a potential model for monoamine-oxidase catalysis. *Journal of the American Chemical Society* **1993,** *115* (23), 10591-10595.
141. Garcia, J.; Silva, E., Flavin-sensitized photooxidation of amino acids present in a parenteral nutrition infusate: Protection by ascorbic acid. *Journal of Nutritional Biochemistry* **1997,** *8* (6), 341-345.
142. Lu, C. Y.; Liu, Y. Y., Electron transfer oxidation of tryptophan and tyrosine by triplet states and oxidized radicals of flavin sensitizers: a laser flash photolysis study. *Biochimica Et Biophysica Acta-General Subjects* **2002,** *1571* (1), 71-76.
143. Martin, C. B.; Tsao, M. L.; Hadad, C. M.; Platz, M. S., The reaction of triplet flavin with indole. A study of the cascade of reactive intermediates using density functional theory and time resolved infrared spectroscopy. *Journal of the American Chemical Society* **2002,** *124* (24), 7226-7234.
144. Huvaere, K.; Cardoso, D. R.; Homem-de-Mello, P.; Westermann, S.; Skibsted, L. H., Light-Induced Oxidation of Unsaturated Lipids as Sensitized by Flavins. *Journal of Physical Chemistry B* **2010,** *114* (16), 5583-5593.
145. Gorner, H., Oxygen uptake after electron transfer from amines, amino acids and ascorbic acid to triplet flavins in air-saturated aqueous solution. *Journal of Photochemistry and Photobiology B-Biology* **2007,** *87* (2), 73-80.
146. Simpson, J. T.; Krantz, A.; Lewis, F. D.; Kokel, B., Photochemical and Photophysical Studies of Amines with Excited Flavins - Relevance to the Mechanism of Action of the Flavin-Dependent Monoamine-Oxidase. *Journal of the American Chemical Society* **1982,** *104* (25), 7155-7161.
147. Fife, D. J.; Moore, W. M., Reduction and Quenching of Photoexcited Flavins by Edta. *Photochemistry and Photobiology* **1979,** *29* (1), 43-47.
148. Heelis, P. F.; Parsons, B. J.; Phillips, G. O.; McKellar, J. F., Photo-Reduction of Flavins by Amino-Acids and Edta - Continuous and Flash-Photolysis Study. *Photochemistry and Photobiology* **1979,** *30* (3), 343-347.
149. Monakhova, Y. B.; Kuballa, T.; Mildau, G.; Kratz, E.; Keck-Wilhelm, A.; Tschiersch, C.; Lachenmeier, D. W., Formaldehyde in hair straightening products: Rapid 1H NMR determination and risk assessment. *Int. J. Cosmetic Sci.* **2013,** *35* (2), 201-206.
150. Whitby, L. G., A new method for preparing flavin-adenine dinucleotide. *Biochemical Journal* **1953,** *54* (3), 437-442.
151. Burkhard, K., *Chemical Photocatalysis*. De Gruyter: Berlin, 2013.

152. Muhldorf, B.; Wolf, R., Visible-Light-Driven Aerobic Photooxidation of Aldehydes to Methyl Esters Catalyzed by Riboflavin Tetraacetate. *Chemcatchem* **2017,** *9* (6), 920-923.
153. Larson, R. A.; Stackhouse, P. L.; Crowley, T. O., Riboflavin tetraacetate - a potentially useful photosensizing agent for the treatment of contaminated waters. *Environmental Science & Technology* **1992,** *26* (9), 1792-1798.
154. Fukuzumi, S.; Yasui, K.; Suenobu, T.; Ohkubo, K.; Fujitsuka, M.; Ito, O., Efficient catalysis of rare-earth metal ions in photoinduced electron-transfer oxidation of benzyl alcohols by a flavin analogue. *Journal of Physical Chemistry A* **2001,** *105* (46), 10501-10510.
155. Remucal, C. K.; McNeill, K., Photosensitized Amino Acid Degradation in the Presence of Riboflavin and Its Derivatives. *Environmental Science & Technology* **2011,** *45* (12), 5230-5237.
156. Golanoski, K. S.; Fang, S.; Del Vecchio, R.; Blough, N. V., Investigating the Mechanism of Phenol Photooxidation by Humic Substances. *Environmental Science & Technology* **2012,** *46* (7), 3912-3920.
157. Zhang, Y.; Del Vecchio, R.; Blough, N. V., Investigating the Mechanism of Hydrogen Peroxide Photoproduction by Humic Substances. *Environmental Science & Technology* **2012,** *46* (21), 11836-11843.
158. Ashoori, M.; Saedisomeolia, A., Riboflavin (vitamin B-2) and oxidative stress: a review. *British Journal of Nutrition* **2014,** *111* (11), 1985-1991.
159. Oster, G.; Holmstrom, B.; Bellin, J. S., Photochemistry of riboflavin. *Experientia* **1962,** *18* (6), 249-&.
160. Land, E. J.; Swallow, A. J., One-electron reactions in biochemical systems as studied by pulse radiolysis. 2. RIboflavin. *Biochemistry* **1969,** *8* (5), 2117-&.
161. de la Rochette, A.; Silva, E.; Birlouez-Aragon, I.; Mancini, M.; Edwards, A. M.; Morliere, P., Riboflavin photodegradation and photosensitizing effects are highly dependent on oxygen and ascorbate concentrations. *Photochemistry and Photobiology* **2000,** *72* (6), 815-820.
162. Enns, K.; Burgess, W. H., Photochemical oxidation of ethylenediaminetetraaccetic acid and methionine by riboflavin. *Journal of the American Chemical Society* **1965,** *87* (24), 5766-&.
163. Armstrong, J. S.; Hemmerich, P.; Traber, R., Flavin sensitized photo-oxidation of (poly)amino acids - fate of the photosubstrate. *Photochemistry and Photobiology* **1982,** *35* (5), 747-751.
164. Melo, T. B.; Ionescu, M. A.; Haggquist, G. W.; Naqvi, K. R., Hydrogen abstraction by triplet flavins. I: time-resolved multi-channel absorption spectra of flash-irradiated riboflavin solutions in water. *Spectroc. Acta Pt. A-Molec. Biomolec. Spectr.* **1999,** *55* (11), 2299-2307.
165. Ahmad, I.; Fasihullah, Q.; Noor, A.; Ansari, I. A.; Ali, Q. N., Photolysis of riboflavin in aqueous solution: a kinetic study. *Int J Pharm* **2004,** *280* (1-2), 199-208.
166. Ivanov, V. L.; Uzhinov, B. M.; Lyashkevich, S. Y., The mechanism of riboflavin fluorescence quenching by nucleophiles. *Moscow University Chemistry Bulletin* **2010,** *65* (4), 229-233.

167. Sharma, A.; Schulman, S. G., *Introduction to fluorescence spectroscopy*. Wiley: New York ;, 1999.
168. Albani, J. R., *Principles and applications of fluoresence spectroscopy*. Blackwell publ.: Oxford, 2007.
169. Hollas, J. M., *Modern spectroscopy*. 4th ed. ed.; J. Wiley: Chichester ;, 2004.
170. Kaparullina, E. N.; Doronina, N. V.; Trotsenko, Y. A., Aerobic degradation of ethylenediaminetetraacetate (review). *Applied Biochemistry and Microbiology* **2011,** *47* (5), 460-473.
171. De la Fuente, J. R.; Canete, A.; Carathanassis, N.; Bernazar, L.; Saitz, C.; Diaz-Hernandez, D., Spectral and Kinetic Study of 3-Methylquinoxalin-2-ones Photoreduced by Amino Acids: N-Phenylglycine Radical Chain Reactions and N-Acetyltryptophan Decarboxylation. *J. Phys. Chem. A* **2016,** *120* (18), 2797-2807.
172. Gould, I. R.; Lenhard, J. R.; Farid, S., A curve-crossing model for oxidative decarboxylation. Kinetics of anilino carboxylate fragmentations. *J. Phys. Chem. A* **2004,** *108* (50), 10949-10956.
173. Su, Z. Y.; Mariano, P. S.; Falvey, D. E.; Yoon, U. C.; Oh, S. W., Dynamics of anilinium radical alpha-heterolytic fragmentation processes. Electrofugal group, substituent, and medium effects on desilylation, decarboxylation, and retro-aldol cleavage pathways. *Journal of the American Chemical Society* **1998,** *120* (41), 10676-10686.
174. Haas, G., Solubility and biologic activity of riboflavin derivatives. *Nutrition Reviews* **1946,** *4* (3), 93-94.
175. Fritz, B. J.; Kasai, S.; Matsui, K., PHOTOCHEMICAL PROPERTIES OF FLAVIN DERIVATIVES. *Photochemistry and Photobiology* **1987,** *45* (1), 113-117.
176. Ahmad, I.; Abbas, S. H.; Anwar, Z.; Sheraz, M. A.; Ahmed, S.; Arsalan, A.; Bano, R., Stability-Indicating Photochemical Method for the Assay of Riboflavin: Lumichrome Method. *Journal of Chemistry* **2015**.
177. Ahmad, I.; Ahmed, S.; Sheraz, M. A.; Vaid, F. H.; Ansari, I. A., Effect of divalent anions on photodegradation kinetics and pathways of riboflavin in aqueous solution. *Int J Pharm* **2010,** *390* (2), 174-82.
178. Ahmad, I.; Anwar, Z.; Iqbal, K.; Ali, S. A.; Mirza, T.; Khurshid, A.; Khurshid, A.; Arsalan, A., Effect of Acetate and Carbonate Buffers on the Photolysis of Riboflavin in Aqueous Solution: A Kinetic Study. *Aaps Pharmscitech* **2014,** *15* (3), 550-559.
179. Ahmad, I.; Fasihullah, Q.; Vaid, F. H., Effect of light intensity and wavelengths on photodegradation reactions of riboflavin in aqueous solution. *J Photochem Photobiol B* **2006,** *82* (1), 21-7.
180. Ahmad, I.; Fasihullah, Q.; Vaid, F. H., A study of simultaneous photolysis and photoaddition reactions of riboflavin in aqueous solution. *J Photochem Photobiol B* **2004,** *75* (1-2), 13-20.
181. Vaid, F. H. M.; Gul, W.; Faiyaz, A.; Anwar, Z.; Ejaz, M. A.; Zahid, S.; Ahmad, I., Divalent anion catalyzed photodegradation of riboflavin: A kinetic study. *Journal of Photochemistry and Photobiology A: Chemistry* **2019,** *371*, 59-66.